



*Nanoparticles: Synthesis, Surface Modification and
Functionalization for Biological and Environmental
Applications*

Dissertation

Zur
Erlangung des Doktorgrades
der Naturwissenschaften
(Dr. rer. nat.)

dem

Fachbereich Physik
der Philipps-Universität Marburg

vorgelegt von

Abuelmagd M. Abdelmonem

Aus

Ägypten

Marburg/Lahn, 2014

Vom Fachbereich Physik der Philipps-Universität als Dissertation
angenommen am

Erstgutachter: Prof. Dr. Wolfgang J. Parak

Zweitgutachter: Prof. Dr. Kerstin Volz

Tag der mündlichen Prüfung: 28 October 2014

Hochschulkenziffer 1180"

Die vorliegende Arbeit wurde am Fachbereich Physik
der Philipps-Universität Marburg unter der Anleitung von

Herrn Prof. Dr. Wolfgang J. Parak

in der Zeit von Januar 2011 bis Oktober 2014 angefertigt.

Dedicated to

The soul of my dear father

Acknowledgements

First of all, I would like to give a special thank to Prof. Wolfgang J. Parak for giving me the opportunity to work and study in his group and supervising me during my PhD thesis. It was my pleasure to work and study at Philipps-Universität Marburg in the Biophotonics Group under the supervision of Prof. Wolfgang J Parak with his continuous support, motivating and kind attitude through thick and thin.

Also I would like to thank my good friends and ex co-supervisors Dr. José Maria Montenegro Martos and Dr. Nadja C. Bigall for supervising me and for their support, constructive discussions, continuous motivation and advices.

As well I would like to thank Dr. Beatriz Pelaz and Dr. Pablo del Pino for their kind co-supervising me as well as having them as good friends and also for continuous collaborative and constructive discussion.

I am very grateful and would like to thank current and old members of the Biophotonics Group for their collaboration, constructive discussions and for sure not only for the work and scientific work but also for the personal cooperation, trips and good times we have spent together.

Also I am very thankful to Stefanie Kramer and Andreas Rentzos for the administrative and the technical support during my PhD in Marburg.

I would like to thank Dr. Nadja, Dr. Bea, and Dr. Pablo for proofreading the thesis.

I would like to extend my thank to our collaborative partners, special thanks to: Dr. Marco Monopli (Centre for BioNano Interactions, University College Dublin) and Dr. Adriele Prina-Mello (Trinity College Dublin) for our joint collaborative works about nanoparticles functionalization and bio nano interactions.

Also I want to thank the DFG, and NAMDIATREAM projects and the members of the project for funding this work.

I would like to express my sincere thanks to my mother, brothers, sisters and my whole family. Really I have no words able to express my sincere gratitude and appreciation for their continuous encouragement and support and for all they did for me at all the times.

Last but not least I'd like to present a special thank to my beloved wife for her help, enduring commitment, patience and great role during my PhD.

Zusammenfassung

Neben der Beschaffenheit des Kernmaterials von Nanopartikeln (NP) spielt ihre Oberfläche eine wichtige Rolle, da durch diese die physikalisch-chemischen Eigenschaften des Nanopartikels maßgeblich beeinflusst werden, was insbesondere die Wechselwirkung mit umgebenden Medien, biologischen Systemen oder der Umgebung beeinflusst, über die Art von möglichen Oberflächenmodifikationen entscheidet und letztendlich damit die Anwendungsbereiche der Nanopartikel definiert.

Das Hauptaugenmerk dieser Dissertation liegt auf der Synthese, der kontrollierten Oberflächenmodifikation, der Funktionalisierung, der Aufreinigung und schließlich der Charakterisierung von unterschiedlichen Arten von Nanopartikeln (plasmonische, magnetische und Halbleiternanopartikel) um am Ende Kolloide in hochgradig stabilen wässrigen Suspensionen zu erhalten, die sich gleichermaßen für umweltbezogene als auch für biologische Anwendungen eignen.

Der größte Teil der im Rahmen dieser Arbeit hergestellten Partikel wurde aus anorganischen Materialien hergestellt (5 nm große Au NP, 12 nm große magnetische NP aus Eisenoxid, 3 nm große Eisen-Platinum Partikel, 8 nm große Kobalt-Platinum NP, CdSe/ZnS Hybridpartikel unterschiedlicher Größenverteilungen von 3-5 nm und 7 nm große Quantenpunkte aus ZnO) und durch hydrophobische organische Moleküle, auch Surfactant- oder Ligandenmoleküle genannt, stabilisiert. Diese Liganden spielen außerdem eine wichtige Rolle um Form und Größe der Partikel während der Synthese zu kontrollieren und verhindern zusätzliche durch stabilisierende Eigenschaften, dass die NP agglomerieren.

Wasserunlösliche (durch hydrophobische Liganden stabilisierte) Nanopartikel, wurden mit Hilfe amphiphiler Polymere, nach einem bereits etablierten Verfahren, von der organischen Phase in wässrige Lösung überführt. Dieses Verfahren ist notwendig, da insbesondere für die meisten bekannten biologischen Anwendungen die Nanomaterialien wasserlöslich sein müssen. Die Stabilisierung der NP in wässriger Lösung basiert dabei auf der Wechselwirkung hydrophober Seitenketten des amphiphilen Polymers, die sich an den ebenfalls hydrophoben NP anlagern, während das hydrophile Rückgrat des Polymers Wasserlöslichkeit garantiert. Dank freier Carboxylatgruppen eignet sich das verwendete Polymer zusätzlich um die nun hydrophile Oberfläche der NP weiter mit beliebigen biologisch aktiven Molekülen zu funktionalisieren.

Die erhaltenen, Polymer-umhüllten NP wurden aufgereinigt und mit Hilfe unterschiedlicher Techniken wie Agarosegelelektrophorese, Größenausschluss-Chromatographie, UV-Vis Spektroskopie, Fluoreszenzspektroskopie (im Falle fluoreszierender Materialien), Transmissionselektronenmikroskopie (TEM) und dynamischer Lichtstreuung (DLS) charakterisiert. Eine schmale Größenverteilung der hydrodynamischen Durchmesser zusammen mit negativer Oberflächenladung (Zeta-Potential) lassen dabei auf eine hohe Qualität und kolloidale Stabilität der synthetisierten monodispersen Nanopartikel schließen.

Des Weiteren wurde die Oberfläche einiger wasserlöslicher, Polymer-umhüllter Nanopartikel entweder mit Fluoreszenzfarbstoffen (z.B. Dy-495, DY-647 oder Rhodamin), oder mit Polyethylenglycol, Folsäure oder *Methotrexat* modifiziert mit dem Ziel, multifunktionale Nanopartikel zu erzeugen, und dadurch ein großes Anwendungsspektrum in biologischen Bereichen zu ermöglichen wie Tracking, Markieren von bestimmten Strukturen, multimodale Bildgebung und gezielter Wirkstofftransport.

Abstract

In addition to the type or nature of the nanoparticles (NPs) core, the surface of the obtained nanoparticles plays a crucial role and has great impact on the physicochemical properties of the nanoparticles which reflect in turn on the nanomaterials interactions (with the surrounding medium, biological systems and environment), functionalities and their possible applications.

The general focus of this doctoral dissertation has been paid to the synthesis, controlled surface modification, functionalization, purification and characterization of different types of (plasmonic, semiconductor and magnetic) nanoparticles providing water soluble and highly colloidal stable nanoparticles proper for environmental and biological applications.

Most of the as synthesized nanoparticles are inorganic particles (e.g. 5 nm Au NPs, 12 nm magnetic iron oxide NPs, 3 nm iron platinum NPs, 8 nm cobalt platinum NPs, CdSe/ZnS core/shell QDs of different sizes from 3-5 nm to 7 nm ZnO QDs) stabilized by hydrophobic organic molecules known as the surfactant or ligand which play an important role to control the shape and growth of the during the nanoparticles synthesis in addition to its role as stabilizing agents preventing the nanoparticles to be agglomerated.

In case of water insoluble (hydrophobically capped) nanoparticles (not suitable for the biological applications), they were transformed from organic phase to aqueous environment using a very general protocol known as amphiphilic polymer coating which is based on the hydrophobic interaction between the hydrophobic ligands on the surface of the nanoparticles and the hydrophobic side chains of the used polymer. The polymer coating of originally organic-solvent soluble nanoparticles converts them to water soluble ones (thanks to the free carboxylate groups on surface) which have the ability to be further functionalized with extra functional and/or biologically active molecules of interest.

The obtained polymer coated nanoparticles were purified and characterized using different techniques, such as agarose gel electrophoresis, size exclusion chromatography, UV-Vis spectroscopy, fluorescence spectroscopy (in case of fluorescent materials), transmission electron microscopy (TEM) and dynamic light scattering (DLS). Monodisperse different types of polymer coated nanoparticles were obtained with a high quality and colloidal stability as inferred from their physicochemical properties such as narrow hydrodynamic diameter distribution and the negative surface charges expressed as zeta potential.

Furthermore, the surface of some water soluble polymer coated nanoparticles was modified with different functionalities such as some fluorophores (e.g. Dy-495, DY-647 and rhodamine), polyethylene glycol, folic acid and methotrexate to obtain multifunctional nanoparticles that could be useful for a wide range of biological applications such as tracking, labeling and multimodal imaging and targeting drug delivery.

Table of Contents

1. Introduction	1
1.1. Types of Inorganic Nanoparticles and Their Physico-Chemical Properties.....	1
1.1.1. Plasmonic Nanoparticles	1
1.1.2. Quantum Dots.....	2
1.1.3. Magnetic Nanomaterials	5
1.2. Application of Nanoparticles.....	8
1.2.1. Industrial and Technical Applications.....	8
1.2.2. Environmental Applications.....	9
1.2.3. Biological Applications.....	9
1.2.3.1. Biomedical Applications.....	9
1.2.3.2. Food and Nutrition Applications	11
1.2.3.3. Agricultural Applications.....	12
1.3. Nanomaterials: Health and Environmental Concerns	13
2. Synthesis, Surface Modification and Characterization of the Nanoparticles	15
2.1. Gold Nanoparticles	15
2.2. Transformation of Organic Soluble to Water Soluble Nanoparticles	17
2.3. Purification of the Coated Nanoparticles.....	20
Gel Electrophoresis.....	20
Size Exclusion Chromatography	21
2.4. UV-Vis Absorption Spectroscopy and Fluorescence Spectroscopy	21
2.5. Dynamic Light Scattering and ζ - Potential Measurements	21
2.6. Transmission Electron Microscopy (TEM).....	22
2.7. Magnetic Nanoparticles	23
2.7.1. Iron Oxide Nanoparticles	23
2.7.2. FePt Nanoparticles	28
2.7.3. CoPt ₃ Nanoparticles.....	31
2.8. Quantum Dots	32
2.8.1. CdSe/ZnS Core Shell Quantum Dots.....	32
Surface Modification of the Red CdSe/ZnS QDs with 2 kDa Diamine PEG	38

2.8.2. ZnO Nanoparticles.....	40
2.8.2.1. Arginine Capped ZnO Nanoparticles	40
2.8.2.2. Polymer Coated ZnO Nanoparticles	43
3. Nanoparticles: Cellular Interactions and Toxicity.....	46
3.1. Effect of PEGylation of the polymer coated Au Nanoparticles on the Cellular Uptake, Interactions and Cytotoxicity.....	46
3.2. Cellular Uptake, Interactions and Cytotoxicity of Polymer Coated CdSE/ZnS core shell QDs: 50	
4. Conclusion and Outlook.....	55
5. Publications.....	57
1.1. Nanoparticles; Synthesis, Surface Modification, Characterization and Bio Interaction ...	57
1.2. Nanoparticles in Sensing Applications	59
1.3. Reviews	60
References.....	61
Appendix.....	85

1. Introduction

Engineered nanomaterials have received a fast growing increased interest in the recent years due to their unique physical and chemical properties which are expected to open new novel avenues of different technological, environmental and biological applications of these nanomaterials in catalysts, semiconductors, sensors, drug carriers, and personal care products. Nanoscience and nanotechnology are believed to be a revolution expected to cause enormous impacts on the human life within the near future. Commercial products that contain synthetic nanomaterials are expected to grow significantly in the coming years ^[1,2].

Before to go ahead forward, it is highly important to make some definitions for nanoscience, nanotechnology and nanoparticles, which it is not so easy because there is no definitive definition for each but we will use the most commons. Nanoscience could be defined as the study of the phenomena and the manipulation of materials at atomic, molecular scales, where the properties strongly differ in comparison to their large scale counterparts and nanotechnology is design, functionalization, characterization and make use of the materials at the nanometer scale. Despite that the term “nanoparticles” refer to the materials in the range less than 1000 nm, but in the field of nanotechnology, the nanoparticles are typically in the size range between 1-100 nm ^[1].

The nanomaterials subject to the fundamental laws of the universe despite that they have properties varying to those of their bulk counterparts. The most important reasons behind that are that effects that are negligible and can be ignored at the big scales cannot be ignored at the nano-scale range such as quantum effects and the high surface area to volume ratio. ^[2]

Nanoparticles can be prepared by an enormous variety of methods which usually are categorized in two main synthetic routes which are the top down and the bottom up approaches. In the top down routes, the nanoparticles are obtained from their bulk materials using different methods and techniques like lithography and laser ablation. In contrary, in the bottom up synthesis, the nanoparticles are obtained from their basic building blocks (atoms or molecules) which react to generate the nanoparticle of the desired shape and size ^[3, 4].

Currently, nanoparticles are made out of an extremely wide variety of materials including inorganic, organic and biomolecules, and hence the nanoparticles might be categorized into two main groups “organic” and “inorganic” nanoparticles.

1.1. Types of Inorganic Nanoparticles and Their Physico-Chemical Properties

1.1.1. Plasmonic Nanoparticles

Plasmonic nanoparticles like silver and gold nanoparticles are a very important class of the inorganic nanoparticles due to their promising different applications from sensing and catalysis to biological applications ^[5-7], which are attributed to their unique electronic and optical properties, mainly the localized surface plasmon resonance (LSPR). In physics, the oscillation of a quasi free electrons gas is known as plasmon. The surface plasmon resonance

is the coherent collective oscillation of the free electrons in the conduction band due to a coherent excitation of the free electrons induced by the interaction with an electromagnetic field. When the frequency of the light (electromagnetic field) interacting with the plasmonic nanoparticle matches the frequency of the oscillating electrons, the frequency of incident photons are in resonance with the collective oscillation of the electrons in the conduction band creating a collective oscillation of electrons in resonance with the incident light frequency, the so called localized surface plasmon resonance (LSPR), on the surface of the nanoparticles^[8-14].

LSPR causes a strong extinction band (absorption and scattering) and strong electromagnetic field near the nanoparticle surface. In addition to the material of the nanoparticles, the LSPR (frequency and intensity) is also highly sensitive to the size and the shape of the nanoparticles as well as the local dielectric constant of the nanoparticles. All these unique properties of the plasmonic nanoparticles are the basis for their pioneering applications in different areas such as catalysis, sensing, Raman spectroscopy and the biological applications from diagnosis to drug delivery^[11, 15-17].

1.1.2. Quantum Dots

Highly fluorescent semiconductor nanocrystals or quantum dots (QDs), also known as artificial atoms, are a class of the inorganic nanomaterials of great importance exhibiting the so-called quantum size effect. Their composition, small size and size tunable unique optical and electronic properties give these dots extraordinary importance. The QDs are able to absorb light at a wavelength shorter than the one corresponding to the band gap energy, and reemit light (fluorescence) but in a color roughly corresponding to the band gap energy. Further characteristic features are narrow and symmetric emission spectra, broad absorption spectra and that different quantum dots with multiple size dependent fluorescence colors can be excited simultaneously using a single excitation wavelength. Furthermore, the largely reduced photobleaching compared to common organic fluorophores should be mentioned^[18-20]. The most striking optical feature of the QDs is that the color of quantum dots (absorption and emission wavelength) is size dependent and hence tunable^[21-23].

The unique properties of the QDs are attributed to the changes in the density of states and the quantum confinement associated with the size reducing to nanoscale of radius smaller than the Bohr radius. Moving down from bulk material to smaller and smaller sizes reaching certain dimensions, a new regime starts to take place making the particles exhibit changes in their optoelectronic properties. When the size is small enough, the charge carriers (electrons and holes) inside the particle start to recognize the volume limitations (the walls) of the particles and the spatial distribution of charge carriers inside the particle get confined to a restricted volume in a phenomenon known as quantum confinement or size quantization. The allowed electronic energy levels are no longer continuous or band-like as in their bulk counterparts and instead they become discrete quantized energy levels^[24-27]. As a consequence of the quantum confinement, due to the increasing in the bandgap, the onset of

the optical absorption and the maximum of the emission spectra are shifted to higher energies with decreasing the size of the nanoparticles ^[28-30].

As it is the case with the bulk semiconductors, when the energy of the incident photons is larger or equal to the bandgap energy, the electrons are photoexcited from the valence band to the conduction band creating a state consisting of an electron and a hole (a so-called exciton) exhibiting also Coulombic interactions between the negatively charged electron and the positively charged hole. The excited electrons can relax back to the valence band by recombining with the hole in processes known as electron hole recombination, which could be either a radiative or a non-radiative process. In the radiative recombination, a photon of a certain energy corresponding to the bandgap of the material is emitted. The energy (wavelength) of the emitted photon depends on the size of the QDs as well as on the material. This mechanism explains why QDs are able to absorb all wavelengths greater than their bandgap converting them to a single color.

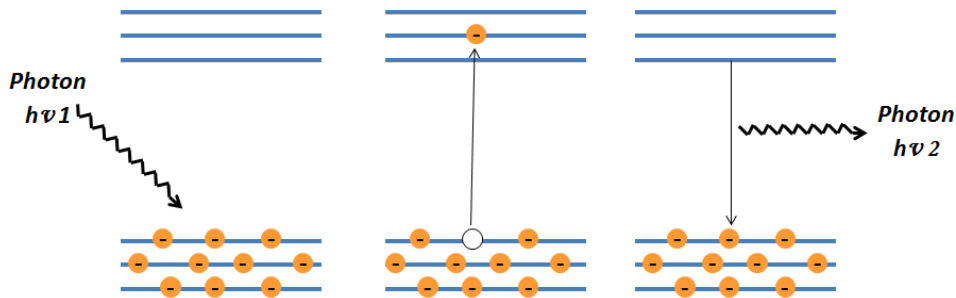


Figure 1.1: Mechanism of photoexcitation and the radiative electron-hole recombination (fluorescence)

The band gap energy in semiconductor quantum dots can be calculated using the Brus equation as follows: ^[31, 32]

$$E_{g(QDs)} = E_{g(bulk)} + \frac{h^2}{8r^2} \left(\frac{1}{m_e} + \frac{1}{m_h} \right) - \frac{1.8e^2}{4\pi\epsilon_0\epsilon r} \quad \text{Equation 1}$$

Where $E_{g(QDs)}$ and $E_{g(bulk)}$ refer to the bandgap energy of QDs and bulk semiconductor, r is the radius of the QDs, m_e and m_h are the effective electron and hole masses, h is the Planck constant, ϵ is the dielectric constant of the solid and ϵ_0 is permittivity of a vacuum;. This equation illustrates that the binding energy in quantum dots is the sum of the bandgap of the bulk material (first term $E_{g(bulk)}$), the quantum confinement (second term) based on the particle-in-a-box confinement of the exciton, and the effect of Coulomb attraction between the electron and the hole included in the third term.

Recently a fast growing interest paid to make use of the unique properties of the nanocrystals QDs in different applications like light emitting diodes and solar energy [33-35], optoelectronics [36] and the biological applications for sensing, labeling, imaging and diagnosis [19, 37-45].

ZnO QDs

Zinc oxide is an important inorganic II-VI semiconductor material with unique optical and electronical properties due to its direct wide bandgap and large exciton binding energy at room temperature. ZnO nanoparticles have a wide bandgap of 3.37 eV and a large exciton binding energy about 60 meV at room temperature. The exciton binding energy of the ZnO nanoparticles in comparison to other QDs e.g. CdSe nanoparticles makes their luminescence efficiency more thermally stable [46, 47]. In the recent years, considerable interest has been paid to ZnO nanoparticles to make use of their promising multifunctional properties such as their direct and wide bandgap [48], the high exciton binding energy, the high electron mobility, high thermal conductivity, strong luminescence, large non-linear optical coefficients, large piezoelectric constants and high transparency in the visible regime [49-57]. As a semiconductor, the optical and electronic properties of ZnO nanocrystals arise from the interaction between electrons and holes and the local environments and exhibit quantum confinement effect [58-61]. When the excitation energy of the photons exceeds the bandgap energy, the electrons in ZnO QDs get excited from the ground state (valence band) to the conduction band. The excited electrons may recombine with holes via radiative or non-radiative electron-hole recombination. The bandgap of the ZnO lies in the near UV region, but the photoluminescence (PL) of ZnO nanoparticles mostly exhibit two emission bands. The first one, the near UV emission arise from (i) the typical exciton emission as a result of the recombination of the photo-excited electrons in the conduction band with holes in the valence band [62] and/or (ii) near-band-edge emission resulting from the recombination of the photo-excited electrons in the conduction band with the holes trapped near the valence band [63]. The second emission maximum lies in the visible part of the spectrum. The mechanism of the visible emission most probably is due to trap emission. However, it is still under debate and not completely understood. There are many mechanisms which have been suggested to explain the visible photoluminescence of the ZnO nanoparticles, such as oxygen vacancies (V_O), zinc vacancies (V_{Zn}), zinc interstitials (Zn_i) [64], oxygen interstitials (O_i), and antisite oxygen (O_{Zn}) [50, 65-68]. Among the different proposed mechanisms, the most widely used are two mechanisms attributing the visible fluorescence to the presence of the oxygen vacancies [69-79].

Figure 1.2 shows a schematic illustration for the UV emission and the most widely suggested two mechanisms explaining the visible emission based on oxygen vacancies.

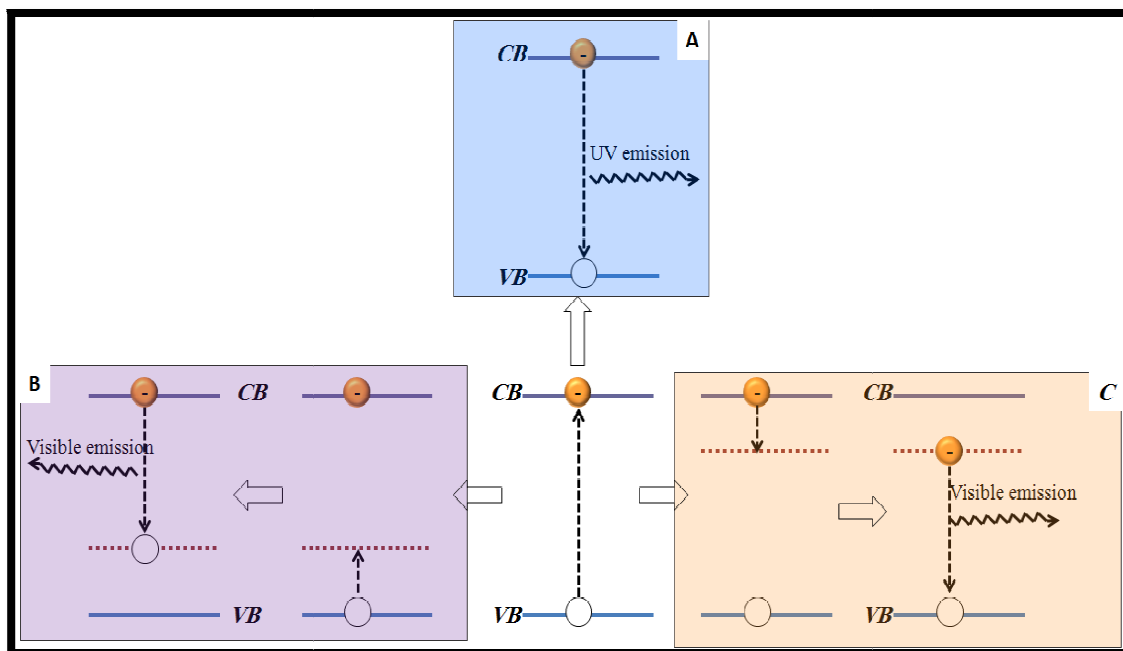


Figure 1.2: Schematic illustration for the UV emission (A), excitonic emission resulting from the recombination of the photoexcited electrons in the conduction band with holes in the valence band and the visible fluorescence resulting from recombining the shallowly trapped electrons with the deeply trapped holes (B) and recombining the deeply trapped electrons with the shallowly trapped holes (C).

As described above, ZnO exhibits promising physical and chemical properties in addition to its biocompatibility, environmental friendliness and low toxicity^[80] (ZnO is generally recognized as safe by the FDA)^[81]. ZnO nanoparticles represent a promising multifunctional material in a variety of applications such as solar cells^[55, 82-92], catalysis^[93-98], electronics, ultraviolet lasers and light emitting devices^[47, 99-105], piezoelectric devices^[53, 54] and sensors^[106-112]. In cosmetic applications, ZnO nanoparticles are used as sunscreens for the protection from the ultraviolet radiation^[113]. Furthermore, the ZnO nanoparticles are highly promising for biological applications^[114] like diagnosis and therapy (nanotheragnostic). Here, for example, applications in the selective destruction of tumors^[115-116], targeted delivery and drug release^[114], labeling and bioimaging^[71, 72, 118] are nowadays intensely investigated.

1.1.3. Magnetic Nanomaterials

Magnetic nanoparticles are a highly important class of nanomaterials expected to extend to different applications due to its unique and tunable magnetic properties which are significantly different from their bulk counterparts.

In order to make the reader understand the properties of magnetic nanoparticles, it is highly important to give a brief general overview about magnetism. The magnetism originates from the electron spin (spin magnetic moment) and the orbital motion (orbital magnetic moment) of the electrons around the nucleus. Any matter consists of atoms, and in the atom the spin

magnetic moments of some electron pairs cancel each other, and the same could happen for the orbital magnetic moments. The overall magnetic moment for an atom is the sum of all orbital and spin magnetic moments in the atom. All materials are magnetic and display some magnetic response which varies about many orders of magnitude between different materials. Some materials display much more magnetism than others where some materials have no collective interaction between the atomic magnetic moments and other materials have a very strong interaction between atomic magnetic moments. Depending on their magnetic responses, the materials can be classified as diamagnetic, paramagnetic, ferromagnetic, ferrimagnetic or antiferromagnetic.

Diamagnetism is an inherent and very weak magnetism in all materials arising from the orbiting electrons and it is observed only upon exposure to an external applied magnetic field. The diamagnetic material is composed of atoms in which all orbital shells are filled and there are no unpaired electrons, i.e. no net magnetic moment but when exposed to a magnetic field, a negative magnetization is obtained and thus the susceptibility is negative according to the Equation 2,

$$\mathbf{M} = \chi \mathbf{H} \quad (\text{Equation 2})$$

The susceptibility in the diamagnetic materials is temperature independent and the magnetization is zero when the field is zero.

Paramagnetism is a magnetism observed in materials in which the atoms contain unpaired electrons and partially filled orbital shells and thus have permanent net dipole magnetic moments. In paramagnetic materials the individual magnetic moments do not magnetically interact with each other. Therefore, in absence of an external magnetic field, the spins are randomly aligned giving a zero net magnetic moment (the magnetization $H=0$). If an external magnetic field is applied, the magnetic moments align along the field direction and partial magnetic alignment occurs producing positive magnetization and positive susceptibility which can be described by the Curie law.

$$M = \chi H = \frac{C}{T} H \quad (\text{Equation 3})$$

Where χ is the susceptibility, C is Curie's constant, H is the magnetic field and T is the absolute temperature.

Ferromagnetism is a very strong form of magnetism observed in materials with strongly interacting magnetic moments due to a process called exchange coupling. In ferromagnetic materials, the magnetic moments interact with each other and align in the same direction resulting in a strong permanent internal magnetic field inside the material which leads to a large net magnetization.

Most of the ferromagnetic materials are comprised of magnetic regions called magnetic domains. Each magnetic domain is a region of the material where the magnetic dipole moments are aligned in one direction. However, not all the various domains should be aligned

in the same direction. The ferromagnetism is strongly temperature-dependent where the magnetization is inversely related to temperature by:

$$\chi = \frac{C}{T - \theta} \quad (\text{Equation 4})$$

Where C is Curie's constant and θ is the Curie temperature (also known as transition temperature) for the material. The Curie temperature is the temperature above which there is no exchange coupling. Above the Curie temperature, a ferromagnetic material behaves as a paramagnetic material [119-122].

Magnetometry (Figure 1.3) is an important measurement that sheds the light on the magnetic properties of a material of interest, by measuring the magnetic response of the material with respect to an external applied magnetic field (H) [123]. The hysteresis loop refers to the case when the magnetic response of the measured material during demagnetization (removal of the applied field) does not match the magnetization curve. It gives many significant parameters such as (i) the saturation magnetization (M_s) which is the maximum magnetization where any increase in the applied magnetic field does not increase in the sample magnetization, the remanent magnetization (M_R) which is the material magnetization when the applied field is zero ($H=0$) and the coercivity (H_c), which is a measurement of the strength of the magnetic field required to remove the remanent magnetization and get zero magnetization).

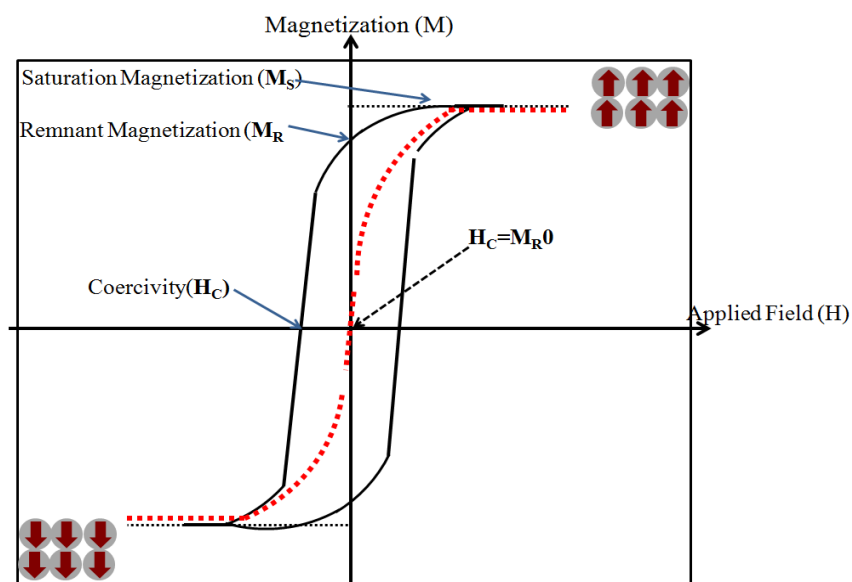


Figure 1.3: Hysteresis loop showing the magnetization (M), saturation magnetization (M_s), remanent magnetization (M_R) and coercivity (H_c) for ferromagnetic (black solid line) and superparamagnetic (red dot line) materials.

The aforementioned magnetic behaviors strongly depend on the size, meaning that the magnetic behavior for a material at a particular temperature can be altered by tuning the size.

The size tunable magnetic properties of the nanoparticles could be attributed to the thermal energy and the single magnetic domain due to the finite size effect. Below a certain size known as critical size, a magnetic nanoparticle becomes a single domain particle exhibiting superparamagnetic behavior at temperature higher than so-called blocking temperature [124-126].

Magnetic fluids or ferrofluids are colloidally stable homogenous suspensions made of magnetic nanoparticles suspended in a solvent (organic or aqueous solvent). The term “ferrofluid” refers to the ferromagnetic behavior of these fluids containing magnetic nanoparticles in response to an external magnetic field because these nanoparticles are attracted to a magnetic field with no residual magnetism after the field is removed. Each of the magnetic nanoparticles is capped with a surfactant which provides the colloidal stability preventing the aggregation of the nanoparticles [127]. Owing to their fascinating properties like small size and superparamagnetic behavior, magnetic nanoparticles and ferrofluids have been extensively studied in several technological and biological applications [22, 127-134].

1.2. Application of Nanoparticles

As briefly mentioned before, in virtue of their fascinating unique properties, the extremely huge diversity of the materials, characteristics, functionalities and surface modifications of the nanomaterials, the nanomaterials are intensively studied to make use of their properties in different applications. Here a brief introduction about the different applications of the nanomaterials is presented in which, and for the simplicity, the different applications are categorized in three classes, (1) industrial and technical applications, (2) environmental and (3) biological applications.

1.2.1. Industrial and Technical Applications

Semiconductor nanocrystals have been intensively studied and used for a variety of technical applications like laser and light-emitting diodes, [46, 47, 99-105, 135-138] and other electrical devices solar cells [33-35, 55, 82-90, 92, 139-141], chemical catalysts [93, 94, 96-98], transistors and optoelectronics [36, 142-147], piezoelectric devices [53, 54]. Quantum dots have been widely studied for sensing applications [148-150], for example ZnO nanoparticles has been used as ultraviolet detectors [151-155], temperature, chemical; pH and gas sensors [106, 108, 109, 111-112, 156-160]. Magnetic nanoparticles have been studied for a variety of technical and industrial applications for example magnetic nanoparticles are expected to find a way in the high density data storage and hard disk devices [161-168] especially magnetic FePt nanoparticles. Magnetic nanoparticles offer promising opportunities in spintronics and electronic devices [169, 170].

In chemistry, magnetic nanoparticles are heavily studied and expected to have promising potential uses as a catalysts and/or catalyst supporting material [171-173] for the chemical synthesis with a fascinating capabilities due to the high surface area and magnetic properties making them recyclable and reusable. As nanocatalysts, magnetic nanoparticles have been studied to catalyze many chemical reactions such as esterification, oxidation and reduction [174-179]. More details and discussion can be found in recent review articles [180, 181]. In addition,

the magnetic nanoparticles have been studied for magnetically guided separation and purification ^[182-189] for the industrial and chemical applications.

1.2.2. Environmental Applications

The environmental applications of the nanomaterials are a highly important area including sensors for the pollution and contamination detection. In this regard there are a huge number of studies of the nanoparticles based sensing and the detection of pollutants like small molecules ^[107] and microbial detection ^[190-194].

The environmental applications of the nanomaterials are not limited to the sensing and detection but extend beyond to environmental remediation using a wide range of techniques like photodegradation or photocatalysis using photoactive nanomaterials ^[98, 195-197], destruction, desorption or magnetically guided separation and purification using magnetic nanomaterials ^[198, 199].

Different types of magnetic nanoparticles like Fe_3O_4 , Fe_2O_3 and MFe_3O_4 with different surface modifications have been widely studied for the environmental remediation and removal of the contaminants, especially heavy metals ^[197, 200-202], water treatment and purification of different pollutants, ranging from heavy metals to carcinogenic aromatic amines ^[203-209].

ZnO nanoparticles are photoactive materials widely reported for the photocatalytic degradation and photo remediation of the environmental pollutants. For example ZnO nanoparticles were used for photocatalytic degradation of cyanide ^[210], ciprofloxacin as an example for antibiotic drug water contamination ^[95] and organic dyes ^[93, 211]. More details about some environmental applications of the nanoparticles could be found in the review article of Tang and Lo ^[129].

1.2.3. Biological Applications

1.2.3.1. Biomedical Applications

In the field of medicine, the applications of nanoparticles include but it is not limited to, targeted drug delivery, magnetically guided drug delivery and drug controlled release, hyperthermia, and non-viral gene delivery for gene therapy.

Despite the gold nanoparticles (Au NPs) have been applied for long time to stain the tissues as electron dense agents in electron microscopy, currently the plasmonic nanoparticles in general and Au NPs in particular, are investigated for a wide range of biomedical applications. Au NPs are widely used in optical microscopy as for diagnosis and bioimaging applications, for example as contrast agents for computed tomography ^[212-217]. Au NPs are also successfully used for the sensitive and early detection of pathogens and infectious diseases ^[218], detection and quantitative determination of tumor markers for early diagnosis of cancer ^[219-221] and selective drug delivery systems for therapeutic purposes ^[222-226].

The noble metal nanoparticles, due to their localized surface plasmon resonance have strong cross section absorption, and have the ability to convert the absorbed light to thermal energy producing local heat which can be used for the photodestruction of the tumors. This process is

typically referred as photothermal therapy [6, 227, 228]. The general mechanism for the phototherapeutic agents could be explained as nonradiative relaxation of the excited electrons from the excited state to the ground state producing thermal energy. The resulting photothermal energy can be employed for the photothermal therapy.

Silver nanoparticles (Ag NPs) as well are investigated in the medical applications and especial interest has been paid to make use of their antimicrobial properties in the medical applications have [229-234].

QDs have promising applications in the medical field for labeling, tracking, sensing diagnosis and bioimaging, mainly due to their tunable photophysical properties [30, 235-238]. Due to their unique luminescence characteristics, QDs are very promising candidates as bioimaging agent, which have been widely reported using different QDs types like CdSe, CdTe, CdSe/ZnS core shell QDs [239-247]. Recently, more interest has been paid to the cadmium free and non toxic quantum dots especially for in vivo applications [248, 249]. Zinc oxide nanocrystals, among the most promising cadmium free quantum dots, have been studied for the cell labeling and bioimaging applications [71-73, 75, 117, 250-254].

In therapeutics, quantum dots can be exploited in different ways, for example as carrier platforms for targeted and controlled release drug delivery [255-257]. ZnO nanoparticles have been widely studied for targeted drug delivery and controlled release [80, 113, 258], for example, the acid induced dissolution of the ZnO nanoparticles was exploited to achieve targeted delivery and drug release of anticancer drug [259, 260]. In addition to the applications of the ZnO quantum dots in the drug delivery and triggered release, ZnO nanoparticles themselves have been studied as anticancer because it was found that ZnO nanoparticles are able to achieve selective destruction of tumors [12-116, 261]. ZnO nanoparticles have many other medical applications [262-264], including antibiotic and antimicrobial activity [265-270], biomedical sensors and clinical diagnosis [271-273] and photodynamic therapy [273-277]. Recently ZnO nanoparticles have been reported as potential phototherapy agents for jaundice disease and it was found that the ZnO nanoparticles were able to catalyze the photodegradation of the bilirubin [278].

Similarly, magnetic nanoparticles have been widely used in a variety of biomedical applications especially the magnetic resonance imaging as MRI contrast agents. Magnetic resonance imaging is a powerful non-invasive imaging technique in the medicine. In MRI, the protons are excited with radio frequency pulses and the induced decay as they relax is measured providing an image of the scanned tissue. The obtained MRI image strongly depends on proton density where the areas of high proton densities exhibit strong signal and appear bright while areas with low proton densities (like tissue with low water content) have a weak signal and appear dark. Different contrast agents have been developed in order to enhance MRI signals and allow soft-tissue discrimination. Superparamagnetic nanoparticles are a unique class of MRI contrast agent currently used to improve the MRI imaging. These contrast agents can accelerate the decay (relaxation) time of protons from excited to ground state and as a result, the regions where the contrast agent is located appear darker than those with no contrast agents. Magnetic nanoparticles have been studied as MRI contrast agents in

a wide range of biomedical imaging *in vivo* and *in vitro*, like in targeted tumor and other pathologies imaging ^[279-281], *in vivo* tracking and monitoring of labeled dendritic cells ^[254], migration of stem cells used for therapeutic applications, multimodal magnetic resonance imaging probes ^[282] and real time *in vivo* molecular imaging like enzyme activity, gene expression, apoptosis detection and biomolecules metabolism ^[283, 284].

In addition to their use in bioimaging as MRI contrast agents, the magnetic nanoparticles have been utilized in a wide variety of biomedical applications both *in vitro* and *in vivo*, for example the targeted drug delivery for a wide range of drugs of different properties e.g. polar, nonpolar and cytotoxic drugs ^[285, 286], magnetic field-assisted transport (magnetically guided) drug delivery ^[287, 288] and magnetofection for gene therapy ^[289-291].

Moreover, a great interest has been paid to the applications of the magnetic nanoparticles as heat mediators in the magnetic hyperthermia ^[292, 293]. Magnetic fluid hyperthermia (MFH) is a promising therapeutic technique used as a potential treatment for cancer using induction of heating of the targeted region, above the body temperature (between 42 and 43 °C). The MFH as a cancer treatment is based on induced direct killing of cancer cells at temperatures of ~ 42°C as a result of the heating of the magnetic nanoparticles when exposed to external alternating AC magnetic fields by the energy loss mechanisms that occur during the reorientation of the magnetization of magnetic nanomaterials ^[294-298].

Other important applications of the magnetic nanoparticles have been focused on the ultrasensitive detection and separation like viruses and other pathogens detection ^[299-304].

1.2.3.2. Food and Nutrition Applications

The applications of nanotechnology and nanomaterials in the food industry and nutrition are relatively new comparing with the other applications in biomedical and information technology industries. Different types of nanoparticles have been investigated to make use of their unique properties in the food science sector.

Nanoparticles have been widely reported as analytic tools and biosensors in the field of food analysis, chemistry and food safety ^[305, 306]. Quantum dots have been widely investigated in this regard ^[306-308] for example, ZnO nanoparticles have been utilized for voltammetric determination of ascorbic acid ^[309] and folic acid ^[310] in the food. CdSe/ZnS QDs were utilized for the fast determination of diquat herbicide in food ^[311].

Au NPs also have been investigated for the food analysis and safety. For example, Au NPs labeled with streptavidin–horseradish peroxidase were used efficiently for the determination of zearalenone (a mycotoxin produced in foods and feeds by some fungi belonging to the genus *Fusarium*) using chemiluminescence immunoassay ^[312]. Recently Au NPs have been widely employed for determination of food ingredients like folic acid, soy protein, antioxidants ^[313-316] and food safety for detection and determination of toxins and pathogens ^[317-321].

Magnetic nanoparticles have a variety of applications in the food sector like magnetic field assisted separation, purification detection and determination in food analysis and safety ^[322].

Magnetic nanoparticles are widely reported for the separation, preconcentration and detection of food pollutants like dyes and heavy metals ^[323-325], food toxins like ochratoxin and aflatoxins ^[326-329] and pathogens like *Escherichia coli* O157:H7, *Cronobacter sakazakii*, *Bacillus anthracis* and *Salmonella* ^[330-334].

Also magnetic nanoparticles have been reported for the magnetically guided separation and purification of food from dyes ^[335], and magnetic separation of free fatty acids with iron oxide nanoparticles and for the deacidification and purification of vegetable oils ^[185].

Other important application of the nanomaterials in the food sector is the use of the nanoparticles in the food packaging and coatings. Organic or polymeric nanoparticles like chitosan nanoparticles are the most reported nanomaterials in food packaging ^[336]. Among the inorganic nanoparticles used in food packaging and coatings, ZnO nanoparticles have been widely studied for the use in the packaging ^[337-341].

The use, design and development of the nanomaterials for the delivery and controlled release of nutrients, nutraceuticals and bioactive food ingredients is a fast growing area of interest to food science and nutrition for the protection and/or enhancing of physicochemical properties, biological activities and enhancing solubility and bioavailability aiming to the designing and development of biologically active functional foods able to perform some physiological health functions beyond the basic nutrition. Lipid based nanomaterials are the most rapidly and widely used for the delivery and controlled release of the nutraceuticals and bioactive food ingredients like vitamins, coenzymes and polyphenols and antioxidants, such as tocopherols, carotenoids and ubiquinones ^[342-346]. One of the few available studies based on the inorganic nanomaterials is the effect of ZnO-ZnS nanocrystals on enhancing the binding affinities of different types of flavanoids with bovine serum albumin and their potential use for food and drug delivery applications ^[347].

1.2.3.3. Agricultural Applications

In the field of agricultural applications of the nanotechnology, nanoparticles could be used as carriers for delivery and controlled release ^[348] of the agrochemicals like fertilizers, pesticides, herbicides and plant growth regulators providing protection, sustainable, prolonged and controlled release for the agrochemicals.

Nanoparticles themselves might work as micronutrients and have stimulating effects on seed germination, growth and production. For example, the treatment of peanut with 25nm ZnO nanoparticles (1000 ppm) promoted seed germination and seedling ^[349]. In another study it was found that the treatment of cucumber with ZnO nanoparticles increased starch and protein content to some extent but significantly decreased the concentration of Cu and Mo micronutrients ^[350]. In another example it was found that anatase TiO₂ nanoparticles (at concentrations from 10-40 mg/ml) cause enhancement in the germination percent and other germination parameters of parsley seeds ^[351]. In study conducted to investigate the effect on seed germination and uptake of FITC labeled silica NPs and CdSe QDs on rice seedlings and

their potential applications as biolabels for plants, good germination was observed in the presence of FITC-labeled silica NPs but the germination was arrested with CdSe QDs ^[352].

Nanomaterials based technologies could be developed and used as sensing and detection systems for real time monitoring and control the field, soil, crop and environment to optimize the resources and maximize the crop production conditions ^[353]. Also nanoparticles might be enables the early detection and diagnosis of pests and plant disease management ^[354].

In the animal production and veterinary, the nanoparticles could be used in different ways like pathogen detection and removal, animal feeding, vaccination and vaccine adjuvant and veterinary medicine as diagnosis, drug delivery, gene therapy and tissue repairing ^[353, 355].

1.3. Nanomaterials: Health and Environmental Concerns

The increased interest about the nanomaterials applications in a huge range of disciplines has generated increased and fast growing concerns about the potential toxicological, health and ecological effects of the nanomaterials. In fact the health and environmental issues related to the design and applications of the nanomaterials are highly complicated. The toxicological, health and environmental effects of the nanomaterials unlike the traditional or the bulk materials do not depend only on the nature or type of material, but also on the size, shape, quality and colloidal stability, surface modification and surface charges, the medium (solvent, buffer or biological media) and a wide range of other physico-chemical properties as well as the continuous changes and transformation of the nanomaterials due to the interaction with the surrounding ^[356].

Surface modification of the nanoparticles strongly affects the chemical and colloidal stability, bio-interaction and then the fate of nanoparticles. As an example for this, the polymer coating of the intrinsically toxic nanoparticles like cadmium based nanocrystals reduces the aggregation, increasing the colloidal stability and hence possibly, it reduces their toxicity ^[357]. Polyethylene glycol on the surface also known as “PEGylation”, effectively increases the stability and furthermore reduces the opsonization and clearance of the nanoparticles by the reticuloendothelial system increasing the circulation time ^[358].

The size of the nanoparticles strongly affects the absorption, distribution, interaction, secretion and fate of the nanoparticles. As an example to study the effect of sizes on the fate of the nanoparticles, different sizes (from 1.4-200 nm) radiolabeled Au NPs were administrated through intra-esophageal instillation. The distribution of the nanoparticles of the different size was quantitatively measured in the organs and tissues after one day. It was found that the highest absorption through the intestine was for the smallest NPs, whereas the 18 nm AuNPs were the highest accumulated in the brain and heart; the 1.4 nm AuNPs were the highest in the blood, liver, spleen, kidneys, and urine. Despite no general rule about accumulation was abstracted, it was clearly stated that for the use of the NPs for specific orally drug delivery, the nanoparticles have to be individually designed according to the targeted organ ^[359].

Surface charges strongly influence the interaction of the nanoparticles with the surroundings and thus their fate, where the nanoparticles with positive charges interact with the cells and biological identities differently than those with negative surface charge. In general the positively charged NPs are incorporated in the cells faster and the nanoparticles have charge-dependent toxicity ^[356, 360].

Chemical and colloidal stability, like aggregation and/or dissolution of the nanoparticles are among the most important parameters that significantly govern the interactions, transformations and fate of the nanomaterials, especially that colloidal stability strongly affect the most of other physicochemical properties ^[356, 361, 362]. Well-dispersed, highly chemical and colloiddally stable nanoparticles are required for the biological applications in particular to address the toxicological and environmental issues for the nanoparticles.

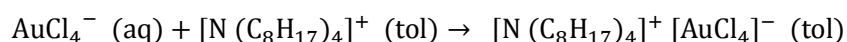
From these few examples and the tiny discussion about the toxicological and environmental aspects of the nanomaterials, it is obviously clear that what is studied till now is not enough and just the beginning, and enormous toxicological and environmental concerns need to be addressed for better understand about the safety of the nanomaterials on the human and environment.

2. Synthesis, Surface Modification and Characterization of the Nanoparticles

This dissertation is written in a cumulative way and represents the synthesis, surface modification, functionalization and characterization of nanoparticles of different types (Plasmonic, fluorescent semiconductor QDs and magnetic). In this chapter, the synthesis, surface modification and characterization of different types of nanoparticles are briefly described. For more experimental details, the reader might be referred to the publications.

2.1. Gold Nanoparticles

Gold nanoparticles (Au NPs) were synthesized according to the Brust two-phase method ^[363] with some modifications. In the first step the AuCl⁺ ions form tetraoctylammonium-gold tetrachloroaurate ion pairs according to the equation:



The Au NPs were obtained by reduction of the gold ions mediated by the NaBH₄ and the color was changed from deep orange to red-violet indicating the nucleation of the gold clusters. TOAB as surfactant is weak ligand because the relatively weak binding compared with thiol containing surfactants like dodecanethiol due to the high binding affinity of the thiol groups to the gold. For this reason, the Au NPs obtained after overnight stirring (to allow the “Ostwald ripening” happens) were subjected to a ligand exchange with dodecanethiol to enhance the colloidal stability. Monodisperse, spherical dodecanethiol capped AuNPs with core diameter of 4.6± 0.9 nm were obtained as it shown in Figure 2.1.

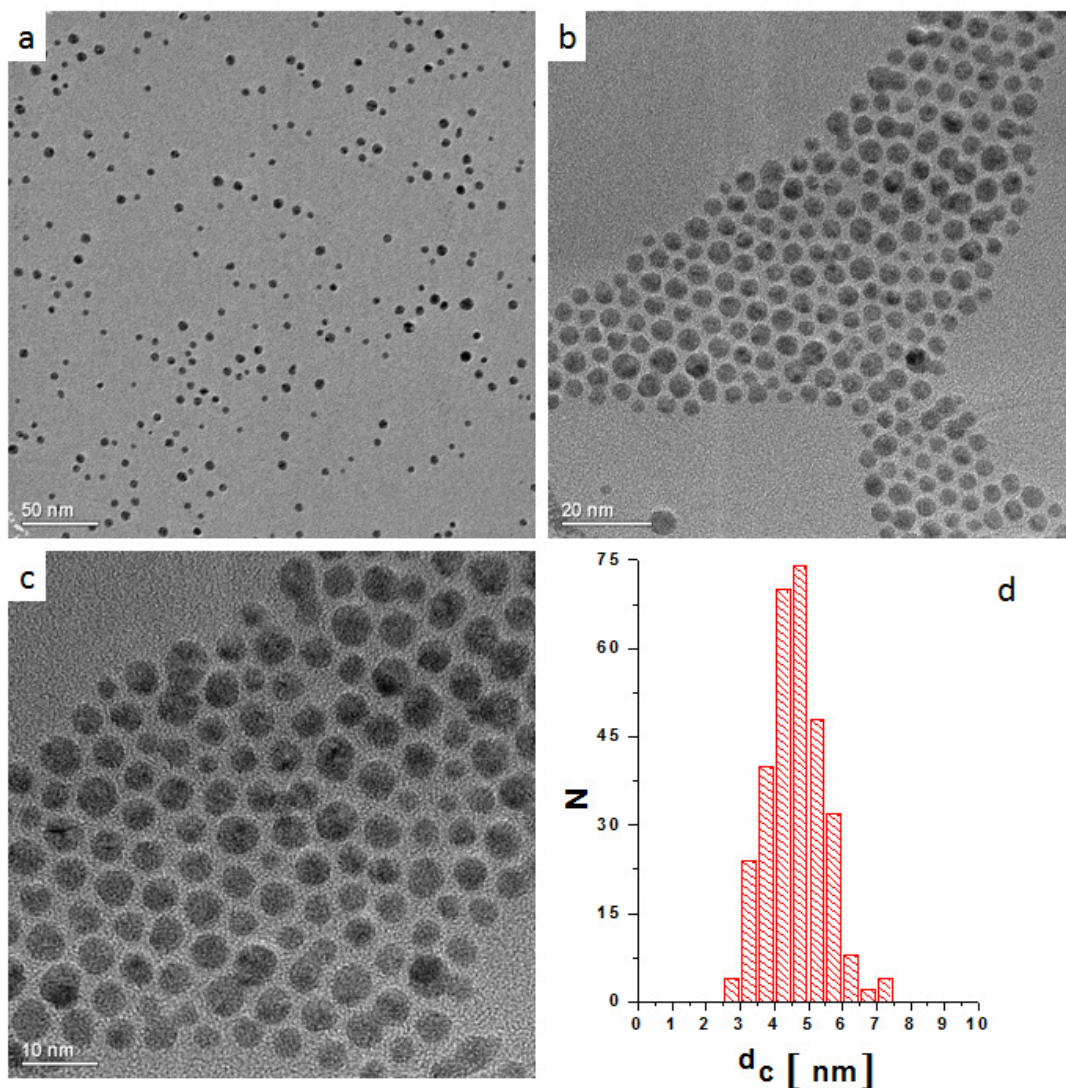


Figure 2.1: TEM images of the Au NPs at different magnifications (low and high) scale bars corresponding to a) 50, b) 20 nm and c) 10 nm. Note that only the inorganic gold cores provide contrast, the organic surfactant shells are not visible. d) Histogram showing the size distribution of the inorganic core diameter (d_c). N refers to the number for each diameter d_c . The average $d_c = 4.6 \pm 0.9$ nm

The AuNPs concentration was determined from its plasmon peak recorded by UV-vis absorption (Figure 2.2) measurement using the Beer-Lambert law:

$$A = \epsilon \cdot l \cdot C \quad (\text{Equation 5})$$

Where; A is the absorbance, ϵ is the molar extinction coefficient of the sample ($M^{-1}cm^{-1}$), Here $\epsilon = 8.7 \times 10^6 M^{-1}cm^{-1}$ corresponding to their plasmon peak at 517 nm is used ^[364], l is the path length (cm) and C is the concentration of the sample (M).

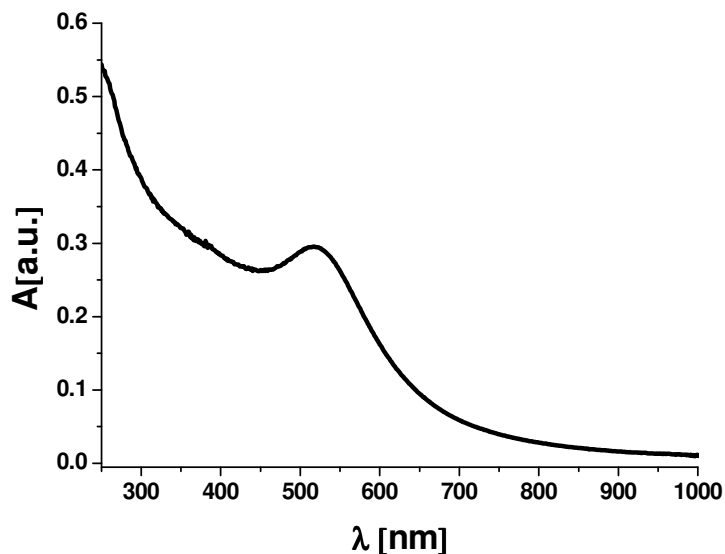


Figure 2.2: Absorption spectra of the 4.6 nm Au NPs.

2.2. Transformation of Organic Soluble to Water Soluble Nanoparticles

For the biological applications of the nanomaterials, it is of great importance to obtain water soluble nanoparticles. In the current work, to achieve phase transfer and transform the organic soluble nanoparticles to aqueous soluble, an amphiphilic polymer coating was utilized. The amphiphilic polymer coating is an efficient and very general strategy to convert hydrophobically capped nanoparticles to water soluble which can be used then for biological applications. In general, the mechanism of the polymer coating is based on the hydrophobic interaction between the hydrophobic surfactant on the surface of the particles and the hydrophobic side chains of the amphiphilic polymer. This universal method can be applied to all NPs having hydrophobic surfactants on the surface regardless the nature of the core [365, 366].

In general, the amphiphilic polymer consists of two moieties of different nature, one hydrophobic and the other hydrophilic. The hydrophobic part is responsible for the interaction with the hydrophobic surfactant on the particles while the hydrophilic part provide the water-solubility. The structure of the amphiphilic polymer used in this work (PMA) is a hydrophilic backbone of poly(isobutylene-alt-maleic anhydride) modified with dodecylamine as hydrophobic part. The hydrophilic backbone not only makes the nanoparticles water soluble but also provides with functionality and plays an important role in the surface modification of the nanoparticles because many molecules of different activities (drugs, chelators, fluorophores) could be covalently attached to the polymer shell around the particles producing multifunctional nanoparticles.

This amphiphilic polymer (PMA) was synthesized as has been reported in literature [366] as follows. Briefly, 2.70 g (15 mmol) of the dodecylamine (98%, Sigma, # D22,220-8) was well dissolved in a 100 mL of anhydrous tetrahydrofuran (99.9%, Aldrich, #186562) then poured

into another bottom-round flask containing 3.084 g (20 mmol expressed as monomer) of the hydrophilic backbone poly(isobutylene-alt-maleic anhydride), average Mw ~ 6,000 g/mol, (Sigma, #531278) and the cloudy mixture was sonicated for few seconds (~20 s) and then heated under reflux for three hours. After three hours, some THF was evaporated using the rotary evaporator and the solution was concentrated to 30-40 mL then heated under reflux overnight. Finally, the solvent was completely evaporated under reduced pressure in the rotary evaporator and the product was redissolved in 40 mL anhydrous chloroform to a final concentration of 0.5 M. The polymer was prepared in anhydrous organic solvents in order to maintain the activity of the maleic anhydride rings. The ratio of dodecylamine to maleic anhydride rings was designed in a way that 75% of the rings react, leaving only 25% of them intact for further modification with other functionalities. The maleic anhydride rings can be opened with the addition of basic water solutions forming negatively charged carboxylate groups, providing colloidal stability in aqueous solutions.

The required amount of polymer for the NPs coating was determined by first calculating the total effective surface area of the hydrophobically capped nanoparticles (A_{NP}). The inorganic core diameter denominated as d_c measured from the TEM images was used to calculate the effective diameter d_{eff} , from the following equation:

$$d_{eff} = d_c + 2L \quad (\text{Equation 6})$$

Where; d_{eff} is the effective diameter, d_c is diameter of inorganic core measured from the TEM images and L is the length of the hydrophobic surfactant on the surface of the nanoparticles. Normally 1 nm is used as L .

The effective diameter was used to calculate the surface area on single nanoparticles and then the total surface area:

$$A_{NP} = 4\pi \left(\frac{d_{eff}}{2} \right)^2 = \pi \cdot d_{eff}^2 \quad (\text{Equation 7})$$

$$A = A_{NP} \cdot C \cdot V \cdot N_A = \pi \cdot d_{eff}^2 \cdot C \cdot V \cdot N_A \quad (\text{Equation 8})$$

Where A_{NP} is the area of a single nanoparticle (nm^2), A is the total surface area of the nanoparticles used for coating, V is the volume of the colloidal NPs solution (L), C is the concentration of NPs solution (mol/L), N_A is the Avogadro's number (6.023×10^{23}).

And the amount of the amphiphilic polymer required for the polymer coating of the hydrophobically capped nanoparticles as follows:

$$V_P = \frac{N_P}{C_P} = \frac{A \cdot R_P}{N_A \cdot C_P} = \frac{\pi \cdot d_{eff}^2 \cdot C \cdot V \cdot R_P}{C_P} \quad (\text{Equation 9})$$

Where; V_P is the volume of the polymer required for the nanoparticles coating, N_P is the number of the polymer monomers required for the coating, C_P is the concentration of the polymer expressed as the monomers concentration in M and R_P is the ratio of numbers of polymer monomers per unit area of nanoparticles (monomer units/ nm^2). Enough monomer should be used for efficient polymer coating and R_P from 60-100 monomers per nm^2 was used

to achieve good coating. Where the less some aggregate was observed and the excess polymer causes difficulties in the next purification steps.

For the polymer coating, the hydrophobically capped nanoparticles in the organic solvent (normally chloroform) is mixed with the calculated amount of the amphiphilic polymer in chloroform and stirred for several minutes at room temperature. After few minutes of stirring, the solvent was completely removed under reduced pressure using the rotary evaporator, gentle stream of nitrogen was passed on the dried film to remove any trace of solvent and then the well dried coated NPs are dissolved in sodium borate buffer (100mM SBB pH 12). The polymer coating process takes place by the hydrophobic interaction between the hydrophobic side chain of the polymer (dodecylamine) and the hydrophobic surfactants on the surface of the nanoparticles. Figure 2-3 illustrate the structure of the used amphiphilic polymer and sketches the polymer coated nanoparticles.

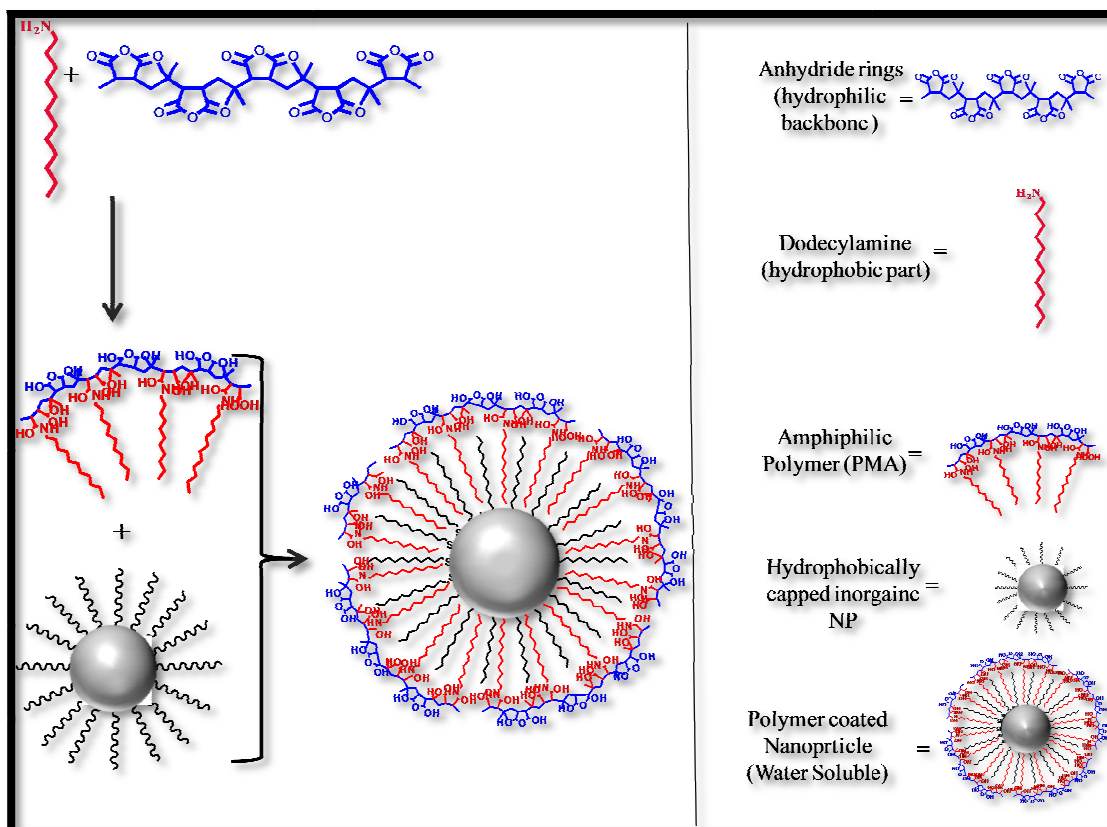


Figure 2-3: Schematic depiction of the polymer coating process and the structure of the used amphiphilic polymer consisting of a polyisobutylene-alt-maleic anhydride hydrophilic backbone (blue) and dodecylamine hydrophobic side chains (red). The anhydride rings of the hydrophilic polymer backbone are covalently connected by amide bonds to the amine groups of hydrocarbon chains.

2.3. Purification of the Coated Nanoparticles

Once nanoparticles are coated and the dried nanoparticles were dissolved in the proper buffer mostly SBB pH 12, the nanoparticles were submitted to successive different purification steps to remove the agglomerated particles and the free micelles (the excess amphiphilic polymer) to get aqueous soluble NPs with good colloidal stability. As a preliminary purification step, the nanoparticles dissolved in the buffer (ultrasonication could be used to aid the dissolve of the agglomerated NPs) were filtered using a 0.22 μm syringe filter to get rid of aggregates. After the filtration, the nanoparticles solution was further purified and concentrated using Amicon centrifuge filters (100 kDa MWCO).

Gel Electrophoresis

Gel electrophoresis was applied as a characterization technique and for the purification of the coated nanoparticles from the free polymer micelles. For the gel electrophoresis, 2% agarose gel was prepared by dissolving 7 g Ultrapure Agarose (Invitrogen, # 16500) in 350 mL 0.5x TBE (Tris-borate-EDTA buffer, pH 8.3) in a 500 mL Erlenmeyer flask. The flask was covered with watch-glass and heated in a microwave oven for about 6 minutes (until the solution boils). The hot, well melted clear agarose gel was poured in a 10 x 15 cm gel tray in a gel caster (BioRad) with a proper comb (1, or multiwells) and covered with aluminum foil then the gel was left at room temperature for one hour to solidify. Then, the comb was removed and the solidified gel was transferred to the electrophoresis chamber (BioRad) filled with 0.5 X TBE.

The concentrated NPs suspension obtained from the centrifuge filter was mixed with 20% of its volume loading buffer (30 % glycerol and 0.3 % Orange G in TBE 0.5x) and carefully loaded to the agarose gel wells and the electrophoresis devices connected to the power source was run for 60 minutes at a constant applied voltage of 100 V (corresponding to 10 V/cm). Commercial 10 nm, phosphine stabilized Au NPs also were loaded in a well and run on the same gel under the same conditions and for the same time as internal standard.

Gel electrophoresis allows efficient separation of the charged materials according to their electrophoretic mobility which depends mainly on the charge to mass ratio. The free empty polymer micelles (the excess of amphiphilic polymer) migrate through the gel network faster than the NPs due to its bigger charge/mass ratio compared to the lower charge/mass ratio of the polymer coated nanoparticles. At the end of the run and after the bands separation, the gel was taken out and digital images were taken using (BioRad Gel Doc) and the taken images were saved as TIFF files. The bands of interest were cut and each band was put in a dialysis membrane (MWCO = 50 kDa) and the dialysis membrane was filled with 0.5x TBE buffer, closed well and put again in the electrophoresis chamber. The coated nanoparticles were extracted from the gel matrix by running the electric field again under the same conditions for about 30 minutes (or until the NPs pass out from the gel). The particles extracted from the gel are trapped inside the dialysis bag because they are not able to pass through the pores of the dialysis membrane due its MWCO. The nanoparticles suspension was transferred to a

centrifuge filter (100kD MWCO) and the TBE was exchanged by many rounds of centrifugation.

Size Exclusion Chromatography

Other main purification technique used for a further purification and also characterization is size exclusion chromatography (SEC). The NPs suspension was purified using a self packed size exclusion gel filtration column connected to a standard high-performance liquid chromatography system (HPLC, Agilent 1100) using Sephacryl S-300 HR (GE Healthcare, #17-0599-10) as stationary phase and sodium borate buffer (SBB pH 9) as mobile phase. About 600 μ L of the sample was injected and run for 140 min at flow rate 1mL per minute. The materials or molecules have different elution pattern according to their size i.e. the materials have size-dependent elution time where the biggest particles are eluted first and smaller molecules remain longer in the column. By this way the polymer-coated nanoparticles could be separated and purified from the free empty micelles (the excess polymer), small molecules or small NPs aggregates.

The sample was eluted and fractionated into vials and fractions of interest (the samples containing the nanoparticles) observed by their characteristic absorption and/or emission peak were collected. The collected solution containing purified polymer coated NPs was transferred to an Amicon centrifuge filter (100 kDa MWCO) and the buffer was exchanged to Millipore water with the aid of several rounds of centrifugation. Finally, the concentrated NPs suspension was purified with a PD- desalting column (GE Healthcare, # 17-0851-01) and filtered with a 0.2 μ m sterile syringe filter in laminar flow and sterile conditions for biological experiments.

2.4. UV-Vis Absorption Spectroscopy and Fluorescence Spectroscopy

The UV/Vis absorption spectra of the nanoparticles samples were measured using a UV-Vis spectrophotometer (Agilent Technologies 8453 UV-Vis spectrometer). The absorption spectra were measured from 200 – 1100 nm after recording background of the blank absorption spectrum of the used solvent.

The photoluminescence (PL) spectra of the luminescent materials and nanoparticles were measured using a fluorometer (a Fluorolog[®]-3 spectrofluorometer, HORIBA JOBIN YVON) in a three window glass cuvette.

2.5. Dynamic Light Scattering and ζ - Potential Measurements

The zeta potential and hydrodynamic diameter of the nanoparticles are important indicators for the colloidal stability and quality on the nanoparticles. The hydrodynamic diameter and the zetapotential were measured using Zetasizer instrument (Nanosizer Nano ZS, Malvern, Worcestershire, UK) equipped with a red laser (HeNe laser operating at $\lambda=632.8$ nm) as light source was used at 173° backscatter detection mode.

The nanoparticles suspended in the proper solvent or buffer were equilibrated at temperature of 25 °C for 5 minutes before the measurement and each sample was measured five times (12 measurements each). All values shown here are the averages of the all measurements. For the

zeta-potential measurements the samples were equilibrated at the same temperature for the same time.

2.6. Transmission Electron Microscopy (TEM)

The size and shape of the nanoparticles were studied by transmission electron microscopy (TEM, Jeol JEM-3010). According to the nature of solvent (aqueous or organic), two methods were used for the preparation of the NPs sample for the TEM measurements. For NPs suspended in organic solvent, the sample was prepared by dipping the copper grid directly in the solution of the proper concentration for few seconds and the grid was dried for short time at room temperature.

In the case of NPs suspended in aqueous solvents, first the copper grids were converted to hydrophilic by placing them in a stream of ethanol in closed tube for about 5 hours before preparing the TEM samples then to prepare the TEM sample, a few microliters ($\sim 25\mu\text{L}$) of the of the sample was dropped on the copper grid and allowed to dry.

Figure 2.4 a and b are images of the water soluble polymer coated Au NPs on both, the gel electrophoresis and the size exclusion chromatography showing a narrow band which is comparable to the 10nm commercial phosphine capped Au NPs indicating the colloidal stability and the narrow size distribution. These results were further confirmed from the narrow hydrodynamic diameter ($d_h = 11.9 \pm 0.7 \text{ nm}$) as measured by the DLS measurements (Figure 2.5) and the negative charges ($\zeta = -32.9 \pm 2.7 \text{ mV}$) stemming from the free carboxylate groups as shown from the zeta potential (Figure 2.6) measurements.

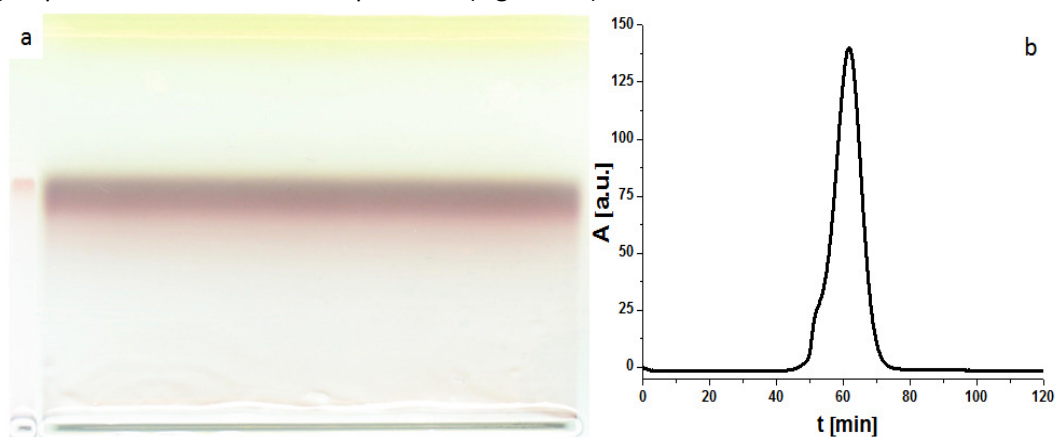


Figure 2.4: a) Gel electrophoresis image of the polymer coated Au NPs on 2 % agarose gel after NPs have run for 1 hour at constant 100V. Left lane is 10 nm phosphine coated Au NPs as control. b) Elution profile of the polymer coated NPs running through a size exclusion column. The absorption of the elutes (A) is plotted versus the elution time (t).

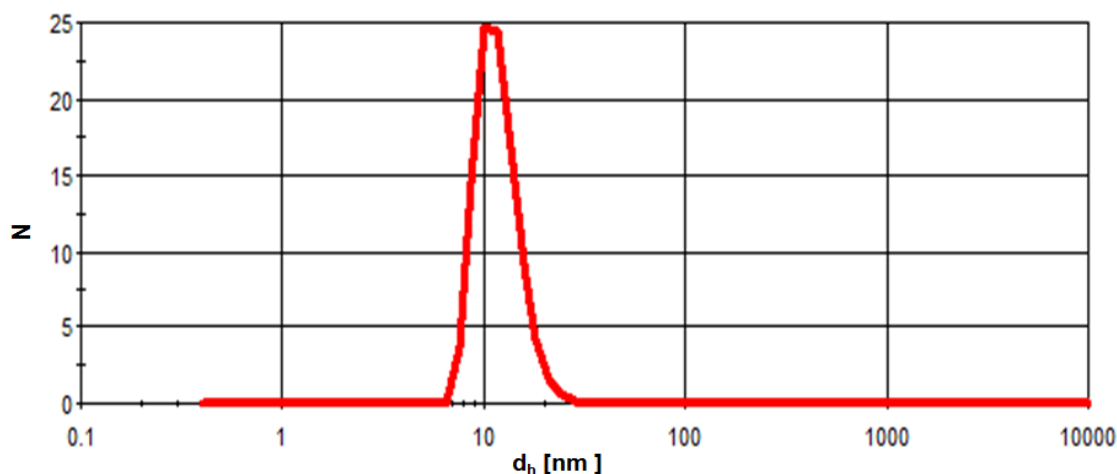


Figure 2.5: Hydrodynamic diameter d_h of the polymer coated Au NPs as determined with DLS. N refers to the number distribution. $d_h = 11.9 \pm 0.7$ nm.

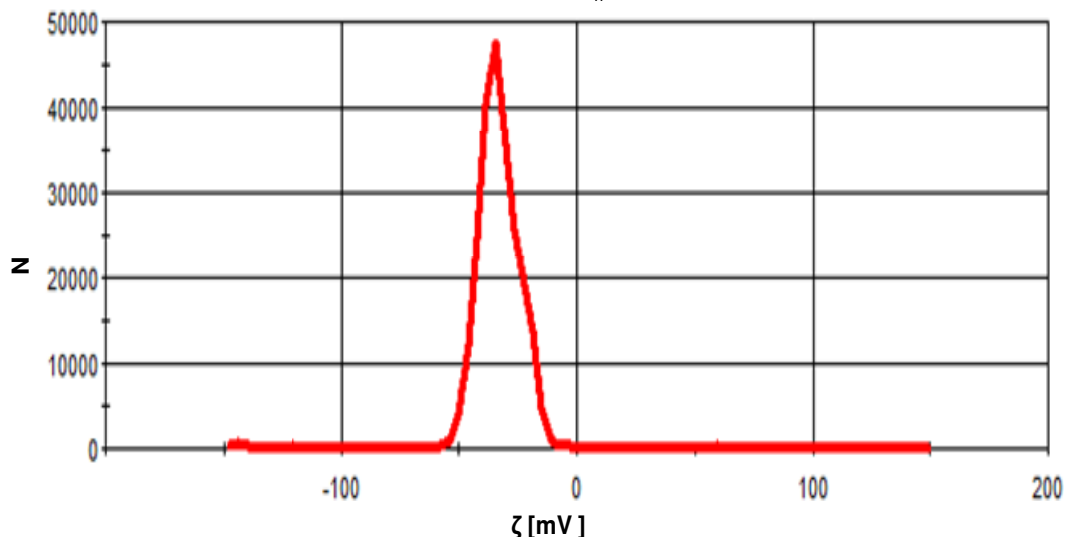


Figure 2.6: Zeta potential distribution of the polymer coated Au NPs. $\zeta = -32.9 \pm 2.7$ mV

2.7. Magnetic Nanoparticles

2.7.1. Iron Oxide Nanoparticles

Monodisperse, oleic acid capped magnetic iron oxide nanoparticles (MIONPs) were synthesized using a previously published protocol^[367] by the thermal decomposition of iron pentacarbonyl in octyl ether as solvent. Briefly, a mixture of octyl ether (10 mL, 99% Sigma-Aldrich #249599) and 1.28 g of oleic acid (90 % Sigma-Aldrich #364525) in three neck round flask was heated to 60 °C and degassed for 20 min. Then the mixture temperature was increased to 100 °C where the iron precursor (0.28 mL of iron pentacarbonyl, 99.99% Sigma-Aldrich #481718), l) was swiftly injected and temperature was increased up to refluxing temperature (~300 °C). The mixture was refluxed at this temperature for 1 hour under vigorous magnetic stirring. The initial yellow color of the mixture changed with the time to black. After one hour, the heating mantle was removed and the mixture was cooled down to

the room temperature (RT) where trimethylamine N-oxide dehydrate (0.34 g, 98% Sigma-Aldrich #T0514) was added and the mixture heated again to 130 °C for 2 h. Again after two hours, the mixture's temperature was increased up to the refluxing temperature using a 15 °C/min speed. The solution was kept at this temperature for extra one hour after which, the heating mantle was removed and the nanoparticles solution was allowed to cool down to the RT. Just the mixture cooled down to the RT, ~ 5-7 mL anhydrous toluene was added followed by 30 mL of anhydrous methanol and the MIONPs were collected by centrifugation at 2000 rpm for 5 min. The supernatant was trashed and particles pellets were redissolved in toluene and the nanoparticles were collected again by adding methanol and centrifugation at 2000 rpm for 5 min. The last washing step was repeated three times again and finally the nanoparticles were dissolved in 20 mL anhydrous chloroform. TEM images of the obtained quasi-spherical iron oxide nanoparticles are shown in Figure 2.7 with inorganic core diameter $d_c = 12.8 \pm 2.1$ nm.

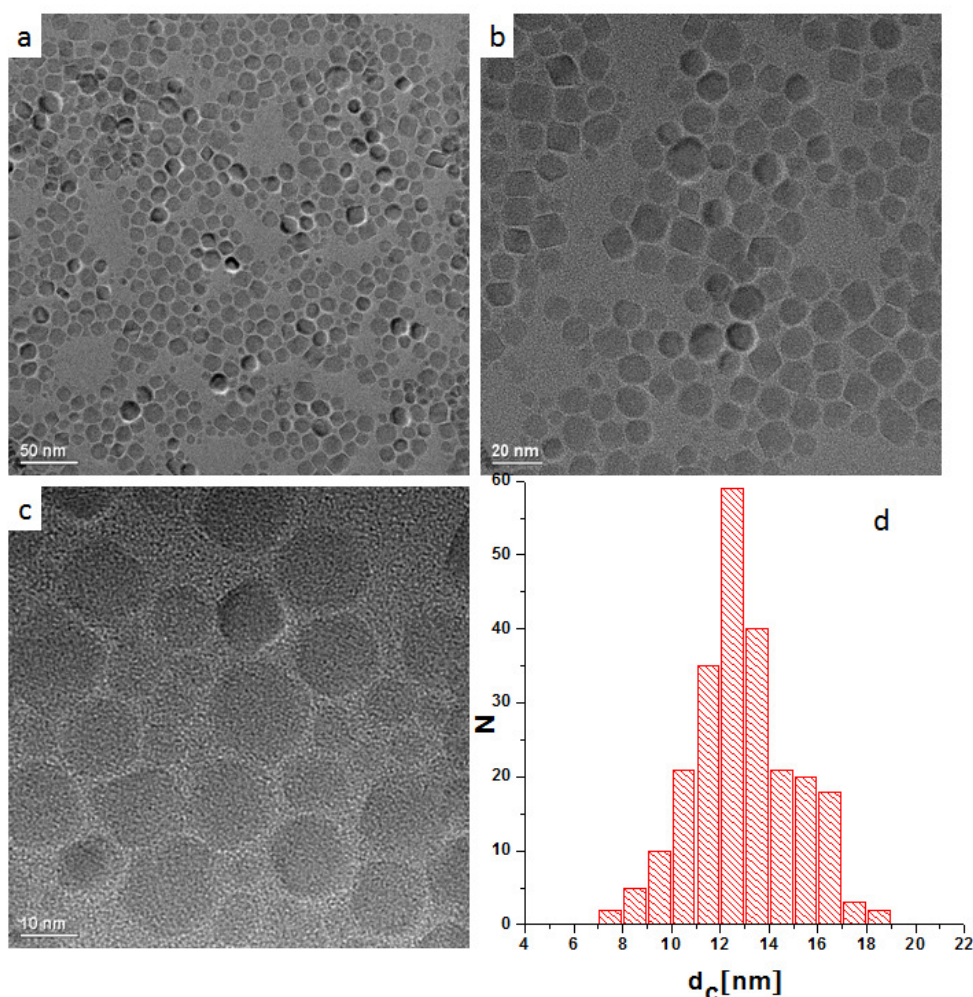


Figure 2.7: TEM images of the iron oxide NPs at different magnifications (low and high) scale bars corresponding to a) 50, b) 20 nm and c) 10 nm. d) Histogram showing the size distribution of the inorganic core diameter (d_c). N refers to the counts for each diameter d_c . The average $d_c = 12.8 \pm 2.1$ nm

The magnetic iron oxide nanoparticles were transferred to water using the polymer coating technique and purified as it described in sections 2.2 - 2.6. Also the surface of the coated magnetic nanoparticles was further functionalized with extra functional molecules for example, surface modification of the MIONPs with fluorescent dyes (e.g. DY-495 and Rhodamine) as it shown in gel images (Figure 2.8), absorption emission spectra (Figure 2.9 and Figure 2.10), hydrodynamic diameter (Figure 2.11). To obtain multifunctional fluorescent magnetic nanoparticles which could be of a great importance in labelling, tracking and multimodal bioimaging like MRI imaging and fluorescence microscopy.

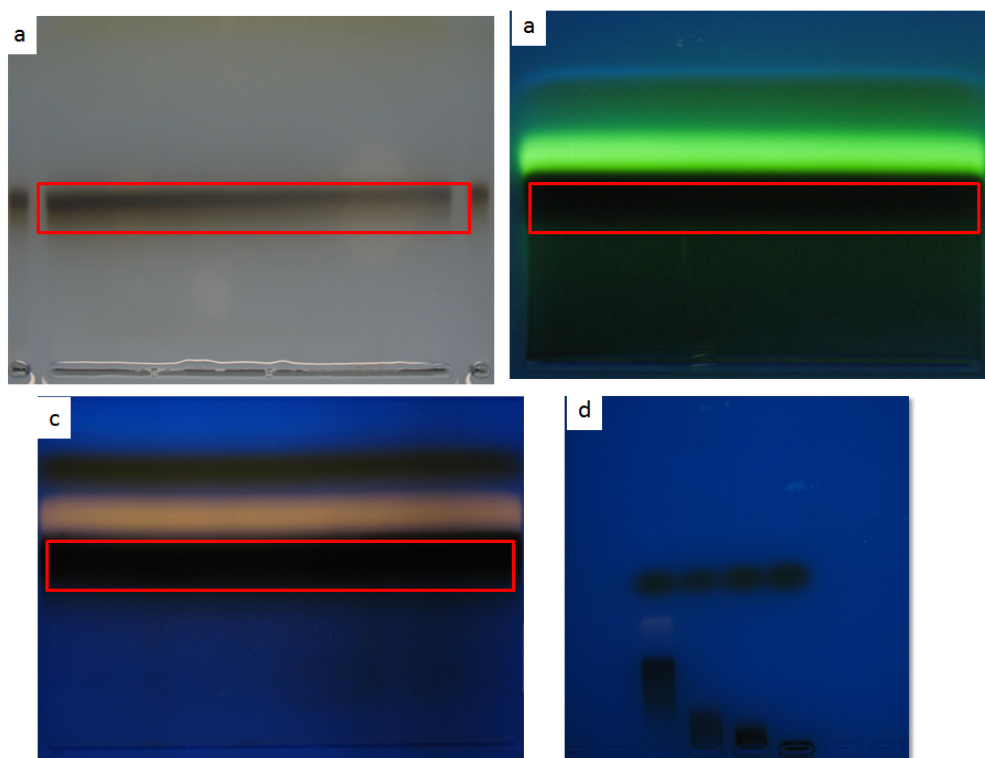


Figure 2.8: Gel electrophoresis images of the polymer coated Iron Oxide NPs with no further surface modification (a), polymer coated MIONPs modified 2% DY-495 (b), modified with 0.5 % Rhodamine (c) and d) is the same (c) but with polyethylene glycol of different molecular weights, 3, 5 and 10 kDa PEG from left to right. On a 2 % agarose gel at constant 100V.

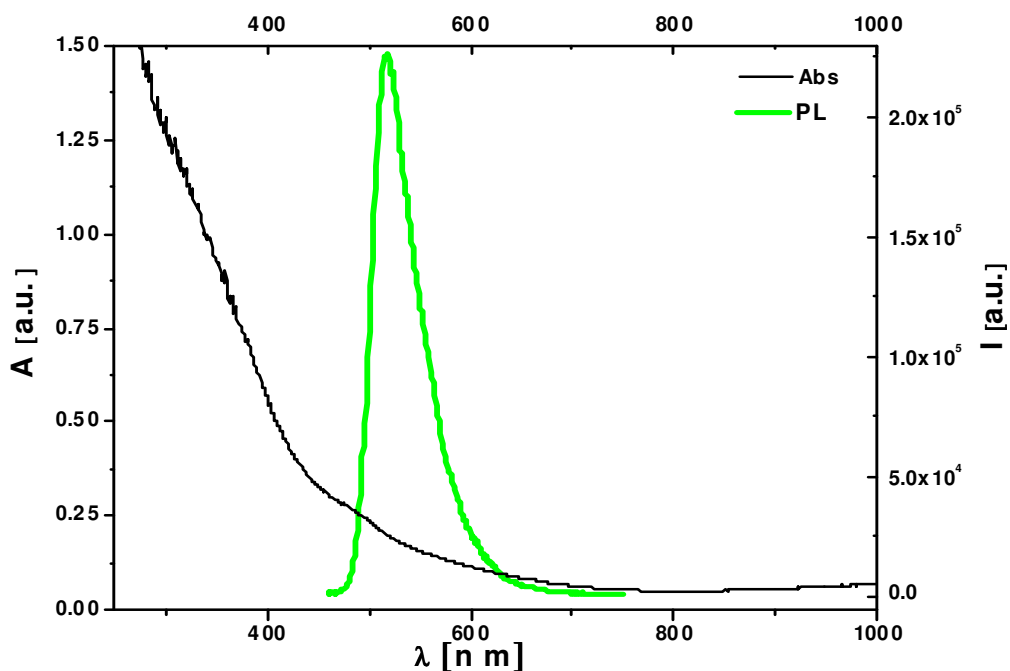


Figure 2.9: Absorption emission spectra of the polymer coated iron oxide NPs modified with Dy-495. The emission maximum is 520 nm and the sample was excited at 450 nm.

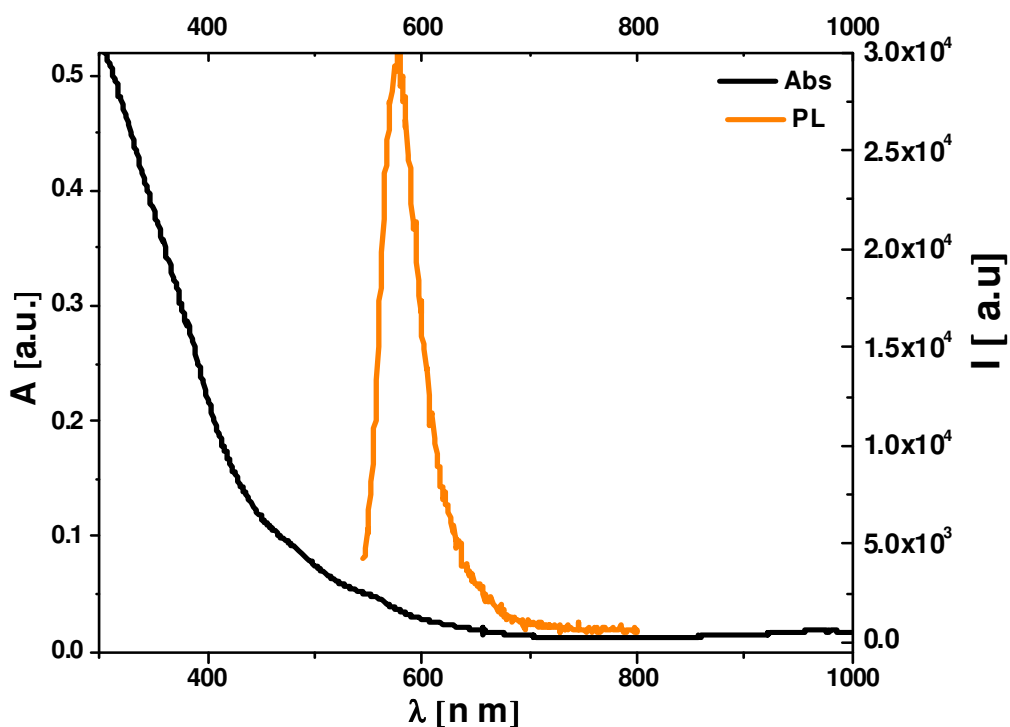


Figure 2.10: Absorption emission spectra of the polymer coated Iron oxide NPs modified with 0.5 % Rhodamine. The sample was excited at 535 nm and the emission maximum is 575 nm.

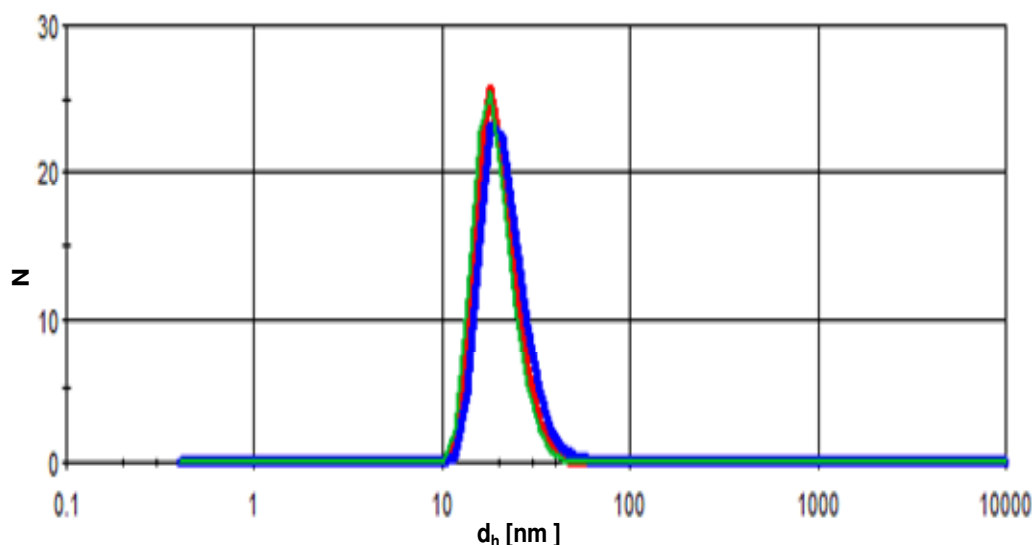


Figure 2.11: Hydrodynamic diameter d_h of the polymer coated MIONPs (green line, $d_h = 19.2 \pm 1.0$), modified with Dy-495 (red line, $d_h = 19.9 \pm 1.4$) and modified with Rhodamine (blue line, $d_h = 21.5 \pm 1.5$) as determined with DLS. N refers to the number distribution.

Nanomaterials combining different functionalities within one entity known as multifunctional nanoparticles offer exceptional and promising prospects in many disciplines especially fundamental biology and biomedical applications like imaging, diagnosis and drug delivery. A variety of nano-theranostics combining several diagnostic (e.g. magnetic resonance imaging, radioactivity and fluorescence) and therapeutic (e.g. targeted drug delivery and hyperthermia) features are currently under intensive investigation in nanomedicine [368-370].

The surface of the coated nanoparticles was modified with methotrexate as an anti-cancer drug. The methotrexate was covalently conjugated to the surface of the polymer coated magnetic iron oxide nanoparticles using amine modified polyethylene glycol (PEG) as crosslinker via EDC chemistry as depicted in Figure 2.12.

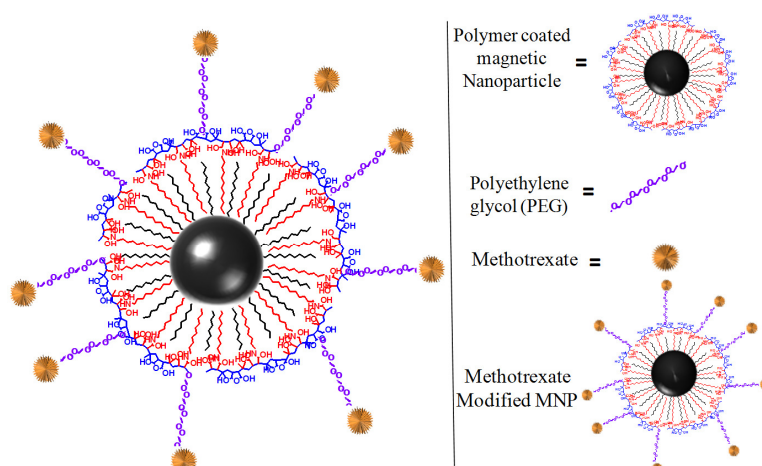


Figure 2.12: Sketch illustrating the polymer coated MIONPs modified with anti-cancer, methotrexate drug.

In Figure 2.13, absorption spectra of the magnetic MIONPs before and after the surface modification with the methotrexate after the purification showing the characteristic peaks of the methotrexate indicating the bioconjugation of the methotrexate to surface of the nanoparticles.

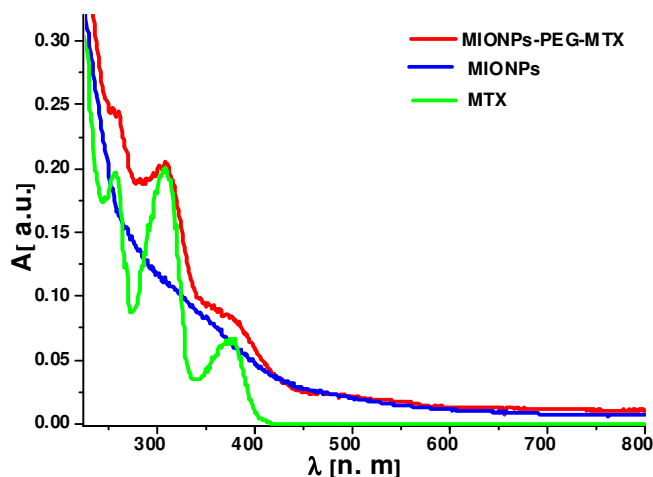


Figure 2.13: Absorption spectra of methotrexate (green line), polymer coated magnetic MIONPs (blue) and MIONPs-MTX bioconjugate after the purification.

2.7.2. FePt Nanoparticles

FePt nanoparticles (NPs) were synthesized by reduction of platinum acetylacetonate [Pt(acac)₂] to Pt by 1,2-hexadecanediol simultaneously with the thermal decomposition of iron pentacarbonyl [Fe(CO)₅] at high temperature in dioctyl ether in the presence of oleylamine and oleic acid [371]. Briefly, 95 mg Pt(acac)₂ (98%, Sigma Aldrich), 195 mg 1,2 hexadecanediol (Tech 90%, Sigma Aldrich) and 10 mL octyl ether (99 %, Sigma Aldrich) were mixed in a 50 mL three necked-bottomed flask under nitrogen atmosphere inside glove-box and the temperature was raised to 100 °C. The mixture was kept at this temperature until turned to a clear translucent yellow solution and then the iron precursor (mixture consisting of 80 μL oleic acid, 80 μL Oleylamine and 65 μL iron pentacarbonyl) was swiftly injected. The temperature of the mixture was gradually increased to 280 °C at a rate of 15 °C/min and kept at this temperature under nitrogen atmosphere and vigorous magnetic stirring for 30 min. After 30 min of stirring, the heating mantle was removed and the NPs solution was cooled down to the room temperature. The as prepared FePt NPs were precipitated by addition of anhydrous methanol (15 mL) and centrifugation for 5 min at 2000 rpm. After centrifugation, the supernatant was discarded and the precipitate containing the hydrophobic FePt NPs was redissolved in anhydrous toluene and washed again by addition of the methanol. The nanoparticles were separated by centrifugation at 2000 rpm for 5 min and finally the hydrophobic FePt NPs were dissolved in anhydrous chloroform.

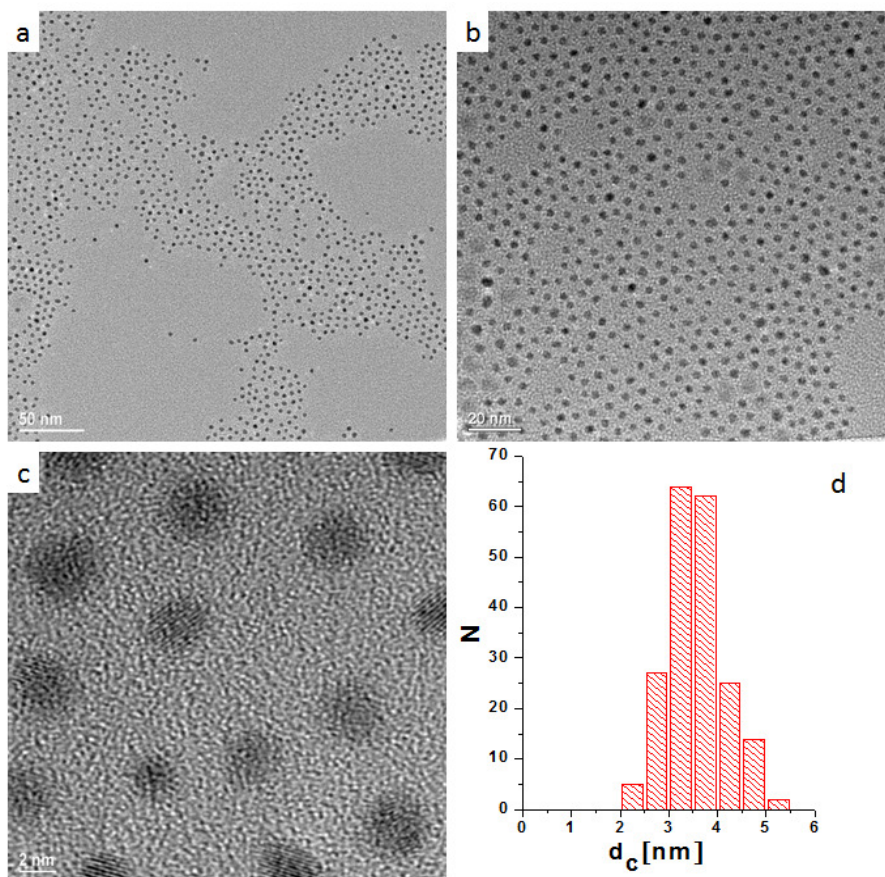


Figure 2.20: TEM images of the polymer coated FePt NPs at different magnifications (low and high) scale bars corresponding to a) 50, b) 20 nm and c) 2 nm and d) Histogram showing the size distribution of the inorganic core diameter (d_c). N refers to the number of for each diameter d_c . The average $d_c = 3.5 \pm 0.6$ nm.

The monodisperse small 3.5nm FePt NPs were transferred to aqueous phase using the polymer coating followed by purification and characterization as described before. Figure 2.20 -2.23 show the TEM images, Gel electrophoresis images, size exclusion chromatography, DLS and zeta potential results indicating a really small colloidal monodisperse water soluble FePt NPs with small and inorganic core, hydrodynamic diameter, narrow size distribution and negative net surface charges.

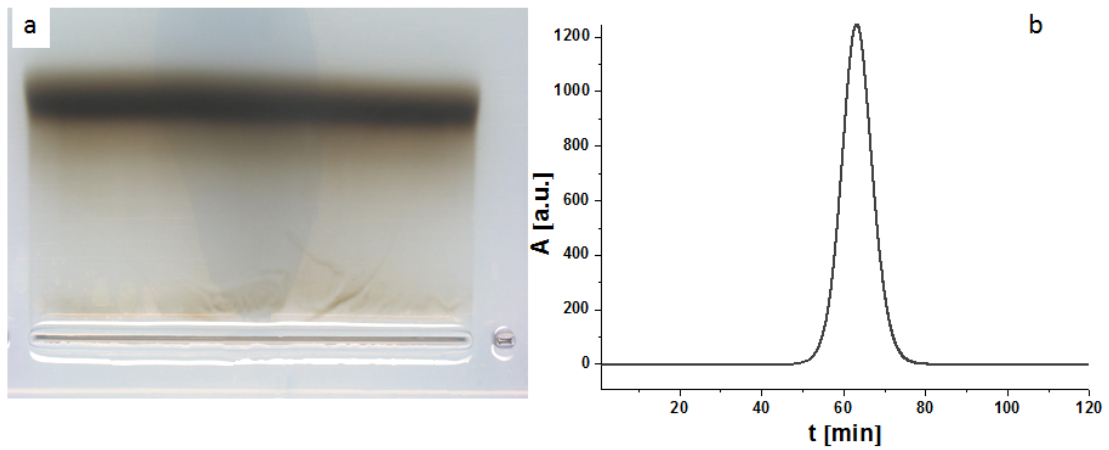


Figure 2.21: a) Gel electrophoresis image of the polymer coated FePt NPs on 2 % agarose gel after NPs have run for 1 hour at constant 100V. b) Elution profile of the polymer coated FePt NPs running through a size exclusion column. The absorption of the elutes A is plotted versus the elution time (t)

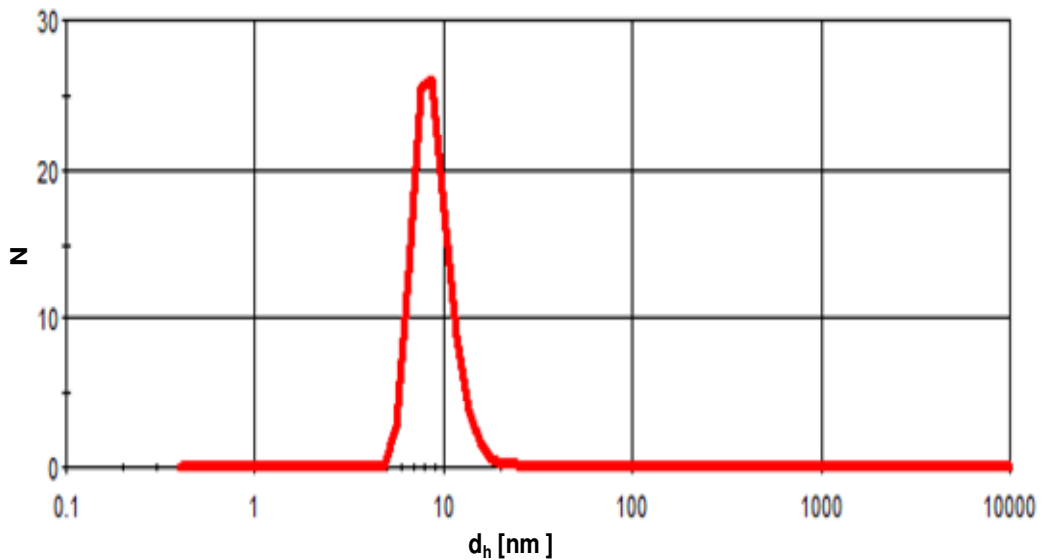


Figure 2.22: Hydrodynamic diameter d_h of the polymer coated FePt NPs as determined with DLS. N refers to the number distribution. $d_h = 9.0 \pm 0.4$ nm.

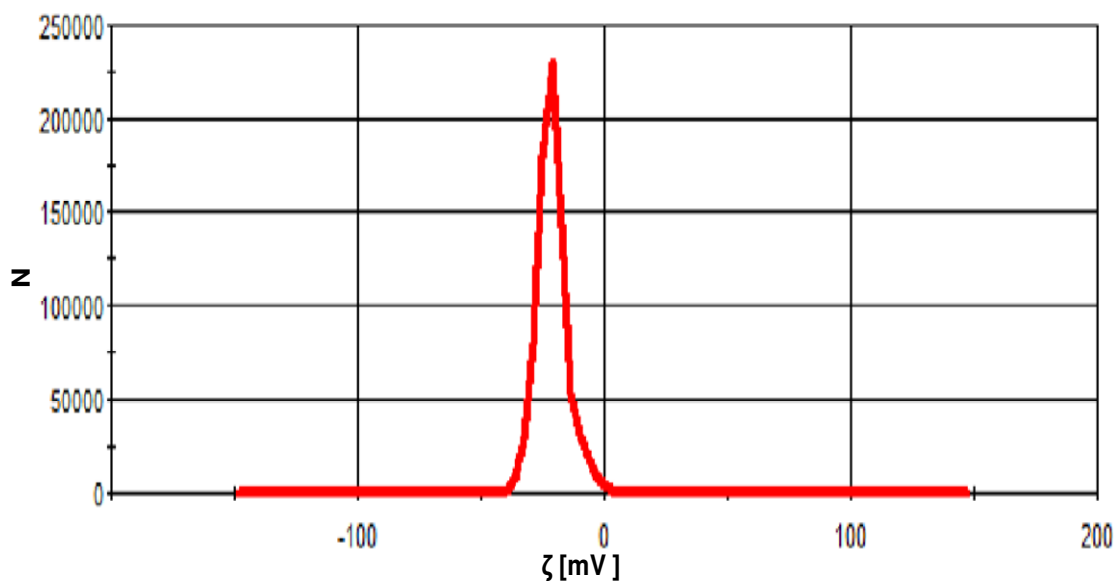


Figure 2.23: Zeta potential distribution of the polymer coated FePt NPs. $\zeta = -28.3 \pm 0.5$ mV.

2.7.3. CoPt₃ Nanoparticles

Cobalt platinum (CoPt₃) nanocrystals with size about 8.6 nm were synthesized according to the previously described method^[372] from cobalt octacarbonyl and platinum acetylacetonate as precursors for cobalt and platinum respectively. Briefly, in a mixture of solvents consisting of diphenyl ether (2.0 ml, 99%, Sigma-Aldrich #24083-4) and hexadecylamine (4.0 g, technical grade, Sigma-Aldrich #H740-8), 33 mg Pt(acac)₂, 0.13 g of 1,2-hexadecanediol (technical grade, Sigma-Aldrich #21374-8) and 0.25 g 1-adamantanecarboxylic acid (99%, Sigma-Aldrich #01823) were heated to 65 °C and the obtained melted clear yellowish mixture was degassed for about 20 minutes. The mixture temperature was increased to 200 °C and a freshly prepared cobalt precursor stock solution (0.015 g of Co₂(CO)₈ (Strem #270400) dissolved in 0.7 ml of 1,2-dichlorobenzene (99%, Sigma-Aldrich #24066-4) was injected and solution was kept at this temperature for 30 min under vigorous stirring then the temperature was increased again to 290 °C and kept for extra 30 min. Finally, the heating mantle was removed and the solution was cooled down to the room temperature and the CoPt₃ NPs were cleaned by methanol and centrifugation as described previously.

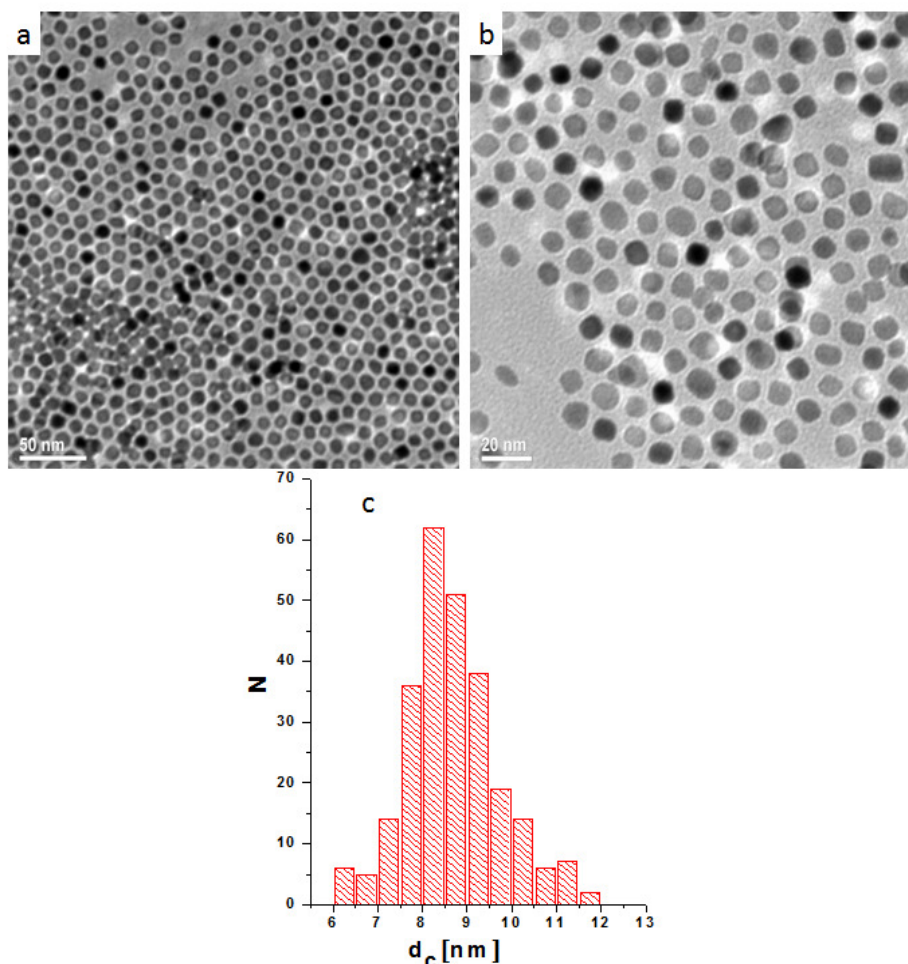


Figure 2.24: a) and b) are TEM images of the uncoated CoPt_3 NPs in chloroform. The scale bars corresponding to 50 and 20 nm. c) Histogram showing the size distribution of the inorganic core diameter (d_c). N refers to the counts for each diameter d_c . The average $d_c = 8.6 \pm 1.0$ nm.

2.8. Quantum Dots

2.8.1. CdSe/ZnS Core Shell Quantum Dots

CdSe QDs cores were prepared according previously published method ^[373] with some modifications using CdO and Selenium as precursors for Cd and Se respectively.

A shell of ZnS was grown around the CdSe QDs to passivate the CdSe QDs core and enhance their fluorescence using diethylzinc and hexamethyldisilathiane as zinc (Zn) and sulfur (S) precursors by drop-wise injection to allow slow and uniform shell growth at relatively low temperature to prevent the nucleation of ZnS QDs. The emission of the CdSe QDs increased after the first few injections, indicating the growth of a ZnS shell. The shell growth was controlled using the UV-Visible and fluorescence spectroscopy. As soon as the brightness (the fluorescence intensity) started to drop, the growth of the ZnS shell was stopped by stopping the ZnS precursor injection and cooling down.

The obtained QDs of the desired size were transferred to water via the amphiphilic polymer coating as described in section 2.2 followed by purification and characterization as described in sections 2.3 – 2.6.

CdSe/ZnS core/shell QDs of different colors (from green to red) and core diameters (from 2.8 – 5 nm) as shown in the TEM images in Figure 2.25 and Figure 2.31 were obtained which were further transformed to aqueous phase via the polymer coating and purified as described before. The resulted polymer coated CdSe/ZnS core/shell QDs showed green (Gel image shown in Figure 2.26 and absorption emission spectra shown in Figure 2.27) and red (Gel image shown in Figure 2.30 and absorption emission spectra shown in Figure 2.33) visible fluorescence, with small core and hydrodynamic diameters and narrow size distribution. These small water soluble fluorescent nanocrystals might be of great importance for many applications for sensing, tracking, bioimaging and other theragnostic applications [39, 42, 374, 375].

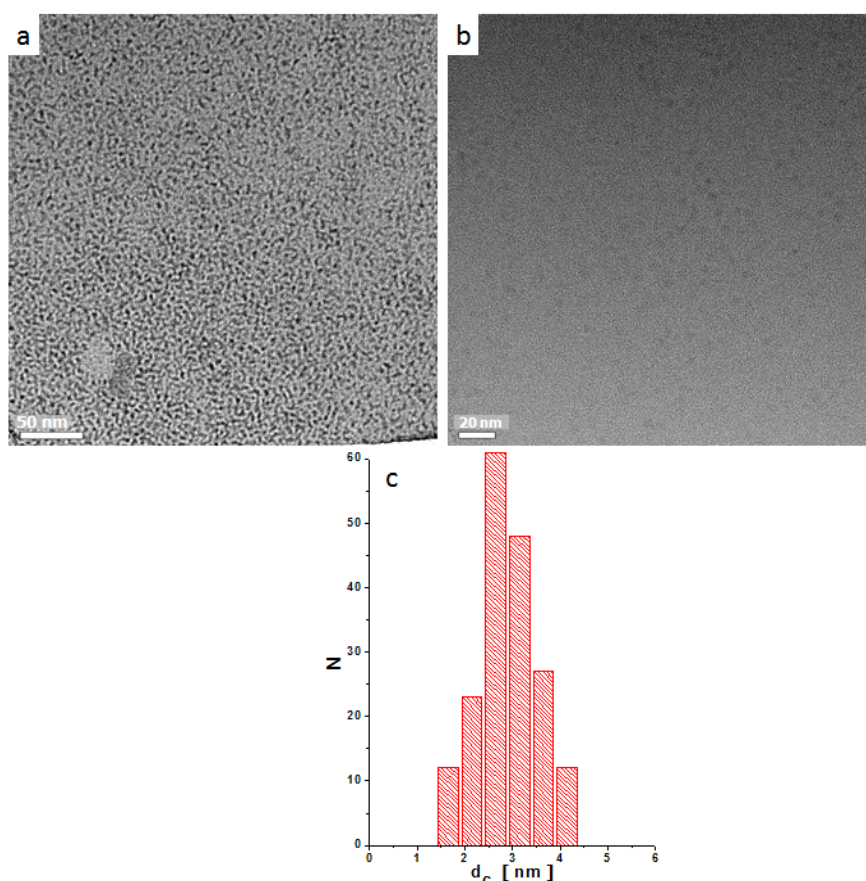


Figure 2.25: TEM images of the polymer coated green luminescent CdSe/ZnS core shell QDs 534 nm. Scale bars are 50 and 20 nm. c) Histogram showing the size distribution of the inorganic core diameter (d_c). N refers to the counts of each diameter. The average $d_c = 2.8 \pm 0.7$ nm.

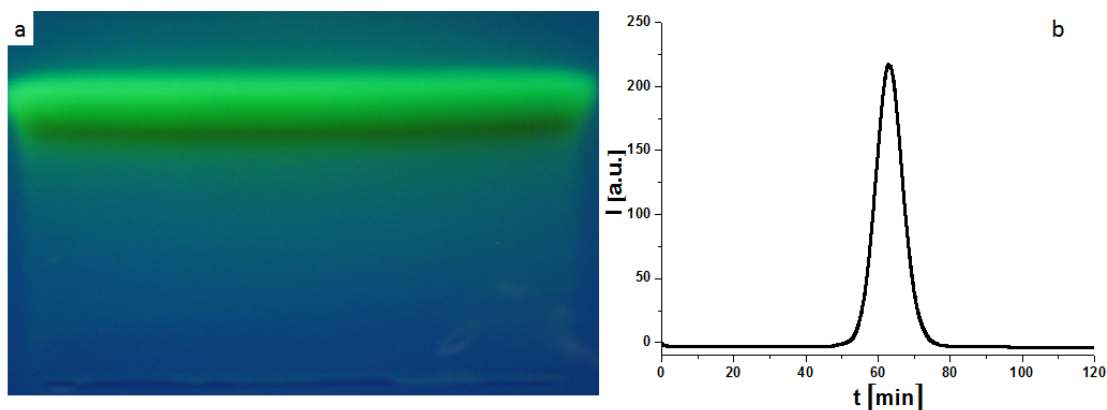


Figure 2.26: a) Gel electrophoresis image of the polymer coated green luminescent CdSe/ZnS core shell QDs 534 nm run on 2 % agarose gel for 1 hour at constant 100V. b) Elution profile of the polymer coated green QDs running through a size exclusion column. The absorption of the elute A is plotted versus the elution time (t).

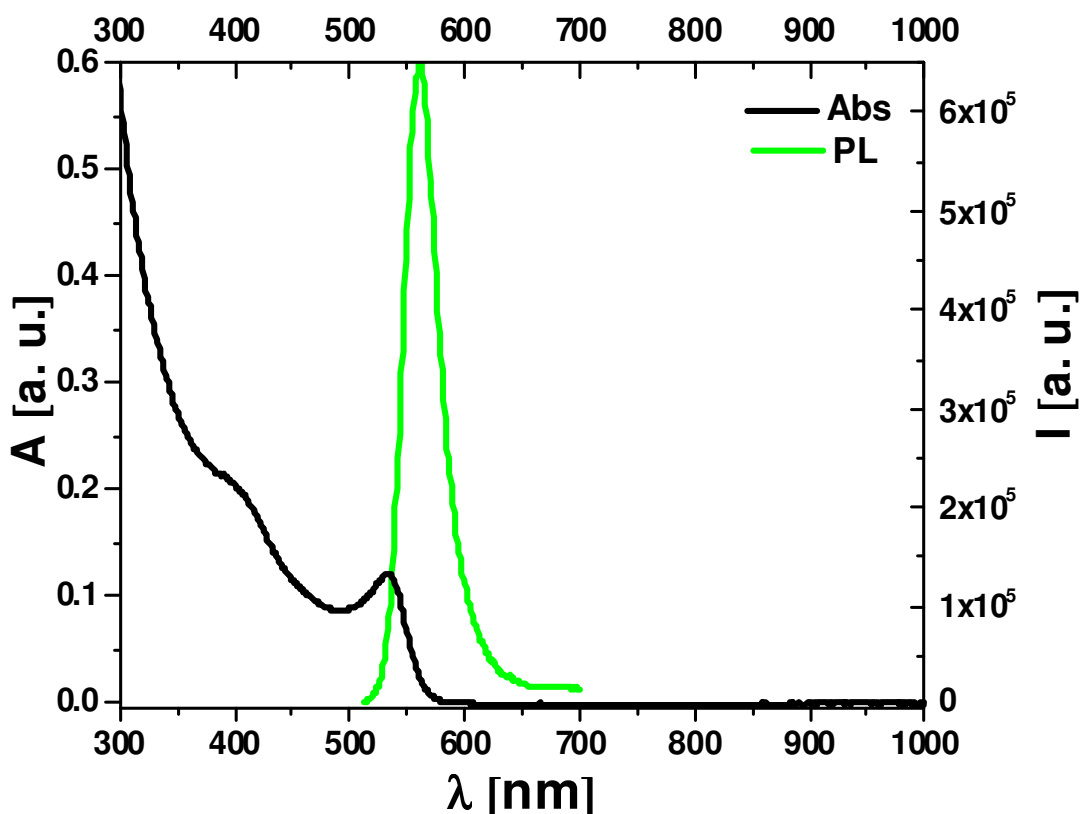


Figure 2.27: Absorption emission spectra of the polymer coated green luminescent CdSe@ZnS core shell QDs 534 nm with absorption/emission max 534/560nm.

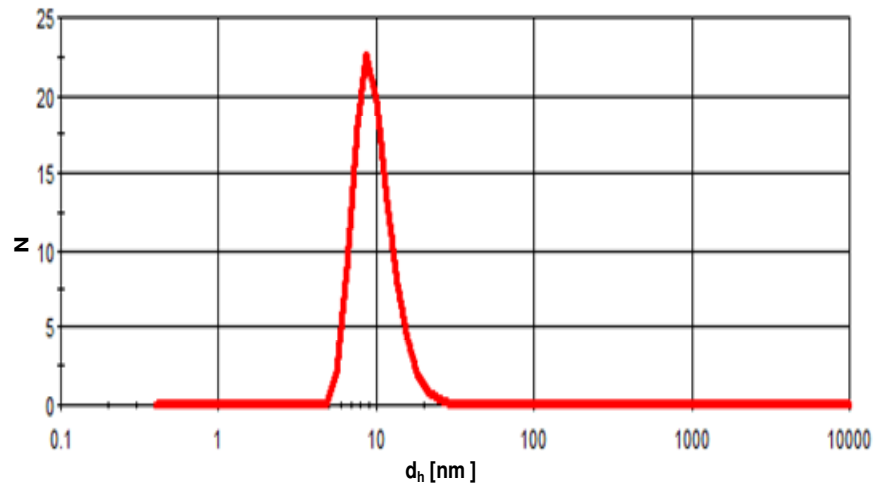


Figure 2.28: Hydrodynamic diameter (d_h) of the polymer coated green luminescent CdSe@ZnS core shell QDs 534 nm N refers to the number distribution. $d_h = 10.0 \pm 1.5$ nm.

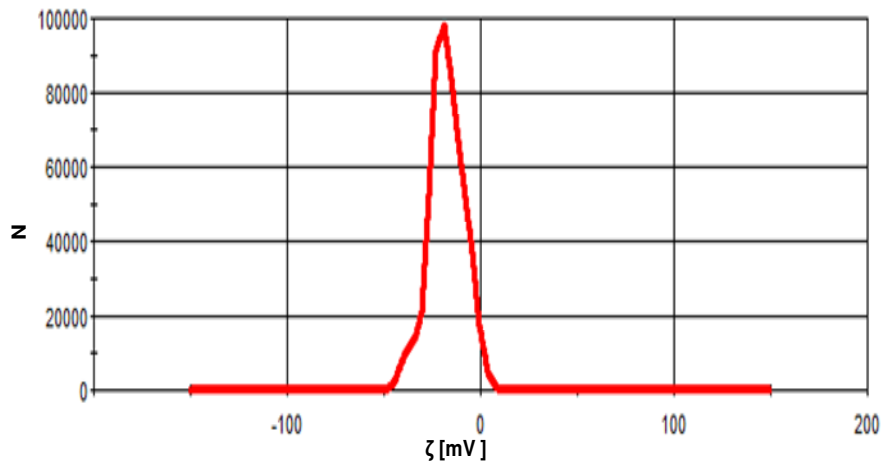


Figure 2.29: Zeta potential distribution of the green luminescent CdSe@ZnS core shell QDs. $\zeta = -22.6 \pm 4.8$ mV.

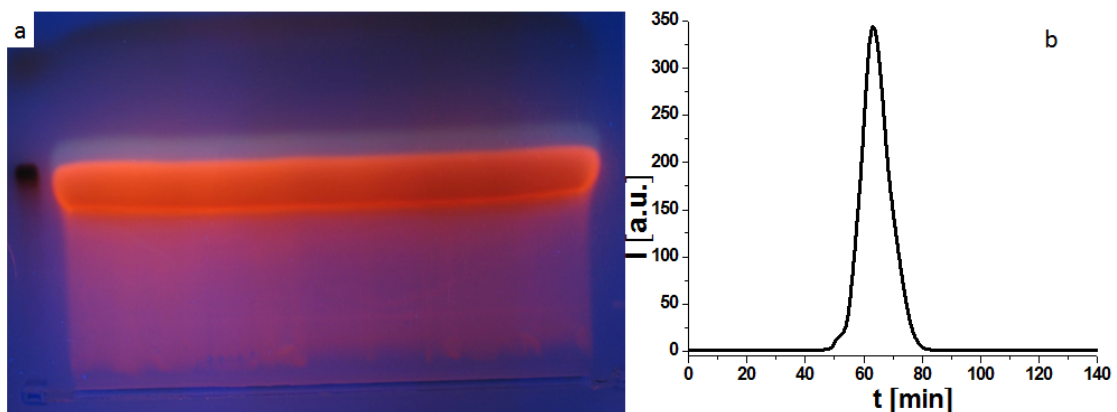


Figure 2.30: a) Gel electrophoresis image of the polymer coated red luminescent CdSe/ZnS core shell QDs 602 nm run on 2 % agarose gel for 1 hour at constant 100V. b) Elution profile of the polymer coated red QDs running through a size exclusion column. The fluorescence intensity of the elute A is plotted versus the elution time (t).

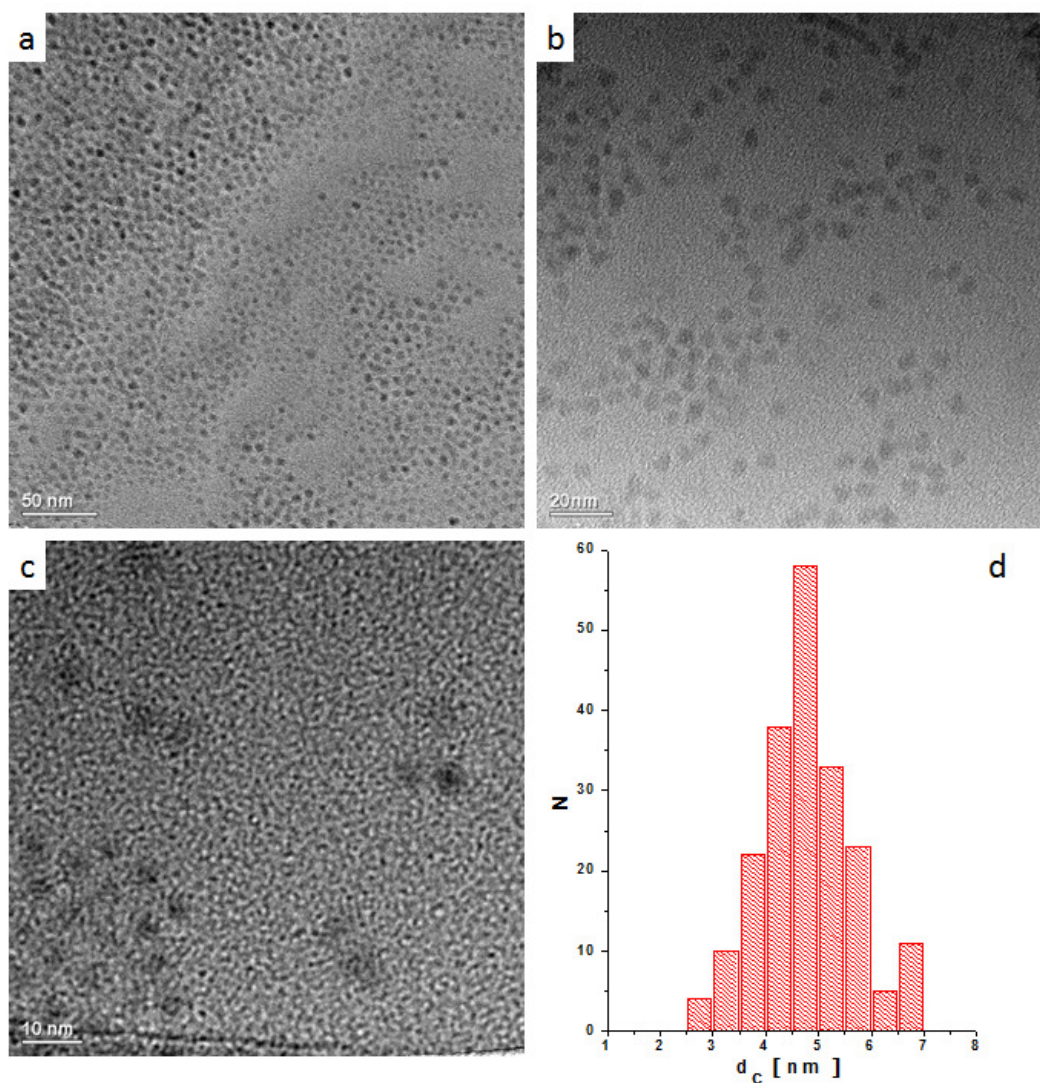


Figure 2.31: TEM images of the red luminescent CdSe/ZnS core shell QDs at different magnifications (low and high). Scale bars corresponding to a) 50, b) 20 nm and c) 10 nm. d) Histogram showing the size distribution of the inorganic core diameter (d_c). N refers to the counts for each diameter d_c . The average $d_c = 4.8 \pm 0.9$ nm.

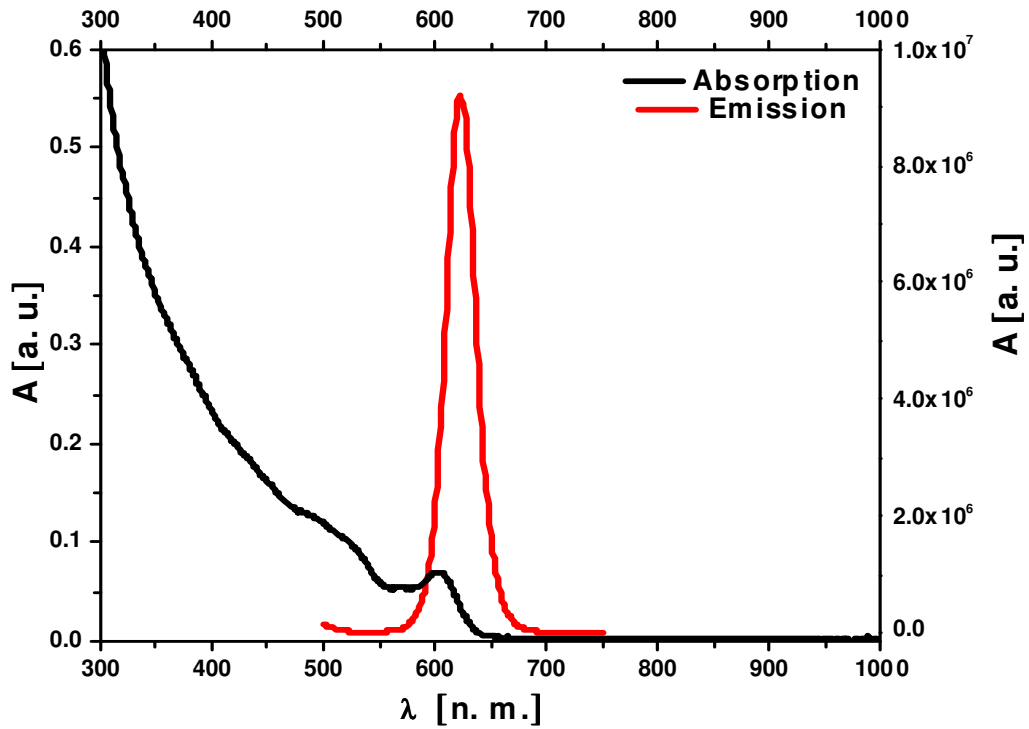


Figure 2.32: Absorption emission spectra of the polymer coated red CdSe@ZnS core shell QDs with absorption/emission max 602/622nm.

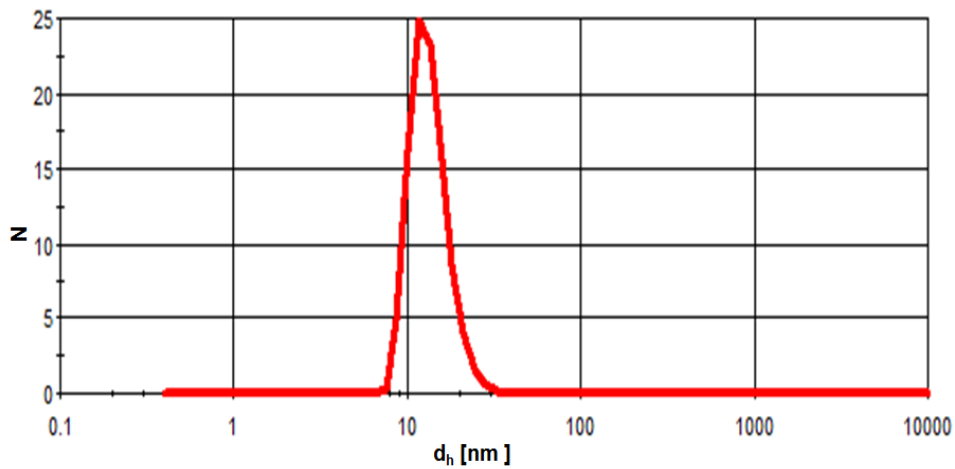


Figure 2.33: Hydrodynamic diameter (d_h) of the polymer coated red luminescent CdSe@ZnS core shell QDs 602 nm N refers to the number distribution. $d_h = 11.6 \pm 1.9$ nm.

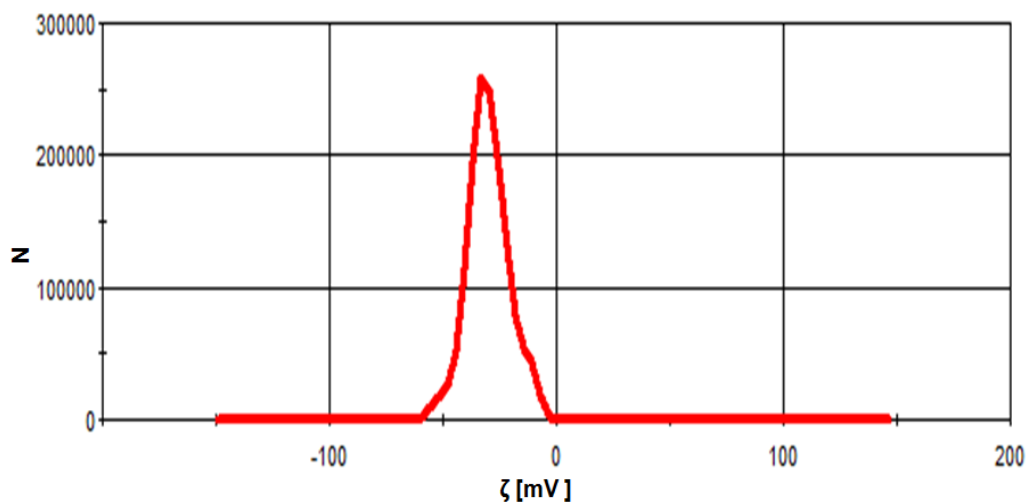


Figure 2.34: Zeta potential distribution of the red luminescent CdSe@ZnS core shell QDs. $\zeta = -30.1 \pm 1.8$ mV.

Surface Modification of the Red CdSe/ZnS QDs with 2 kDa Diamine PEG

The surface of the purified polymer coated red CdSe/ZnS core/shell QDs obtained from the last step was further modified with 2 kDa diamine polyethylene glycol. Briefly, a 10 μ L of the previously prepared polymer coated CdSe/ZnS QDs (5.4×10^{-6} M in Sodium borate buffer, SBB pH=9) was mixed with 13.8 μ L (0.5M) freshly prepared solution of 1-ethyl-3-(3-dimethylaminopropyl) carbodiimide (EDC, Sigma-Aldrich, # E7750) so the molar ratio of the QDs to the EDC was kept at 1:128000, and the mixture shaken for few minutes then 54 μ L of 100, 50, 25 or 12.5 mM solution of PEG-(NH₂)₂-2 kDa (Rapp polymer, # 11-2000-2) was added to each tube to get QDs:PEG molar ratios 1:100000, 1:50000, 1:25000 or 1:12500 respectively. The mixture was shaken and kept for 2 hours at room temperature. After 2 h, the PEGylated CdSe/ZnS QDs were run on 2 % agarose gel for one hour at constant voltage of 100 V, with 10 nm phosphine capped AuNPs as control.

Figure 2.35 a shows the difference in the retardation and electrophoretic mobility of the polymer coated CdSe/ZnS QDs modified with the diamine PEG at different molar ratios. The polymer coated QDs and the control (commercial 10 nm phosphine coated gold NPs) has comparable retardation and electrophoretic mobility, while the electrophoretic mobility of the PEGylated polymer coated QDs were more retarded. The electrophoretic mobility was more reduced with increasing the molar ratio of the polyethylene glycol from 12500 to 100000. The reduced mobility of the polymer coated QDs with increasing the molar ratio of PEG could be attributed to the increase of the size as indicated from the hydrodynamic diameter measured by the DLS and also to the reduction in the number of the negative charges due to the reduction in the free carboxylate groups which covalently linked to the amine groups of the polyethylene glycol forming amide bonds in aid of the EDC chemistry.

Finally, big batch of the polymer coated CdSe/ZnS core shell QDs was prepared using molar ratio 1:128000:100000 of polymer coated QDs:EDC:PEG and the PEGylated QDs was purified and characterized as described before in sections 2.3 – 2.6.

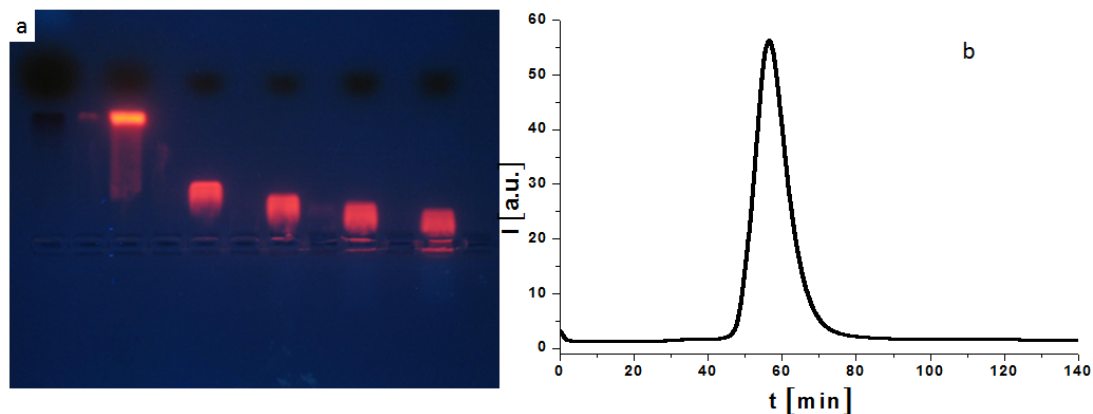


Figure 2.35: a) Gel electrophoresis image of the polymer coated CdSe/ZnS core shell QDs 602 modified with 2 kDa diamine PEG on a 2 % agarose gel. Lanes from left to right are 10 nm phosphine coated Au NPs (run as control in the left), coated QDs, 12500:1, 25000:1, 50000:1 and 100000:1 PEG:QDs. b) Elution profile of the polymer coated QDs modified 2kDa PEG (saturated) running through a size exclusion column. The fluorescence intensity of the elutes A is plotted versus the elution time (t).

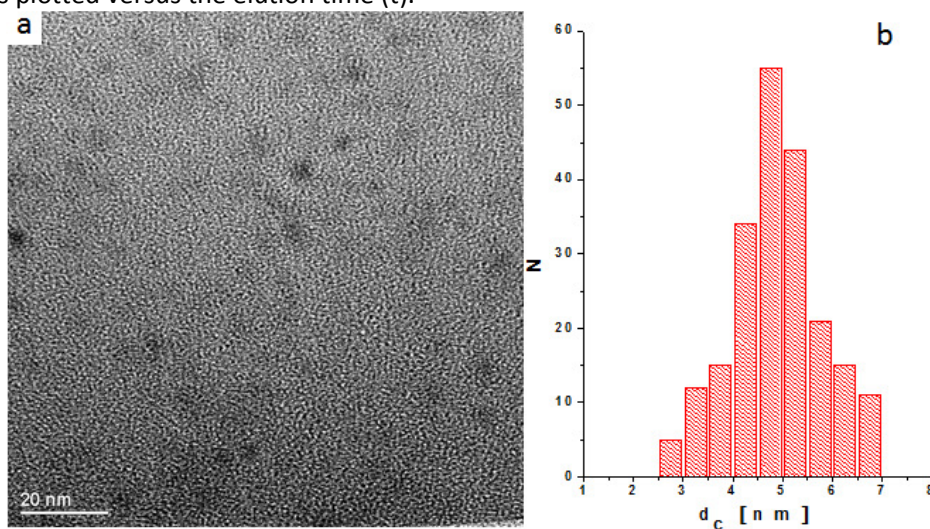


Figure 2.36: TEM image (a) and size distribution (b) of the polymer coated red CdSe@ZnS core shell QDs modified with 2 kDa PEG with an average core diameter $d_c=4.89\pm 1.2$.

From the DLS and zeta potential it was found that the hydrodynamic diameter (d_h) was increased from 11.6 ± 1.9 nm for the only polymer coated (no PEG in the sell) QDs to 18.66 ± 2.83 nm for the polymer coated QDs modified with 2 kDa PEG (Figure 2.19). Also in the same manner, the zeta potential was increased to -6.0 ± 3.9 mV compared to -30.1 ± 1.8 mV for the polymer coated QDs before the modification with 2kDa PEG. These results of the hydrodynamic diameter and zeta potential are in coincidence with the gel image and the reduced electrophoretic mobility as a result of the QDs PEGylation.

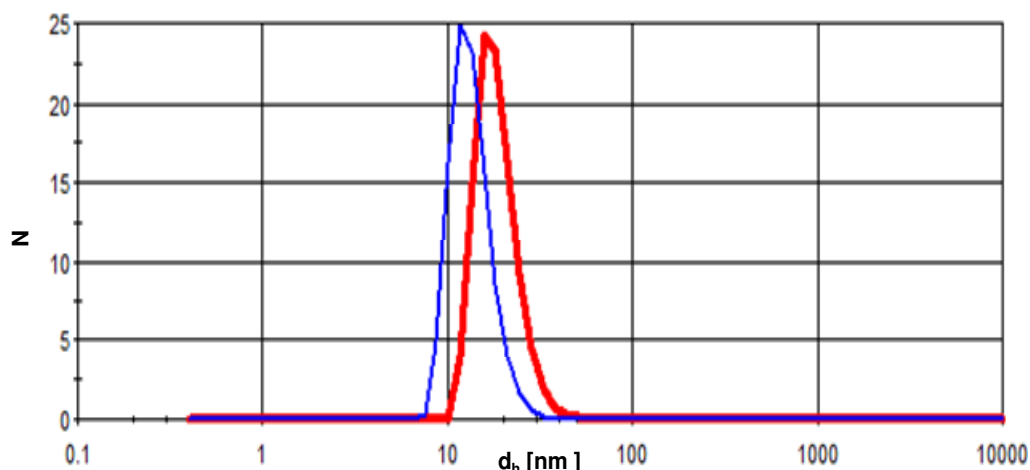


Figure 2.37: Hydrodynamic diameter d_h of the polymer coated red CdSe/ZnS core shell QDs before (blue line) and after PEGylation with 2 kDa PEG (red line) as determined with DLS. N refers to the number distribution. The hydrodynamic diameter d_h increased from 11.6 ± 1.9 for the non-PEGylated to 18.8 ± 2.8 nm for the polymer coated QDs modified with 2 kDa PEG.

2.8.2. ZnO Nanoparticles

2.8.2.1. Arginine Capped ZnO Nanoparticles

Arginine capped ZnO nanocrystals were prepared as follow; $Zn(Ac)_2 \cdot 2H_2O$ (1.46 g) was dissolved in 62.5 mL of methanol and heated to 60 °C. A solutions consisting of KOH (0.7 g dissolved in 32.5 mL methanol) and arginine solution (10 mL, 0.2 M in Millipore water) were mixed and added dropwise over about 10 minutes with vigorous magnetic stirring. Zinc hydroxide was precipitated and the solution became cloudy after about 5 minutes of the arginine and KOH addition. The mixture was stirred for 1 hour then the heater and the stirrer were removed and the solution was cooled to RT and precipitated with the aid of centrifuge at 2000 rpm for 5 minutes. The precipitate was dissolved in methanol and precipitated by centrifugation at 2000 rpm for 5 minutes. The last washing step was repeated twice and finally the ZnO nanocrystals were dissolved in 40 mL Millipore water giving clear transparent solution which was filtrated using 0.22 μm filter for further purification.

By this method, water soluble positively charged ZnO nanocrystals were directly obtained with no need for polymer coating or other phase transfer methods to get water soluble nanoparticles. The core diameter of inorganic ZnO core is 6.8 ± 1.9 nm as it shown in the TEM images in Figure 2.38. These obtained ZnO nanocrystals show a hydrodynamic diameter about 18 nm (Figure 2.39) and positive surface charge with zeta potential $\zeta + 26.6 \pm 0.4$ mV (Figure 2.40).

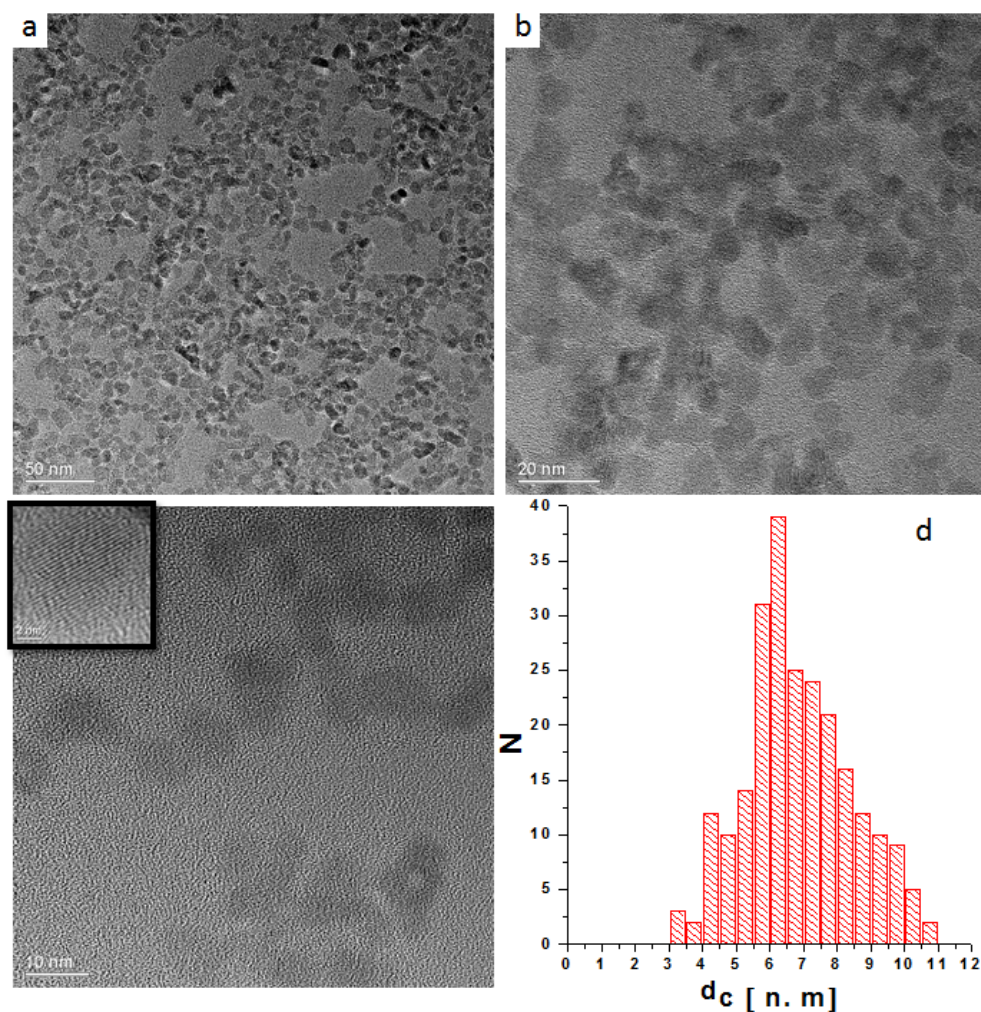


Figure 2.38: TEM images of the positively charged (arginine capped) ZnO nanocrystals at different magnifications (low and high). Scale bars corresponding to 50 (a), 20 (b) and 10 (c) nm. d) Histogram showing the size distribution of the inorganic core diameter (d_c). N refers to the counts for each diameter d_c . The average $d_c = 6.8 \pm 1.9$ nm.

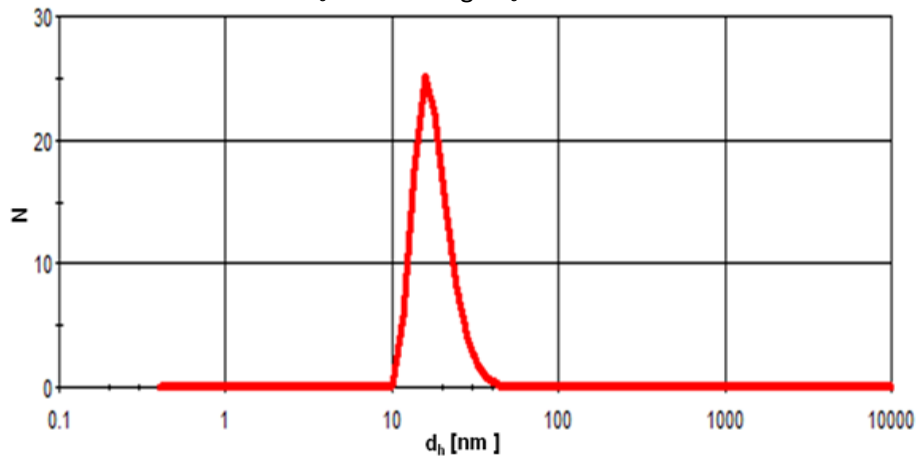


Figure 2.39: Hydrodynamic diameter (d_h) of the positively charged (arginine capped) ZnO nanocrystals with $d_h = 18.1 \pm 0.9$ nm.

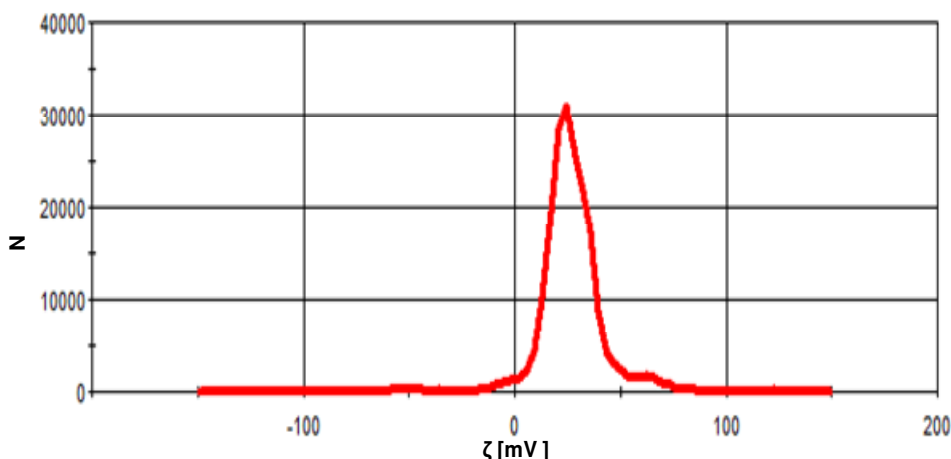


Figure 2.40: Zeta potential distribution of the positively charged (arginine capped) ZnO nanocrystals. $\zeta = +26.6 \pm 0.4$ mV.

The obtained ZnO nanocrystals have two emission bands, the first one is a narrow peak in the UV region with maximum intensity at 365 nm and the second is a wide peak in the visible band with a maximum intensity at 521 nm in the green region (Figure 2.41). The first one, the near UV emission arising from (i) the typical exciton emission as a result of the recombination of the photo-excited electrons in conduction band with holes in the valence band ^[62] (ii) near-band-edge emission resulting from the recombination of the photo-excited electrons in conduction band with the holes trapped near the valence band. The second one, the visible photoluminescence might be attributed to the oxygen vacancies ^[69-79].

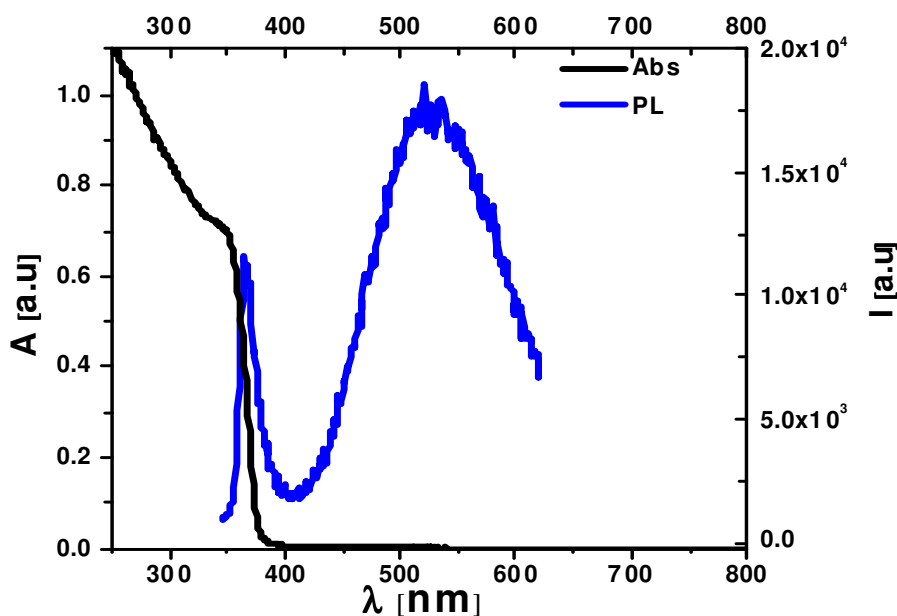


Figure 2.41: Absorption emission spectra of the positively charged (arginine capped) ZnO nanocrystals showing two fluorescence band one in the UV region with intensity max at 365nm and the other one in the visible region with intensity max at 521 nm. The excitation wavelength was 335 nm.

2.8.2.2. Polymer Coated ZnO Nanoparticles

Oleic acid capped ZnO nanocrystals were prepared with a modified method reported in literature ^[376] as follow. In details, 1.46g of zinc acetate dihydrate (# 383058, Sigma-Aldrich) was dissolved in 62.5 mL of methanol (#8388.6, Carl Roth) and heated to 60 °C. Solution of KOH (#5658.1, Carl Roth, 0.7 g) dissolved in 32.5 mL methanol was added dropwise over about 10 minutes under magnetically vigorous stirring. After about 5 minutes of the starting of the KOH addition, zinc hydroxide was precipitated and the solution became cloudy. The stirring was continued after the complete addition of the KOH solution, and the solution converted from cloudy to translucent after 20 minutes. At this point the solution was sonicated for 10 minutes and 1 mL of oleic acid (#364525, Sigma-Aldrich) was added. The mixture was sonicated again for extra 5 minutes and then stirred for 10 minutes. The stirring was stopped and the heater removed. The nanoparticles were cooled to RT and precipitated with the aid of centrifuge at 2000 rpm for 5 minutes. The precipitate was dissolved in chloroform (#Y015.2, Carl Roth) and then methanol added and precipitated again using the centrifuge at 2000 rpm for 5 minutes. The last washing step was repeated twice and finally the ZnO nanocrystals were dissolved in 25mL chloroform giving clear transparent solution.

The as prepared ZnO nanocrystals obtained from this method are hydrophobically capped (oleic acid capped particles), were converted to water soluble by the polymer coating protocol (section 2.2) and purified using gel electrophoresis and size exclusion chromatography as described in sections 2.3- 2.6 and shown in Figure 2.42.

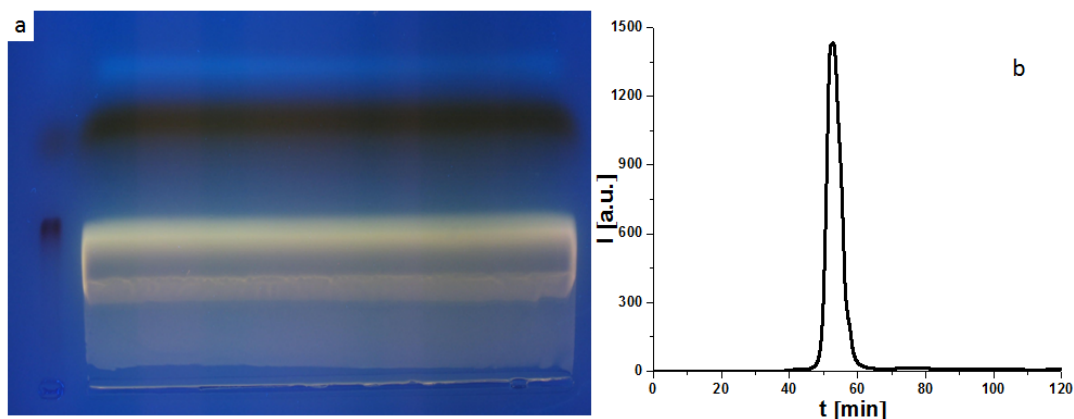


Figure 2.42: a) Gel electrophoresis image of the polymer coated ZnO nanocrystals on a 2 % agarose gel. The sample was run for 60 minutes at constant voltage 100 V. b) Elution profile of the polymer coated nanocrystals running through a size exclusion column. The fluorescence intensity of the elute A is plotted versus the elution time (t).

The water soluble resulted ZnO nanocrystals obtained, have inorganic core diameter 6.7 ± 1.5 nm as shown TEM images and size distribution histogram (Figure 2.43), and hydrodynamic diameter (d_h) 18.4 ± 1.4 nm with negative surface charge -35.2 ± 3.6 mV as shown in hydrodynamic diameter distribution measured by the DLS and shown in Figure 2.44 and the zeta potential distribution show in Figure 2.45.

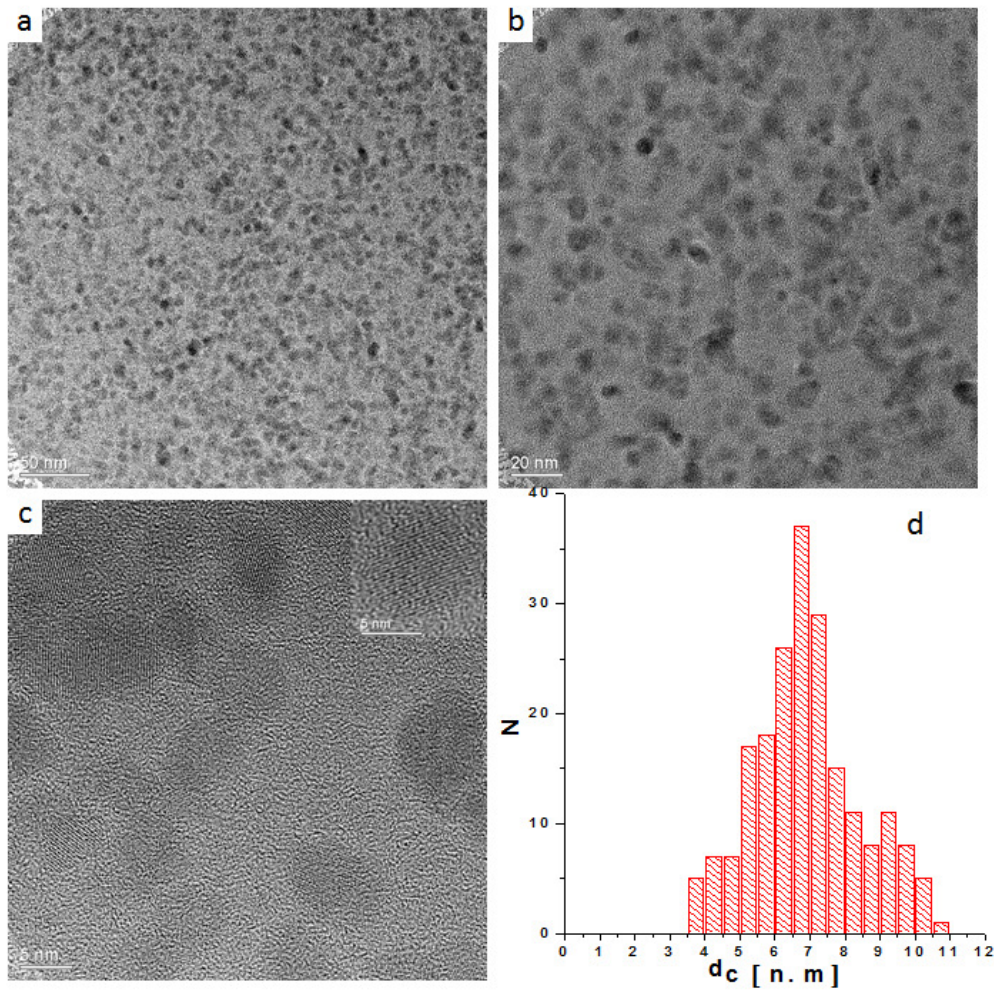


Figure 2.43: TEM images of the polymer coated ZnO nanocrystals at different magnifications (low and high). Scale bars corresponding to a) 50, b) 20 nm and c) 5 nm. d) Histogram showing the size distribution of the inorganic core diameter (d_c). The average $d_c = 6.7 \pm 1.5$ nm.

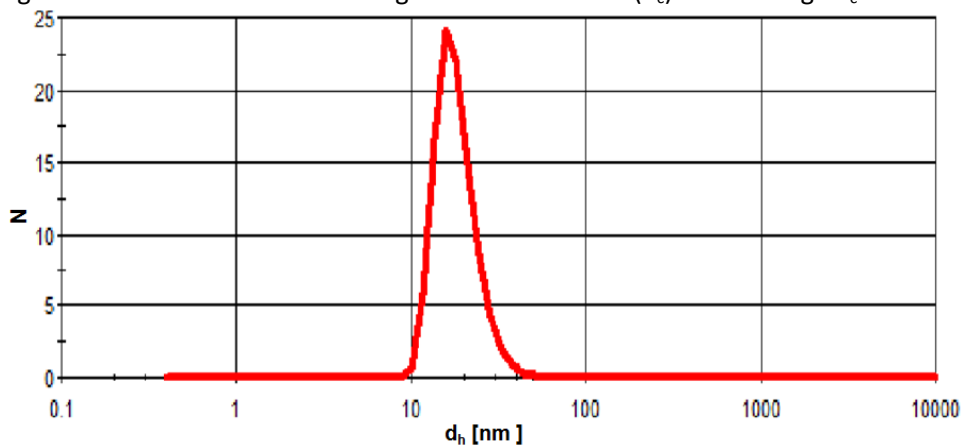


Figure 2.44: Hydrodynamic diameter (d_h) of the polymer coated ZnO nanocrystals with $d_h = 18.4 \pm 1.4$ nm.

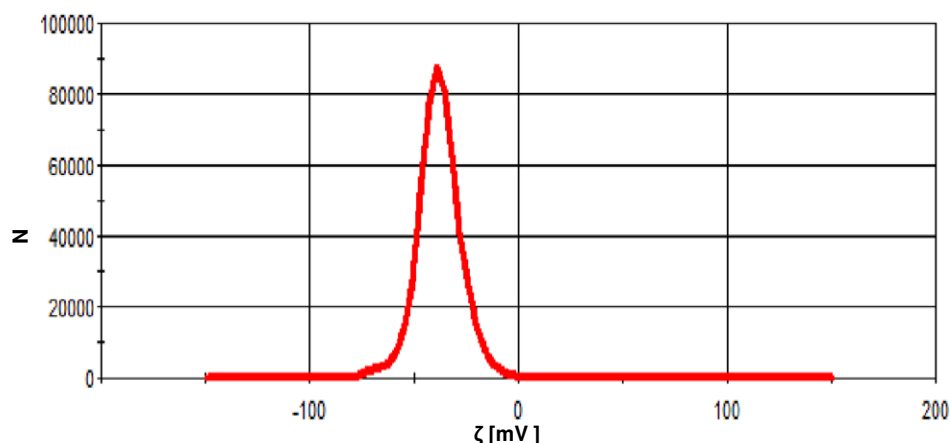


Figure 2.45: Zeta potential of the polymer coated ZnO nanocrystals. $\zeta = -35.2 \pm 3.6$ mV.

As shown in the gel images (Figure 2.42), the obtained polymer coated ZnO nanocrystals have strong visible fluorescence. As the case with the positively charged arginine capped ZnO nanocrystals, the negatively charged polymer coated ZnO nanocrystals also showed two emission bands, but unlike to arginine capped ZnO nanocrystals, the first narrow peak in the UV region is relatively small with maximum intensity at 364 nm and the second is a wide peak in the visible band with a maximum intensity at 543 nm (Figure 2.46). The first one, the near UV emission arising from (i) the typical exciton emission as a result of the recombination of the photo-excited electrons in conduction band with holes in the valence band^[62] (ii) near-band-edge emission resulting from the recombination of the photo-excited electrons in conduction band with the holes trapped near the valence band. The second one, the visible photoluminescence might be attributed to the oxygen vacancies^[69-79]. The strong visible fluorescence in case of polymer coated ZnO nanocrystals might be mean more oxygen vacancies compared to the arginine capped.

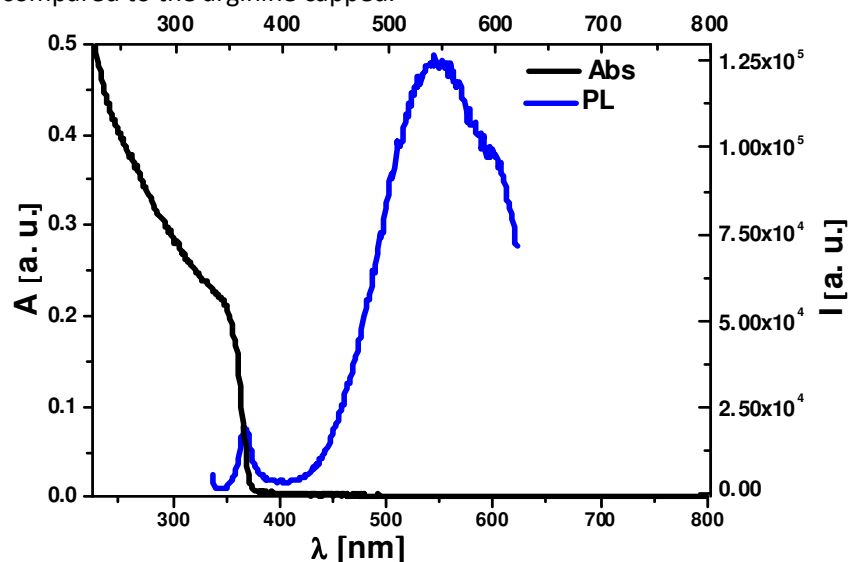


Figure 2.46: Absorption emission spectra of the polymer coated ZnO nanocrystals showing two fluorescence band one in the UV region with intensity max at 364 nm and the other one in the visible region with intensity max at 543 nm. The excitation wavelength was 325 nm.

3. Nanoparticles: Cellular Interactions and Toxicity

This chapter is dedicated to shed the light on some conducted biological studies on some of the obtained nanoparticles to investigate the nano-bio interactions/transformations and then possible utilization of these nanomaterials in the biological and environmental applications. Cell experiments were carried out by the group of Prof. Stefaan De Smedt, Laboratory for General Biochemistry and Physical Pharmacy, Faculty of Pharmaceutical Sciences, Ghent University, Belgium.

3.1. Effect of PEGylation of the polymer coated Au Nanoparticles on the Cellular Uptake, Interactions and Cytotoxicity

PEGylation of the nanoparticles is widely used mechanism for many biological and physicochemical purposes like modification the surface properties, enhancing the colloidal stability and increasing the circulation time. Here in this chapter we have prepared Au NPs PEGylated with methoxy 2kDa-Polyethylene glycol (mPEG) followed by studying the multi toxicological parameters and cellular interaction. The polymer coated gold NPs were modified and saturated with mPEG-NH₂ via EDC chemistry and purified as previously published elsewhere [377]. The polymer coated Au NPs obtained as described in sections 2.1-2.6 was modified with mPEG as follows. In an eppendorf tube, 100 μ L of the previously prepared polymer coated Au NPs (3.1 μ M in sodium borate buffer (SBB pH 9) was mixed with 397 μ L (0.1 M) of freshly prepared solution of 1-ethyl-3-(3-dimethylaminopropyl) carbodiimide (EDC, Sigma-Aldrich, # E7750) and the mixture was shaken for 2 minutes then 155 μ L (1X 10⁻³M) solution of mPEG-NH₂ -2 kDa (Rapp polymer, #12-2000-2) was added. The mixture was shaken and kept for 2 hours at room temperature. The molar ratio between the Au NPs: mPEG-NH₂: EDC are 1:500:128000 which designed to insure sufficient saturation of the surface of the NPs with the mPEG. After 2 h, the PEGylated god nanoparticles (mPEG-PMA-Au NPs) were purified using gel electrophoresis and size exclusion chromatography and characterized as described in section 2.2-2.6. Figure 3.1 is a schematic sketch showing the surface modification process of the polymer coated Au NPs with 2kDa MeO-PEG-NH₂.

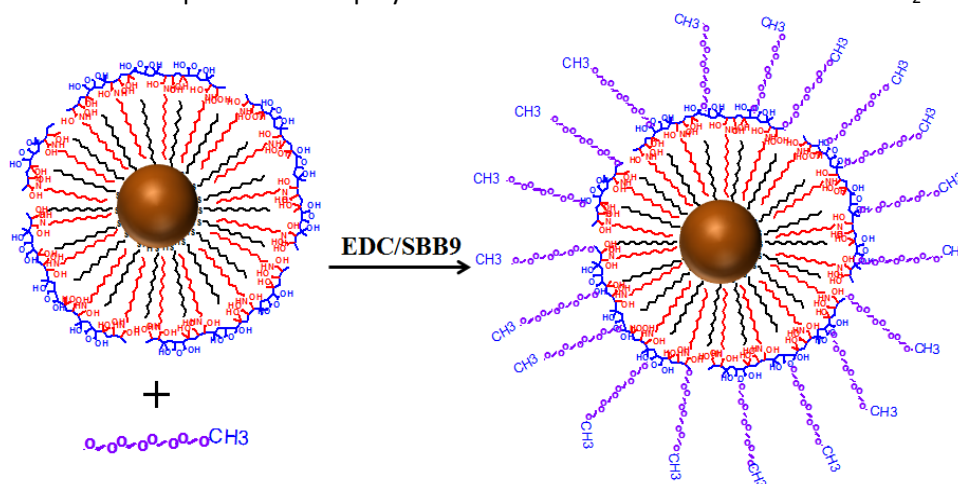


Figure 3.1: Schematic illustration for the surface modification of the polymer coated Au NPs with 2kDa MeO-PEG-NH₂.

The polymer coated Au NPs modified with mPEG are more retarded on the gel comparing to the non-PEGylated polymer coated Au NPs due to the increase in hydrodynamic diameter and the decrease of net negative surface charges of the mPEG modified Au NPs (Figure 3.2). In the size exclusion chromatography, the PEGylated polymer coated Au NPs had less elution or retention time and appear first (dashed line Figure 3.2 b) owing to their big size in comparison to non PEGylated NPs (solid line Figure 3.2 b) .

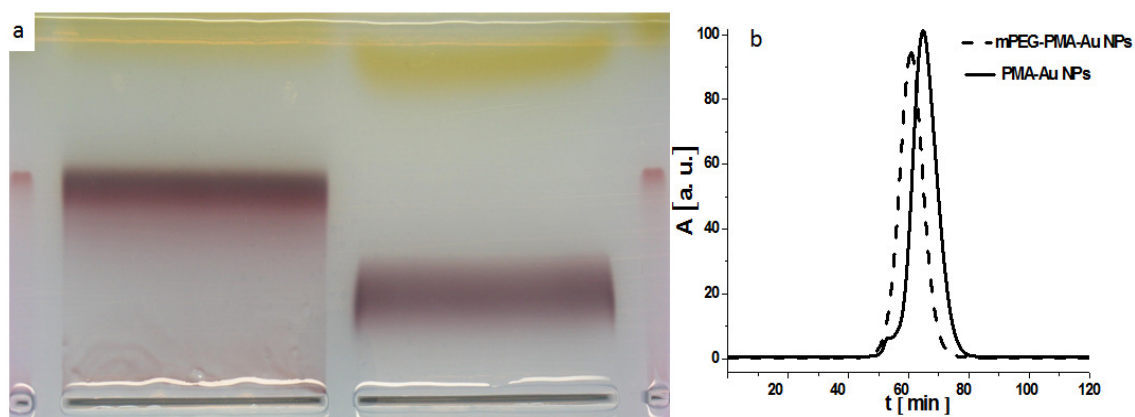


Figure 3.2: a) Gel electrophoresis image of the polymer coated Au NPs (left) and polymer coated Au NPs modified with 2kDa mPEG (right) on a 2 % agarose gel. b) elution profile of the polymer coated Au NPs before (solid line) and after modification with 2 kDa mPEG (dashed line) running through a size exclusion column. The absorption of the elute A is plotted versus the elution time (t).

The number distribution of hydrodynamic diameter d_h of the mPEG-PMA-Au NPs measured by the DLS was increased to 21.7 ± 2.9 nm compared to the polymer coated Au NPs used before PEGylation (d_h was 12.6 ± 1.1 nm). On other hand, the measured zeta potential for the PEGylated Au NPs was reduced to -7.6 ± 0.8 mV in comparison to the zeta potential of the original polymer coated Au NPs before the PEGylation (-31.9 ± 5.2) which could be attributed to the PEGylation and reduction in the free carboxylate groups due to the PEG linkage.

Table 3.1: Hydrodynamic diameters (d_h expressed as number distribution) and zeta potential (ζ) of the polymer coated Au NPs before and after the modification with 2kDa PEG-OCH₃ as measured in SBB pH9 using DLS.

Sample	d_h [nm]	ζ [mV]
Coated Au NPs	12.6 ± 1.1	-31.9 ± 5.2
Coated Au NPs modified with 2kDa mPEG	21.7 ± 2.9	-7.6 ± 0.8

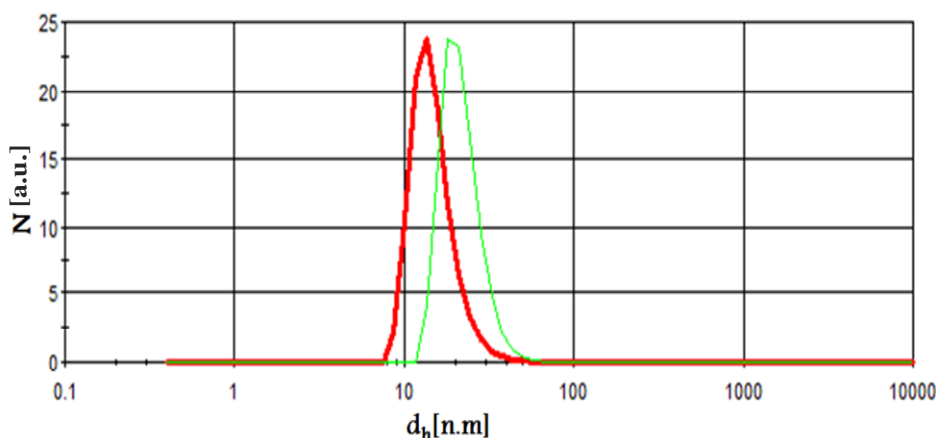


Figure 3.3: Hydrodynamic diameter (d_h) of the polymer coated Au NPs before (red line) and after modification (green line) with mPEG of 2 kDa as determined with DLS.

Cellular Uptake of the PEGylated Au NPs

The uptake and interactions nanoparticles with the cells studies were performed according to standard published protocols [378, 379]. Three types of cells, human umbilical vein endothelial cells (HUVECs), murine C17.2 neural progenitor cells, and rat PC12 pheochromocytoma cells were used. Briefly the cells seeded in 25 cm² cell culture flasks were incubated with 50 nM polymer coated Au NPs for 24 h at 37°C and 5% CO₂. After 24 h, the cells were washed three times with PBS buffer and the cells were detached using trypsination for few minutes. The cells were collected by centrifugation and treated with 2% paraformaldehyde (PFA) for 20 min for cell fixation and then the cells were washed three times with PBS. The cells were then pelleted at 4×10^5 cells/condition in 0.2 M cacodylate buffer (pH 7.4) and postfixed using 1% osmium tetroxide (dissolved in the same buffer) for 1 h at 4 °C. The cell pellets dehydrated with ethanol were then embedded in Epon-Araldite and thin sections (70 nm) were stained with uranyl acetate (5%) and then with the citrate (1%). Finally the samples scanned using transmission electron microscope.

For quantitative cellular uptake of the NPs, C17.2, HUVEC or PC12 cells were incubated with different concentrations (from 0 to 800 nM) for 24 h. The cells were trypsinated and centrifuged as described above followed by fixation in PFA after which the cells were washed three times with PBS and kept as a pellet of 4×10^5 cells/condition in 0.5 mL PBS. Aqua regia (2 mL) was added and the samples were digested in microwave (MLS 1200 Mega, Milestone, and Shelton, CT, USA). The digested samples were diluted to the proper concentration and the gold concentrations were measured by inductively coupled plasma mass spectrometry (ICP-MS) analysis.

PEGylated polymer coated Au NPs were found to be uptaken by all the tested cells (HUVECs, murine C17.2 and PC12) as indicated from the TEM images (Figure 3.4 A) and the ICP measurements (Table 3.2) but the PEGylation significantly reduced the uptake of the polymer coated Au NP. The intracellular distribution of the Au NPs was not affected by PEGylation of the polymer coated Au NPs compared to the coated Au NPs with no PEG on the surface [378].

The uptake pattern measured by TEM and inductively coupled plasma–mass spectrometry (ICP–MS) after 24 h was significantly different between the different cells where the highest uptake level was found to be for HUVECs, followed by C17.2 and PC12 cells, clearly indicating that uptake level of the PEGylated NPs is cell type dependent and should be addressed individually.

Au NPs [nM]	Cellular levels of PEGylated Au NPs (in 10 ⁵ NPs/cell)		
	HUVEC	C17.2	PC12
50	5.2	2.9	2.4
100	9.3	4.5	3.9
200	16.7	7.8	6.9
400	27.4	13.3	12.2
800	46.4	22.9	19.6

Table 3.2: Change of the cellular levels of the PEGylated Au NPs for the different tested cells at different concentrations (from 50 to 800 nM Au NPs) as determined by ICP-MS.

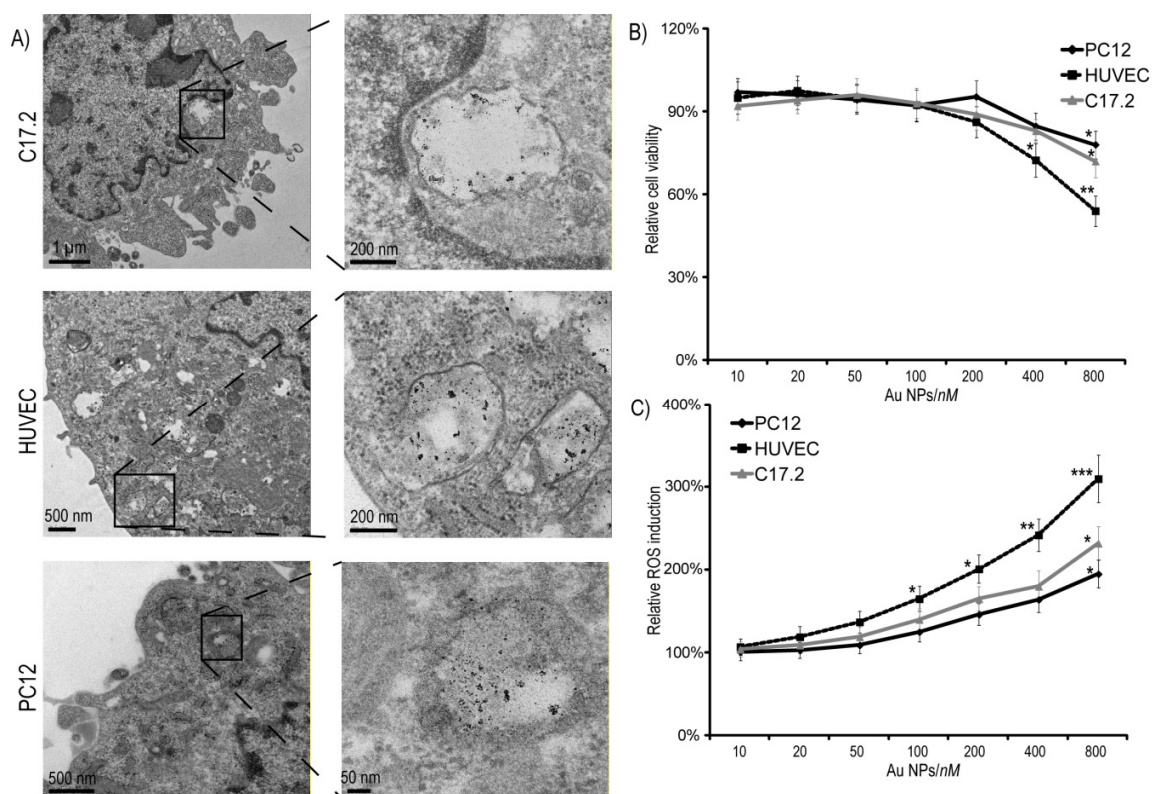


Figure 3.4: A) TEM images of C17.2, HUVEC and PC12 cells incubated with 50 nM of PEGylated polymer coated Au NPs for 24 h revealing clear cellular uptake. B) Cell viability and C) ROS induction of the cells treated with the PEGylated polymer coated Au NPs. The data are the mean of 5 measurements (n=5) + SEM relative to untreated control cells. The statistical significance levels are indicated (*: p < 0.05, **: p < 0.01, ***: p < 0.001).^[379]

Viability test

MTT assay was employed to quantitatively assess the cell viability of the C17.2, HUVEC and PC12 cells exposed to different concentrations of the PEGylated Au NPs. For this purpose, the cells were seeded at density of 5×10^4 cells/well in 96-well plates (200 μ L/well) and incubated overnight. On the next day, the cells were incubated for 24 h with different concentrations (0, 10, 20, 50, 100, 200, 400 or 800) of the PEGylated polymer coated Au NPs. Then the MTT (dimethylthiazol-2-yl)-2,5-diphenyltetrazolium bromide; Sigma-Aldrich, Bornem, Belgium) assay was conducted according to the manufacturer's protocol where 25 μ L MTT solution (5 mg/ml) was added per well and incubated for 4 h. The data are expressed as percentage to the untreated control cells.

The effect of PEGylation of the polymer coated Au NPs on the cell viability, as inferred from the MTT toxicological measurements (Figure 3.4 B) clearly revealed that the cell viability was affected at the higher NPs concentrations ($\leq 400 \times 10^{-9}$ M) in cell type dependent manner. The cell viability of cells was related to the uptake level where the highest toxicity levels were reported to the HUVECs compared to those with the less uptake levels (C17.2 and PC12 cells). Another toxicological parameter, induction of reactive oxygen species (ROS) was also performed and showed again concentration dependent effect (Figure 3.4 C).

3.2. Cellular Uptake, Interactions and Cytotoxicity of Polymer Coated CdSe/ZnS core shell QDs:

CdSe/ZnS core/shell QDs were prepared as described in section 2.7 followed by polymer coating purification using gel electrophoresis (Figure 3.5 A) and size exclusion chromatography (Figure 3.5 B). The water soluble polymer coated QDs have absorption emission max at 587/597nm (Figure 3.6), quantum yield 6.7%, inorganic core diameter (d_c) 4.7 ± 0.9 nm as measured by the TEM (TEM images Figure 3.7), hydrodynamic diameter $d_h = 11.0 \pm 3$ nm (Figure 3.8) and negative surface charges ($\zeta = -18 \pm 1$ mV, Figure 3.9).

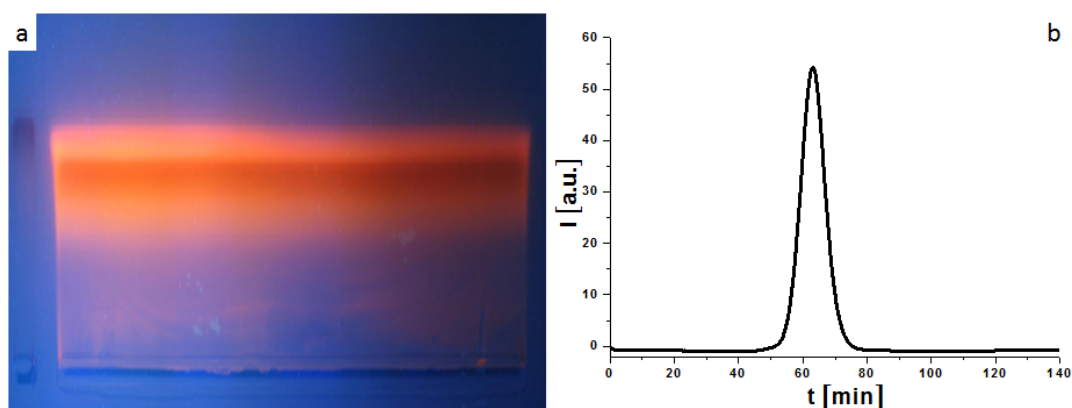


Figure 3.5: a) Gel electrophoresis image of the polymer coated red luminescent CdSe/ZnS core shell QDs 587 nm run on 2 % agarose gel for 1 hour at constant 100V. b) Elution profile of the polymer coated green QDs running through a size exclusion column. The absorption of the elutes A is plotted versus the elution time (t).

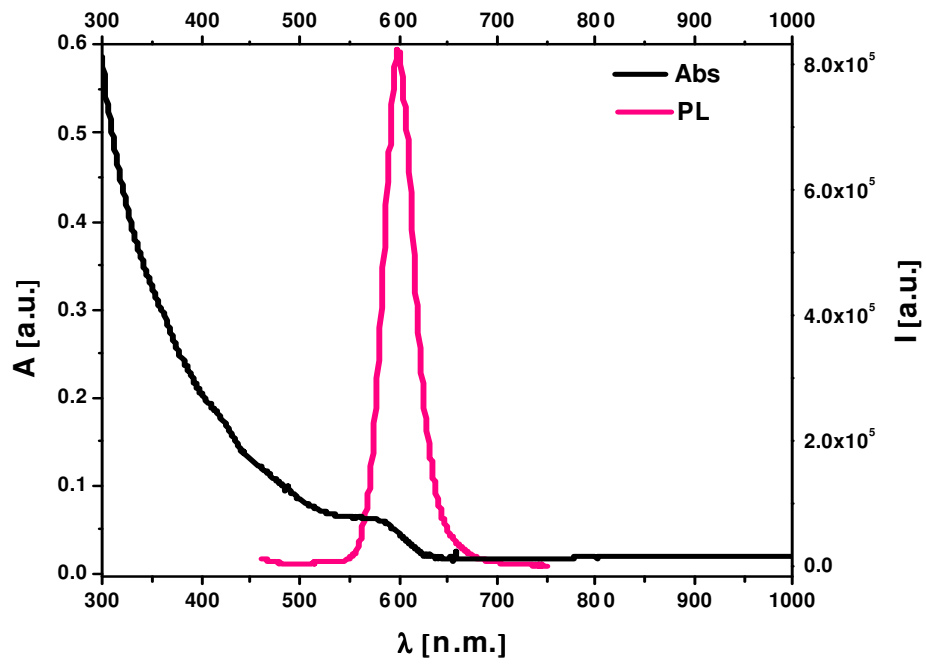


Figure 3.6: Absorption emission spectra of the polymer coated red CdSe@ZnS QDs 587 nm with absorption/emission max 587/599 nm.

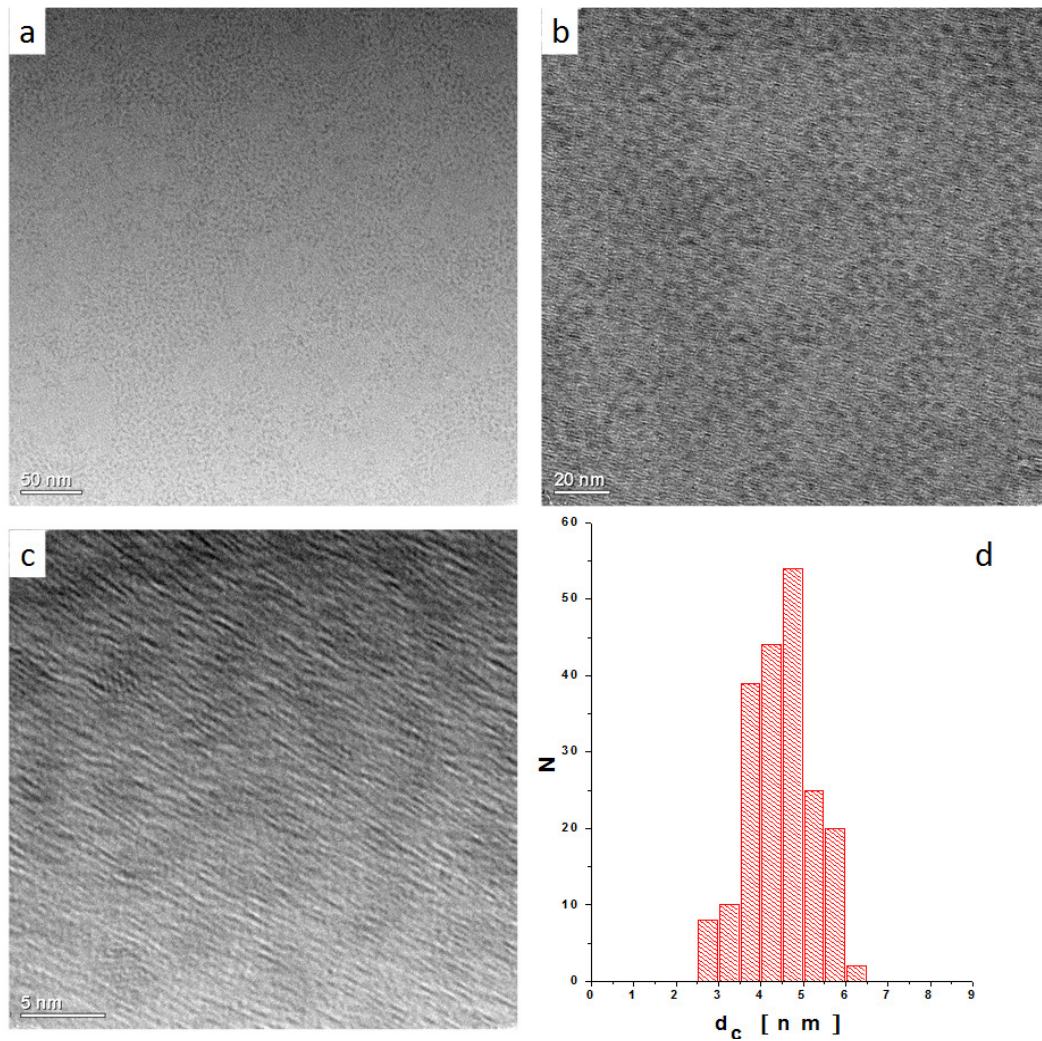


Figure 3.7: TEM images of the red luminescent CdSe/ZnS QDs at different magnifications (low and high). Scale bars corresponding to a) 50, b) 20 nm and c) 10 nm. d) Histogram showing the size distribution of the inorganic core diameter (d_c). N refers to the counts of each diameter. The average $d_c = 4.4 \pm 0.8$ nm

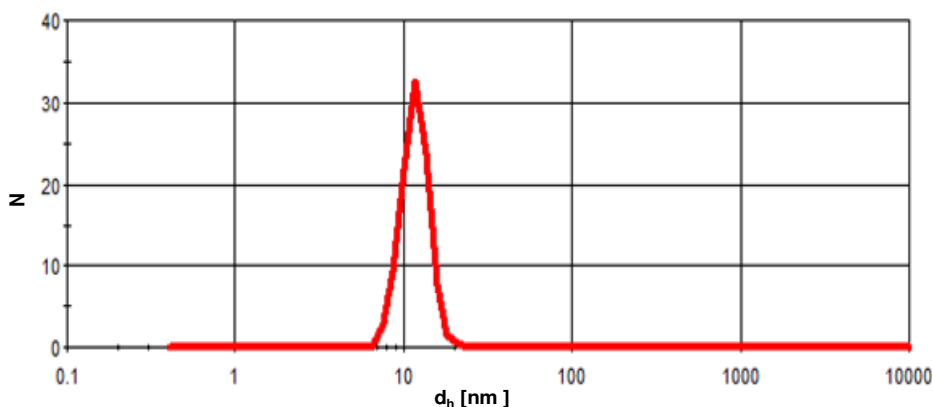


Figure 3.8: Hydrodynamic diameter (d_h) of the polymer coated red luminescent CdSe@ZnS QDs 587 nm. N refers to the number distribution. $d_h = 11.0 \pm 3$ nm.

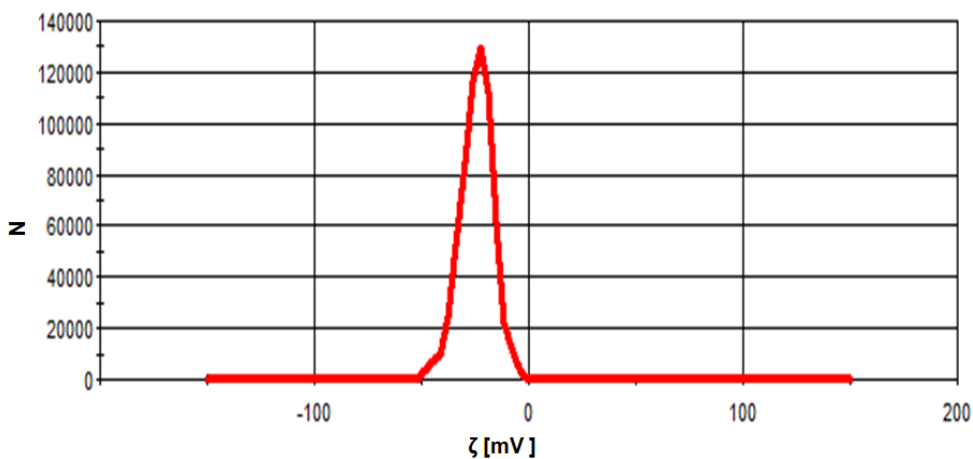


Figure 3.9: Zeta potential distribution of the polymer coated red CdSe@ZnS core shell QDs. $\zeta = -25.3 \pm 2.9$ mV.

A multiparametric toxicological method was used to evaluate the toxicity of water soluble, colloiddally stable red luminescent QDs using the same cell lines mentioned above (HUVECs, C17.2 and PC12) in order to address the nontoxic concentration applicable in the cell labeling. The results indicated that the polymer coated red luminescent QDs showed concentration-dependent toxicity as inferred from the MTT assay (Figure 3.10 A) and ROS measurements (Figure 3.10 B) with non-toxic concentration 2 nM. Figure 3.11 shows some confocal images showing the uptake of these polymer coated red CdSs/ZnS core/shell QDs and then the potential applications as labeling agent for bioimaging and tracking.

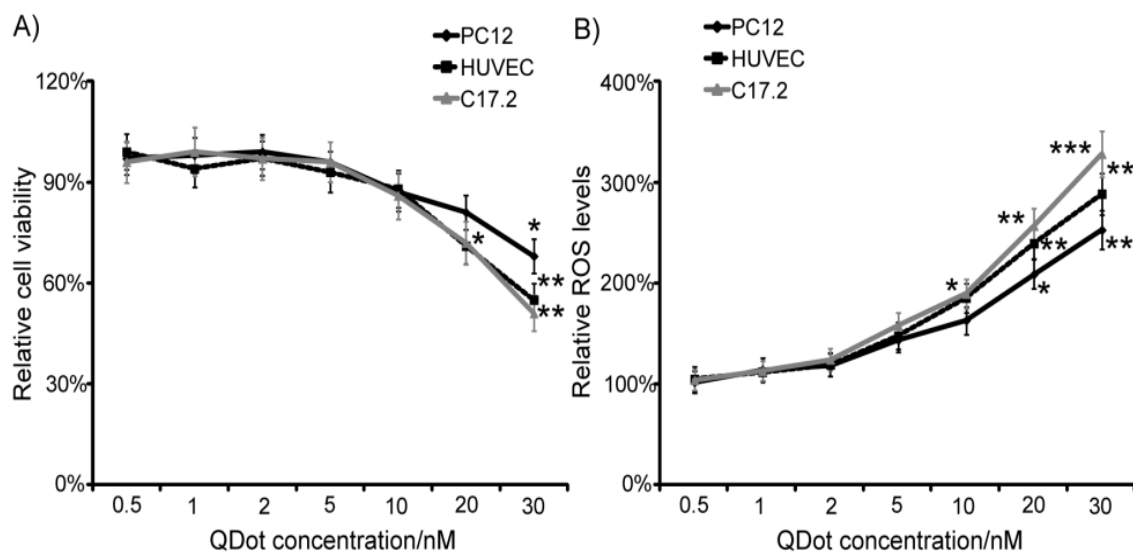


Figure 3.10: A) Cell viability and B) ROS induction of the PC12, HUVEC and C17.2 cells incubated with the polymer coated red luminescent CdSe/ZnS QDs. The statistical significance levels are indicated (*: $p < 0.05$, **: $p < 0.01$, ***: $p < 0.001$).^[380]

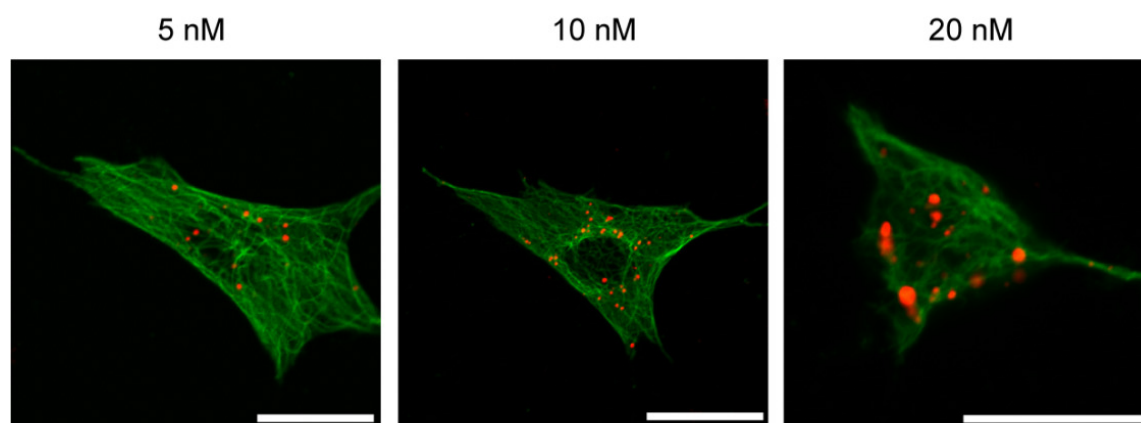


Figure 3.11: Confocal microscope images of HUVEC cells incubated with red luminescent polymer coated CdSe/ZnS QDs for 24 h at 5 nM (left column), 10 nM (middle row) and 20 nM (right column). The shown images are merged images of QDs (red) and α -tubulin cytoskeleton (green). Scale bars corresponding to 50 μm .⁽³⁸⁰⁾

4. Conclusion and Outlook

In summary, in the present study, magnetic, fluorescent and noble metal nanoparticles were synthesized. Most of the as synthesized nanoparticles prepared in this thesis are capped with hydrophobic ligands giving the nanoparticles the hydrophobic nature and making them water insoluble. Very general amphiphilic polymer coating protocol was harnessed to convert the hydrophobic nanoparticles from the organic solvent to aqueous phase where the nanoparticles get wrapped by the polymer shell. Further surface modification, bioconjugation and functionalization easily can be performed on the obtained polymer coated nanoparticles directly by modification of the amphiphilic polymer before the coating or indirectly by modification of the coated nanoparticles via the EDC chemistry and activation of the free carboxylic groups on the surface of particles.

Also different general purification strategies like ultrafiltration, gel electrophoresis and size exclusion chromatography were utilized for the purification during the polymer coating, surface modification and functionalization to obtain well purified and defined nanoparticles.

The colloidal stability and physicochemical properties of the nanoparticles at the different modification stages were investigated using different characterization techniques like TEM, DLS, UV-visible spectroscopy and fluorescence spectroscopy.

Covalently attachment of functional molecules to the surface of the nanoparticles or what is known as nanoparticles conjugation and/or functionalization is a promising approach in the materials sciences which could provide the basis for functional designed materials toward a wide range of different applications especially biological and environmental applications. Multifunctional nanoparticles which combine different functionalities (e.g. magnetic, fluorescent, radioactivity, therapeutic, specific targeting and controlled release) are of significant importance and expected to have a great impact in different areas in particular the biological and biomedical applications for diagnosis (like MRI and fluorescence multimodal imaging), targeting and therapy (controlled release and drug delivery). Here in this work different types of nanoparticles easily and effectively have been functionalized. For example, magnetic iron oxide nanoparticles were covalently functionalized with different fluorophores like tetramethylrhodamine cadaverine (TAMRA), DY-495 and DY-647 via activation of the free carboxylate groups using EDC chemistry. These fluorescent magnetic nanoparticles could be employed as multifunctional material for magnetic guided separation and purification, tracking, sensing and multimodal imaging using MRI and optical (fluorescence) imaging. Also, the surface of the coated magnetic iron oxide nanoparticles was modified for the therapeutic and targeted delivery purposes. The methotrexate as anti-cancer drug and folic (for targeted delivery) were covalently linked to the surface of the polymer coated magnetic iron oxide nanoparticles and polyethylene glycol (PEG) was employed as a crosslinker. These methotrexate functionalized magnetic nanoparticles is

considered a good example for the multifunctional nanoparticles in the therapeutic and diagnostic medical applications.

Zinc oxide nanoparticles have earned great importance for the environmental and biological applications in the recent few years. In this work positively charged arginine capped zinc oxide nanocrystals were directly prepared with no need for phase transfer polymer coating and further purification steps using gel electrophoresis and size exclusion chromatography required for the purification of the polymer coated nanoparticles to get rid of the free polymer micelles. The size of the inorganic ZnO cores prepared in this method has comparable size for the oleic acid capped ZnO. The negatively charged polymer coated ZnO nanocrystals and the positively charged arginine capped ZnO, both have similar hydrodynamic diameter but different surface charges and surface chemistry which might lead to *in vitro* and *in vivo* different biological interactions.

Beside the nature, size and shape of the engineered nanomaterials, the surface modification and functionalization of the nanomaterials could increase the diversity of nanomaterials properties and their different applications. A huge number of nanoparticles of different types, shape sizes can be synthesized and their surfaces might be modified, conjugated and functionalized with enormous number of the different materials with different properties and functionalities aiming to increase the stability, tailor, tuning the surface properties and/or incorporate novel functionalities with a final purpose to make use of the combined unique properties (fluorescence, plasmonic, optical or magnetic) of the core and surface tuned properties.

A major task for the future is to optimize the surface modification and the physicochemical properties of the engineered nanomaterials to achieve maximum functionalities and benefits for human being and environment as well as to get rid, overcome or reduce the possible side effects of the nanomaterials on human health and environment.

5. Publications

1.1. Nanoparticles; Synthesis, Surface Modification, Characterization and Bio Interaction

A1 – Kreyling, W.; Abdelmonem, A. M.; Ali, Z.; Haberl, N.; Hartmann, R.; Hirn, S; de Aberasturi, j. D.; Khadem-Saba1, G.; Montenegro, J.; Rejman, J.; Rojo, T.; de Larramendi I.; Wenk1, A.; Parak, W. J., In vivo integrity of colloidal nanoparticles. *NATURE NANOTECHNOLOGY*. (In Revision).

This paper is dedicated to address the integrity of the colloidal polymer coated nanoparticles *in vivo*.

Well colloiddally stable radioactive gold (^{198}Au) nanoparticles were labeled with radioactive indium (^{111}In) via DOTA chelator covalently attached to the surface of the polymer coated ^{198}Au NPs. The multimodal radioactive ^{198}Au NPs- ^{111}In nanoparticles were intravenously administered to rats. The distribution of the whole ^{198}Au NPs- ^{111}In nanoparticles, ^{198}Au NPs cores and the radioactive 111-Indium in the body were probed by the gamma spectroscopy. The biodistribution data clearly indicate that, *in vivo* the polymer shell at least partially detaches from nanoparticle core. The suggested mechanism for the partial removal of the polymer shell could be attributed to the enzymatic degradation in particular the hydrolytic affect proteolytic enzymes and breaking the amide bonds. This suggested hypothesis was tested in tube using external proetolytic enzymes and it was found that the proteolytic enzymes able to cause partially release of the polymer shell. The results of this paper indicate that the physicochemical properties of the nanoparticles even the well defined highly stable nanoparticles of could be dramatically changed *in vivo*.

Contribution to this paper;

Synthesis of hydrophobically capped 4.5 nm Au nanoparticles, 4.8 nm red luminescent CdSe/ZnS core shell quantum dots, the amphiphilc polymer, DY-495 modified polymer, DY-636 modified polymer and the polymer modified with 1,4,7,10-tetraazacyclododecane-1,4,7,10-tetraacetic acid (DOTA) as chelator for the indium, polymer coating of the Au NPs with the plain polymer, polymer coating with the chelator and fluorophores modified polymers, decoration of the polymer coated radioactive gold nanoparticles (^{198}Au NPs) with the radioactive indium (^{111}In) and nonradioactive indium, purification and characterization of the nanoparticles and quantum dots of the different modifications using ultrafiltration, gel electrophoresis, size exclusion chromatography (SEC) and PD-10 desalting columns, sterilizing the modified nanoparticles for the biological applications, full characterization of the different nanoparticles and quantum dots before and after surface modification with dynamic light scattering (DLS), Doppler Anemometry, UV-Vis spectroscopy and fluorescence spectroscopy. Data analysis, editorial works for the paper and writing most of the supporting information.

A2 – Mahmoudi, M.; Abdelmonem, A. M.; Behzadi, S.; Clement, J.; Dutz, S.; Ejtehadi, M.; Hartmann, R.; Kantner, K.; Linne, U.; Maffre, P.; Metzler, S.; Moghadam, M.; Pfeiffer, C.; Rezaei, M.; Ruiz-Lozano, P.; Serpooshan, V.; Shokrgozar, M.; Nienhaus, G.; Parak, W., Temperature: The "Ignored" Factor at the NanoBio Interface. *ACS NANO*. 2013, 7, (8), 6555-6562.

This article was dedicated to study the effect of the temperature on interaction of the nanoparticles with biomolecules especially proteins and the protein corona formation on the surface of the nanoparticles. In this paper it was clearly found that the protein corona formation (both the degree of coverage and composition of protein corona adsorbed on the surface of the nanoparticles) is strongly temperature dependent which might affect in turn on the cellular uptake of these nanoparticles.

Contribution to this paper;

Synthesis of oleic acid capped FePt nanoparticles, the amphiphilic polymer and the modified polymer, polymer coating of the nanoparticles, purification and characterization of the coated FePt nanoparticles with gel electrophoresis and size exclusion chromatography (SEC), full characterization of the nanoparticles before and after surface modification with dynamic light scattering (DLS), Doppler Anemometry, UV-Vis spectroscopy and fluorescence spectroscopy. Surface modification of the polymer coated FePt NPs with bovine serum albumin (BSA). Transmission electron microscope (TEM) measurements of all nanoparticles used in this article, some editorial works for the paper and writing a big part of the supporting information.

A3 – Soenen, S. J.; Manshian, B. B.; Abdelmonem, A. M.; Montenegro, J.-M.; Tan, S.; Balcaen, L.; Frank Vanhaecke; Brisson, A. R.; Parak, W. J.; Smedt, S. C. D.; Braeckmans, K., The Cellular Interactions of PEGylated Gold Nanoparticles: Effect of PEGylation on Cellular Uptake and Cytotoxicity. *Part. Part. Syst. Charact.* **2014**, doi: 10.1002/ppsc.201300357.

PEGylation of the nanoparticles is widely used mechanism for many biological and physicochemical purposes like modification of the surface properties, enhancing the colloidal stability and increasing the circulation time. In this article, the cellular interaction and toxicological effect of the polymer coated Au NPs modified with methoxy polyethylene glycol (mPEG) have been investigated.

Contribution to this paper; Synthesis of dodecanethiol capped 4.6 nm Au NPs and the amphiphilic polymer, polymer coating of the Au NPs, modification of the coated Au NPs with polyethylene glycol (PEG-2kDa), purification and characterization of the coated and PEGylated Au NPs using gel electrophoresis and SEC, full characterization of the Au NPs before and after surface modification with dynamic light scattering (DLS), Doppler Anemometry, transmission electron microscope, UV-Vis spectroscopy in addition to some editorial works in the main paper and the supporting information.

A4 – Soenen, S.; Montenegro, J.; Abdelmonem, A.; Manshian, B.; Doak, S.; Parak, W.; De Smedt, S.; Braeckmans, K., The effect of nanoparticle degradation on poly(methacrylic acid)-coated quantum dot toxicity: The importance of particle functionality assessment in toxicology. *ACTA BIOMATERIALIA* **2014**, 10, (2), 732-741.

A growing great interest recently has been paid to the unique properties of the colloidal fluorescent semiconductor nanocrystals for a wide range of technological and biological applications from sensing, tracking, bioimaging to the theranostic applications powered by their optical and fluorescence properties. The biological applications of the heavy metal containing QDs are a matter of debate due to the toxic effects which might estimate from the possible intracellular degradation of the QDs inside the different cellular compartments. In this article, a multiparametric toxicological evaluation was performed to evaluate cytotoxicity, the intracellular fate and functionality of the well characterized polymer coated red CdSe/ZnS core/shell QDs. The QDs exposed to acidic pH inside the endosomes were partially degraded and released cadmium ions resulting in reduced fluorescence intensity and triggering particle toxicity.

Contribution to this paper;

Preparation of hydrophobically capped red luminescent CdSe/ZnS core/shell QDs with emission maximum at 597nm, the amphiphilic polymer, coating of the CdSe/ZnS QDs, purification and characterization of the coated using gel electrophoresis and SEC and full characterization of the QDs using DLS, Doppler Anemometry, TEM, UV-Vis spectroscopy and fluorescence spectroscopy. Studying the effect of pH on the degradation and chemical stability of the CdSe/ZnS QDs. Also I have contributed to some editorial works and supporting information writing.

1.2. Nanoparticles in Sensing Applications

A5 – Riedel, M.; Göbel, G.; Abdelmonem, A. M.; Parak, W. J.; Lisdat, F., Photoelectrochemical Sensor based on Quantum Dots and Sarcosine Oxidase. *ChemPhysChem* **2013**, 14, 2338-2342.

Sarcosine, also known as N-methylglycine, is a natural nonprotein amino acid formed as intermediate and byproduct in the glycine metabolism both anabolism and catabolism. High sarcosine level is related to some disorders and diseases like kidney diseases and prostate cancer. Recently sarcosine has been extensively investigated as a biomarker for prostate cancer diagnosis. In this paper the CdSe/ZnS core/shell quantum dots have been utilized for the Sarcosine detection.

In this study, a sarcosine photoelectrochemical sensor based on the CdSe/ZnS core shell QDs is reported. To achieve this purpose, 1,4-benzenedithiol (BDT) capped CdSe/ZnS core shell QDs were prepared then electrodes were modified by the BDT capped QDs followed by immobilization of the sarcosine oxidase enzyme (SOD) on the QDs using polyelectrolyte layer by layer (LBL) assembly and the dependence of photocurrent on the oxygen is evaluated under illumination.

Contribution to this paper;

Synthesis of green fluorescent CdSe/ZnS core/shell quantum dots dispersed in toluene and characterization of the prepared QDs using TEM, UV-Vis spectroscopy and fluorescence spectroscopy. Editorial works for the paper and writing the supporting information.

1.3. Reviews

A6 – Fadeel, B.; Feliu, N.; Vogt, C.; Abdelmonem, A. M.; Parak, W. J., Bridge over troubled waters: understanding the synthetic and biological identities of engineered nanomaterials. Wiley Interdisciplinary Reviews-Nanomedicine And Nanobiotechnology 2013, 5, (2), 111-129.

Due to the fast growing interest in the design, manipulation and applications engineered nanomaterials and their potential adverse effect on the environment and human health, this review tries to shed light on the effect of the different physicochemical properties of the nanoparticles on the environmental and toxicological aspects of the nanoparticles. Special interest has been paid to the interaction of the nanomaterials with the biological systems and biomolecules and the impact of bio-corona formation and its biological identity on the biological behavior.

A7 – Carregal-Romero, S.; Caballero-Diaz, E.; Beqa, L.; Abdelmonem, A. M.; Ochs, M.; Hühn, D.; Suau, B. S.; Valcarcel, M.; Parak, W. J., Multiplexed Sensing and Imaging with Colloidal Nano- and Microparticles. Annual Review of Analytical Chemistry 2013, 6, 53-81.

Making use of the unique properties of the different types of engineered micro- and nano-materials (luminescent, plasmonic and magnetic) in the sensing and imaging applications is extremely fascinating and fast growing field.

In the multiplexed sensing, different types of analytes could be probed, detected and/or determined in parallel. The multiplexed or multimodal imaging implies that different types of materials/tissues can be imaged simultaneously or that different imaging modalities or techniques could be combined together in single system to make use of the different functionalities like luminescence, plasmonic and magnetic properties. This review focuses on the multiplexed sensing, bioimaging applications and concepts of different techniques based on nano and microparticles. After a brief introduction to the main detection, sensing and imaging modes, we present to the multiplexed applications and the promising advantageous of combining different types of individual NPs into multifunctional system and finally address to the challenges and the future prospects of the hybrid nano- and micro inorganic materials in the multiplexed sensing and imaging.

References

1. Dowling, A. P., Development of nanotechnologies. *Nano Today* **2004**, 7, (12), 30-35.
2. Nagarajan, R.; Hatton, T. A., Nanoparticles: Building Blocks for Nanotechnology. In *Nanoparticles: Synthesis, Stabilization, Passivation, and Functionalization*, ACS Symposium Series; American Chemical Society: Washington, DC. **2008**.
3. Yu, H.; Regulacio, M.; Ye, E.; Han, M., Chemical routes to top-down nanofabrication. *CHEMICAL SOCIETY REVIEWS* **2013**, 42, (14), 6006-6018.
4. Deguchi, S.; Mukai, S.; Sakaguchi, H.; Nonomura, Y., Non-Engineered Nanoparticles of C-60. *SCIENTIFIC REPORTS* **2013**, 3.
5. Jain, P. K.; Huang, X. H.; El-Sayed, I. H.; El-Sayed, M. A., Noble Metals on the Nanoscale: Optical and Photothermal Properties and Some Applications in Imaging, Sensing, Biology, and Medicine. *Accounts Of Chemical Research* **2008**, 41, (12), 1578-1586.
6. Huang, X.; El-Sayed, I. H.; Qian, W.; El-Sayed, M. A., Cancer Cell Imaging and Photothermal Therapy in the Near-Infrared Region by Using Gold Nanorods. *Journal of the American Chemical Society* **2006**, 128, 2115-2120.
7. Fong, K.; Yung, L., Localized surface plasmon resonance: a unique property of plasmonic nanoparticles for nucleic acid detection. *NANOSCALE* **2013**, 5, (24), 12043-12071.
8. Schuller, J.; Barnard, E.; Cai, W.; Jun, Y.; White, J.; Brongersma, M., Plasmonics for extreme light concentration and manipulation. *NATURE MATERIALS* **2010**, 9, (3), 193-204.
9. Nordlander, P., Molecular Tuning of Quantum Plasmon Resonances. *Science* **2014**, 343, 1444-1445.
10. Zhang, T.; Lu, G.; Shen, H.; Shi, K.; Jiang, Y.; Xu, D.; Gong, Q., Photoluminescence of a single complex plasmonic nanoparticle. *SCIENTIFIC REPORTS* **2014**, 4.
11. Al-Akraa, I.; Mohammad, A.; El-Deab, M.; El-Anadouli, B., Self-Assembling of Gold Nanoparticles Array for Electro-Sensing Applications. *INTERNATIONAL JOURNAL OF ELECTROCHEMICAL SCIENCE* **2013**, 8, (1), 458-466.
12. Ghosh, S. K.; Pal, T., Interparticle Coupling Effect on the Surface Plasmon Resonance of Gold Nanoparticles: From Theory to Applications. *Chemical Reviews* **2007**, 107, 4797-4862.
13. Xiang, G.; Zhang, N.; Zhou, X., Localized Surface Plasmon Resonance Biosensing with Large Area of Gold Nanoholes Fabricated by Nanosphere Lithography. *NANOSCALE RESEARCH LETTERS* **2010**, 5, (5), 818-822.
14. Link, S.; El-Sayed, M. A., Spectral Properties and Relaxation Dynamics of Surface Plasmon Electronic Oscillations in Gold and Silver Nanodots and Nanorods. *J. Phys. Chem B* **1999**, 103, 8410-8426.
15. Dreaden, E. C.; Alkilany, A. M.; Huang, X.; Murphy, C. J.; El-Sayed, M. A., The Golden Age: Gold Nanoparticles for Biomedicine. *Chemical Society Reviews* **2012**, 41, (7), 2740-2779.
16. Eustis, S.; El-Sayed, M. A., Why Gold Nanoparticles are More Precious than Pretty Gold: Noble Metal Surface Plasmon Resonance and its Enhancement of the Radiative and Nonradiative Properties of Nanocrystals of Different Shapes. *Chemical Society Reviews* **2006**, 35, 209-217.
17. Stockman, M., NANOSCIENCE Dark-hot resonances. *NATURE* **2010**, 467, (7315), 541-542.
18. Resch-Genger, U.; Grabolle, M.; Cavaliere-Jaricot, S.; Nitschke, R.; Nann, T., Quantum dots versus organic dyes as fluorescent labels. *NATURE METHODS* **2008**, 5, (9), 763-775.
19. Jamieson, T.; Bakhshi, R.; Petrova, D.; Pocock, R.; Imani, M.; Seifalian, A. M., Biological applications of quantum dots. *Biomaterials* **2007**, 28, (31), 4717-4732.

20. Tomczak, N.; Liu, R.; Vancso, J., Polymer-coated quantum dots. *NANOSCALE* **2013**, *5*, (24), 12018-12032.
21. Dohnalova, K.; Poddubny, A. N.; Prokofiev, A. A.; de Boer, W. D. A. M.; Umesh, C. P.; Paulusse, J. M. J.; Zuilhof, H.; Gregorkiewicz, T., Surface brightens up Si quantum dots: direct bandgap-like size-tunable emission. *Light Sci Appl* **2013**, *2*, e47.
22. Mocatta, D.; Cohen, G.; Schattner, J.; Millo, O.; Rabani, E.; Banin, U., Heavily Doped Semiconductor Nanocrystal Quantum Dots. *Science* **2011**, *332*, (6025), 77-81.
23. Baskoutas, S.; Terzis, A., Size-dependent band gap of colloidal quantum dots. *JOURNAL OF APPLIED PHYSICS* **2006**, *99*, (1).
24. Efros, A. L.; Rosen, M.; Kuno, M.; Nirmal, M.; Norris, D. J.; Bawendi, M., Band-edge exciton in quantum dots of semiconductors with a degenerate valence band: Dark and bright exciton states. *Physical Review B* **1996**, *54*, (7), 4843-4856.
25. Alivisatos, A. P., Semiconductor Clusters, Nanocrystals, and Quantum Dots. *Science* **1996**, *271*, (16 February), 933-937.
26. Smith, A. M.; Gao, X.; Nie, S., Quantum Dot Nanocrystals for In Vivo Molecular and Cellular Imaging. *Photochemistry and Photobiology* **2004**, *80*, 377-385.
27. Karrai, K.; Warburton, R. J.; Schulhauser, C.; Högele, A.; Urbaszek, B.; McGhee, E. J.; Govorov, A. O.; Garcia, J. M.; Gerardot, B. D.; Petroff, P. M., Hybridization of electronic states in quantum dots through photon emission. *Nature* **2004**, *427*, 135-138.
28. Kim, S.; Fisher, B.; Eisler, H.-J.; Bawendi, M., Type-II Quantum Dots: CdTe/CdSe(Core/Shell) and CdSe/ZnTe(Core/Shell) Heterostructures. *Journal of the American Chemical Society* **2003**, *125*, (38), 11466-11467.
29. Qu, L.; Peng, X., Control of Photoluminescence Properties of CdSe Nanocrystals in Growth. *Journal of the American Chemical Society* **2002**, *124*, (9), 2049-2055.
30. Bailey, R. E.; Smith, A. M.; Nie, S., Quantum dots in biology and medicine. *Physica* **2004**, *E* *25*, 1-12.
31. Brus, L., Electronic Wave Functions in Semiconductor Clusters: Experiment and Theory. *J. Phys. Chem* **1986**, *90*, 2555-2560.
32. Murphy, C.; Coffey, J., Quantum dots: A primer. *APPLIED SPECTROSCOPY* **2002**, *56*, (1), 16A-27A.
33. Bae, W.; Park, Y.; Lim, J.; Lee, D.; Padilha, L.; McDaniel, H.; Robel, I.; Lee, C.; Pietryga, J.; Klimov, V., Controlling the influence of Auger recombination on the performance of quantum-dot light-emitting diodes. *NATURE COMMUNICATIONS* **2013**, *4*.
34. Tex, D.; Kamiya, I.; Kanemitsu, Y., Control of hot-carrier relaxation for realizing ideal quantum-dot intermediate-band solar cells. *SCIENTIFIC REPORTS* **2014**, *4*.
35. Adhyaksa, G.; Lee, G.; Baek, S.; Lee, J.; Kang, J., Broadband energy transfer to sensitizing dyes by mobile quantum dot mediators in solar cells. *SCIENTIFIC REPORTS* **2013**, *3*.
36. Kobak, J.; Smolenski, T.; Goryca, M.; Papaj, M.; Gietka, K.; Bogucki, A.; Koperski, M.; Rousset, J.; Suffczynski, J.; Janik, E.; Nawrocki, M.; Golnik, A.; Kossacki, P.; Pacuski, W., Designing quantum dots for solotronics. *NATURE COMMUNICATIONS* **2014**, *5*.
37. Ma, W.; Qin, L.; Liu, F.; Gu, Z.; Wang, J.; Pan, Z.; James, T.; Long, Y., Ubiquinone-quantum dot bioconjugates for in vitro and intracellular complex I sensing. *SCIENTIFIC REPORTS* **2013**, *3*.
38. Freeman, R.; Girsh, J.; Willner, I., Nucleic Acid/Quantum Dots (QDs) Hybrid Systems for Optical and Photoelectrochemical Sensing. *ACS APPLIED MATERIALS & INTERFACES* **2013**, *5*, (8), 2815-2834.
39. Biermann, B.; Sokoll, S.; Klueva, J.; Missler, M.; Wiegert, J.; Sibarita, J.; Heine, M., Imaging of molecular surface dynamics in brain slices using single-particle tracking. *NATURE COMMUNICATIONS* **2014**, *5*.

40. Bruchez, M. J.; Moronne, M.; Gin, P.; Weiss, S.; Alivisatos, A. P., Semiconductor Nanocrystals as Fluorescent Biological Labels. *Science* **1998**, *281*, (5385), 2013-2016.
41. Jin, Y.; Gao, X., Plasmonic fluorescent quantum dots. *NATURE NANOTECHNOLOGY* **2009**, *4*, (9), 571-576.
42. Medintz, I. L.; Uyeda, H. T.; Goldman, E. R.; Mattoussi, H., Quantum Dot Bioconjugates for Imaging, Labelling and Sensing. *Nat. Mater.* **2005**, *4*, (6), 435-446.
43. Michalet, X.; Pinaud, F. F.; Bentolila, L. A.; Tsay, J. M.; Doose, S.; Li, J. J.; Sundaresan, G.; Wu, A. M.; Gambhir, S. S.; Weiss, S., Quantum Dots for Live Cells, in Vivo Imaging, and Diagnostics. *Science* **2005**, *307*, (5709), 538-544.
44. Chan, W. C. W.; Nie, S., Quantum Dot Bioconjugates for Ultrasensitive Nonisotopic Detection. *Science* **1998**, *281*, 2016-2018.
45. Gill, R.; Zayats, M.; Willner, I., Semiconductor Quantum Dots for Bioanalysis. *Angewandte Chemie International Edition* **2008**, *47*, (40), 7602-7625.
46. Son, D.; Kwon, B.; Park, D.; Seo, W.; Yi, Y.; Angadi, B.; Lee, C.; Choi, W., Emissive ZnO-graphene quantum dots for white-light-emitting diodes. *NATURE NANOTECHNOLOGY* **2012**, *7*, (7), 465-471.
47. Chen, J.; Zhao, D.; Li, C.; Xu, F.; Lei, W.; Sun, L.; Nathan, A.; Sun, X., All Solution-processed Stable White Quantum Dot Light-emitting Diodes with Hybrid ZnO@TiO₂ as Blue Emitters. *SCIENTIFIC REPORTS* **2014**, *4*.
48. Janotti, A.; Van de Walle, C., Fundamentals of zinc oxide as a semiconductor. *REPORTS ON PROGRESS IN PHYSICS* **2009**, *72*, (12).
49. Prajapati, O.; Rohatgi, N., Flow Boiling Heat Transfer Enhancement by Using ZnO-Water Nanofluids. *SCIENCE AND TECHNOLOGY OF NUCLEAR INSTALLATIONS* **2014**.
50. Sreeja, R.; John, J.; Aneesh, P.; Jayaraj, M., Linear and nonlinear optical properties of luminescent ZnO nanoparticles embedded in PMMA matrix. *OPTICS COMMUNICATIONS* **2010**, *283*, (14), 2908-2913.
51. Jeeju, P.; Jayalekshmi, S.; Chandrasekharan, K.; Sudheesh, P., Size dependent nonlinear optical properties of spin coated zinc oxide-polystyrene nanocomposite films. *OPTICS COMMUNICATIONS* **2012**, *285*, (24), 5433-5439.
52. Kachynski, A.; Kuzmin, A.; Nyk, M.; Roy, I.; Prasad, P., Zinc oxide nanocrystals for nonresonant nonlinear optical microscopy in biology and medicine. *JOURNAL OF PHYSICAL CHEMISTRY C* **2008**, *112*, (29), 10721-10724.
53. Zhang, F.; Ding, Y.; Zhang, Y.; Zhang, X.; Wang, Z., Piezo-phototronic Effect Enhanced Visible and Ultraviolet Photodetection Using a ZnO-CdS Core-Shell Micro/nanowire. *ACS NANO* **2012**, *6*, (10), 9229-9236.
54. Zhang, F.; Niu, S.; Guo, W.; Zhu, G.; Liu, Y.; Zhang, X.; Wang, Z., Piezo-phototronic Effect Enhanced Visible/UV Photodetector of a Carbon-Fiber/ZnO-CdS Double-Shell Microwire. *ACS NANO* **2013**, *7*, (5), 4537-4544.
55. Patidar, D.; Kaswan, A.; Saxena, N.; Sharma, K., Monodispersed ZnO Nanoparticles and Their Use in Heterojunction Solar Cell. *SCIENTIFIC WORLD JOURNAL* **2013**.
56. Baxter, J.; Schmuttenmaer, C., Conductivity of ZnO nanowires, nanoparticles, and thin films using time-resolved terahertz spectroscopy. *JOURNAL OF PHYSICAL CHEMISTRY B* **2006**, *110*, (50), 25229-25239.
57. Jin, Z.; Gao, L.; Zhou, Q.; Wang, J., High-performance flexible ultraviolet photoconductors based on solution-processed ultrathin ZnO/Au nanoparticle composite films. **2014**, *4*: 4268 | DOI: 10.1038/srep04268.

58. Manzoor, U.; Islam, M.; Tabassam, L.; Rahman, S., Quantum confinement effect in ZnO nanoparticles synthesized by co-precipitate method. *PHYSICA E-LOW-DIMENSIONAL SYSTEMS & NANOSTRUCTURES* **2009**, 41, (9), 1669-1672.
59. Tachikawa, S.; Noguchi, A.; Tsuge, T.; Hara, M.; Odawara, O.; Wada, H., Optical Properties of ZnO Nanoparticles Capped with Polymers. *MATERIALS* **2011**, 4, (6), 1132-1143.
60. Fu, Z.; Cui, Y.; Zhang, S.; Chen, J.; Yu, D.; Zhang, S.; Niu, L.; Jiang, J., Study on the quantum confinement effect on ultraviolet photoluminescence of crystalline ZnO nanoparticles with nearly uniform size. *APPLIED PHYSICS LETTERS* **2007**, 90, (26).
61. Rajalakshmi, M.; Arora, A.; Bendre, B.; Mahamuni, S., Optical phonon confinement in zinc oxide nanoparticles. *JOURNAL OF APPLIED PHYSICS* **2000**, 87, (5), 2445-2448.
62. Wang, Y.; Thomas, P.; O'Brien, P., Nanocrystalline ZnO with ultraviolet luminescence. *JOURNAL OF PHYSICAL CHEMISTRY B* **2006**, 110, (9), 4099-4104.
63. Xiong, H., Photoluminescent ZnO nanoparticles modified by polymers. *JOURNAL OF MATERIALS CHEMISTRY* **2010**, 20, (21), 4251-4262.
64. Sharma, A.; Singh, B.; Dhar, S.; Gondorf, A.; Spasova, M., Effect of surface groups on the luminescence property of ZnO nanoparticles synthesized by sol-gel route. *SURFACE SCIENCE* **2012**, 606, (3-4), L13-L17.
65. Zhang, L.; Yin, L.; Wang, C.; Lun, N.; Qi, Y.; Xiang, D., Origin of Visible Photoluminescence of ZnO Quantum Dots: Defect-Dependent and Size-Dependent. *JOURNAL OF PHYSICAL CHEMISTRY C* **2010**, 114, (21), 9651-9658.
66. Kim, D.; Lee, G.; Kim, Y., Interaction of zinc interstitial with oxygen vacancy in zinc oxide: An origin of n-type doping. *SOLID STATE COMMUNICATIONS* **2012**, 152, (18), 1711-1714.
67. Layek, A.; Manna, B.; Chowdhury, A., Carrier recombination dynamics through defect states of ZnO nanocrystals: From nanoparticles to nanorods. *CHEMICAL PHYSICS LETTERS* **2012**, 539, 133-138.
68. Liu, D.; Li, G.; Su, Y.; Chen, J., Highly luminescent ZnO nanocrystals stabilized by ionic-liquid components. *ANGEWANDTE CHEMIE-INTERNATIONAL EDITION* **2006**, 45, (44), 7370-7373.
69. Xu, X.; Xu, C.; Wang, X.; Lin, Y.; Dai, J.; Hu, J., Control mechanism behind broad fluorescence from violet to orange in ZnO quantum dots. *CRYSTENGCOMM* **2013**, 15, (5), 977-981.
70. Asok, A.; Gandhi, M.; Kulkarni, A., Enhanced visible photoluminescence in ZnO quantum dots by promotion of oxygen vacancy formation. *NANOSCALE* **2012**, 4, (16), 4943-4946.
71. Tang, X.; Choo, E.; Li, L.; Ding, J.; Xue, J., Synthesis of ZnO Nanoparticles with Tunable Emission Colors and Their Cell Labeling Applications. *CHEMISTRY OF MATERIALS* **2010**, 22, (11), 3383-3388.
72. Hong, H.; Shi, J.; Yang, Y.; Zhang, Y.; Engle, J.; Nickles, R.; Wang, X.; Cai, W., Cancer-Targeted Optical Imaging with Fluorescent Zinc Oxide Nanowires. *NANO LETTERS* **2011**, 11, (9), 3744-3750.
73. Liu, Y.; Ai, K.; Yuan, Q.; Lu, L., Fluorescence-enhanced gadolinium-doped zinc oxide quantum dots for magnetic resonance and fluorescence imaging. *BIOMATERIALS* **2011**, 32, (4), 1185-1192.
74. Sikora, B.; Fronc, K.; Kaminska, I.; Koper, K.; Stepień, P.; Elbaum, D., Luminescence of colloidal ZnO nanoparticles synthesized in alcohols and biological application of ZnO passivated by MgO. *JOURNAL OF PHYSICS-CONDENSED MATTER* **2013**, 25, (19).
75. Zhang, H.; Xiong, H.; Ren, Q.; Xia, Y.; Kong, J., ZnO@silica core-shell nanoparticles with remarkable luminescence and stability in cell imaging. *JOURNAL OF MATERIALS CHEMISTRY* **2012**, 22, (26), 13159-13165.
76. Rubio-Garcia, J.; Dazzazi, A.; Coppel, Y.; Mascialchi, P.; Salome, L.; Bouhaouss, A.; Kahn, M.; Gauffre, F., Transfer of hydrophobic ZnO nanocrystals to water: an investigation of the

- transfer mechanism and luminescent properties. *JOURNAL OF MATERIALS CHEMISTRY* **2012**, 22, (29), 14538-14545.
77. Patra, M.; Manoth, M.; Singh, V.; Gowd, G.; Choudhry, V.; Vadera, S.; Kumar, N., Synthesis of stable dispersion of ZnO quantum dots in aqueous medium showing visible emission from bluish green to yellow. *JOURNAL OF LUMINESCENCE* **2009**, 129, (3), 320-324.
78. Dazzazi, A.; Coppel, Y.; In, M.; Chassenieux, C.; Mascaldi, P.; Salome, L.; Bouhaouss, A.; Kahn, M.; Gauffre, F., Oligomeric and polymeric surfactants for the transfer of luminescent ZnO nanocrystals to water. *JOURNAL OF MATERIALS CHEMISTRY C* **2013**, 1, (11), 2158-2165.
79. Xiong, H.; Shchukin, D.; Mohwald, H.; Xu, Y.; Xia, Y., Sonochemical Synthesis of Highly Luminescent Zinc Oxide Nanoparticles Doped with Magnesium(II). *ANGEWANDTE CHEMIE-INTERNATIONAL EDITION* **2009**, 48, (15), 2727-2731.
80. Xiong, H., ZnO Nanoparticles Applied to Bioimaging and Drug Delivery. *ADVANCED MATERIALS* **2013**, 25, (37), 5329-5335.
81. FDA, <http://www.fda.gov/food/ingredientspackaginglabeling/gras/scogs/ucm261016.htm>.
82. Beek, W.; Wienk, M.; Kemerink, M.; Yang, X.; Janssen, R., Hybrid zinc oxide conjugated polymer bulk heterojunction solar cells. *JOURNAL OF PHYSICAL CHEMISTRY B* **2005**, 109, (19), 9505-9516.
83. Bu, I.; Cole, M., One-pot synthesis of intercalating ZnO nanoparticles for enhanced dye-sensitized solar cells. *MATERIALS LETTERS* **2013**, 90, 56-59.
84. Chou, C.; Li, C.; Lee, C.; Lin, L.; Yeh, M.; Vittal, R.; Ho, K., ZnO nanowire/nanoparticles composite films for the photoanodes of quantum dot-sensitized solar cells. *ELECTROCHIMICA ACTA* **2013**, 88, 35-43.
85. Gao, R.; Liang, Z.; Tian, J.; Zhang, Q.; Wang, L.; Cao, G., ZnO nanocrystallite aggregates synthesized through interface precipitation for dye-sensitized solar cells. *NANO ENERGY* **2013**, 2, (1), 40-48.
86. Kaur, M.; Verma, N., Study on CaCO₃-coated ZnO nanoparticles based dye sensitized solar cell. *JOURNAL OF MATERIALS SCIENCE-MATERIALS IN ELECTRONICS* **2013**, 24, (12), 4980-4986.
87. Krebs, F.; Thomann, Y.; Thomann, R.; Andreasen, J., A simple nanostructured polymer/ZnO hybrid solar cell - preparation and operation in air. *NANOTECHNOLOGY* **2008**, 19, (42).
88. Li, F.; Du, Y.; Chen, Y.; Chen, L.; Zhao, J.; Wang, P., Direct application of P3HT-DOPO@ZnO nanocomposites in hybrid bulk heterojunction solar cells via grafting P3HT onto ZnO nanoparticles. *SOLAR ENERGY MATERIALS AND SOLAR CELLS* **2012**, 97, 64-70.
89. Rhodes, R.; Horie, M.; Chen, H.; Wang, Z.; Turner, M.; Saunders, B., Aggregation of zinc oxide nanoparticles: From non-aqueous dispersions to composites used as photoactive layers in hybrid solar cells. *JOURNAL OF COLLOID AND INTERFACE SCIENCE* **2010**, 344, (2), 261-271.
90. Seow, Z.; Wong, A.; Thavasi, V.; Jose, R.; Ramakrishna, S.; Ho, G., Controlled synthesis and application of ZnO nanoparticles, nanorods and nanospheres in dye-sensitized solar cells. *NANOTECHNOLOGY* **2009**, 20, (4).
91. Shi, Y.; Li, F.; Chen, Y., Controlling morphology and improving the photovoltaic performances of P3HT/ZnO hybrid solar cells via P3HT-b-PEO as an interfacial compatibilizer. *NEW JOURNAL OF CHEMISTRY* **2013**, 37, (1), 236-244.
92. Zhang, Q.; Chou, T.; Russo, B.; Jenekhe, S.; Cao, G., Aggregation of ZnO nanocrystallites for high conversion efficiency in dye-sensitized solar cells. *ANGEWANDTE CHEMIE-INTERNATIONAL EDITION* **2008**, 47, (13), 2402-2406.
93. Cheng, C.; Amini, A.; Zhu, C.; Xu, Z.; Song, H.; Wang, N., Enhanced photocatalytic performance of TiO₂-ZnO hybrid nanostructures. *SCIENTIFIC REPORTS* **2014**, 4.

94. Behrens, M.; Lolli, G.; Muratova, N.; Kasatkin, I.; Havecker, M.; d'Alnoncourt, R.; Storcheva, O.; Kohler, K.; Muhler, M.; Schlogl, R., The effect of Al-doping on ZnO nanoparticles applied as catalyst support. *PHYSICAL CHEMISTRY CHEMICAL PHYSICS* **2013**, 15, (5), 1374-1381.
95. El-Kemary, M.; El-Shamy, H.; El-Mehasseb, I., Photocatalytic degradation of ciprofloxacin drug in water using ZnO nanoparticles. *JOURNAL OF LUMINESCENCE* **2010**, 130, (12), 2327-2331.
96. Liao, F.; Zeng, Z.; Eley, C.; Lu, Q.; Hong, X.; Tsang, S., Electronic Modulation of a Copper/Zinc Oxide Catalyst by a Heterojunction for Selective Hydrogenation of Carbon Dioxide to Methanol. *ANGEWANDTE CHEMIE-INTERNATIONAL EDITION* **2012**, 51, (24), 5832-5836.
97. Nagajyothi, P.; An, T.; Sreekanth, T.; Lee, J.; Lee, D.; Lee, K., Green route biosynthesis: Characterization and catalytic activity of ZnO nanoparticles. *MATERIALS LETTERS* **2013**, 108, 160-163.
98. Xiao, F.; Wang, F.; Fu, X.; Zheng, Y., A green and facile self-assembly preparation of gold nanoparticles/ZnO nanocomposite for photocatalytic and photoelectrochemical applications. *JOURNAL OF MATERIALS CHEMISTRY* **2012**, 22, (7), 2868-2877.
99. Ryu, S.; Kim, S.; Kim, C.; Jo, S.; Lee, J., Multi-stacked organic light-emitting diodes using zinc oxide nanoparticle interfacial layers. *CURRENT APPLIED PHYSICS* **2012**, 12, (5), 1378-1380.
100. Neshataeva, E.; Kummell, T.; Bacher, G.; Ebbers, A., All-inorganic light emitting device based on ZnO nanoparticles. *APPLIED PHYSICS LETTERS* **2009**, 94, (9).
101. Kumar, P.; Panchakarla, L.; Bhat, S.; Maitra, U.; Subrahmanyam, K.; Rao, C., Photoluminescence, white light emitting properties and related aspects of ZnO nanoparticles admixed with graphene and GaN. *NANOTECHNOLOGY* **2010**, 21, (38).
102. Qian, L.; Zheng, Y.; Xue, J.; Holloway, P., Stable and efficient quantum-dot light-emitting diodes based on solution-processed multilayer structures. *NATURE PHOTONICS* **2011**, 5, (9), 543-548.
103. Kwak, J.; Bae, W.; Lee, D.; Park, I.; Lim, J.; Park, M.; Cho, H.; Woo, H.; Yoon, D.; Char, K.; Lee, S.; Lee, C., Bright and Efficient Full-Color Colloidal Quantum Dot Light-Emitting Diodes Using an Inverted Device Structure. *NANO LETTERS* **2012**, 12, (5), 2362-2366.
104. Bhaumik, S.; Pal, A., All-Inorganic Light-Emitting Diodes Based on Solution-Processed Nontoxic and Earth-Abundant Nanocrystals. *IEEE JOURNAL OF QUANTUM ELECTRONICS* **2013**, 49, (3), 325-330.
105. Chawla, S.; Saroha, M.; Kotnala, R., White Light Emitting Magnetic ZnO:Sm Nanoparticles Prepared by Inclusive Co-Precipitation Synthesis. *ELECTRONIC MATERIALS LETTERS* **2014**, 10, (1), 73-80.
106. Waclawik, E.; Chang, J.; Ponzoni, A.; Concina, I.; Zappa, D.; Comini, E.; Motta, N.; Faglia, G.; Sberveglieri, G., Functionalised zinc oxide nanowire gas sensors: Enhanced NO₂ gas sensor response by chemical modification of nanowire surfaces. *BEILSTEIN JOURNAL OF NANOTECHNOLOGY* **2012**, 3, 368-377.
107. Zhao, D.; Song, H.; Hao, L.; Liu, X.; Zhang, L.; Lv, Y., Luminescent ZnO quantum dots for sensitive and selective detection of dopamine. *TALANTA* **2013**, 107, 133-139.
108. Ahmad, M.; Chang, J.; Ahmad, M.; Waclawik, E.; Wlodarski, W., Non-aqueous synthesis of hexagonal ZnO nanopyramids: Gas sensing properties. *SENSORS AND ACTUATORS B-CHEMICAL* **2013**, 177, 286-294.
109. Bai, S.; Chen, L.; Hu, J.; Li, D.; Luo, R.; Chen, A.; Chung, C., Synthesis of quantum size ZnO crystals and their gas sensing properties for NO₂. *SENSORS AND ACTUATORS B-CHEMICAL* **2011**, 159, (1), 97-102.

110. Choi, M.; McBean, K.; Ng, P.; McDonagh, A.; Maynard, P.; Lennard, C.; Roux, C., An evaluation of nanostructured zinc oxide as a fluorescent powder for fingerprint detection. *JOURNAL OF MATERIALS SCIENCE* **2008**, 43, (2), 732-737.
111. Gurav, K.; Gang, M.; Shin, S.; Patil, U.; Deshmukh, P.; Agawane, G.; Suryawanshi, M.; Pawar, S.; Patil, P.; Lokhande, C.; Kim, J., Gas sensing properties of hydrothermally grown ZnO nanorods with different aspect ratios. *SENSORS AND ACTUATORS B-CHEMICAL* **2014**, 190, 439-445.
112. Li, D.; Hu, J.; Fan, F.; Bai, S.; Luo, R.; Chen, A.; Liu, C., Quantum-sized ZnO nanoparticles synthesized in aqueous medium for toxic gases detection. *JOURNAL OF ALLOYS AND COMPOUNDS* **2012**, 539, 205-209.
113. Faure, B.; Salazar-Alvarez, G.; Ahniyaz, A.; Villaluenga, I.; Berriozabal, G.; De Miguel, Y.; Bergstrom, L., Dispersion and surface functionalization of oxide nanoparticles for transparent photocatalytic and UV-protecting coatings and sunscreens. *SCIENCE AND TECHNOLOGY OF ADVANCED MATERIALS* **2013**, 14, (2).
114. Rasmussen, J.; Martinez, E.; Louka, P.; Wingett, D., Zinc oxide nanoparticles for selective destruction of tumor cells and potential for drug delivery applications. *EXPERT OPINION ON DRUG DELIVERY* **2010**, 7, (9), 1063-1077.
115. Akhtar, M.; Ahamed, M.; Kumar, S.; Khan, M.; Ahmad, J.; Alrokayan, S., Zinc oxide nanoparticles selectively induce apoptosis in human cancer cells through reactive oxygen species. *INTERNATIONAL JOURNAL OF NANOMEDICINE* **2012**, 7, 845-857.
116. Prasanth, R.; Gopinath, D., Effect of ZnO nanoparticles on nasopharyngeal cancer cells viability and respiration. *APPLIED PHYSICS LETTERS* **2013**, 102, (11).
117. Hanley, C.; Layne, J.; Punnoose, A.; Reddy, K.; Coombs, I.; Coombs, A.; Feris, K.; Wingett, D., Preferential killing of cancer cells and activated human T cells using ZnO nanoparticles. *NANOTECHNOLOGY* **2008**, 19, (29).
118. Tang, X.; Choo, E.; Li, L.; Ding, J.; Xue, J., One-Pot Synthesis of Water-Stable ZnO Nanoparticles via a Polyol Hydrolysis Route and Their Cell Labeling Applications. *LANGMUIR* **2009**, 25, (9), 5271-5275.
119. Halliday, D.; Resnick, R.; Walker, J., *Fundamentals of Physics*, 5th ed., John Wiley & Sons, Inc., New York. **1997**.
120. Kittel, C., *Introduction to Solid State Physics*, 7th ed., John Wiley & Sons, Inc., New York. **1996**.
121. Jakubovics, J. P., *Magnetism and Magnetic Materials*", 2nd ed., The Institute of Materials, Cambridge. **1994**.
122. Pillai, S. O., *Solid state physics*. 6th ed. New Dehli: New Age International (P) Limited, Publishers. **2005**.
123. Figuerola, A.; Di Corato, R.; Manna, L.; Pellegrino, T., From iron oxide nanoparticles towards advanced iron-based inorganic materials designed for biomedical applications. *Pharmacological Research* **2010**, 62, (2), 126-143.
124. Demortiere, A.; Panissod, P.; Pichon, B.; Pourroy, G.; Guillon, D.; Donnio, B.; Begin-Colin, S., Size-dependent properties of magnetic iron oxide nanocrystals. *NANOSCALE* **2011**, 3, (1), 225-232.
125. Lu, A. H.; Salabas, E. L.; Schuth, F., *Magnetic Nanoparticles: Synthesis, Protection, Functionalization, and Application*. *Angewandte Chemie, International Edition* **2007**, 46, (8), 1222-1244.
126. Tan, Y.; Zhuang, Z.; Peng, Q.; Li, Y., Room-temperature soft magnetic iron oxide nanocrystals: Synthesis, characterization, and size-dependent magnetic properties. *CHEMISTRY OF MATERIALS* **2008**, 20, (15), 5029-5034.

127. Shubayev, V. I.; Pisanic, T. R.; Jin, S. H., Magnetic nanoparticles for theragnostics. *Advanced Drug Delivery Reviews* **2009**, 61, (6), 467-477.
128. Jin, Y.; Jia, C.; Huang, S.; O'Donnell, M.; Gao, X., Multifunctional nanoparticles as coupled contrast agents. *NATURE COMMUNICATIONS* **2010**, 1.
129. Tang, S.; Lo, I., Magnetic nanoparticles: Essential factors for sustainable environmental applications. *WATER RESEARCH* **2013**, 47, (8), 2613-2632.
130. Lee, J.; Jang, J.; Choi, J.; Moon, S.; Noh, S.; Kim, J.; Kim, J.; Kim, I.; Park, K.; Cheon, J., Exchange-coupled magnetic nanoparticles for efficient heat induction. *NATURE NANOTECHNOLOGY* **2011**, 6, (7), 418-422.
131. Mahmoudi, M.; Sant, S.; Wang, B.; Laurent, S.; Sen, T., Superparamagnetic iron oxide nanoparticles (SPIONs): development, surface modification and applications in chemotherapy. *Advanced drug delivery reviews* **2011**, 63, (1), 24-46.
132. Kozakova, Z.; Kuritka, I.; Babayan, V.; Kazantseva, N.; Pastorek, M., Magnetic Iron Oxide Nanoparticles for High Frequency Applications. *IEEE TRANSACTIONS ON MAGNETICS* **2013**, 49, (3), 995-999.
133. Stelter, L.; Pinkernelle, J. G.; Michel, R.; Schwartlander, R.; Raschzok, N.; Morgul, M. H.; Koch, M.; Denecke, T.; Ruf, J.; Baumler, H.; Jordan, A.; Hamm, B.; Sauer, I. M.; Teichgraber, U., Modification of aminosilanized superparamagnetic nanoparticles: feasibility of multimodal detection using 3T MRI, small animal PET, and fluorescence imaging. *Mol Imaging Biol* **2009**, 12, (1), 25-34.
134. Lai, J.; Lai, W.; Chen, C.; Chen, S.; Chiang, C., Multifunctional magnetic plasmonic nanoparticles for applications of magnetic/photo-thermal hyperthermia and surface enhanced Raman spectroscopy. *JOURNAL OF MAGNETISM AND MAGNETIC MATERIALS* **2013**, 331, 204-207.
135. Bruggemann, C.; Akimov, A.; Scherbakov, A.; Bombeck, M.; Schneider, C.; Hofling, S.; Forchel, A.; Yakovlev, D.; Bayer, M., Laser mode feeding by shaking quantum dots in a planar microcavity. *NATURE PHOTONICS* **2012**, 6, (1), 30-34.
136. Lim, J.; Park, M.; Bae, W.; Lee, D.; Lee, S.; Lee, C.; Char, K., Highly Efficient Cadmium-Free Quantum Dot Light-Emitting Diodes Enabled by the Direct Formation of Excitons within InP@ZnSeS Quantum Dots. *ACS NANO* **2013**, 7, (10), 9019-9026.
137. Bae, W.; Kwak, J.; Lim, J.; Lee, D.; Nam, M.; Char, K.; Lee, C.; Lee, S., Multicolored Light-Emitting Diodes Based on All-Quantum-Dot Multilayer Films Using Layer-by-Layer Assembly Method. *NANO LETTERS* **2010**, 10, (7), 2368-2373.
138. Sun, L.; Choi, J.; Stachnik, D.; Bartnik, A.; Hyun, B.; Malliaras, G.; Hanrath, T.; Wise, F., Bright infrared quantum-dot light-emitting diodes through inter-dot spacing control. *NATURE NANOTECHNOLOGY* **2012**, 7, (6), 369-373.
139. Etgar, L.; Park, J.; Barolo, C.; Lesnyak, V.; Panda, S.; Quagliotto, P.; Hickey, S.; Nazeeruddin, M.; Eychmuller, A.; Viscardi, G.; Gratzel, M., Enhancing the efficiency of a dye sensitized solar cell due to the energy transfer between CdSe quantum dots and a designed squaraine dye. *RSC ADVANCES* **2012**, 2, (7), 2748-2752.
140. Prezhdo, O., Quantum dots for solar energy harvesting: Artificial atoms, molecules, or small pieces of bulk? *ABSTRACTS OF PAPERS OF THE AMERICAN CHEMICAL SOCIETY* **2012**, 243.
141. Lin, C.; Huang, K.; Ho, S.; Huang, M.; He, J., An energy-harvesting scheme utilizing Ga-rich CuIn(1-x)Ga_xSe₂ quantum dots for dye-sensitized solar cells. *APPLIED PHYSICS LETTERS* **2012**, 101, (12).
142. Hirschmann, J.; Faber, H.; Halik, M., Concept of a thin film memory transistor based on ZnO nanoparticles insulated by a ligand shell. *NANOSCALE* **2012**, 4, (2), 444-447.

143. Aleshin, A.; Shcherbakov, I.; Petrov, V.; Titkov, A., Solution-processed polyfluorene-ZnO nanoparticles ambipolar light-emitting field-effect transistor. *ORGANIC ELECTRONICS* **2011**, 12, (8), 1285-1292.
144. Cha, S.; Jang, J.; Choi, Y.; Amaratunga, G.; Ho, G.; Welland, M.; Hasko, D.; Kang, D.; Kim, J., High performance ZnO nanowire field effect transistor using self-aligned nanogap gate electrodes. *APPLIED PHYSICS LETTERS* **2006**, 89, (26).
145. Nedic, S.; Chun, Y.; Hong, W.; Chu, D.; Welland, M., High performance non-volatile ferroelectric copolymer memory based on a ZnO nanowire transistor fabricated on a transparent substrate. *APPLIED PHYSICS LETTERS* **2014**, 104, (3).
146. Sohn, J.; Choi, S.; Morris, S.; Bendall, J.; Coles, H.; Hong, W.; Jo, G.; Lee, T.; Welland, M., Novel Nonvolatile Memory with Multibit Storage Based on a ZnO Nanowire Transistor. *NANO LETTERS* **2010**, 10, (11), 4316-4320.
147. Baskoutas, S.; Bester, G., Conventional Optics from Unconventional Electronics in ZnO Quantum Dots. *JOURNAL OF PHYSICAL CHEMISTRY C* **2010**, 114, (20), 9301-9307.
148. Noipa, T.; Tuntulani, T.; Ngeontae, W., Cu²⁺-modulated cysteamine-capped CdS quantum dots as a turn-on fluorescence sensor for cyanide recognition. *TALANTA* **2013**, 105, 320-326.
149. Liang, R.; Tian, R.; Shi, W.; Liu, Z.; Yan, D.; Wei, M.; Evans, D.; Duan, X., A temperature sensor based on CdTe quantum dots-layered double hydroxide ultrathin films via layer-by-layer assembly. *CHEMICAL COMMUNICATIONS* **2013**, 49, (10), 969-971.
150. Chen, G.; Tsai, H.; Lai, P.; Liao, M., Functionalized Mn²⁺-Doped Zinc Sulfide Quantum Dots as a Metal Ion Sensor for Industrial Wastes. *SENSORS AND MATERIALS* **2013**, 25, (6), 437-442.
151. Lee, K.; Oh, H.; Jo, M.; Lee, K.; Yang, S., An ultraviolet sensor using spin-coated ZnO nanoparticles based on surface acoustic waves. *MICROELECTRONIC ENGINEERING* **2013**, 111, 105-109.
152. Yi, F.; Liao, Q.; Huang, Y.; Gu, Y.; Zhang, Y., Self-powered ultraviolet photodetector based on a single ZnO tetrapod/PEDOT:PSS heterostructure. *SEMICONDUCTOR SCIENCE AND TECHNOLOGY* **2013**, 28, (10).
153. Li, Q.; Wei, L.; Xie, Y.; Zhang, K.; Liu, L.; Zhu, D.; Jiao, J.; Chen, Y.; Yan, S.; Liu, G.; Mei, L., ZnO nanoneedle/H₂O solid-liquid heterojunction-based self-powered ultraviolet detector. *NANOSCALE RESEARCH LETTERS* **2013**, 8.
154. Chai, G.; Lupan, O.; Chow, L.; Heinrich, H., Crossed zinc oxide nanorods for ultraviolet radiation detection. *SENSORS AND ACTUATORS A-PHYSICAL* **2009**, 150, (2), 184-187.
155. Game, O.; Singh, U.; Kumari, T.; Banpurkar, A.; Ogale, S., ZnO(N)-Spiro-MeOTAD hybrid photodiode: an efficient self-powered fast-response UV (visible) photosensor. *NANOSCALE* **2014**, 6, (1), 503-513.
156. Shinde, S.; Nanda, K., Wide-Range Temperature Sensing using Highly Sensitive Green-Luminescent ZnO and PMMA-ZnO Film as a Non-Contact Optical Probe. *ANGEWANDTE CHEMIE-INTERNATIONAL EDITION* **2013**, 52, (43), 11325-11328.
157. Costello, B.; Ewen, R.; Ratcliffe, N.; Richards, M., Highly sensitive room temperature sensors based on the UV-LED activation of zinc oxide nanoparticles. *SENSORS AND ACTUATORS B-CHEMICAL* **2008**, 134, (2), 945-952.
158. Oh, H.; Lee, K.; Baek, J.; Yang, S.; Lee, K., Development of a high sensitive pH sensor based on shear horizontal surface acoustic wave with ZnO nanoparticles. *MICROELECTRONIC ENGINEERING* **2013**, 111, 154-159.
159. Xue, F.; Zhang, L.; Tang, W.; Zhang, C.; Du, W.; Wang, Z. L., Piezotronic Effect on ZnO Nanowire Film Based Temperature Sensor. *ACS Applied Materials & Interfaces* **2014**.

160. Nguyen, V.; Rouxel, D.; Vincent, B.; Badie, L.; Dos Santos, F.; Lamouroux, E.; Fort, Y., Influence of cluster size and surface functionalization of ZnO nanoparticles on the morphology, thermomechanical and piezoelectric properties of P(VDF-TrFE) nanocomposite films. *APPLIED SURFACE SCIENCE* **2013**, 279, 204-211.
161. Singamaneni, S.; Bliznyuk, V.; Binek, C.; Tsymbal, E., Magnetic nanoparticles: recent advances in synthesis, self-assembly and applications. *JOURNAL OF MATERIALS CHEMISTRY* **2011**, 21, (42), 16819-16845.
162. Tanase, M.; Zhu, J.; Liu, C.; Shukla, N.; Klemmer, T.; Weller, D.; Laughlin, D., Structure optimization of FePt nanoparticles of various sizes for magnetic data storage. *METALLURGICAL AND MATERIALS TRANSACTIONS A-PHYSICAL METALLURGY AND MATERIALS SCIENCE* **2007**, 38A, (4), 798-810.
163. Zhang, H.; Liu, Y.; Sun, S., Synthesis and assembly of magnetic nanoparticles for information and energy storage applications. *FRONTIERS OF PHYSICS IN CHINA* **2010**, 5, (4), 347-356.
164. Ohashi, K., Nano-storage technology and electroplating, large magnetic moment of Co-Fe-Ni. *ELECTROCHEMISTRY* **2002**, 70, (11), 884-888.
165. Saini, D.; Chauhan, R.; Kumar, S., Effects of annealing on structural and magnetic properties of template synthesized cobalt nanowires useful as data storage and nano devices. *JOURNAL OF MATERIALS SCIENCE-MATERIALS IN ELECTRONICS* **2014**, 25, (1), 124-127.
166. Tagawa, N.; Hayashi, T.; Mori, A., Effects of moving three-dimensional nano-textured disk surfaces on thin film gas lubrication characteristics for flying head slider bearings in magnetic disk storage. *JOURNAL OF TRIBOLOGY-TRANSACTIONS OF THE ASME* **2001**, 123, (1), 151-158.
167. Reiss, G.; Hutten, A., Magnetic nanoparticles - Applications beyond data storage. *NATURE MATERIALS* **2005**, 4, (10), 725-726.
168. Carbone, C.; Gardonio, S.; Moras, P.; Lounis, S.; Heide, M.; Bihlmayer, G.; Atodiressei, N.; Dederichs, P.; Blugel, S.; Vlaic, S.; Lehnert, A.; Ouazi, S.; Rusponi, S.; Brune, H.; Honolka, J.; Enders, A.; Kern, K.; Stepanow, S.; Krull, C.; Balashov, T.; Mugarza, A.; Gambardella, P., Self-Assembled Nanometer-Scale Magnetic Networks on Surfaces: Fundamental Interactions and Functional Properties. *ADVANCED FUNCTIONAL MATERIALS* **2011**, 21, (7), 1212-1228.
169. Dmitriev, A.; Talantsev, A.; Zaitsev, S.; Koplak, O.; Morgunov, R., Nano- and heterostructures of magnetic semiconductors for spintronics. *RUSSIAN CHEMICAL BULLETIN* **2011**, 60, (6), 1051-1057.
170. Szczytko, J.; Osewski, P.; Bystrzejewski, M.; Borysiuk, J.; Grabias, A.; Hucko, A.; Lange, H.; Majhofer, A.; Twardowski, A., Carbon-encapsulated magnetic nanoparticles based on Fe, Mn, and Cr for spintronics applications. *ACTA PHYSICA POLONICA A* **2007**, 112, (2), 305-310.
171. Wang, X.; Liu, D.; Song, S.; Zhang, H., CeO₂-Based Pd(Pt) Nanoparticles Grafted onto Fe₃O₄/Graphene: A General Self-Assembly Approach To Fabricate Highly Efficient Catalysts with Magnetic Recyclable Capability. *CHEMISTRY-A EUROPEAN JOURNAL* **2013**, 19, (16), 5169-5173.
172. Kainz, Q.; Reiser, O., Polymer- and Dendrimer-Coated Magnetic Nanoparticles as Versatile Supports for Catalysts, Scavengers, and Reagents. *ACCOUNTS OF CHEMICAL RESEARCH* **2014**, 47, (2), 667-677.
173. Keller, M.; Colliere, V.; Reiser, O.; Caminade, A.; Majoral, J.; Ouali, A., Pyrene-Tagged Dendritic Catalysts Noncovalently Grafted onto Magnetic Co/C Nanoparticles: An Efficient and Recyclable System for Drug Synthesis. *ANGEWANDTE CHEMIE-INTERNATIONAL EDITION* **2013**, 52, (13), 3626-3629.

174. Zhang, M.; Sun, Q.; Yan, Z.; Jing, J.; Wei, W.; Jiang, D.; Xie, J.; Chen, M., Ni/MWCNT-Supported Palladium Nanoparticles as Magnetic Catalysts for Selective Oxidation of Benzyl Alcohol. *AUSTRALIAN JOURNAL OF CHEMISTRY* **2013**, 66, (5), 564-571.
175. Zillillah, Z.; Tan, G.; Li, Z., Sulfonic acid-functionalized magnetic nanoparticles as efficient and reusable catalysts for esterification of free fatty acid in grease in two-step biodiesel production. *ABSTRACTS OF PAPERS OF THE AMERICAN CHEMICAL SOCIETY* **2013**, 245.
176. Vaquer, L.; Riente, P.; Sala, X.; Jansat, S.; Benet-Buchholz, J.; Llobet, A.; Pericas, M., Molecular ruthenium complexes anchored on magnetic nanoparticles that act as powerful and magnetically recyclable stereospecific epoxidation catalysts. *CATALYSIS SCIENCE & TECHNOLOGY* **2013**, 3, (3), 706-714.
177. Crosswhite, M.; Hunt, J.; Southworth, T.; Serniak, K.; Ferrari, A.; Stiegman, A., Development of Magnetic Nanoparticles as Microwave-Specific Catalysts for the Rapid, Low-Temperature Synthesis of Formalin Solutions. *ACS CATALYSIS* **2013**, 3, (6), 1318-1323.
178. Feng, J.; Su, L.; Ma, Y.; Ren, C.; Guo, Q.; Chen, X., CuFe₂O₄ magnetic nanoparticles: A simple and efficient catalyst for the reduction of nitrophenol. *CHEMICAL ENGINEERING JOURNAL* **2013**, 221, 16-24.
179. Xiong, R.; Wang, Y.; Zhang, X.; Lu, C.; Lan, L., In situ growth of gold nanoparticles on magnetic gamma-Fe₂O₃@cellulose nanocomposites: a highly active and recyclable catalyst for reduction of 4-nitrophenol. *RSC ADVANCES* **2014**, 4, (13), 6454-6462.
180. Shylesh, S.; Schunemann, V.; Thiel, W., Magnetically Separable Nanocatalysts: Bridges between Homogeneous and Heterogeneous Catalysis. *ANGEWANDTE CHEMIE-INTERNATIONAL EDITION* **2010**, 49, (20), 3428-3459.
181. Zamborini, F. P.; Bao, L.; Dasari, R., Nanoparticles in Measurement Science. *Analytical Chemistry* **2012**, 84, (2), 541-576.
182. Aigner, W.; Niesar, S.; Mehmedovic, E.; Opel, M.; Wagner, F.; Wiggers, H.; Stutzmann, M., Separation of semiconducting and ferromagnetic FeSi₂-nanoparticles by magnetic filtering. *JOURNAL OF APPLIED PHYSICS* **2013**, 114, (13).
183. Anirudhan, T.; Rejeena, S.; Binusree, J., Adsorptive Separation of Myoglobin from Aqueous Solutions Using Iron Oxide Magnetic Nanoparticles Modified with Functionalized Nanocrystalline Cellulose. *JOURNAL OF CHEMICAL AND ENGINEERING DATA* **2013**, 58, (5), 1329-1339.
184. Bagheri, A.; Behbahani, M.; Amini, M.; Sadeghi, O.; Tootoonchi, A.; Dahaghin, Z., Preconcentration and separation of ultra-trace palladium ion using pyridine-functionalized magnetic nanoparticles. *MICROCHIMICA ACTA* **2012**, 178, (3-4), 261-268.
185. Cano, M.; Sbagoud, K.; Allard, E.; Larpent, C., Magnetic separation of fatty acids with iron oxide nanoparticles and application to extractive deacidification of vegetable oils. *GREEN CHEMISTRY* **2012**, 14, (6), 1786-1795.
186. Ghosh, S.; Fang, T.; Uddin, M.; Hidajat, K., Enantioselective separation of chiral aromatic amino acids with surface functionalized magnetic nanoparticles. *COLLOIDS AND SURFACES B-BIOINTERFACES* **2013**, 105, 267-277.
187. Dudek, G.; Turczyn, R.; Strzelewicz, A.; Krasowska, M.; Rybak, A.; Grzywna, Z., Studies of separation of vapours and gases through composite membranes with ferroferric oxide magnetic nanoparticles. *SEPARATION AND PURIFICATION TECHNOLOGY* **2013**, 109, 55-63.
188. Mwilu, S.; Siska, E.; Baig, R.; Varma, R.; Heithmar, E.; Rogers, K., Separation and measurement of silver nanoparticles and silver ions using magnetic particles. *SCIENCE OF THE TOTAL ENVIRONMENT* **2014**, 472, 316-323.
189. Sayin, S.; Ozcan, F.; Yilmaz, M., Two novel calixarene functionalized iron oxide magnetite nanoparticles as a platform for magnetic separation in the liquid-liquid/solid-liquid

- extraction of oxyanions. *MATERIALS SCIENCE & ENGINEERING C-MATERIALS FOR BIOLOGICAL APPLICATIONS* **2013**, 33, (4), 2433-2439.
190. Li, X.; Rotello, V., Nanoparticles for rapid detection of microbial threats. *NANOMEDICINE* **2011**, 6, (8), 1295-1296.
191. Chen, L.; Razavi, F.; Mumin, A.; Guo, X.; Sham, T.; Zhang, J., Multifunctional nanoparticles for rapid bacterial capture, detection, and decontamination. *RSC ADVANCES* **2013**, 3, (7), 2390-2397.
192. Goransson, J.; De La Torre, T.; Stromberg, M.; Russell, C.; Svedlindh, P.; Stromme, M.; Nilsson, M., Sensitive Detection of Bacterial DNA by Magnetic Nanoparticles. *ANALYTICAL CHEMISTRY* **2010**, 82, (22), 9138-9140.
193. Kim, Y.; Kim, K.; Hong, T., The Detection of Genomic DNA from Bacterial Cells using Iron Oxide Nanoparticles Synthesized by a Hydrothermal Process. *METALS AND MATERIALS INTERNATIONAL* **2010**, 16, (2), 225-228.
194. Qi, P.; Zhang, D.; Wan, Y., Sulfate-reducing bacteria detection based on the photocatalytic property of microbial synthesized ZnS nanoparticles. *ANALYTICA CHIMICA ACTA* **2013**, 800, 65-70.
195. Rahman, Q.; Ahmad, M.; Misra, S.; Lohani, M., Effective photocatalytic degradation of rhodamine B dye by ZnO nanoparticles. *MATERIALS LETTERS* **2013**, 91, 170-174.
196. Sudha, M.; Senthilkumar, S.; Hariharan, R.; Suganthi, A.; Rajarajan, M., Synthesis, characterization and study of photocatalytic activity of surface modified ZnO nanoparticles by PEG capping. *JOURNAL OF SOL-GEL SCIENCE AND TECHNOLOGY* **2013**, 65, (3), 301-310.
197. Sartori, A.; Visentin, F.; El Habra, N.; De Zorzi, C.; Natali, M.; Garoli, D.; Gerbasi, R.; Casarin, M.; Rossetto, G., Preparation of tetrapod-like ZnO/TiO₂ core-shell nanostructures as photocatalytic powder. *CRYSTAL RESEARCH AND TECHNOLOGY* **2011**, 46, (8), 885-890.
198. Zargoosh, K.; Abedini, H.; Abdolmaleki, A.; Molavian, M., Effective Removal of Heavy Metal Ions from Industrial Wastes Using Thiosalicylhydrazide-Modified Magnetic Nanoparticles. *INDUSTRIAL & ENGINEERING CHEMISTRY RESEARCH* **2013**, 52, (42), 14944-14954.
199. Markova, Z.; Siskova, K.; Filip, J.; Cuda, J.; Kolar, M.; Safarova, K.; Medrik, I.; Zboril, R., Air Stable Magnetic Bimetallic Fe-Ag Nanoparticles for Advanced Antimicrobial Treatment and Phosphorus Removal. *ENVIRONMENTAL SCIENCE & TECHNOLOGY* **2013**, 47, (10), 5285-5293.
200. Ge, F.; Li, M.; Ye, H.; Zhao, B., Effective removal of heavy metal ions Cd²⁺, Zn²⁺, Pb²⁺, Cu²⁺ from aqueous solution by polymer-modified magnetic nanoparticles. *JOURNAL OF HAZARDOUS MATERIALS* **2012**, 211, 366-372.
201. Wang, H.; Yu, Y.; Chen, Q.; Cheng, K., Carboxyl-functionalized nanoparticles with magnetic core and mesopore carbon shell as adsorbents for the removal of heavy metal ions from aqueous solution. *DALTON TRANSACTIONS* **2011**, 40, (3), 559-563.
202. Mahdavi, S.; Jalali, M.; Afkhami, A., Removal of heavy metals from aqueous solutions using Fe₃O₄, ZnO, and CuO nanoparticles. *JOURNAL OF NANOPARTICLE RESEARCH* **2012**, 14, (8).
203. Tao, L.; Xu, L.; Wang, J.; Shi, Z., Removal of Heavy Metal Ions in Environmental Water by Recycling Magnetic Nanoparticles. *MATERIALS AND MANUFACTURING PROCESSES* **2013**, 29, (1), 69-73.
204. Bavio, M.; Lista, A., Synthesis and Characterization of Hybrid-Magnetic Nanoparticles and Their Application for Removal of Arsenic from Groundwater. *SCIENTIFIC WORLD JOURNAL* **2013**.
205. Feitoza, N.; Goncalves, T.; Mesquita, J.; Menegucci, J.; Santos, M.; Chaker, J.; Cunha, R.; Medeiros, A.; Rubim, J.; Sousa, M., Fabrication of glycine-functionalized maghemite

- nanoparticles for magnetic removal of copper from wastewater. *JOURNAL OF HAZARDOUS MATERIALS* **2014**, 264, 153-160.
206. Ferroudj, N.; Nzimoto, J.; Davidson, A.; Talbot, D.; Briot, E.; Dupuis, V.; Bee, A.; Medjram, M.; Abramson, S., Maghemite nanoparticles and maghemite/silica nanocomposite microspheres as magnetic Fenton catalysts for the removal of water pollutants. *APPLIED CATALYSIS B-ENVIRONMENTAL* **2013**, 136, 9-18.
207. Arslan, M.; Sayin, S.; Yilmaz, M., Removal of Carcinogenic Azo Dyes from Water by New Cyclodextrin-Immobilized Iron Oxide Magnetic Nanoparticles. *WATER AIR AND SOIL POLLUTION* **2013**, 224, (5).
208. Bao, X.; Qiang, Z.; Ling, W.; Chang, J., Sonochemical synthesis of MFe₂O₄ magnetic nanoparticles for adsorptive removal of tetracyclines from water. *SEPARATION AND PURIFICATION TECHNOLOGY* **2013**, 117, 104-110.
209. Aksoy, T.; Erdemir, S.; Yildiz, H.; Yilmaz, M., Novel Water-Soluble Calix[4,6]arene Appended Magnetic Nanoparticles for the Removal of the Carcinogenic Aromatic Amines. *WATER AIR AND SOIL POLLUTION* **2012**, 223, (7), 4129-4139.
210. Bagabas, A.; Alshammari, A.; Aboud, M. F.; Kosslick3, H., Room-temperature synthesis of zinc oxide nanoparticles in different media and their application in cyanide photodegradation. *Nanoscale Research Letters* **2013**, 8, 516-525.
211. Comparelli, R.; Fanizza, E.; Curri, M.; Cozzoli, P.; Mascolo, G.; Agostiano, A., UV-induced photocatalytic degradation of azo dyes by organic-capped ZnO nanocrystals immobilized onto substrates. *APPLIED CATALYSIS B-ENVIRONMENTAL* **2005**, 60, (1-2), 1-11.
212. Hutter, E.; Maysinger, D., Gold Nanoparticles and Quantum Dots for Bioimaging. *MICROSCOPY RESEARCH AND TECHNIQUE* **2011**, 74, (7), 592-604.
213. Browning, L.; Huang, T.; Xu, X., Real-time in vivo imaging of size-dependent transport and toxicity of gold nanoparticles in zebrafish embryos using single nanoparticle plasmonic spectroscopy. *INTERFACE FOCUS* **2013**, 3, (3).
214. Kim, D.; Park, S.; Lee, J. H.; Jeong, Y. Y.; Jon, S., Antibiofouling polymer-coated gold nanoparticles as a contrast agent for in vivo x-ray computed tomography imaging. *Journal Of The American Chemical Society* **2007**, 129, (24), 7661-7665.
215. Peng, C.; Qin, J.; Zhou, B.; Chen, Q.; Shen, M.; Zhu, M.; Lu, X.; Shi, X., Targeted tumor CT imaging using folic acid-modified PEGylated dendrimer-entrapped gold nanoparticles. *POLYMER CHEMISTRY* **2013**, 4, (16), 4412-4424.
216. Zhang, Q.; Iwakuma, N.; Sharma, P.; Moudgil, B.; Wu, C.; McNeill, J.; Jiang, H.; Grobmyer, S., Gold nanoparticles as a contrast agent for in vivo tumor imaging with photoacoustic tomography. *NANOTECHNOLOGY* **2009**, 20, (39).
217. Peng, C.; Li, K.; Cao, X.; Xiao, T.; Hon, W.; Zheng, L.; Guo, R.; Shen, M.; Zhang, G.; Shi, X., Facile formation of dendrimer-stabilized gold nanoparticles modified with diatrizoic acid for enhanced computed tomography imaging applications. *NANOSCALE* **2012**, 4, (21), 6768-6778.
218. Lin, M.; Pei, H.; Yang, F.; Fan, C.; Zuo, X., Applications of Gold Nanoparticles in the Detection and Identification of Infectious Diseases and Biothreats. *ADVANCED MATERIALS* **2013**, 25, (25), 3490-3496.
219. Mieszawska, A.; Mulder, W.; Fayad, Z.; Cormode, D., Multifunctional Gold Nanoparticles for Diagnosis and Therapy of Disease. *MOLECULAR PHARMACEUTICS* **2013**, 10, (3), 831-847.
220. Springer, T.; Homola, J., Biofunctionalized gold nanoparticles for SPR-biosensor-based detection of CEA in blood plasma. *ANALYTICAL AND BIOANALYTICAL CHEMISTRY* **2012**, 404, (10), 2869-2875.

221. Tang, H.; Chen, J.; Nie, L.; Kuang, Y.; Yao, S., A label-free electrochemical immunoassay for carcinoembryonic antigen (CEA) based on gold nanoparticles (AuNPs) and nonconductive polymer film. *BIOSENSORS & BIOELECTRONICS* **2007**, *22*, (6), 1061-1067.
222. Asadishad, B.; Vosoughi, M.; Alamzadeh, I.; Tavakoli, A., Synthesis of Folate-Modified, Polyethylene Glycol-Functionalized Gold Nanoparticles for Targeted Drug Delivery. *JOURNAL OF DISPERSION SCIENCE AND TECHNOLOGY* **2010**, *31*, (4), 492-500.
223. Brown, S.; Nativo, P.; Smith, J.; Stirling, D.; Edwards, P.; Venugopal, B.; Flint, D.; Plumb, J.; Graham, D.; Wheate, N., Gold Nanoparticles for the Improved Anticancer Drug Delivery of the Active Component of Oxaliplatin. *JOURNAL OF THE AMERICAN CHEMICAL SOCIETY* **2010**, *132*, (13), 4678-4684.
224. Cheng, Y.; Dai, Q.; Morshed, R.; Han, Y.; Auffinger, B.; Wainwright, D.; Zhang, L.; Tobias, A.; Rincon, E.; Thaci, B.; Ahmed, A.; He, C.; Lesniak, M., GOLD NANOPARTICLES AS A DRUG DELIVERY SYSTEM FOR MALIGNANT BRAIN TUMORS. *NEURO-ONCOLOGY* **2013**, *15*, 39-40.
225. Park, H.; Tsutsumi, H.; Mihara, H., Cell-selective intracellular drug delivery using doxorubicin and alpha-helical peptides conjugated to gold nanoparticles. *BIOMATERIALS* **2014**, *35*, (10), 3480-3487.
226. Sun, X.; Zhang, G.; Keynton, R.; O'Toole, M.; Patel, D.; Gobin, A., Enhanced drug delivery via hyperthermal membrane disruption using targeted gold nanoparticles with PEGylated Protein-G as a cofactor. *NANOMEDICINE-NANOTECHNOLOGY BIOLOGY AND MEDICINE* **2013**, *9*, (8), 1214-1222.
227. Huang, X.; Jain, P.; El-Sayed, I.; El-Sayed, M., Plasmonic photothermal therapy (PPTT) using gold nanoparticles. *LASERS IN MEDICAL SCIENCE* **2008**, *23*, (3), 217-228.
228. Hainfeld, J.; O'Connor, M.; Lin, P.; Qian, L.; Slatkin, D.; Smilowitz, H., Infrared-Transparent Gold Nanoparticles Converted by Tumors to Infrared Absorbers Cure Tumors in Mice by Photothermal Therapy. *PLOS ONE* **2014**, *9*, (2).
229. Im, A.; Kim, J.; Kim, H.; Cho, S.; Park, Y.; Kim, Y., Wound healing and antibacterial activities of chondroitin sulfate- and acharan sulfate-reduced silver nanoparticles. *NANOTECHNOLOGY* **2013**, *24*, (39).
230. Kwan, K.; Liu, X.; To, M.; Yeung, K.; Ho, C.; Wong, K., Modulation of collagen alignment by silver nanoparticles results in better mechanical properties in wound healing. *NANOMEDICINE-NANOTECHNOLOGY BIOLOGY AND MEDICINE* **2011**, *7*, (4), 497-504.
231. Kwan, K.; Liu, X.; Yeung, K., Silver nanoparticles improve wound healing. *NANOMEDICINE* **2011**, *6*, (4), 595-596.
232. Mishra, M.; Kumar, H.; Tripathi, K., Diabetic delayed wound healing and the role of silver nanoparticles. *DIGEST JOURNAL OF NANOMATERIALS AND BIOSTRUCTURES* **2008**, *3*, (2), 49-54.
233. Rigo, C.; Ferroni, L.; Tocco, I.; Roman, M.; Munivrana, I.; Gardin, C.; Cairns, W.; Vindigni, V.; Azzena, B.; Barbante, C.; Zavan, B., Active Silver Nanoparticles for Wound Healing. *INTERNATIONAL JOURNAL OF MOLECULAR SCIENCES* **2013**, *14*, (3), 4817-4840.
234. Wu, J.; Zheng, Y.; Song, W.; Luan, J.; Wen, X.; Wu, Z.; Chen, X.; Wang, Q.; Guo, S., In situ synthesis of silver-nanoparticles/bacterial cellulose composites for slow-released antimicrobial wound dressing. *CARBOHYDRATE POLYMERS* **2014**, *102*, 762-771.
235. Mazumder, S.; Dey, R.; Mitra, M.; Mukherjee, S.; Das, G., Review: Biofunctionalized Quantum Dots in Biology and Medicine. *JOURNAL OF NANOMATERIALS* **2009**.
236. Erathodiyil, N.; Ying, J. Y., Functionalization of Inorganic Nanoparticles for Bioimaging Applications. *Accounts Of Chemical Research* **2011**, *44*, (10), 925-935.
237. Selvan, S. T.; Tan, T. T. Y.; Yi, D. K.; Jana, N. R., Functional and Multifunctional Nanoparticles for Bioimaging and Biosensing. *Langmuir* **2009**, *26*, (14), 11631-11641.

238. Sharma, P.; Brown, S.; Walter, G.; Santra, S.; Moudgil, B., Nanoparticles for bioimaging. *Advances in Colloid and Interface Science* **2006**, 123-126, 471-485.
239. Murcia, M.; Shaw, D.; Long, E.; Naumann, C., Fluorescence correlation spectroscopy of CdSe/ZnS quantum dot optical bioimaging probes with ultra-thin biocompatible coatings. *OPTICS COMMUNICATIONS* **2008**, 281, (7), 1771-1780.
240. Vannoy, C.; Xu, J.; Leblanc, R., Bioimaging and Self-Assembly of Lysozyme Fibrils Utilizing CdSe/ZnS Quantum Dots. *JOURNAL OF PHYSICAL CHEMISTRY C* **2010**, 114, (2), 766-773.
241. Vibin, M.; Vinayakan, R.; John, A.; Raji, V.; Rejiya, C.; Vinesh, N.; Abraham, A., Cytotoxicity and fluorescence studies of silica-coated CdSe quantum dots for bioimaging applications. *JOURNAL OF NANOPARTICLE RESEARCH* **2011**, 13, (6), 2587-2596.
242. Zhang, Y.; Li, Y.; Yan, X., Aqueous Layer-by-Layer Epitaxy of Type-II CdTe/CdSe Quantum Dots with Near-infrared Fluorescence for Bioimaging Applications. *SMALL* **2009**, 5, (2), 185-189.
243. Sun, X.; Huang, X.; Guo, J.; Zhu, W.; Ding, Y.; Niu, G.; Wang, A.; Kiesewetter, D.; Wang, Z.; Sun, S.; Chen, X., Self-illuminating Cu-64-Doped CdSe/ZnS Nanocrystals for in Vivo Tumor Imaging. *JOURNAL OF THE AMERICAN CHEMICAL SOCIETY* **2014**, 136, (5), 1706-1709.
244. Hu, D.; Zhang, P.; Gong, P.; Lian, S.; Lu, Y.; Gao, D.; Cai, L., A fast synthesis of near-infrared emitting CdTe/CdSe quantum dots with small hydrodynamic diameter for in vivo imaging probes. *NANOSCALE* **2011**, 3, (11), 4724-4732.
245. Kim, J.; Cho, K.; Tran, T.; Nurunnabi, M.; Moon, T.; Hong, S.; Lee, Y., In vivo NIR imaging with CdTe/CdSe quantum dots entrapped in PLGA nanospheres. *JOURNAL OF COLLOID AND INTERFACE SCIENCE* **2011**, 353, (2), 363-371.
246. Liu, W.; Choi, H.; Zimmer, J.; Tanaka, E.; Frangioni, J.; Bawendi, M., Compact cysteine-coated CdSe(ZnCdS) quantum dots for in vivo applications. *JOURNAL OF THE AMERICAN CHEMICAL SOCIETY* **2007**, 129, (47), 14530-+.
247. Taniguchi, S.; Green, M.; Rizvi, S.; Seifalian, A., The one-pot synthesis of core/shell/shell CdTe/CdSe/ZnSe quantum dots in aqueous media for in vivo deep tissue imaging. *JOURNAL OF MATERIALS CHEMISTRY* **2011**, 21, (9), 2877-2882.
248. Li, L.; Daou, T. J.; Texier, I.; Tran, T. K. C.; Nguyen, Q. L.; Reiss, P., Highly Luminescent CuInS₂/ZnS Core/Shell Nanocrystals: Cadmium-Free Quantum Dots for In Vivo Imaging. *Chemistry Of Materials* **2009**, 21, (12), 2422-2429.
249. Mandal, G.; Darragh, M.; Wang, Y.; Heyes, C., Cadmium-free quantum dots as time-gated bioimaging probes in highly-autofluorescent human breast cancer cells. *CHEMICAL COMMUNICATIONS* **2013**, 49, (6), 624-626.
250. Song, Z.; Kelf, T.; Sanchez, W.; Roberts, M.; Ricka, J.; Frenz, M.; Zvyagin, A., Characterization of optical properties of ZnO nanoparticles for quantitative imaging of transdermal transport. *BIOMEDICAL OPTICS EXPRESS* **2011**, 2, (12), 3321-3333.
251. Wu, Y.; Lim, C.; Fu, S.; Tok, A.; Lau, H.; Boey, F.; Zeng, X., Surface modifications of ZnO quantum dots for bio-imaging. *NANOTECHNOLOGY* **2007**, 18, (21).
252. Balti, I.; Barrere, A.; Gueguen, V.; Poussard, L.; Pavon-Djavid, G.; Meddahi-Pelle, A.; Rabu, P.; Smiri, L.; Jouini, N.; Chaubet, F., Preparation of cytocompatible luminescent and magnetic nanohybrids based on ZnO, Zn_{0.95}Ni_{0.05}O and core@shell ZnO@Fe₂O₃ polymer grafted nanoparticles for biomedical imaging. *JOURNAL OF NANOPARTICLE RESEARCH* **2012**, 14, (12).
253. Lee, C.; Jeong, H.; Yun, K.; Kim, D.; Sohn, M.; Lee, J.; Jeong, J.; Lim, S., Optical imaging to trace near infrared fluorescent zinc oxide nanoparticles following oral exposure. *INTERNATIONAL JOURNAL OF NANOMEDICINE* **2012**, 7, 3203-3209.

254. Cho, N.; Cheong, T.; Min, J.; Wu, J.; Lee, S.; Kim, D.; Yang, J.; Kim, S.; Kim, Y.; Seong, S., A multifunctional core-shell nanoparticle for dendritic cell-based cancer immunotherapy. *NATURE NANOTECHNOLOGY* **2011**, 6, (10), 675-682.
255. Probst, C.; Zrazhevskiy, P.; Bagalkot, V.; Gao, X., Quantum dots as a platform for nanoparticle drug delivery vehicle design. *ADVANCED DRUG DELIVERY REVIEWS* **2013**, 65, (5), 703-718.
256. Lee, S.; Harrison, B.; Czerw, R.; Yoo, J.; Atala, A.; Lim, J., Regulated Heparin Release using Novel Quantum Dots for Potential Application to Vascular Graft Engineering. *JOURNAL OF MACROMOLECULAR SCIENCE PART A-PURE AND APPLIED CHEMISTRY* **2009**, 46, (12), 1191-1198.
257. Chen, T.; Zhao, T.; Wei, D.; Wei, Y.; Li, Y.; Zhang, H., Core-shell nanocarriers with ZnO quantum dots-conjugated Au nanoparticle for tumor-targeted drug delivery. *CARBOHYDRATE POLYMERS* **2013**, 92, (2), 1124-1132.
258. Zhang, H.; Chen, B.; Jiang, H.; Wang, C.; Wang, H.; Wang, X., A strategy for ZnO nanorod mediated multi-mode cancer treatment. *BIOMATERIALS* **2011**, 32, (7), 1906-1914.
259. Muharnmad, F.; Guo, M.; Qi, W.; Sun, F.; Wang, A.; Guo, Y.; Zhu, G., pH-Triggered Controlled Drug Release from Mesoporous Silica Nanoparticles via Intracellular Dissolution of ZnO Nanolids. *JOURNAL OF THE AMERICAN CHEMICAL SOCIETY* **2011**, 133, (23), 8778-8781.
260. Muhammad, F.; Guo, M.; Guo, Y.; Qi, W.; Qu, F.; Sun, F.; Zhao, H.; Zhu, G., Acid degradable ZnO quantum dots as a platform for targeted delivery of an anticancer drug. *JOURNAL OF MATERIALS CHEMISTRY* **2011**, 21, (35), 13406-13412.
261. Thurber, A.; Wingett, D.; Rasmussen, J.; Layne, J.; Johnson, L.; Tenne, D.; Zhang, J.; Hanna, C.; Punnoose, A., Improving the selective cancer killing ability of ZnO nanoparticles using Fe doping. *NANOTOXICOLOGY* **2012**, 6, (4), 440-452.
262. Ansari, S.; Husain, Q.; Qayyum, S.; Azam, A., Designing and surface modification of zinc oxide nanoparticles for biomedical applications. *FOOD AND CHEMICAL TOXICOLOGY* **2011**, 49, (9), 2107-2115.
263. Riggio, C.; Raffa, V.; Cuschieri, A., Synthesis, characterisation and dispersion of zinc oxide nanorods for biomedical applications. *MICRO & NANO LETTERS* **2010**, 5, (5), 355-360.
264. Hahm, J., Zinc Oxide Nanomaterials for Biomedical Fluorescence Detection. *JOURNAL OF NANOSCIENCE AND NANOTECHNOLOGY* **2014**, 14, (1), 475-486.
265. Bhande, R.; Khobragade, C.; Mane, R.; Bhande, S., Enhanced synergism of antibiotics with zinc oxide nanoparticles against extended spectrum beta-lactamase producers implicated in urinary tract infections. *JOURNAL OF NANOPARTICLE RESEARCH* **2013**, 15, (1).
266. Aleno, R.; Diaz, L.; Medina, E.; Del Canto, H.; Ferrer, E., Antimicrobial effects of enhanced antibiotics mixed with silver, gold and ZnO nanoparticles. *ABSTRACTS OF PAPERS OF THE AMERICAN CHEMICAL SOCIETY* **2012**, 243.
267. Luo, Z.; Wu, Q.; Xue, J.; Ding, Y., Selectively Enhanced Antibacterial Effects and Ultraviolet Activation of Antibiotics with ZnO Nanorods Against Escherichia Coli. *JOURNAL OF BIOMEDICAL NANOTECHNOLOGY* **2013**, 9, (1), 69-76.
268. Gao, S.; Jia, X.; Li, Z.; Chen, Y.; Jiang, K., Antibiotic-inspired zinc oxide with morphology-dependent photocatalytic activity. *CANADIAN JOURNAL OF CHEMISTRY-REVUE CANADIENNE DE CHIMIE* **2011**, 89, (5), 590-597.
269. Hsu, S.; Lin, Y.; Huang, S.; Lem, K.; Nguyen, D.; Lee, D., Synthesis of water-dispersible zinc oxide quantum dots with antibacterial activity and low cytotoxicity for cell labeling. *NANOTECHNOLOGY* **2013**, 24, (47).
270. Lipovsky, A.; Nitzan, Y.; Gedanken, A.; Lubart, R., Antifungal activity of ZnO nanoparticles- the role of ROS mediated cell injury. *Nanotechnology* **2011**, 22, (10).

271. Umar, A.; Rahman, M.; Vaseem, M.; Hahn, Y., Ultra-sensitive cholesterol biosensor based on low-temperature grown ZnO nanoparticles. *ELECTROCHEMISTRY COMMUNICATIONS* **2009**, *11*, (1), 118-121.
272. Sudhagar, S.; Sathya, S.; Pandian, K.; Lakshmi, B., Targeting and sensing cancer cells with ZnO nanoprobe in vitro. *BIOTECHNOLOGY LETTERS* **2011**, *33*, (9), 1891-1896.
273. Wei, X.; Wang, W.; Chen, K., ZnO:Er,Yb,Gd Particles Designed for Magnetic-Fluorescent Imaging and Near-Infrared Light Triggered Photodynamic Therapy. *JOURNAL OF PHYSICAL CHEMISTRY C* **2013**, *117*, (45), 23716-23729.
274. Senthilkumar, S.; Hariharan, R.; Suganthi, A.; Ashokkumar, M.; Rajarajan, M.; Pitchumani, K., Synergistic photodynamic action of ZnO nanomaterials encapsulated meso-tetra (4-sulfonatophenyl) porphyrin. *POWDER TECHNOLOGY* **2013**, *237*, 497-505.
275. Hariharan, R.; Senthilkumar, S.; Suganthi, A.; Rajarajan, M., Synthesis and characterization of daunorubicin modified ZnO/PVP nanorods and its photodynamic action. *JOURNAL OF PHOTOCHEMISTRY AND PHOTOBIOLOGY A-CHEMISTRY* **2013**, *252*, 107-115.
276. Hu, Z.; Li, J.; Li, C.; Zhao, S.; Li, N.; Wang, Y.; Wei, F.; Chen, L.; Huang, Y., Folic acid-conjugated graphene-ZnO nanohybrid for targeting photodynamic therapy under visible light irradiation. *JOURNAL OF MATERIALS CHEMISTRY B* **2013**, *1*, (38), 5003-5013.
277. Li, J.; Guo, D.; Wang, X.; Wang, H.; Jiang, H.; Chen, B., The Photodynamic Effect of Different Size ZnO Nanoparticles on Cancer Cell Proliferation In Vitro. *NANOSCALE RESEARCH LETTERS* **2010**, *5*, (6), 1063-1071.
278. Bora, T.; Lakshman, K.; Sarkar, S.; Makhal, A.; Sardar, S.; Pal, S.; Dutta, J., Modulation of defect-mediated energy transfer from ZnO nanoparticles for the photocatalytic degradation of bilirubin. *BEILSTEIN JOURNAL OF NANOTECHNOLOGY* **2013**, *4*, 714-725.
279. Yin, S.; Li, Z.; Cheng, L.; Wang, C.; Liu, Y.; Chen, Q.; Gong, H.; Guo, L.; Li, Y.; Liu, Z., Magnetic PEGylated Pt3Co nanoparticles as a novel MR contrast agent: in vivo MR imaging and long-term toxicity study. *NANOSCALE* **2013**, *5*, (24), 12464-12473.
280. Weinstein, J.; Varallyay, C.; Dosa, E.; Gahramanov, S.; Hamilton, B.; Rooney, W.; Muldoon, L.; Neuwelt, E., Superparamagnetic iron oxide nanoparticles: diagnostic magnetic resonance imaging and potential therapeutic applications in neurooncology and central nervous system inflammatory pathologies, a review. *JOURNAL OF CEREBRAL BLOOD FLOW AND METABOLISM* **2010**, *30*, (1), 15-35.
281. Lacroix, L.; Delpech, F.; Nayral, C.; Lachaize, S.; Chaudret, B., New generation of magnetic and luminescent nanoparticles for in vivo real-time imaging. *INTERFACE FOCUS* **2013**, *3*, (3).
282. Fu, A.; Wilson, R.; Smith, B.; Mullenix, J.; Earhart, C.; Akin, D.; Guccione, S.; Wang, S.; Gambhir, S., Fluorescent Magnetic Nanoparticles for Magnetically Enhanced Cancer Imaging and Targeting in Living Subjects. *ACS NANO* **2012**, *6*, (8), 6862-6869.
283. Bruns, O. T.; Ittrich, H.; Peldschus, K.; Kaul, M. G.; Tromsdorf, U. I.; Lauterwasser, J.; Nikolic, M. S.; Mollwitz, B.; Merkel, M.; Bigall, N. C.; Sapra, S.; Reimer, R.; Hohenberg, H.; Weller, H.; Eychmuller, A.; Adam, G.; Beisiegel, U.; Heeren, J., Real-time magnetic resonance imaging and quantification of lipoprotein metabolism in vivo using nanocrystals. *Nature Nanotechnology* **2009**, *4*, (3), 193-201.
284. Wang, E.; Wang, A., Nanoparticles and their applications in cell and molecular biology. *INTEGRATIVE BIOLOGY* **2014**, *6*, (1), 9-26.
285. Sahoo, B.; Devi, K.; Banerjee, R.; Maiti, T.; Pramanik, P.; Dhara, D., Thermal and pH Responsive Polymer-Tethered Multifunctional Magnetic Nanoparticles for Targeted Delivery of Anticancer Drug. *ACS APPLIED MATERIALS & INTERFACES* **2013**, *5*, (9), 3884-3893.

286. Shen, J.; Gao, F.; Yin, T.; Zhang, H.; Ma, M.; Yang, Y.; Yue, F., cRGD-functionalized polymeric magnetic nanoparticles as a dual-drug delivery system for safe targeted cancer therapy. *PHARMACOLOGICAL RESEARCH* **2013**, *70*, (1), 102-115.
287. Sahiner, N.; Ilgin, P., Soft Core-Shell Polymeric Nanoparticles with Magnetic Property for Potential Guided Drug Delivery. *CURRENT NANOSCIENCE* **2010**, *6*, (5), 483-491.
288. Chorny, M.; Alferiev, I.; Fishbein, I.; Tengood, J.; Folchman-Wagner, Z.; Forbes, S.; Levy, R., Formulation and In Vitro Characterization of Composite Biodegradable Magnetic Nanoparticles for Magnetically Guided Cell Delivery. *PHARMACEUTICAL RESEARCH* **2012**, *29*, (5), 1232-1241.
289. Takafuji, M.; Kitaura, K.; Nishiyama, T.; Govindarajan, S.; Gopal, V.; Imamura, T.; Ihara, H., Chemically tunable cationic polymer-bonded magnetic nanoparticles for gene magnetofection. *JOURNAL OF MATERIALS CHEMISTRY B* **2014**, *2*, (6), 644-650.
290. Sukoyan, M.; Khrapov, E.; Voronina, E.; Boyarskikh, U.; Gubanov, A.; Itin, V.; Magaeva, A.; Nayden, E.; Terekhova, O.; Filipenko, M., Magnetofection of Human Somatic Cells with Magnetite and Cobalt Ferrosipinel Nanoparticles. *BULLETIN OF EXPERIMENTAL BIOLOGY AND MEDICINE* **2013**, *154*, (5), 673-676.
291. Mykhaylyk, O.; Plank, C., Magnetic nanoparticles for Gene delivery. *BIOMEDICAL ENGINEERING-BIOMEDIZINISCHE TECHNIK* **2012**, *57*.
292. Jordan, A.; Scholz, R.; Wust, P.; Fahling, H.; Felix, R., Magnetic fluid hyperthermia (MFH): cancer treatment with AC magnetic field induced excitation of biocompatible superparamagnetic nanoparticles. *J. Magn. Magn. Mater.* **1999**, *201*, 413-419.
293. Guardia, P.; Di Corato, R.; Lartigue, L.; Wilhelm, C.; Espinosa, A.; Garcia-Hernandez, M.; Gazeau, F.; Manna, L.; Pellegrino, T., Water-Soluble Iron Oxide Nanocubes with High Values of Specific Absorption Rate for Cancer Cell Hyperthermia Treatment. *Acs Nano* **2012**, *6*, (4), 3080-3091.
294. Jadhav, N.; Prasad, A.; Kumar, A.; Mishra, R.; Dhara, S.; Babu, K.; Prajapat, C.; Misra, N.; Ningthoujam, R.; Pandey, B.; Vatsa, R., Synthesis of oleic acid functionalized Fe₃O₄ magnetic nanoparticles and studying their interaction with tumor cells for potential hyperthermia applications. *COLLOIDS AND SURFACES B-BIOINTERFACES* **2013**, *108*, 158-168.
295. Martinez-Boubeta, C.; Simeonidis, K.; Makridis, A.; Angelakeris, M.; Iglesias, O.; Guardia, P.; Cabot, A.; Yedra, L.; Estrade, S.; Peiro, F.; Saghi, Z.; Midgley, P.; Conde-Leboran, I.; Serantes, D.; Baldomir, D., Learning from Nature to Improve the Heat Generation of Iron-Oxide Nanoparticles for Magnetic Hyperthermia Applications. *SCIENTIFIC REPORTS* **2013**, *3*.
296. Prasad, A.; Parchur, A.; Juluri, R.; Jadhav, N.; Pandey, B.; Ningthoujam, R.; Vatsa, R., Bi-functional properties of Fe₃O₄@YPO₄:Eu hybrid nanoparticles: hyperthermia application. *DALTON TRANSACTIONS* **2013**, *42*, (14), 4885-4896.
297. Yoo, D.; Jeong, H.; Preihs, C.; Choi, J.; Shin, T.; Sessler, J.; Cheon, J., Double-Effector Nanoparticles: A Synergistic Approach to Apoptotic Hyperthermia. *ANGEWANDTE CHEMIE-INTERNATIONAL EDITION* **2012**, *51*, (50), 12482-12485.
298. Goya, G.; Lima, E.; Arelaro, A.; Torres, T.; Rechenberg, H.; Rossi, L.; Marquina, C.; Ibarra, M., Magnetic Hyperthermia With Fe₃O₄ Nanoparticles: The Influence of Particle Size on Energy Absorption. *IEEE TRANSACTIONS ON MAGNETICS* **2008**, *44*, (11), 4444-4447.
299. Yassin, A.; Elwaseef, A.; Elnashar, M.; Oldenburg, J.; Mayer, G.; Potzsch, B.; Muller, J., Protamine-adsorbed magnetic nanoparticles for efficient isolation and concentration of hepatitis-C virus from human plasma samples. *CHEMICAL COMMUNICATIONS* **2014**, *50*, (5), 590-592.
300. Enomoto, T.; Kawano, M.; Fukuda, H.; Sawada, W.; Inoue, T.; Haw, K.; Kita, Y.; Sakamoto, S.; Yamaguchi, Y.; Imai, T.; Hatakeyama, M.; Saito, S.; Sandhu, A.; Matsui, M.; Aoki, I.; Handa,

- H., Viral protein-coating of magnetic nanoparticles using simian virus 40 VP1. *JOURNAL OF BIOTECHNOLOGY* **2013**, 167, (1), 8-15.
301. Zou, X.; Huang, H.; Gao, Y.; Su, X., Detection of avian influenza virus based on magnetic silica nanoparticles resonance light scattering system. *ANALYST* **2012**, 137, (3), 648-653.
302. Chao, M.; Li, C.; Wang, F.; Li, Z.; Li, X.; He, N., Chemiluminescence detection of hepatitis B virus (HBV) based on magnetic nanoparticles and whole genome amplification. *ABSTRACTS OF PAPERS OF THE AMERICAN CHEMICAL SOCIETY* **2012**, 243.
303. Elingarami, S.; Liu, M.; Li, Z.; He, N., Surface-Engineered Magnetic Nanoparticles for Molecular Detection of Infectious Agents and Cancer. *JOURNAL OF NANOSCIENCE AND NANOTECHNOLOGY* **2013**, 13, (5), 3204-3213.
304. McNally, A., MAGNETIC SENSORS Nanoparticles detect infection. *NATURE NANOTECHNOLOGY* **2013**, 8, (5), 315-316.
305. Duncan, T., Applications of nanotechnology in food packaging and food safety: Barrier materials, antimicrobials and sensors. *JOURNAL OF COLLOID AND INTERFACE SCIENCE* **2011**, 363, (1), 1-24.
306. Vinayaka, A.; Thakur, M., Focus on quantum dots as potential fluorescent probes for monitoring food toxicants and foodborne pathogens. *ANALYTICAL AND BIOANALYTICAL CHEMISTRY* **2010**, 397, (4), 1445-1455.
307. Werlin, R.; Priester, J.; Mielke, R.; Kramer, S.; Jackson, S.; Stoimenov, P.; Stucky, G.; Cherr, G.; Orias, E.; Holden, P., Biomagnification of cadmium selenide quantum dots in a simple experimental microbial food chain. *NATURE NANOTECHNOLOGY* **2011**, 6, (1), 65-71.
308. Zhao, Y.; Ye, M.; Chao, Q.; Jia, N.; Ge, Y.; Shen, H., Simultaneous Detection of Multifood-Borne Pathogenic Bacteria Based on Functionalized Quantum Dots Coupled with Immunomagnetic Separation in Food Samples. *JOURNAL OF AGRICULTURAL AND FOOD CHEMISTRY* **2009**, 57, (2), 517-524.
309. Bijad, M.; Karimi-Maleh, H.; Khalilzadeh, M., Application of ZnO/CNTs Nanocomposite Ionic Liquid Paste Electrode as a Sensitive Voltammetric Sensor for Determination of Ascorbic Acid in Food Samples. *FOOD ANALYTICAL METHODS* **2013**, 6, (6), 1639-1647.
310. Taherkhani, A.; Jamali, T.; Hadadzadeh, H.; Karimi-Maleh, H.; Beitollahi, H.; Taghavi, M.; Karimi, F., ZnO nanoparticle-modified ionic liquid-carbon paste electrode for voltammetric determination of folic acid in food and pharmaceutical samples. *IONICS* **2014**, 20, (3), 421-429.
311. Carrillo-Carrion, C.; Simonet, B.; Valcarcel, M., Rapid fluorescence determination of diquat herbicide in food grains using quantum dots as new reducing agent. *ANALYTICA CHIMICA ACTA* **2011**, 692, (1-2), 103-108.
312. Wang, Y.; Yan, Y.; Ji, W.; Wang, H.; Zou, Q.; Sun, J., Novel Chemiluminescence immunoassay for the Determination of Zearalenone in Food Samples Using Gold Nanoparticles Labeled with Streptavidin-Horseradish Peroxidase. *JOURNAL OF AGRICULTURAL AND FOOD CHEMISTRY* **2013**, 61, (18), 4250-4256.
313. Mirmoghtadaie, L.; Ensafi, A.; Kadivar, M.; Shahedi, M.; Ganjali, M., Highly Selective, Sensitive and Fast Determination of Folic Acid in Food Samples Using New Electrodeposited Gold Nanoparticles by Differential Pulse Voltammetry. *INTERNATIONAL JOURNAL OF ELECTROCHEMICAL SCIENCE* **2013**, 8, (3), 3755-3767.
314. Sanchez-Martinez, M.; Aguilar-Caballos, M.; Gomez-Hens, A., Homogeneous immunoassay for soy protein determination in food samples using gold nanoparticles as labels and light scattering detection. *ANALYTICA CHIMICA ACTA* **2009**, 636, (1), 58-62.

315. Lin, X.; Ni, Y.; Kokot, S., Glassy carbon electrodes modified with gold nanoparticles for the simultaneous determination of three food antioxidants. *ANALYTICA CHIMICA ACTA* **2013**, 765, 54-62.
316. Manso, J.; Mena, M.; Yanez-Sedeno, P.; Pingarron, J., Bienzyme amperometric biosensor using gold nanoparticle-modified electrodes for the determination of inulin in foods. *ANALYTICAL BIOCHEMISTRY* **2008**, 375, (2), 345-353.
317. Yang, J.; Ko, S.; Gunasekaran, S., Colorimetric biosensor based on gold nanoparticles for self-indicating toxin detections in food via competitive binding with toxin analogs. *ABSTRACTS OF PAPERS OF THE AMERICAN CHEMICAL SOCIETY* **2012**, 244.
318. Tang, D.; Tang, J.; Su, B.; Chen, G., Gold nanoparticles-decorated amine-terminated poly(amidoamine) dendrimer for sensitive electrochemical immunoassay of brevetoxins in food samples. *BIOSENSORS & BIOELECTRONICS* **2011**, 26, (5), 2090-2096.
319. Prasad, D.; Shankaracharya; Vidyarthi, A., Gold nanoparticles-based colorimetric assay for rapid detection of Salmonella species in food samples. *WORLD JOURNAL OF MICROBIOLOGY & BIOTECHNOLOGY* **2011**, 27, (9), 2227-2230.
320. Liao, J.; Li, H., Lateral flow immunodipstick for visual detection of aflatoxin B-1 in food using immuno-nanoparticles composed of a silver core and a gold shell. *MICROCHIMICA ACTA* **2010**, 171, (3-4), 289-295.
321. Chen, S.; Wu, V.; Chuang, Y.; Lin, C., Using oligonucleotide-functionalized Au nanoparticles to rapidly detect foodborne pathogens on a piezoelectric biosensor. *JOURNAL OF MICROBIOLOGICAL METHODS* **2008**, 73, (1), 7-17.
322. Cao, M.; Li, Z.; Wang, J.; Ge, W.; Yue, T.; Li, R.; Colvin, V.; Yu, W., Food related applications of magnetic iron oxide nanoparticles: Enzyme immobilization, protein purification, and food analysis. *TRENDS IN FOOD SCIENCE & TECHNOLOGY* **2012**, 27, (1), 47-56.
323. Zhang, J.; Shao, J.; Guo, P.; Huang, Y., A simple and fast Fe₃O₄ magnetic nanoparticles-based dispersion solid phase extraction of Sudan dyes from food and water samples coupled with high-performance liquid chromatography. *ANALYTICAL METHODS* **2013**, 5, (10), 2503-2510.
324. Bagheri, H.; Afkhami, A.; Saber-Tehrani, M.; Khoshshafar, H., Preparation and characterization of magnetic nanocomposite of Schiff base/silica/magnetite as a preconcentration phase for the trace determination of heavy metal ions in water, food and biological samples using atomic absorption spectrometry. *TALANTA* **2012**, 97, 87-95.
325. Lu, F.; Sun, M.; Fan, L.; Qiu, H.; Li, X.; Luo, C., Flow injection chemiluminescence sensor based on core-shell magnetic molecularly imprinted nanoparticles for determination of chrysoidine in food samples. *SENSORS AND ACTUATORS B-CHEMICAL* **2012**, 173, 591-598.
326. Wu, X.; Hu, J.; Zhu, B.; Lu, L.; Huang, X.; Pang, D., Aptamer-targeted magnetic nanospheres as a solid-phase extraction sorbent for determination of ochratoxin A in food samples. *JOURNAL OF CHROMATOGRAPHY A* **2011**, 1218, (41), 7341-7346.
327. Tang, D.; Yu, Y.; Niessner, R.; Miro, M.; Knopp, D., Magnetic bead-based fluorescence immunoassay for aflatoxin B-1 in food using biofunctionalized rhodamine B-doped silica nanoparticles. *ANALYST* **2010**, 135, (10), 2661-2667.
328. Tang, D.; Zhong, Z.; Niessner, R.; Knopp, D., Multifunctional magnetic bead-based electrochemical immunoassay for the detection of aflatoxin B(1) in food. *ANALYST* **2009**, 134, (8), 1554-1560.
329. Tang, D.; Saucedo, J.; Lin, Z.; Ott, S.; Basova, E.; Goryacheva, I.; Biselli, S.; Lin, J.; Niessner, R.; Knopp, D., Magnetic nanogold microspheres-based lateral-flow immunodipstick for rapid detection of aflatoxin B-2 in food. *BIOSENSORS & BIOELECTRONICS* **2009**, 25, (2), 514-518.

330. Ozalp, V.; Bayramoglu, G.; Arica, M.; Oktem, H., Design of a core-shell type immuno-magnetic separation system and multiplex PCR for rapid detection of pathogens from food samples. *APPLIED MICROBIOLOGY AND BIOTECHNOLOGY* **2013**, *97*, (21), 9541-9551.
331. Ravindranath, S.; Mauer, L.; Deb-Roy, C.; Irudayaraj, J., Biofunctionalized Magnetic Nanoparticle Integrated Mid-infrared Pathogen Sensor for Food Matrixes. *ANALYTICAL CHEMISTRY* **2009**, *81*, (8), 2840-2846.
332. Zhao, Y.; Yao, Y.; Xiao, M.; Chen, Y.; Lee, C.; Zhang, L.; Zhang, K.; Yang, S.; Gu, M., Rapid detection of Cronobacter sakazakii in dairy food by biofunctionalized magnetic nanoparticle based on nuclear magnetic resonance. *FOOD CONTROL* **2013**, *34*, (2), 436-443.
333. Pal, S.; Alocilja, E., Electrically active polyaniline coated magnetic (EAPM) nanoparticle as novel transducer in biosensor for detection of Bacillus anthracis spores in food samples. *BIOSENSORS & BIOELECTRONICS* **2009**, *24*, (5), 1437-1444.
334. Wang, Y.; Ravindranath, S.; Irudayaraj, J., Separation and detection of multiple pathogens in a food matrix by magnetic SERS nanoprobe. *ANALYTICAL AND BIOANALYTICAL CHEMISTRY* **2011**, *399*, (3), 1271-1278.
335. Zhou, Z.; Lin, S.; Yue, T.; Lee, T., Adsorption of food dyes from aqueous solution by glutaraldehyde cross-linked magnetic chitosan nanoparticles. *JOURNAL OF FOOD ENGINEERING* **2014**, *126*, 133-141.
336. Aresta, A.; Calvano, C.; Trapani, A.; Cellamare, S.; Zamboni, C.; De Giglio, E., Development and analytical characterization of vitamin(s)-loaded chitosan nanoparticles for potential food packaging applications. *JOURNAL OF NANOPARTICLE RESEARCH* **2013**, *15*, (4).
337. Akbar, A.; Anal, A., Zinc oxide nanoparticles loaded active packaging, a challenge study against Salmonella typhimurium and Staphylococcus aureus in ready-to-eat poultry meat. *FOOD CONTROL* **2014**, *38*, 88-95.
338. Lepot, N.; Van Bael, M.; Van den Rul, H.; D'Haen, J.; Peeters, R.; Franco, D.; Mullens, J., Influence of Incorporation of ZnO Nanoparticles and Biaxial Orientation on Mechanical and Oxygen Barrier Properties of Polypropylene Films for Food Packaging Applications. *JOURNAL OF APPLIED POLYMER SCIENCE* **2011**, *120*, (3), 1616-1623.
339. Tankhiwale, R.; Bajpai, S., Preparation, characterization and antibacterial applications of ZnO-nanoparticles coated polyethylene films for food packaging. *COLLOIDS AND SURFACES B-BIOINTERFACES* **2012**, *90*, 16-20.
340. Espitia, P.; Soares, N.; Coimbra, J.; de Andrade, N.; Cruz, R.; Medeiros, E., Zinc Oxide Nanoparticles: Synthesis, Antimicrobial Activity and Food Packaging Applications. *FOOD AND BIOPROCESS TECHNOLOGY* **2012**, *5*, (5), 1447-1464.
341. Li, X.; Xing, Y.; Jiang, Y.; Ding, Y.; Li, W., Antimicrobial activities of ZnO powder-coated PVC film to inactivate food pathogens. *INTERNATIONAL JOURNAL OF FOOD SCIENCE AND TECHNOLOGY* **2009**, *44*, (11), 2161-2168.
342. Lacatusu, I.; Badea, N.; Murariu, A.; Oprea, O.; Bojin, D.; Meghea, A., Antioxidant Activity of Solid Lipid Nanoparticles Loaded with Umbelliferone. *SOFT MATERIALS* **2013**, *11*, (1), 75-84.
343. Neves, A.; Lucio, M.; Martins, S.; Lima, J.; Reis, S., Novel resveratrol nanodelivery systems based on lipid nanoparticles to enhance its oral bioavailability. *INTERNATIONAL JOURNAL OF NANOMEDICINE* **2013**, *8*, 177-187.
344. Fathi, M.; Varshosaz, J.; Mohebbi, M.; Shahidi, F., Hesperetin-Loaded Solid Lipid Nanoparticles and Nanostructure Lipid Carriers for Food Fortification: Preparation, Characterization, and Modeling. *FOOD AND BIOPROCESS TECHNOLOGY* **2013**, *6*, (6), 1464-1475.

345. Shukat, R.; Relkin, P., Lipid nanoparticles as vitamin matrix carriers in liquid food systems: On the role of high-pressure homogenisation, droplet size and adsorbed materials. *COLLOIDS AND SURFACES B-BIOINTERFACES* **2011**, *86*, (1), 119-124.
346. Weiss, J.; Decker, E.; McClements, D.; Kristbergsson, K.; Helgason, T.; Awad, T., Solid lipid nanoparticles as delivery systems for bioactive food components. *FOOD BIOPHYSICS* **2008**, *3*, (2), 146-154.
347. Xiao, J.; Wu, M.; Kai, G.; Wang, F.; Cao, H.; Yu, X., ZnO-ZnS QDs interfacial heterostructure for drug and food delivery application: enhancement of the binding affinities of flavonoid aglycones to bovine serum albumin. *NANOMEDICINE-NANOTECHNOLOGY BIOLOGY AND MEDICINE* **2011**, *7*, (6), 850-858.
348. Cota-Arriola, O.; Cortez-Rocha, M.; Burgos-Hernandez, A.; Ezquerro-Brauer, J.; Plascencia-Jatomea, M., Controlled release matrices and micro/nanoparticles of chitosan with antimicrobial potential: development of new strategies for microbial control in agriculture. *JOURNAL OF THE SCIENCE OF FOOD AND AGRICULTURE* **2013**, *93*, (7), 1525-1536.
349. Prasad, T.; Sudhakar, P.; Sreenivasulu, Y.; Latha, P.; Munaswamy, V.; Reddy, K.; Sreeprasad, T.; Sajanalal, P.; Pradeep, T., EFFECT OF NANOSCALE ZINC OXIDE PARTICLES ON THE GERMINATION, GROWTH AND YIELD OF PEANUT. *JOURNAL OF PLANT NUTRITION* **2012**, *35*, (6), 905-927.
350. Zhao, L.; Peralta-Videa, J. R.; Rico, C. M.; Hernandez-Viezas, J. A.; Sun, Y.; Niu, G.; Servin, A.; Nunez, J. E.; Duarte-Gardea, M.; Gardea-Torresdey, J. L., CeO₂ and ZnO Nanoparticles Change the Nutritional Qualities of Cucumber (*Cucumis sativus*). *Journal of Agricultural and Food Chemistry* **2014**, *62*, (13), 2752-2759.
351. Dehkourdi, E.; Mosavi, M., Effect of Anatase Nanoparticles (TiO₂) on Parsley Seed Germination (*Petroselinum crispum*) In Vitro. *BIOLOGICAL TRACE ELEMENT RESEARCH* **2013**, *155*, (2), 283-286.
352. Nair, R.; Poulouse, A.; Nagaoka, Y.; Yoshida, Y.; Maekawa, T.; Kumar, D., Uptake of FITC Labeled Silica Nanoparticles and Quantum Dots by Rice Seedlings: Effects on Seed Germination and Their Potential as Biolabels for Plants. *JOURNAL OF FLUORESCENCE* **2011**, *21*, (6), 2057-2068.
353. Chen, H.; Yada, R., Nanotechnologies in agriculture: New tools for sustainable development. *TRENDS IN FOOD SCIENCE & TECHNOLOGY* **2011**, *22*, (11), 585-594.
354. Ghormade, V.; Deshpande, M.; Paknikar, K., Perspectives for nano-biotechnology enabled protection and nutrition of plants. *BIOTECHNOLOGY ADVANCES* **2011**, *29*, (6), 792-803.
355. Kuzma, J., Nanotechnology in animal production-Upstream assessment of applications. *LIVESTOCK SCIENCE* **2010**, *130*, (1-3), 14-24.
356. Fadeel, B.; Feliu, N.; Vogt, C.; Abdelmonem, A. M.; Parak, W. J., Bridge over troubled waters: understanding the synthetic and biological identities of engineered nanomaterials. *Wiley Interdisciplinary Reviews-Nanomedicine And Nanobiotechnology* **2013**, *5*, (2), 111-129.
357. Kirchner, C.; T., L.; Kudera, S.; Pellegrino, T.; Muñoz Javier, A.; Gaub, H. E.; Stölzle, S.; Fertig, N.; Parak, W. J., Cytotoxicity of Colloidal CdSe and CdSe/ZnS Nanoparticles. *Nano Letters* **2005**, *5*, (2), 331-338.
358. Prencipe, G.; Tabakman, S. M.; Welsher, K.; Liu, Z.; Goodwin, A. P.; Zhang, L.; Henry, J.; Dai, H. J., PEG Branched Polymer for Functionalization of Nanomaterials with Ultralong Blood Circulation. *Journal of the American Chemical Society* **2009**, *131*, (13), 4783-4787.
359. Schleh, C.; Semmler-Behnke, M.; Lipka, J.; Wenk, A.; Hirn, S.; Schaeffler, M.; Schmid, G.; Simon, U.; Kreyling, W. G., Size and surface charge of gold nanoparticles determine absorption across intestinal barriers and accumulation in secondary target organs after oral administration. *Nanotoxicology* **2012**, *6*, (1), 36-46.

360. El Badawy, A.; Silva, R.; Morris, B.; Scheckel, K.; Suidan, M.; Tolaymat, T., Surface Charge-Dependent Toxicity of Silver Nanoparticles. *ENVIRONMENTAL SCIENCE & TECHNOLOGY* **2011**, 45, (1), 283-287.
361. Auffan, M.; Rose, J.; Wiesner, M.; Bottero, J., Chemical stability of metallic nanoparticles: A parameter controlling their potential cellular toxicity in vitro. *ENVIRONMENTAL POLLUTION* **2009**, 157, (4), 1127-1133.
362. Levard, C.; Hotze, E.; Lowry, G.; Brown, G., Environmental Transformations of Silver Nanoparticles: Impact on Stability and Toxicity. *ENVIRONMENTAL SCIENCE & TECHNOLOGY* **2012**, 46, (13), 6900-6914.
363. Brust, M.; Walker, M.; Bethell, D.; Schiffrin, D. J.; Whyman, R., Synthesis of Thiol-Derivatized Gold Nanoparticles in a 2-Phase Liquid-Liquid System. *J. Chem. Soc., Chem. Commun.* **1994**, (7), 801-802.
364. Dulkeith, E. Optische Charakterisierung von Hybridsystemen aus Gold Nanopartikeln und Farbstoffmolekülen. Dissertation, Ludwig Maximilians Universität München, 2004.
365. Pellegrino, T.; Manna, L.; Kudera, S.; Liedl, T.; Koktysh, D.; Rogach, A. L.; Keller, S.; Rädler, J.; Natile, G.; Parak, W. J., Hydrophobic Nanocrystals Coated with an Amphiphilic Polymer Shell: A General Route to Water Soluble Nanocrystals. *Nano Letters* **2004**, 4, (4), 703-707.
366. Lin, C.-A. J.; Sperling, R. A.; Li, J. K.; Yang, T.-Y.; Li, P.-Y.; Zanella, M.; Chang, W. H.; Parak, W. J., Design of an Amphiphilic Polymer for Nanoparticle Coating and Functionalization. *Small* **2008**, 4, (3), 334-341.
367. Hyeon, T.; Lee, S. S.; Park, J.; Chung, Y.; Bin Na, H., Synthesis of Highly Crystalline and Monodisperse Maghemite Nanocrystallites without a Size-Selection Process. *J. Am. Chem. Soc.* **2001**, 123, (51), 12798-12801.
368. Di Corato, R.; Bigall, N. C.; Ragusa, A.; Dorfs, D.; Genovese, A.; Marotta, R.; Manna, L.; Pellegrino, T., Multifunctional Nanobeads Based on Quantum Dots and Magnetic Nanoparticles: Synthesis and Cancer Cell Targeting and Sorting. *ACS Nano* **2011**, 5, (2), 1109-1121.
369. Hariri, G.; Wellons, M. S.; Morris, W. H., III; Lukehart, C. M.; Hallahan, D. E., Multifunctional FePt Nanoparticles for Radiation-Guided Targeting and Imaging of Cancer. *Annals Of Biomedical Engineering* **2011**, 39, (3), 946-952.
370. Sanvicens, N.; Marco, M. P., Multifunctional nanoparticles - properties and prospects for their use in human medicine. *Trends In Biotechnology* **2008**, 26, (8), 425-433.
371. Sun, S.; Murray, C. B.; Weller, D.; Folks, L.; Moser, A., Monodisperse FePt Nanoparticles and Ferromagnetic FePt Nanocrystal Superlattices. *Science* **2000**, 287, (March 17), 1989-1992.
372. Shevchenko, E. V.; Talapin, D. V.; Rogach, A. L.; Kornowski, A.; Haase, M.; Weller, H., Colloidal Synthesis and Self-Assembly of CoPt₃ Nanocrystals. *JACS* **2002**, 124, 11480-11485.
373. Reiss, P.; Bleuse, J.; Pron, A., Highly Luminescent CdSe/ZnSe Core/Shell Nanocrystals of Low Size Dispersion. *Nano Letters* **2002**, 2, (7), 781-784.
374. Ho, Y.; Leong, K., Quantum dot-based theranostics. *NANOSCALE* **2010**, 2, (1), 60-68.
375. Liu, L.; Miao, Q.; Liang, G., Quantum Dots as Multifunctional Materials for Tumor Imaging and Therapy. *MATERIALS* **2013**, 6, (2), 483-499.
376. Pacholski, C.; Kornowski, A.; Weller, H., Self-assembly of ZnO: From nanodots, to nanorods. *ANGEWANDTE CHEMIE-INTERNATIONAL EDITION* **2002**, 41, (7), 1188-+.
377. McCormick, L.; Slater, G.; Karger, A.; Vreeland, W.; Barron, A.; Desruisseaux, C.; Drouin, G., Capillary electrophoretic separation of uncharged polymers using polyelectrolyte engines - Theoretical model. *Journal of Chromatography A* **2001**, 924, (1-2), 43-52.
378. Soenen, S. J.; Manshian, B.; Montenegro, J. M.; Amin, F.; Meermann, B.; Thiron, T.; Cornelissen, M.; Vanhaecke, F.; Shareen, D.; Parak, W. J.; De Smedt, S.; Braeckmans, K.,

- Cytotoxic Effects of Gold Nanoparticles: A Multiparametric Study. *ACS Nano* **2012**, 6, (7), 5767-5783.
379. Soenen, S. J.; Manshian, B. B.; Abdelmonem, A. M.; Montenegro, J.-M.; Tan, S.; Balcaen, L.; Frank Vanhaecke; Brisson, A. R.; Parak, W. J.; Smedt, S. C. D.; Braeckmans, K., The Cellular Interactions of PEGylated Gold Nanoparticles: Effect of PEGylation on Cellular Uptake and Cytotoxicity. *Part. Part. Syst. Charact.* **2014**, doi: 10.1002/ppsc.201300357.
380. Soenen, S.; Montenegro, J.; Abdelmonem, A.; Manshian, B.; Doak, S.; Parak, W.; De Smedt, S.; Braeckmans, K., The effect of nanoparticle degradation on poly(methacrylic acid)-coated quantum dot toxicity: The importance of particle functionality assessment in toxicology. *ACTA BIOMATERIALIA* **2014**, 10, (2), 732-741.

Appendix

Wissenschaftlicher Werdegang

Persönliche Angaben

Name: Abuelmagd

Geburtsdatum: 26.05.1978

Staatsangehörigkeit: Ägypter

Vorname: Abuelmagd

Geburtsort: Qena/Ägypten

Ausbildung

- ◆ Januar 2011 – Oktober 2014 Doktorarbeit, AG, Biophotonik (Prof. W. J. Parak), Fachbereich Physik, Philipps-Universität Marburg

Thema: **Nanoparticles: Synthesis, Surface Modification and Functionalization for Biological and Environmental Applications“**

Betreuer: **Prof. Dr. Wolfgang J. Parak**

- ◆ Aug 2010- Jan 2011: Exchange Ph.D. Student at the group of Photodynamic Therapy and Cellular Biophysics with Prof. Barbara. Krammer , Salzburg, Universität Salzburg –Salzburg- Austria
- ◆ Sept 2009- August 2010 : *Ph.D. Student at the Dept of Laser Applications in Photochemistry and Photobiology, National Institute of Laser Enhanced Sciences (NILES), Cairo University, Giza, Egypt*
Title of Ph. D Thesis "Au-Fe Core Shell Nanomaterials: Synthesis, Characterization and In vivo Photobiological Studies"
- ◆ Sept 2008- June 2009 : *Pre-Doctorate Student at the Dept of Laser Applications in Photochemistry and Photobiology, National Institute of Laser Enhanced Sciences (NILES), Cairo University, Giza, Egypt*
- ◆ May 2005- May 2008: *M.Sc. at Dept of Biochemistry, Fac. Agric., Cairo University, Giza, Egypt,*
Thema: **“Biochemical Studies On Kenaf Oil”**
- ◆ Sept 2004- May 2005: *Pre-Master Student at Biochemistry Dept, Fac. Agric., Cairo University, Giza, Egypt.*
- ◆ Jun 2007- May 2010: *Research Assistant at the Dept of Special Food and Nutrition Researches, Food Technology Research Institute – Giza – Egypt.*
- ◆ Oct 2003- Jun 2007: *Specialist at the Dept of Special Food and Nutrition Researches, Food Technology Research Institute – Giza – Egypt.*
- ◆ Jan 2003- May 2003: *Research Assistant and M.Sc. student at Food Science and Technology Dept. Assiut University, Assiut – Egypt.*
- ◆ Sept 1997- June 2001 *B.Sc. at Food and Science Technology Department, Fac. Agric., Assiut University, Egypt, May 2001*

Wissenschaftliche Veröffentlichungen

1. Kreyling, W.; Abdelmonem, A. M.; Ali, Z.; Haberl, N.; Hartmann, R.; Hirn, S.; de Aberasturi, J. D.; Khadem-Saba1, G.; Montenegro, J.; Rejman, J.; Rojo, T.; de Larramendi I.; Wenk1, A.; Parak, W. J., In vivo integrity of colloidal nanoparticles. *NATURE NANOTECHNOLOGY*. (In Revision).
2. Abdelmonem, A. M.; Amin, R. M., Rapid Green Synthesis of Metal Nanoparticles Using Pomegranate Polyphenols. *International Journal of Sciences: Basic and Applied Research* 2014, 15, (1), 57-65.
3. Amin, R. M.; Abdelmonem, A. M.; Verwanger, T.; Elsherbini, E.; Krammer, B., Cytotoxicity of Magnetic Nanoparticles on Normal and Malignant Human Skin Cells. *Nano Life* 2014, 4, (1), 1440002 (8 pages).
4. Mahmoudi, M.; Abdelmonem, A. M.; Behzadi, S.; Clement, J.; Dutz, S.; Ejtehadi, M.; Hartmann, R.; Kantner, K.; Linne, U.; Maffre, P.; Metzler, S.; Moghadam, M.; Pfeiffer, C.; Rezaei, M.; Ruiz-Lozano, P.; Serpooshan, V.; Shokrgozar, M.; Nienhaus, G.; Parak, W., Temperature: The "Ignored" Factor at the NanoBio Interface. *ACS NANO*. 2013, 7, (8), 6555-6562.
5. Soenen, S. J.; Manshian, B. B.; Abdelmonem, A. M.; Montenegro, J.-M.; Tan, S.; Balcaen, L.; Frank Vanhaecke; Brisson, A. R.; Parak, W. J.; Smedt, S. C. D.; Braeckmans, K., The Cellular Interactions of PEGylated Gold Nanoparticles: Effect of PEGylation on Cellular Uptake and Cytotoxicity. *Part. Part. Syst. Charact.* 2014, doi: 10.1002/ppsc.201300357.
6. Soenen, S.; Montenegro, J.; Abdelmonem, A. M.; Manshian, B.; Doak, S.; Parak, W.; De Smedt, S.; Braeckmans, K., The effect of nanoparticle degradation on poly(methacrylic acid)-coated quantum dot toxicity: The importance of particle functionality assessment in toxicology. *ACTA BIOMATERIALIA* 2014, 10, (2), 732-741.
7. Riedel, M.; Göbel, G.; Abdelmonem, A. M.; Parak, W. J.; Lisdat, F., Photoelectrochemical Sensor based on Quantum Dots and Sarcosine Oxidase. *ChemPhysChem* 2013, 14, 2338-2342.
8. Carregal-Romero, S.; Caballero-Diaz, E.; Beqa, L.; Abdelmonem, A. M.; Ochs, M.; Hühn, D.; Suau, B. S.; Valcarcel, M.; Parak, W. J., Multiplexed Sensing and Imaging with Colloidal Nano- and Microparticles. *Annual Review of Analytical Chemistry* 2013, 6, 53-81.
9. M. Abdelmonem, S. S. Paradinas, D. Sasse, N. C. Bigall, W. J. Parak. (2013). Methotrexate-modified Iron Oxide Nanoparticles; Multifunctional Nano-theragnostic for MRI and Drug Delivery. Bioimaging, sensing, and therapeutic applications of nanomaterials 3th -6th March 2013, Villars-sur-Ollon, Switzerland. (Poster).
10. Fadeel, B.; Feliu, N.; Vogt, C.; Abdelmonem, A. M.; Parak, W. J., Bridge over troubled waters: understanding the synthetic and biological identities of engineered nanomaterials. *Wiley Interdisciplinary Reviews-Nanomedicine And Nanobiotechnology* 2013, 5, (2), 111-129.
11. S. S. Paradinas, A. M. Abdelmonem, D. Sasse, N. C. Bigall, W. J. Parak. (2012). Methotrexate-PEG Modified Superparamagnetic Nanoparticles for MRI and Drug Delivery. The Fifth International Conference NANAX 5 of Nanoscience and Nanocrystals, 7th - 11th May 2012, Fuengirola, Spain. (Poster).
12. M. Abdelmonem, Z. Ali, J. M. Montenegro, N. C. Bigall, & W. Parak. (2012). Multifunctional Radioactive ¹¹¹In Decorated Radioactive Au-198 Nanoparticles.

The Fifth International Conference NANAX 5 of Nanoscience and Nanocrystals, 7th – 11th May 2012, Fuengirola, Spain. (*Poster*).

13. M. Abdelmonem. (2008). *Biochemical Studies on Kenaf Oil*. MSc. Thesis, Biochemistry Dept, Cairo University.
14. M. Abdelmonem. (2007). Physico-Chemical Properties of Kenaf (*Hibiscus Cannabinus L.*) Seed Oil. Research Bulletin, Ain Shams University

In vivo integrity of colloidal nanoparticles

Wolfgang Kreyling^{1*}, Abuelmagd M. Abdelmonem^{2†}, Zulqurnain Ali^{2,3}, Nadine Haberl^{1,4}, Raimo Hartmann², Stephanie Hirn^{1,4}, Dorleta Jimenez de Aberasturi^{2,5}, Gülnaz Khadem-Saba^{1,6}, Jose-Maria Montenegro^{2,7}, Joana Rejman², Teofilo Rojo⁴, Idoia Ruiz de Larramendi⁴, Alexander Wenk¹, Wolfgang J. Parak^{2*}

¹ Institute of Lung Biology and Disease and Institute of Epidemiology 2, Helmholtz Zentrum München – German Research for Center for Environmental Health, 85764 Neuherberg / Munich, Germany

² Fachbereich Physik, Philipps Universität Marburg, Marburg, Germany

³ present address: Department of Physics, Air University, Sector E-9, 44000 Islamabad, Pakistan

⁴ present address: Walter Brendel Centre of Experimental Medicine, Ludwig-Maximilians-University, 81377 Munich, Germany

⁵ Department of Inorganic Chemistry, UPV/EHU, Bilbao, Spain

⁶ present address: Department of Chemistry, Industrial Biocatalysis, Technische Universität München (TUM), 85748 Garching, Germany

⁷ present address: Central Research Services, University of Malaga, 29071 Málaga, Spain.

† authors listed in alphabetic order

* corresponding authors: kreyling@helmholtz-muenchen.de, wolfgang.parak@physik.uni-marburg.de

Abstract

Colloidal nanoparticles composed out of a 4 nm monodisperse, radioactively labelled gold core (^{198}Au) and a radioactively labelled polymer shell (^{111}In) were administered *via* intravenous injection to rats. These nanoparticles have excellent colloidal stability *in vitro*. Independent biodistribution data obtained from the ^{198}Au and ^{111}In labels indicate that *in vivo* the polymer shell comes at least partially off the nanoparticle core. This demonstrates that even high quality nanoparticles with well defined colloidal properties *in vitro*, can radically change their physico-chemical properties in *in vivo* scenarios. Additional “in test tube” and *in vitro* data suggest that degradation of the polymer shell may be caused by proteolytic enzymes. Thus physicochemical characterization as performed of the nanoparticles in media outside cells has to be considered to apply only partly for internalized nanoparticles.

Keywords

in vivo biokinetics, intravenous injection, colloidal nanoparticles, radioactive detection, enzymatic degradation

Introduction

The interaction of colloidal nanoparticles (NPs) with living organisms is of utmost importance. Currently many clinical applications of NPs are envisaged, and for such intended use their properties and mechanisms of interaction need to be well understood. Naturally, in addition to those opportunities NPs offer, their potential risks need to be considered as well. Besides exposure scenarios based on intended use of NPs on humans for medical applications, also unintended exposure due to environmental contamination has to be taken into account. Here, in order to predict risks in a quantitative way, data about the interaction of NPs with organisms are highly needed. Preferentially mechanisms of interaction could be correlated with the physico-chemical properties of the NPs, which would facilitate theoretical extrapolation to new classes of NP materials¹⁻³. However, even in *in vitro* experiments the interaction of NPs with cells can not be correlated to their physico-chemical properties in a straight-forward way. We know that the hydrodynamic diameter^{4,5}, the charge⁶⁻⁸, the shape⁹⁻¹¹, the colloidal stability, the inertness¹²⁻¹⁴, and the protein corona¹⁵⁻¹⁷ of NPs can have profound effect on their interaction with cells. However, unfortunately most of these parameters are entangled and their effects are hard to pinpoint separately¹⁸. Nevertheless, on an *in vitro* level NPs interaction with cells has been investigated with a set of established techniques, which has led to a large base of knowledge. It is for example well known that for many NPs colloidal properties may change upon their internalization by cells^{19,20}. This involves the decrease of pH in endo/-lysosomal compartments²¹. Reduced pH can trigger agglomeration of NPs, which are often stabilized by negatively charged groups (such as -COO⁻) having pK_a values higher than the pH in the intracellular compartment in which the NPs are typically located after incorporation, thus leading to loss of charge and in consequence agglomeration²². Reduced pH also can enhance corrosion of NPs²³ and in this way result in release of toxic ions, as it is for example the case for CdSe or Ag NPs^{13, 24-26}. Uptake even may result in a phase separation of different compartments within one NP²⁷. Besides changing the NP core properties, uptake by cells can also lead to a removal of their surface capping as well *in vitro*^{20, 28, 29} as *in vivo*^{30, 31}. NP internalization also involves the presence of intracellular enzymes, which may degrade the protein corona adsorbed to the NP surface, or even may modify the surface chemistry of the NPs^{19, 29, 32}. As already mentioned, these conclusions could be drawn as the fate of NPs and their properties during their life cycle can be observed *in vitro* in model environments by a set of sophisticated optical techniques. Fluorescence correlation spectroscopy (FCS)³³ is an example in this direction, which allows for

determining hydrodynamic radii on a single NP basis. Another important technique is confocal microscopy, which allows for tracing of different (fluorescently labelled) parts of NPs inside cells^{7, 20}. However, unfortunately these techniques are relatively hard to apply *in vivo*. While recording of biodistributions of NPs is widely reported in literature³⁴⁻⁴¹, and has been reviewed recently⁴², these data do not give direct insight in the physico-chemical properties of the NPs *in vivo*. Though tricks and experimental models exist which allow for accessing NPs directly *in vivo*^{43, 44}, the investigation about the *in vivo* fate of the physico-chemical properties of NPs remains an experimental challenge. Thus, biodistribution can be only correlated to the physico-chemical properties of the NPs before NPs administration, but not to the actual *in vivo* physico-chemical properties. Most important hereby is the question about the integrity of the NPs themselves. Obviously NPs with poor *in vitro* properties (*i.e.* in particular under presence of salt and proteins), such as low colloidal stability or degradation by release of ions / ligands from their surface, will perform even worse *in vivo*. But what happens to NPs which are well characterized and have been reported to be stable *in vitro*? In order to trace the fate of the different NPs compounds, involving an inorganic core, the organic surface capping, and the adsorbed protein corona each of the compounds of the NPs needed to be tagged individually with a label allowing for *in vivo* detection. In this work we have individually labelled the core and the shell of monodisperse Au NPs with radioisotopes⁴⁵ and followed their respective *in vivo* biodistribution. Equal biokinetics of both radiolabels would indicate *in vivo* integrity of the NPs, while different biodistribution of core and shell would indicate (partial) *in vivo* degradation of the NPs.

Materials and Methods

NPs preparation and characterization: In this study we decided to individually label inorganic cores and their organic surface capping with radionuclides. Radioactive labelling with γ -emitters are very well suited for quantitatively recording *in vivo* biodistributions of NPs^{42, 46}. Gamma-radiation is barely absorbed by tissue, it is not changed by conditions in different compartments of an organism (fluorescence can be for example quenched depending on the local pH), and by using radioisotope emitters at different energies multiple labels can be observed. As NP material we used Au, as these NPs can be conveniently made radioactive by neutron irradiation as described earlier³⁴. Neutron activated Au cores contain the isotope ¹⁹⁸Au, which emits γ -radiation at 315 keV and 412 keV. There are no naked NPs in biological environments and in

order to stabilize them an organic coating (either artificial or natural by proteins) is required¹⁸. We chose a polymer-coating procedure for providing colloidal stability to the Au NPs⁴⁷. The entire system (small Au cores of core diameter $d_c = 4 \pm 2$ nm with polymer coating leading to a hydrodynamic diameter of $d_c = 13 \pm 1$ nm, cf. the Results section) was chosen on purpose, as these NPs have been characterized in detail in the last decade⁴⁷. It has to be pointed out however, that these NPs are smaller than 30 nm core Au NPs which are frequently proposed for therapeutic applications (e.g. AurimuneTM⁴⁸⁻⁵⁰ and AuroshellTM^{51, 52}) and thus will result in a different biodistribution⁵³. As coating we chose a previously established polymer-coating procedure⁴⁷ as this coating can be used for NPs with cores of most materials and thus is very universal, and has been characterized in detail *in vitro* concerning physicochemical properties (in particular concerning colloidal stability^{8, 54}), NP incorporation⁸, and cytotoxic properties⁵⁵⁻⁵⁷. It is also compatible with basic *in vivo* requirements³⁵. Most important, the polymer shell can be easily individually labelled. By introduction of 1,4,7,10-tetraazacyclododecane-1,4,7,10-tetraacetic acid (DOTA) as chelator specific for indium, the radioisotope ¹¹¹In was integrated into the polymer shell⁴⁵. Carrier-free ¹¹¹In was purchased from Perkin & Elmer. ¹¹¹In emits γ -radiation at 171 keV and 245 keV and thus can be in principle independently recorded from ¹⁹⁸Au at higher γ -energies of 315 keV and 412 keV after correction of the Compton irradiation of ¹⁹⁸Au in the ¹¹¹In photopeak. The geometry of these NPs is shown in Figure 1. Gamma-emission spectra were in agreement with our previous study⁴⁵. Purification of the NPs from unbound ¹¹¹In ions was achieved by extensive washing steps with size exclusion columns⁴⁵, yielding to a NPs solution in which virtually no free ¹¹¹In or ¹⁹⁸Au (which might have been removed from the Au core) existed. Based on the reaction protocol and stringent purification we assume strong linkage of DOTA as the chelator for ¹¹¹In to the polymer shell around the ¹⁹⁸Au NPs. Linkage however also partly may involve electrostatic binding of the positively charged ¹¹¹In ions to the negatively charged polymer shell (see the Supporting Information for a detailed experimental assessment). In addition to polymer coated Au NPs with radioactive double label (¹⁹⁸Au and ¹¹¹In label in the Au core and the polymer shell with incorporated DOTA, respectively) we also used polymer coated quantum dots (CdSe/ZnS QDs) with double fluorescence label, which were synthesized according to previous reports⁴⁵. The intrinsic fluorescence of the inorganic QDs (@ 605 nm) hereby was the label for core of the NPs. The fluorophore DY495 was covalently attached to the polymer shell and thus formed the shell label.

Animals: Healthy, female Wistar-Kyoto rats (WKY/Kyo@Rj rats, Janvier, Le Genest Saint Isle, France), 8–10 weeks of age (approximately 250 g body weight) were housed in pairs in humidity and temperature-controlled ventilated cages on a 12 h day/night cycle. Rodent diet and water were provided *ad libitum*. All experiments were conducted under German federal guidelines for the use and care of laboratory animals and were approved by the Regierung von Oberbayern (Government of District of Upper Bavaria, Approval No. 55.2-1-54-2531-26-10) and by the Institutional Animal Care and Use Committee of the Helmholtz Center Munich.

NPs administration and animal maintenance in metabolic cages: The entire administration has been already described previously³⁴⁻³⁷. Briefly, the rats were anesthetized by inhalation of 5 % isoflurane until muscular tonus relaxed. NPs suspensions (50 to 70 μL containing 1-10 μg of double-labelled gold NPs) were administered to the animals *via* intravenous injection into the tail vein of the animal. After administration of the NPs suspensions, rats were kept individually in metabolic cages for separate collection of total urine and feces.

Sample preparation and radio analysis: One hour or 24 hours post exposure, rats were anesthetized (5 % isoflurane inhalation) and euthanized by exsanguination *via* the abdominal aorta. Approximately 70 % of the total blood volume was withdrawn. Radio analysis was performed on at least four rats for each time point according to the previous description³⁴⁻³⁷. Briefly, total organs, tissues, body fluids, the remaining carcass, and total excretion were sampled and γ -spectrometrically analysed as previously described³⁴⁻³⁷. The ^{198}Au or ^{111}In radioactivities of all samples were measured without any further physico-chemical preparation of the samples by gamma-spectroscopy. Small organ and tissue samples were analyzed in a lead-shielded, 10 mL well type NaI(Tl) scintillation detector while a lead-shielded, 1 L well type NaI(Tl) scintillation detector was used for large samples like the remaining carcass. The Compton correction was carried out using the gamma acquisition analysis software Genie 2000 (Canberra Industries, Rüsselsheim, Germany). The count rates were adjusted for physical decay and background radiation. Additionally, the ^{198}Au or ^{111}In count rates were calibrated to either a ^{198}Au or ^{111}In reference source at a reference date in order to correlate ^{198}Au and ^{111}In radioactivities to the numbers and masses of the Au NPs. Samples yielding net counts (*i.e.* background-corrected counts) in the photo-peak region-of-interest of the ^{198}Au gamma spectrum were defined to be below the detection limit when they were less than three standard deviations of the background

counts of this region-of-interest. While dissecting, no organs were cut and all fluids were cannulated when necessary in order to avoid any cross contamination. By this approach we quantitatively determined the entire ^{198}Au and ^{111}In dose independently from each other in the entire animal by analysing for each radio-isotope each organ and tissue and total excretion. Thus, for each radio-isotope a 100 % balance of the biodistribution was performed.

Blood correction: Blood contents of organs and the remaining body were calculated according to the findings of Oeff *et al.*⁵⁸ as described previously³⁴⁻³⁷.

Calculations and statistical analysis: All calculated data are given as a percentage of the relevant integral radioactivity of all samples in each animal with the standard error of the mean (SEM).

Accompanying “in test tube” and in vitro experiments with QDs: In order to support the *in vivo* observations as obtained with polymer-coated Au NPs with double radionucleotide labelling additional “in test tube” and *in vitro* experiments were performed with polymer-coated QDs with double fluorescence labelling (one colour for the inorganic NP core, one colour for the organic polymer shell) which had similar geometry, surface chemistry, and colloidal properties. “In test tube” polymer coated QDs were incubated with different proteolytic enzymes and resulting fragments of the DY495-labelled polymer shell / released DY495 were separated from the NPs by filtration. The amount of released fluorescence label by enzymatic degradation from the polymer coating was quantified with fluorescence spectroscopy. For *in vitro* experiments Huvec and Kupffer cells (which are relevant for NPs incorporated in the liver) were exposed to polymer coated QDs labelled with different fluorophore labels in their polymer shell. Colocalization experiments between the QD core and the polymer shell label were performed. The fluorescence spectra of exocytosed QDs and QDs found in cell lysate were compared (for details see the Supporting Information).

Results

Characteristics of the double radio-labelled Au NPs using ^{198}Au and ^{111}In : The prepared Au NPs had a core diameter of $d_c = 4 \pm 2 \text{ nm}$ (as determined by transmission electron microscopy, TEM), a hydrodynamic diameter of $d_h = 13 \pm 1 \text{ nm}$ (as determined by dynamic light scattering, DLS),

and a zeta-potential of -46 ± 16 mV (as determined *via* Laser Doppler Velocimetry, LDV, *cf.* the Supporting Information for more details). The QDs had a core diameter of $d_c = 3 \pm 1$ nm (as determined by TEM) and a ζ -potential of 28 ± 4 mV (as determined by LDV). Due to the intrinsic fluorescence of the QDs we were unable to measure their hydrodynamic diameter with DLS. However, as Au NPs and QDs had a similar core size and also a similar polymer was used for coating, leading to highly negatively charged NPs, in accordance with previous studies⁵⁹ we assume similar colloidal properties.

In vivo biodistribution of core (¹⁹⁸Au) and shell (¹¹¹In): Note, if both radio-labels are firmly attached to the gold NPs the biodistribution is expected to be identical at any retention time. In Figure 2 the quantitatively balanced biodistribution (*i.e.* the sum of all ¹⁹⁸Au radioactivities and of all ¹¹¹In radioactivities as detected in all organs is 100%, respectively) of the NP core radio-label ¹⁹⁸Au and the NP shell radio-label ¹¹¹In are shown 1 h and 24 h after intravenous (*i.v.*) injection on a logarithmic scale (the same data as plotted on a linear scale are shown in the Supporting Information). One hour after *i.v.* injection liver retention is dominant by far followed by the spleen for both radio-isotopes. Also the retention in the remaining carcass consisting of soft tissues, skin and skeleton is almost 10% for both radioactivities. There is a striking difference between both radio-isotopes with much more ¹¹¹In in blood and urine than ¹⁹⁸Au. There are only very slight differences in the ¹⁹⁸Au patterns as observed after 1-hour *versus* 24-hours, in agreement with previous studies³⁵. In contrast, there are considerable variations in kidneys, blood, remainder, and in fecal and urinary excretion of the ¹¹¹In label of the shell. Concerning the stability of the radioactive labels the ¹⁹⁸Au within the stable ¹⁹⁷Au matrix as a result of the neutron-activation of the original gold NPs has been shown to dissolve negligibly out of the gold NPs cores and, thus, the gold NPs are virtually insoluble⁶⁰. Therefore the ¹⁹⁸Au label indicates the biokinetics of the gold NPs which does not change much between 1 and 24 hours. However, in order to analyse the data more rigorously by calculating the ¹¹¹In to ¹⁹⁸Au ratio for each organ and tissue and each time point, major differences between the retention of the two radio-isotopes become evident. This is shown in Figure 2e (one hour) and Figure 2f (24 hours). After one hour the isotope ratios of the organs deviate between 0.5 and 1.8 from unity (*cf.* the table corresponding to the data of Figure 2 in the Supporting Information). However, the ¹¹¹In retention in blood and urine is two orders of magnitude higher than the ¹⁹⁸Au content. Similarly, the ¹¹¹In retention in the gastro-intestinal-tract and feces is ten-fold higher than the ¹⁹⁸Au retention and

excretion. After 24 hours the ratios in liver and spleen – those organs which retain most of both radio-isotopes – remain virtually unchanged. Yet, remarkable changes of the ^{111}In to ^{198}Au ratio are observed elsewhere with a large increase in the kidneys from 1.6 to 5.6 and a two-fold increase in the remainder from one to 24 hours. In contrast, the ^{111}In to ^{198}Au ratio decreases massively a ten-fold in blood and it increases four-fold in GIT and feces. These changes are mainly caused by changes of the ^{111}In retention, while the ^{198}Au retention remained rather unchanged between 1 and 24 hours. This differential behaviour indicates dissociation and removal of the ^{111}In label from the shell of the initial NP. The stability of the ^{111}In label (concerning its location in regard to the Au NPs) is more complicated to discuss. We had already performed auxiliary biokinetics studies in C57 BL6 mice using a soluble form of the ^{111}In radio-isotope (as free ion) and of a complex of ^{111}In with the chelator diethylene triamine pentaacetic acid (DTPA) in order to distinguish the biodistribution of the soluble form (^{111}In ions) from the chelated form (^{111}In -DTPA) and from the particulate form (polymer coated Au NPs with ^{111}In in the polymer shell) using the same quantitative approach (cf. Figure 3 and the Supporting Information). The biodistribution of the ^{111}In ions is remarkably different to the one of chelated ^{111}In (cf. Figure 3). While ^{111}In ions are barely excreted in urine, the chelated form of ^{111}In is in particular excreted in the urine at both time points. The 24 hours biodistribution of the ^{111}In ions appears to be similar in most organs and in the remainder compared to the biodistribution of the initially administered particulate form, but it differs in blood and excreta when comparing Figure 2d with Figure 3. The biodistribution of the particulate form thus resembles more the one of the chelated form, in particular, when concerning excretion in urine. Admittedly the biodistribution data obtained from mice cannot be compared directly to the rat data due to possible species differences. Yet they are suitable to serve as trend indicators in case there are major similarities or major differences between the soluble ionic ^{111}In in mice and the ^{111}In in rats, which may or may not have left within the shell of the double labelled Au NPs. Clearly the soluble ^{111}In ions are also retained predominantly in the liver, spleen, lungs, and the remaining carcass, like the ^{111}In of the shell label of core-shell Au NPs does. Hence, these data are an additional indicator for a NP-free retention of the ^{111}In label supporting our above noted conclusions based on the comparison of Figure 2a versus Figure 2c after 1 h and Figure 2b versus Figure 2d after 24 h, that part of the ^{111}In label had come off the Au NPs. Interestingly, the differences in Figures 2d and 3 for blood and urine indicate that not the ^{111}In ion may have come off the gold NP but parts or the entire polymer shell may have been removed from the NP in the complex biological system of

the rat body. This is supported by the differing data obtained from GIT-feces which represent the hepato-biliary clearance (HBC) of ^{111}In from the liver *via* the bile into the lower intestine ³⁶. The HBC of the Au NPs is lower (Figure 2b), but the HBC of ^{111}In shells is 25-fold higher (Figure 2d). The HBC of free ^{111}In ions is in-between (Figure 3). In particular, the data of the initially administered particulate form of ^{111}In are similar with the chelated form of ^{111}In , which is another indication that not the ^{111}In itself may have come off the NPs, but parts of the polymer shell with the chelated ^{111}In . While our biodistribution analysis employing radioactive labels allows us to conclude which percentage of the labelled parts of the NPs (the ^{198}Au -labelled core and the ^{111}In -labelled (fragmented) polymer shell) is found in the respective organs, our data do not provide information about the distribution within the organs, *i.e.* in which cells NPs have been incorporated. As we anticipated to administer a very low NP dose in order to prevent any toxic effect eventually caused by a high mass dose of Au NPs, the number of NPs is so low that they are significantly (in terms of absolute mass) only found in the prominent organs of accumulation (in particular the liver), *cf.* Figure 2, which also is in line with our previous publication ³⁶. In principle histological studies on each of the investigated organs (by using for example silver staining ⁶¹) would allow for determining the NP distribution within each organ. In the present study such analysis was not performed, assuming that the NP distribution within the different organs will be similar to the one of other NPs, which have been investigated. In a previous study it has been found for example, that within the liver (which as mentioned is the organ of main interest) Au NPs with $d_c = 18$ nm were prominently found in Kupffer cells, but also in hepatocytes and in endothelial cells ³⁶.

Enzymatic degradation of the polymer shell: The data shown in Figure 5a demonstrate that after incubation of the QDs with different proteolytic enzymes such as those found in serum, - trypsin, pronase, proteinase 3, and cathepsin G - part of the DY495 label is removed from the QDs, be it in its free form, or bound to released polymer molecules. Presence of proteolytic enzymes thus degrades the polymer shell "in test tube".

In vitro degradation of the polymer shell: Huvec and Kupffer cells were incubated with QDs. Colocalization analysis of the fluorescence originating from the QD core and the fluorescence originating from the fluorescence label of the polymer shell indicate that after several hours the polymer shell label is partly displaced from the QD label, which is in agreement with findings of

others²⁰. In the medium the fluorescence of exocytosed QDs has a lower fraction of QD fluorescence compared to DY495 fluorescence, as it is found for QDs inside cells which have been analysed after cell lysis. Also these data indicate that the DY495-labelled polymer shell and / or the DY495 label partly come off the QDs and are preferentially exocytosed, *cf.* Figure 5b.

Discussion

Remarks on the stability of ¹⁹⁸Au within the core of the Au NPs: The isotope ratio of ¹⁹⁸Au to stable ¹⁹⁷Au is $6.6 \cdot 10^{-6}$ for the ~4 nm sized monodisperse Au cores used. Note that this ratio is extremely low, so that statistically only one ¹⁹⁸Au isotope can be found in one Au NP and only one out of 50 Au NPs contains one radioactive ¹⁹⁸Au atom at all. In addition, when calculating the number of Au atoms on the surface of the ~4 nm Au NPs over the total number of Au atoms contained in one Au NP this ratio is 0.3. Since the neutron irradiation process in the nuclear reactor leads to an isotropic and statistically determined nuclear conversion reaction of stable ¹⁹⁷Au into radioactive ¹⁹⁸Au, about one third of the radio-labelled atoms are on the surface and two thirds are distributed within the cores of the Au NPs. Even the fraction on the Au NPs surface is still mainly bound tightly within the matrix of the Au NPs lattice. Hence, release of Au atoms from the Au NPs surface at best will be rather small. Since ¹⁹⁸Au ions released from Au NPs would have been excreted predominantly *via* urine the observed ¹⁹⁸Au percentage in urine of 0.02% indicates a much lower leaching than the ¹⁹⁸Au surface fraction. This was confirmed in a recent publication⁶⁰, in which we compared the biokinetics of dissolved Au ions versus Au NPs and found that the entire biokinetics patterns is very distinct between the two forms supporting the notion, that dissolution or dissociation of the ¹⁹⁸Au label is negligible. The observed urinary NPs excretion is consistent with our previous data of 5 nm Au NPs coated with triphenylphosphine^{35,36}. In addition, this fraction of Au atoms being eventually detachable was washed away during the thorough washing procedures after first the neutron irradiation and multiple times after the Au NPs surface coating by the polymer molecules and the additional labelling with radioactive ¹¹¹In ions. Hence, virtually the entire ¹⁹⁸Au radio-labels are firmly bound to the Au NPs which were finally administered to the animals.

Remarks on the stability of ¹¹¹In within the shell of the Au NPs: ¹¹¹In is specifically chelated by ABz-DOTA (S-2-(4-Aminobenzyl)-modified DOTA, whereby the amino group is used for linkage of the chelator to the polymer shell), which itself is covalently attached to the polymer

shell. However, positively charged ^{111}In can also electrostatically adsorb to the negatively charged polymer surface of the Au NPs. X-ray photoelectron spectroscopy (XPS) data reveal that Au NPs bearing ABz-DOTA in their shell bind at least twice more ^{111}In than Au NPs without ABz-DOTA (*cf.* the Supporting Information). Inductively coupled plasma mass spectrometry (ICP-MS) data of our previous study suggest an even higher increase in attachment upon presence of ABz-DOTA ⁴⁵. Thus we assume that at least 50% of ^{111}In is chelated by ABz-DOTA. ABz-DOTA is linked *via* amide-bond formation to the polymer shell. ^1H NMR data clearly show presence of ABz-DOTA in the polymer shell, but however do not **prove** covalent character of bonding. However, XPS data suggest a higher amount of amide-bonds in the polymer shell after attachment of ABz-DOTA, which would be in line with the assumption of covalent linkage (*cf.* the Supporting Information). Though our data do not permit a final proof of covalent attachment of ABz-DOTA, the used reaction scheme for conjugation, stringent purification protocols which would have removed adsorbed ABz-DOTA, and XPS data suggest at least a high fraction of covalent attachment.

Results indicate that the biodistribution of ^{111}In and ^{198}Au are not the same: The two patterns of biokinetics clearly indicate different biokinetic fates of the two radio-labels, ***cf.* Figure 2**. Since the ^{198}Au label is firmly bound to the core of the stable ^{197}Au NPs it is an indicator of the biokinetics of the Au NPs themselves. Hence, the ^{111}In label had come off the NP surface. Furthermore, the auxiliary studies on the 24 h biodistribution of the pure, soluble, ^{111}In ions intravenously injected **in C57 Bl6 mice** is rather similar to the pattern of the ^{111}In in the predominant sites of retention – liver, spleen, lungs and the remaining carcass - which originally was bound to the polymer on the surface of the Au NPs. **While biodistribution of pure, soluble, ^{111}In ions and chelated ^{111}In in mice will not be identical to the corresponding biodistribution in rats, the data still show a trend, in particular pointing out that free and chelated ^{111}In have a completely different biodistribution, *cf.* Figure 3. Whereas the Au NPs (^{198}Au label), and the ionic form of ^{111}In were barely excreted in urine, chelated ^{111}In and the particulate form of In (^{111}In label of the polymer shell) were found in significant amounts in urine (*cf.* Figures 2 and 3). Thus we conclude that the ^{111}In was not predominantly released from the polymer (as free ion), as in this case much fewer ^{111}In would be expected to be found in the urine. Thus the most likely explanation is that** at least fragments or the entire polymer molecule was detached from the Au NPs surface. **This is also indicated by the fact that the ^{111}In bound to the polymer shell is excreted**

via urine, as chelated ^{111}In . As less ^{111}In -labelled polymer than chelated ^{111}In is excreted the polymer fragments detached from the Au NP surface seem to be bigger than one individual ^{111}In -DTPA complex, which makes filtering in the kidney less efficient. This is indeed was rather surprising to us, since the polymer binding and its molecular stability was considered to be fairly stable. However, similar findings have been claimed *in vitro*²⁰. Yet it indicates that the plethora of enzymes and proteins in the extracellular body fluids and within the intracellular cytosols of endocytotic cells may possess the capacity to crack these bindings, as will be discussed in the next section. Even considering the fact that at maximum 50% of attached ^{111}In may be only electrostatically adsorbed to the NP surface and not chelated by ABz-DOTA, the ratio of ^{111}In to ^{198}Au changed by much more than 50% after *i.v.* injection, see Figures 2e,f. Thus a significant part of the released ^{111}In must have come off the NP surface still chelated by DOTA. However, our biokinetic data cannot discriminate whether the entire polymer shell with DOTA-chelated ^{111}In was removed from the Au NPs surface or only in part. As the exact amount of polymer on the NP surface is unknown (the added part of polymer is known, but not the attached one after stringent purification) it is hard to estimate the average number of ^{111}In ions per polymer molecule on the NP surface. In addition, we cannot fully exclude release of DOTA (together with chelated ^{111}In) from the polymer shell. However, as we assume covalent attachment of DOTA to the polymer shell, whereas the polymer shell itself is bound to the Au cores only *via* hydrophobic interaction⁴⁷ it is rather likely that DOTA-chelated ^{111}In came off the Au NPs with fragments of the polymer shell.

Remarks on the influence of the surface chemistry of the Au NPs: In a previous report we studied the biokinetics of 5 nm core Au NPs coated either with triphenylphosphine sulfonate (TPPS), or with a polymer shell similar to the one used in this study, which had been further conjugated with polyethylene glycol (PEG) of either 750 Da or 10 kDa molecular weight³⁵. We found a prolonged time of NP circulation - as predicted for intravenously administered PEGylated NPs - only for the Au NPs coated with the long chain PEG (10 kDa). The short chain (750 Da) PEGylated Au NPs showed a similar pattern as the TPPS coated Au NPs. Already in this previous report we discussed this finding as an indication for a possible instability of the short-chain PEG coating. Comparing the 24 h biodistribution of the ^{198}Au core from the present study to that of 5 nm Au NPs coated with TPPS of our previous study^{35,36} the similarity in each organ, tissue and body fluid is remarkable (*cf.* Figure 4). Since the protein corona plays a significant role

in the determination of the biokinetic fate of the intravenously injected Au NPs, the similar patterns indicate that the protein coronas seem to be very similar. On the other hand, it appears unlikely that the two different coating molecules – polymer versus TPPS – bind exactly the same pattern of serum proteins. However, for the TPPS coated Au NPs it was shown that the coating was rather quickly removed in a cellular *in vitro* assay⁶². This suggests that also the polymer coated Au NPs get rid of major parts of their polymer coating *in vivo* and the protein corona is formed on a partly “naked” surface of the Au NPs. If this is true and taking into account the similarity shown in Figure 4, it appears likely that the polymer shell of the Au NPs in our present study was also partly stripped off resulting in a similar protein corona on partly “naked” Au NP surface and hence to a similar biodistribution. This is all in line with our final conclusion that under *in vivo* scenarios part of the organic coating around inorganic NP cores is displaced.

Remarks about potential consequences for drug targeting with NPs: While NPs may lose part of their original colloidal stability after intravenous administration by loss of the original organic coating, possible consequences for drug targeting will depend on the precise kinetics. Figure 2e, f demonstrates that while after 1 h the polymer shell around the Au NPs in blood still seems to be dominantly intact, after 24 hours a significant part of the polymer shell of Au NPs circulating in blood is already removed. Once the NPs have reached their potential target (*e.g.* a tumour), loss of the polymer shell will have little consequences, whereas partial degradation already in blood may lead to reduced retention times in blood. Thus, the time scale for the degradation of the polymer shell needs to be put into context with the retention time of the NPs in blood. Future studies in which degradation is kept constant, while retention times are increased, *e.g.* by further overcoating with PEG³⁵ may provide important additional information.

The partly removal of the polymer shell may be caused by enzymatic degradation: Our working hypothesis for explaining the *in vivo* degradation of the polymer shell is proteolytic digestion. Proteolytic enzymes cut amide bonds and thus could directly release the shell label (DOTA chelator for ¹¹¹In or DY495 fluorophore) or cause release of polymer molecules by cutting the hydrophobic side chains, which are attached to the polymer backbone *via* amide bonds. "In test tube" data demonstrate that proteolytic enzymes in fact cause (partial) release of the polymer shell from the NPs. Both, in blood and after internalization by cells, NPs are in fact exposed to proteolytic enzymes, which makes the above described scenario plausible. Our *in vitro* data

demonstrated that also for NPs incorporated by cells (typically in endo/lysosomal compartments) there is a (partial) separation of the organic shell from the inorganic NP core. While these data are clearly not sufficient to ultimately prove a pathway for the in vivo degradation of the NPs, they suggest degradation by proteolytic enzymes as likely scenario.

Acknowledgements

This work was supported by DFG (grant PA794/11-1 to WJP, grant SPP1313 to WGK) and EU-FP7 (ENPRA NMP4-SL-2009-228789 and Neuronano NMP4-SL-2008-214547 to WGK). The authors would like to thank Nadine Senger and Sebastian Kaidel (Helmholtz Centre Munich) for technical assistance and to Dominik Hühn, Dr. Ron Gill, Dr. Markus Klapper, and Prof. Dr. Kenneth Dawson for helpful scientific discussions.

Figures

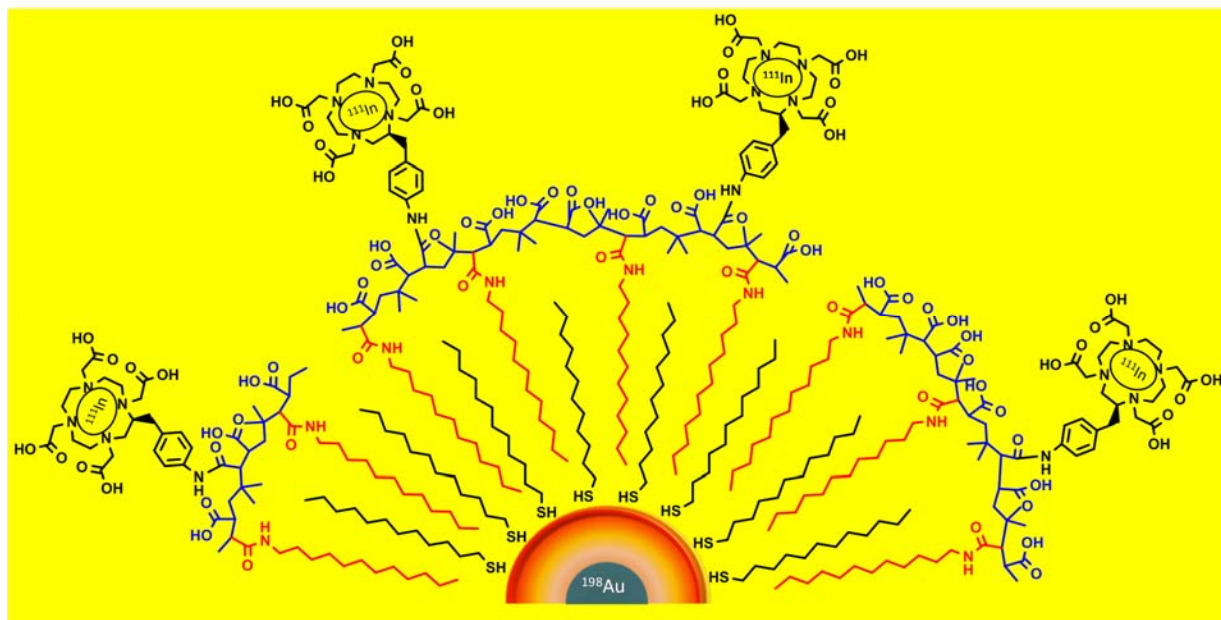


Figure 1: Sketch of the NPs with double radio-label.

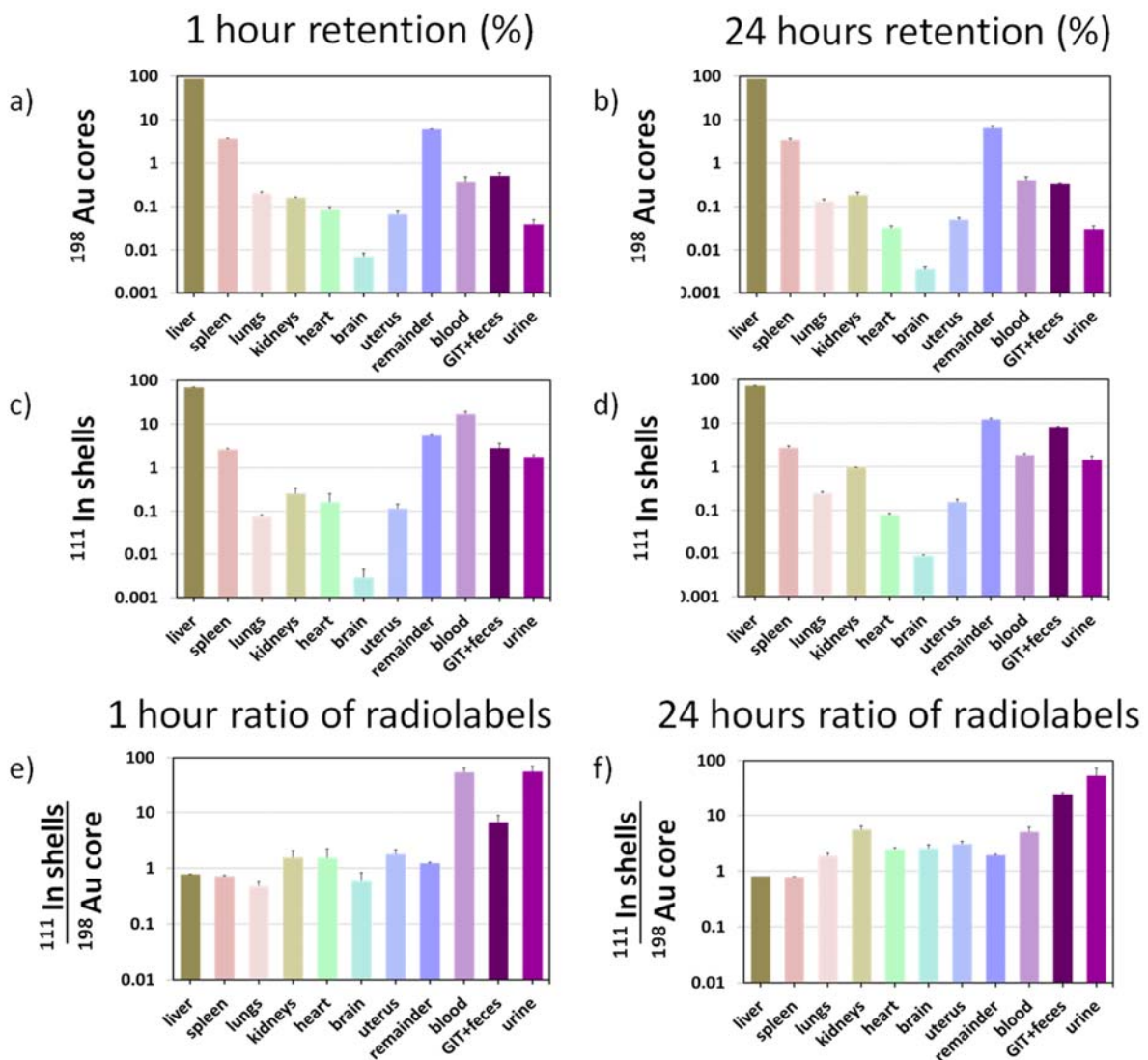


Figure 2: Quantitative balance of the 1 hour and 24 hours biodistribution of double-labelled Au NPs ($d_c = 4 \pm 2$ nm) with a ^{198}Au core radio-label and an ^{111}In shell radio-label in Wistar-Kyoto rats. Mean data (\pm SEM) are given in percent of administered dose ($n = 4$). “Remainder” represents radio-labels found in the remaining rest of the carcass, including soft tissues, skin and skeleton, after sampling of all organs and tissues. “GIT+feces” represents the radio-labels found in the gastro-intestinal-tract and in feces (note that after 1 hour no radio-labels were found in feces). “Blood” represents the total content of radio-labels as calculated from the measured content in the blood sample and the estimate of the total blood volume (*cf.* Methods). a, b) biodistribution of the ^{198}Au NP core radio-label. c, d) biodistribution of the ^{111}In shell radio-label. e, f) ratio of ^{111}In shell to ^{198}Au NP radio-label in each organ and tissue.

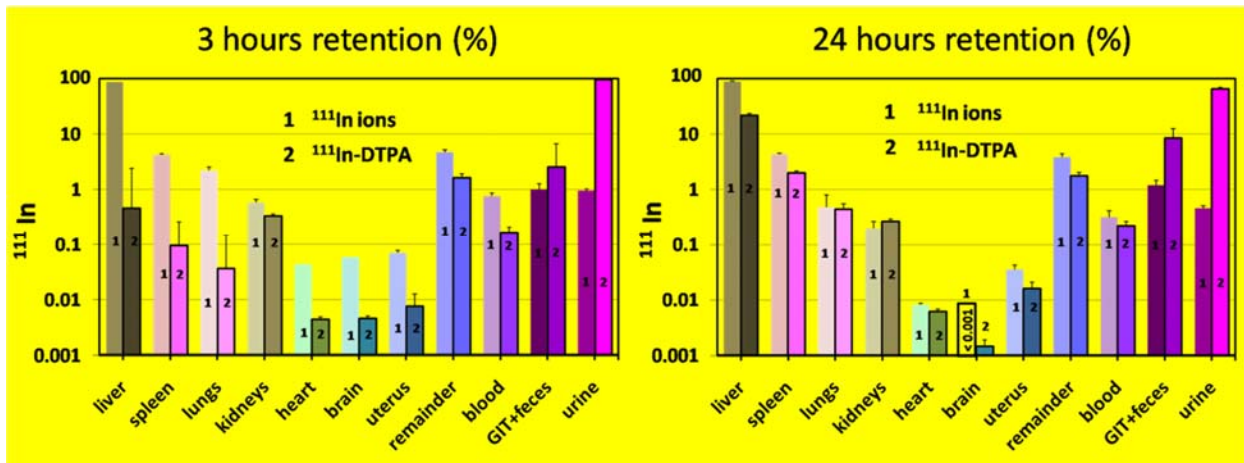


Figure 3: 3 and 24 hours biodistribution of soluble free ^{111}In ions and of ^{111}In -DTPA chelate complexes after intravenous administration in C57 Bl6 mice. Mean data (\pm SEM) are given in percent of administered dose ($n = 4$).

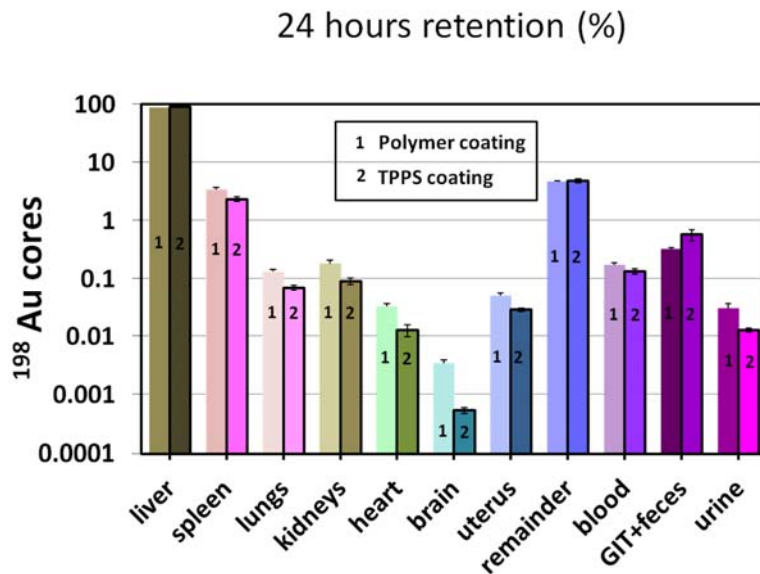


Figure 4: 24 hours biodistribution of monodisperse Au NPs ($d_c = 5 \text{ nm}$) coated with triphenylphosphine (TPPS) (data taken from our previous study³⁵) and of Au NPs ($d_c = 4 \pm 2 \text{ nm}$) coated with a DOTA-modified polymer shell (data taken from Figure 2b) in Wistar-Kyoto rats. Mean data (\pm SEM) are given in percent of administered dose ($n = 4$).

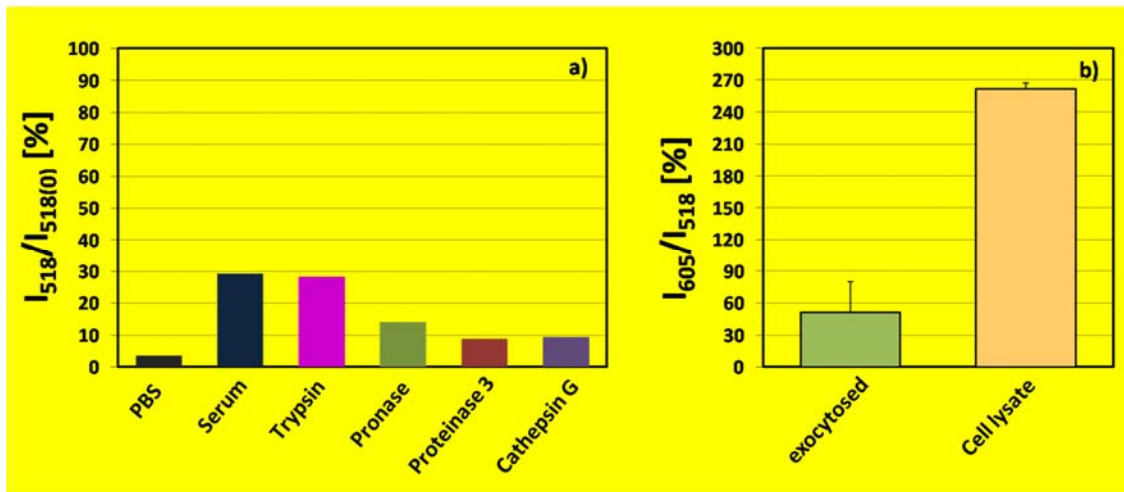


Figure 5: a) Fraction $I_{518}/I_{518(0)}$ of DY495 label released from the shell around the QDs after 24 h "in test tube" incubation with phosphate buffered saline (PBS, pH = 7.4), fetal bovine serum (FBS, 10%), trypsin (0.05%), pronase (0.2 units/mL), proteinase 3 (0.003 units/mL), and cathepsin G (13 units/mL) as quantified by the fluorescence I_{518} of DY495 (@ 518 nm) of the released DY495 label after separation of by ultrafiltration, as compared to the original fluorescence $I_{518(0)}$ of the DY495 label attached to the QDs. b) Ratio of QD and DY495 fluorescence (I_{605}/I_{518}) for exocytosed QDs and QDs found inside cells (cell lysate) after Kupffer cells had been incubated with the QDs for 22 h followed by additional 3 h incubation after having removed the free QDs from the medium.

References

1. Rivera Gil, P., Oberdorster, G., Elder, A., Puentes, V. F. & Parak, W. J. Correlating physico-chemical with toxicological properties of nanoparticles: The present and the future. *ACS Nano* **4**, 5527-5531 (2010).
2. Goy-Lopez, S. et al. Physicochemical characteristics of protein-NP bioconjugates: The role of particle curvature and solution conditions on human serum albumin conformation and fibrillogenesis inhibition. *Langmuir* **28**, 9113-9126 (2012).
3. Soenen, S. J. H. et al. Intracellular nanoparticle coating stability determines nanoparticle diagnostics efficacy and cell functionality. *Small* **6**, 2136-2145 (2010).
4. Chithrani, B. D., Ghazani, A. A. & Chan, W. C. Determining the size and shape dependence of gold nanoparticle uptake into mammalian cells. *Nano Lett.* **6**, 662-668 (2006).
5. Chithrani, B. D. & Chan, W. C. W. Elucidating the mechanism of cellular uptake and removal of protein-coated gold nanoparticles of different sizes and shapes. *Nano Lett.* **7**, 1542-1550 (2007).
6. Lin, J., Zhang, H., Chen, Z. & Zheng, Y. Penetration of lipid membranes by gold nanoparticles: Insights into cellular uptake, cytotoxicity, and their relationship. *ACS Nano* **4**, 5421-5429 (2010).
7. Schweiger, C. et al. Quantification of the internalization patterns of superparamagnetic iron oxide nanoparticles with opposite charge. *J. Nanobiotechnol.* **10**, 28 (2012).
8. Hühn, D. et al. Polymer-coated nanoparticles interacting with proteins and cells: Focusing on the sign of the net charge. *ACS Nano* **7**, 3253-3263 (2013).
9. Albanese, A., Sykes, E. A. & Chan, W. C. Rough around the edges: The inflammatory response of microglial cells to spiky nanoparticles. *ACS Nano* **4**, 2490-2493 (2010).
10. Huang, X., Teng, X., Chen, D., Tang, F. & He, J. The effect of the shape of mesoporous silica nanoparticles on cellular uptake and cell function. *Biomaterials* **31**, 438-448 (2010).
11. Qiu, Y. et al. Surface chemistry and aspect ratio mediated cellular uptake of Au nanorods. *Biomaterials* **31**, 7606-7619 (2010).
12. AshaRani, P. V., Low Kah Mun, G., Hande, M. P. & Valiyaveetil, S. Cytotoxicity and genotoxicity of silver nanoparticles in human cells. *ACS Nano* **3**, 279-290 (2009).
13. Kittler, S., Greulich, C., Diendorf, J., Koller, M. & Epple, M. Toxicity of silver nanoparticles increases during storage because of slow dissolution under release of silver ions. *Chem. Mater.* **22**, 4548-4554 (2010).
14. Casals, E., Gonzalez, E. & Puentes, V. F. Reactivity of inorganic nanoparticles in biological environments: Insights into nanotoxicity mechanisms. *J. Phys. D. Appl. Phys.* **45**, 443001 (2012).

15. Walczyk, D., Bombelli, F. B., Monopoli, M. P., Lynch, I. & Dawson, K. A. What the cell "sees" in bionanoscience. *J. Am. Chem. Soc.* **132**, 5761-5768 (2010).
16. Lesniak, A. et al. Effects of the presence or absence of a protein corona on silica nanoparticle uptake and impact on cells. *ACS Nano* **6**, 5845-5857 (2012).
17. Mahmoudi, M. et al. Temperature: The "ignored" factor at the nanobio interface. *ACS Nano* **7**, 6555–6562 (2013).
18. Rivera Gil, P. et al. The challenge to relate the physicochemical properties of colloidal nanoparticles to their cytotoxicity. *Acc. Chem. Res.* **46**, 743-749 (2013).
19. Chanana, M., Rivera Gil, P., Correa-Duarte, M. A., Parak, W. J. & Liz-Marzán, L. M. Physicochemical properties of protein-coated gold nanoparticles in biological fluids and cells before and after proteolytic digestion. *Angew. Chem., Int. Ed.* **52**, 4179–4183 (2013).
20. Chen, H. W., Zou, P., Connarn, J., Paholak, H. & Sun, D. X. Intracellular dissociation of a polymer coating from nanoparticles. *Nano Res.* **5**, 815-825 (2012).
21. Kreyling, W. G. et al. Interspecies comparison of phagolysosomal pH in alveolar macrophages. *Inhal. Toxicol.* **3**, 91-100 (1991).
22. Soenen, S. J. H. et al. Intracellular nanoparticle coating stability determines nanoparticle diagnostics efficacy and cell functionality. *Small* **6**, 2136-2145 (2010).
23. Levy, M. et al. Long term in vivo biotransformation of iron oxide nanoparticles. *Biomaterials* **32**, 3988-3999 (2011).
24. Derfus, A. M., Chan, W. C. W. & Bhatia, S. N. Probing the cytotoxicity of semiconductor quantum dots. *Nano Lett.* **4**, 11-18 (2004).
25. Kirchner, C. et al. Cytotoxicity of colloidal CdSe and CdSe/ZnS nanoparticles. *Nano Lett.* **5**, 331-338 (2005).
26. Caballero-Díaz, E. et al. The toxicity of silver nanoparticles depends on their uptake by cells and thus on their surface chemistry. *Part. Part. Syst. Char.* **30**, 1079–1085 (2013).
27. Wu, Y. et al. Fe@Au as the nano transformer in anti-cancer therapy: Role of the zero-valent iron in the time dependent self-detoxification and cancer selective activation. *Adv. Funct. Mater.* (in press).
28. Lunov, O. et al. Lysosomal degradation of the carboxydextran shell of coated superparamagnetic iron oxide nanoparticles and the fate of professional phagocytes. *Biomaterials* **31**, 9015-9022 (2010).
29. Sée, V. et al. Cathepsin I digestion of nanobioconjugates upon endocytosis. *ACS Nano* **3**, 2461-2468 (2009).

30. Tietze, R. et al. Efficient drug-delivery using magnetic nanoparticles - biodistribution and therapeutic effects in tumour bearing rabbits. *Nanomed. Nanotechnol. Biol. Med.* **9**, 961-971 (2013).
31. Ducongé, F. et al. Fluorine-18-labeled phospholipid quantum dot micelles for *in vivo* multimodal imaging from whole body to cellular scales. *Bioconjugate Chem.* **19**, 1921-1926 (2008).
32. Wang, F. et al. The biomolecular corona is retained during nanoparticle uptake and protects the cells from the damage induced by cationic nanoparticles until degraded in the lysosomes. *Nanomed. Nanotechnol.* **9**, 1159-1168 (2013).
33. Röcker, C., Pötzl, M., Zhang, F., Parak, W. J. & Nienhaus, G. U. A quantitative fluorescence study of protein monolayer formation on colloidal nanoparticles. *Nat. Nanotechnol.* **4**, 577-580 (2009).
34. Semmler-Behnke, M. et al. Biodistribution of 1.4- and 18-nm gold particles in rats. *Small* **4**, 2108-2111 (2008).
35. Lipka, M. et al. Biodistribution of PEG-modified gold nanoparticles following intratracheal instillation and intravenous injection. *Biomaterials* **31**, 6574-6581 (2010).
36. Hirn, S. et al. Particle size-dependent and surface charge-dependent biodistribution of gold nanoparticles after intravenous administration. *Eur. J. Pharm. Biopharm.* **77**, 407-416 (2011).
37. Schleh, C. et al. Size and surface charge of gold nanoparticles determine absorption across intestinal barriers and accumulation in secondary target organs after oral administration. *Nanotoxicology* **6**, 36-46 (2012).
38. Almeida, J. P., Chen, A. L., Foster, A. & Drezek, R. *In vivo* biodistribution of nanoparticles. *Nanomedicine* **6**, 815-835 (2011).
39. Poon, Z., Lee, J. B., Morton, S. W. & Hammond, P. T. Controlling *in vivo* stability and biodistribution in electrostatically assembled nanoparticles for systemic delivery. *Nano Lett.* **11**, 2096-2103 (2011).
40. Wang, Y. L., Seebald, J. L., Szeto, D. P. & Irudayaraj, J. Biocompatibility and biodistribution of surface-enhanced raman scattering nanoprobe in zebrafish embryos: *In vivo* and multiplex imaging. *ACS Nano* **4**, 4039-4053 (2010).
41. Gutiérrez, L. et al. Ac magnetic susceptibility study of *in vivo* nanoparticle biodistribution. *J. Phys. D. Appl. Phys.* **44** (2011).
42. Kreyling, W. G., Semmler-Behnke, M., Takenaka, S. & Moller, W. Differences in the biokinetics of inhaled nano- versus micrometer-sized particles. *Acc. Chem. Res.* **46**, 714-722 (2013).
43. Praetner, M. et al. The contribution of the capillary endothelium to blood clearance and tissue deposition of anionic quantum dots *in vivo*. *Biomaterials* **31**, 6692-6700 (2010).

44. Samkoe, K. S., Karotki, A., Cramb, D. T., Wilson, B. C. & Clancy, A. A. Complete blood vessel occlusion in the chick chorioallantoic membrane using two-photon excitation photodynamic therapy: Implications for treatment of wet age-related macular degeneration. *J. Biomed. Opt.* **12**, 034025 (2007).
45. Ali, Z. et al. Multifunctional nanoparticles for dual imaging. *Anal. Chem.* **83**, 2877-2882 (2011).
46. Geiser, M. & Kreyling, W. G. Deposition and biokinetics of inhaled nanoparticles. *Part. Fibre Toxicol.* **7**, 1-17 (2010).
47. Pellegrino, T. et al. Hydrophobic nanocrystals coated with an amphiphilic polymer shell: A general route to water soluble nanocrystals. *Nano Lett.* **4**, 703-707 (2004).
48. Libutti, S. K. et al. Phase I and pharmacokinetic studies of CYT-6091, a novel PEGylated colloidal gold-rhTNF nanomedicine. *Clin. Cancer Res.* **16**, 6139-6149 (2010).
49. Goel, R., Shah, N., Visaria, R., Paciotti, G. F. & Bischof, J. C. Biodistribution of TNS- α -coated gold nanoparticles in an *in vivo* model system. *Nanomedicine* **4**, 401-410 (2009).
50. Aurimmune™. (<http://www.cytimmune.com/go.cfm?do=page.view&pid=26>).
51. Gad, S. C., Sharp, K. L., Montgomery, C., Payne, J. D. & Goodrich, G. P. Evaluation of the toxicity of intravenous delivery of auroshell particles (gold-silica nanoshells). *Int. J. Toxicol.* **31**, 584-594 (2012).
52. Erickson, T. A. & Tunnell, J. W. in *Nanomaterials For The Life Sciences: Mixed Metal Nanomaterials* (ed. Kumar, C. S. S. R.) (Wiley-VCH, Weinheim, 2009).
53. Longmire, M., Choyke, P. L. & Kobayashi, H. Clearance properties of nano-sized particles and molecules as imaging agents: Considerations and caveats. *Nanomedicine* **3**, 703-717 (2008).
54. Charron, G. et al. On the use of pH titration to quantitatively characterize colloidal nanoparticles. *Langmuir* **28**, 15141-15149 (2012).
55. Harakeh, S. et al. The effect of PEG-coated gold nanoparticles on the anti-proliferative potential of specific nutrient synergy. *Nanotoxicology* **4**, 177-185 (2010).
56. Soenen, S. J. et al. Cytotoxic effects of gold nanoparticles: A multiparametric study. *ACS Nano* **6**, 5767-5783 (2012).
57. Lehmann, A. D. et al. Fluorescent-magnetic hybrid nanoparticles induce a dose-dependent increase in proinflammatory response in lung cells *in vitro* correlated with intracellular localization. *Small* **6**, 753-762 (2010).
58. Oeff, K., Krentz, K. & Kessel, M. J-131-clearance der normalen und pathologischen magenschleimhaut. *Klinische Wochenschrift* **33**, 59-63 (1955).

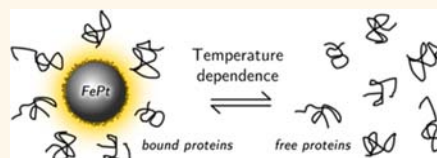
59. Sperling, R. A. et al. Size determination of (bio-) conjugated water-soluble colloidal nanoparticles: A comparison of different techniques. *J. Phys. Chem. C* **111**, 11552-11559 (2007).
60. Kreyling, W. G. et al. Air-blood barrier translocation of tracheally instilled gold nanoparticles inversely depends on particle size. *ACS Nano* **8**, 222-233 (2014).
61. Perrault, S. D., Walkey, C., Jennings, T., Fischer, H. C. & Chan, W. C. W. Mediating tumor targeting efficiency of nanoparticles through design. *Nano Lett.* **9**, 1909-1915 (2009).
62. Pan, Y. et al. Gold nanoparticles of diameter 1.4 nm trigger necrosis by oxidative stress and mitochondrial damage. *Small* **5**, 2067-2076 (2009).

Temperature: The “Ignored” Factor at the NanoBio Interface

Morteza Mahmoudi,^{†,*} Abuelmagd M. Abdelmonem,^{‡,¶} Shahed Behzadi,[†] Joachim H. Clement,[§] Silvio Dutz,[⊥] Mohammad R. Ejtehadi,^{||} Raimo Hartmann,[‡] Karsten Kantner,[‡] Uwe Linne,[‡] Pauline Maffre,[#] Scott Metzler,[△] Mojghan K. Moghadam,[⊗] Christian Pfeiffer,[‡] Meisam Rezaei,^{||} Pilar Ruiz-Lozano,[△] Vahid Serpooshan,[△] Mohammad A. Shokrgozar,[⊗] G. Ulrich Nienhaus,^{∞,#,*} and Wolfgang J. Parak^{‡,▽,*}

[†]Nanotechnology Research Center and Department of Nanotechnology, Faculty of Pharmacy, Tehran University of Medical Sciences, Tehran, Iran, [‡]Fachbereich Physik/Chemie, Philipps-Universität Marburg, Marburg, Germany, [§]Department of Hematology/Oncology, University Hospital Jena, Friedrich-Schiller University Jena, Jena, Germany, [⊥]Department Nano Biophotonics, Institute of Photonic Technology, Jena, Germany, ^{||}Department of Physics, Sharif University of Technology, Tehran, Iran, [∞]Department of Physics, University of Illinois at Urbana-Champaign, Urbana, Illinois, United States, [#]Institute of Applied Physics and Center for Functional Nanostructures (CFN) and Institute of Toxicology and Genetics (ITG), Karlsruhe Institute of Technology (KIT), Karlsruhe, Germany, [△]Department of Pediatrics, Division of Cardiology, School of Medicine, Stanford University, Stanford, California, United States, [⊗]National Cell Bank, Pasteur Institute of Iran, Tehran, Iran, and [▽]CIC Biomagune, San Sebastian, Spain. *Contributing authors in alphabetic order.

ABSTRACT Upon incorporation of nanoparticles (NPs) into the body, they are exposed to biological fluids, and their interaction with the dissolved biomolecules leads to the formation of the so-called protein corona on the surface of the NPs. The composition of the corona plays a crucial role in the biological fate of the NPs. While the effects of various physicochemical parameters on the composition of the corona have been explored in depth, the role of temperature upon its formation has received much less attention. In this work, we have probed the effect of temperature on the protein composition on the surface of a set of NPs with various surface chemistries and electric charges. Our results indicate that the degree of protein coverage and the composition of the adsorbed proteins on the NPs' surface depend on the temperature at which the protein corona is formed. Also, the uptake of NPs is affected by the temperature. Temperature is, thus, an important parameter that needs to be carefully controlled in quantitative studies of bionano interactions.



KEYWORDS: colloidal magnetic nanoparticles · protein corona · temperature dependence · uptake by cells · protein adsorption

Nanoparticles (NPs) are presently being employed in a wide variety of biomedical and biotechnological applications. In some applications, such as targeted drug delivery, researchers aim to develop NPs such that they are selectively incorporated by specific cell types in living tissue. In other applications, such as NP-based contrast agents for magnetic resonance imaging, NPs should stay in the bloodstream and subsequently be cleared by the kidneys, but not be internalized by cells. It is known that cellular NP uptake is strongly influenced by the NP size as well as their surface properties, including decoration by functional groups and biomolecules. A detailed understanding of the interactions between NPs and different cell types is key to understanding and controlling cellular uptake mechanisms.^{1–4}

NPs entering the human body first come in contact with a biological fluid, *e.g.*, blood or lung-lining fluid. They interact with the dissolved biomacromolecules, in particular

proteins, and an adsorption layer of proteins, the so-called “protein corona”, forms around the NPs.^{5–7} While protein adsorption onto planar surfaces has been investigated for decades, detailed studies of NP–protein interactions have only started recently.^{8–13} Studies have especially focused on the effects of physicochemical parameters of NPs (*e.g.*, size, shape, composition, surface roughness, porosity, surface charge) on the formation of the protein corona.¹⁴ The temperature, however, at which the NPs and the protein are maintained in solution likewise should be an important factor influencing the corona composition. For example, it has been shown that the composition of the protein corona formed upon NP exposure to heat-inactivated proteins (preheating at 56 °C) and non-heat-inactivated proteins is different.¹⁵ As a result, significant differences were observed in the amounts of NPs taken up by cells. However, temperature effects close to physiological temperature (*i.e.*, not involving denaturation) on the

* Address correspondence to Mahmoudi-M@TUMS.ac.ir; uli@uiuc.edu; wolfgang.parak@physik.uni-marburg.de.

Received for review November 16, 2012 and accepted June 30, 2013.

Published online July 01, 2013
10.1021/nn305337c

© 2013 American Chemical Society

protein corona have not yet been studied in detail. Those effects may be relevant for *in vivo* applications of NPs because body temperature can vary significantly. The mean human body temperature ranges from 35.8 to 37.2 °C and varies for different parts of the body.¹⁶ It decreases during sleep and increases by up to 2 °C during physical activities and can even climb to 41 °C in the case of fever.¹⁷ It is also known that the temperature in peripheral parts of the body (*e.g.*, skin) during exposure to cold weather can drop to 28 °C.¹⁸ Very recently, even the intracellular temperature of living cells was shown to be inhomogeneous.^{19,20}

If protein adsorption onto the surface of NPs depends on the body temperature, it may also result in a significant effect on the cellular uptake of NPs *in vivo*. Therefore, we have studied the influence of near-physiological temperature variation on the formation of the protein corona, using superparamagnetic NPs synthesized from different materials with different surface coatings and thus different ζ -potentials as model NPs. Magnetic NPs enable effective magnetic washing and separation, which is beneficial for handling of small amounts of NP sample. Precisely defined and well-characterized polymer-coated FePt NPs were incubated with human serum albumin (HSA) and apo-transferrin (apo-Tf) at different concentrations and temperatures, and the monolayer formation of adsorbed proteins was quantified by using fluorescence correlation spectroscopy (FCS). Moreover, larger FeO_x NPs (superparamagnetic iron oxide NPs, SPIONs) with positive and negative charge and also with neutral surfaces were incubated in fetal bovine serum (FBS) at different temperatures, and the compositions of the resulting coronae were analyzed as a function of the incubation temperature. We have also assessed the effect of the temperature-dependent corona composition on cellular uptake.

RESULTS AND DISCUSSION

Temperature Dependence of HSA and apo-Tf Monolayer Formation on FePt NPs. For our protein adsorption studies we used fluorescently labeled, negatively charged polymer-coated FePt NPs. The inorganic core diameter, d_c , was determined by transmission electron microscopy (TEM). The hydrodynamic diameter, d_h , was measured by dynamic light scattering (DLS, *cf.* Table 1) and fluorescence correlation spectroscopy (FCS, *cf.* Table 2) at room temperature in phosphate-buffered saline (PBS). Results obtained with the FCS method ($d_h = 12.0 \pm 0.2$ nm and 10 ± 0.4 nm for two different batches at room temperature) are very precise and reproducible and have been verified in several independent studies.^{21–24} The DLS data on bare NPs without proteins ($d_h = 10 \pm 5$ nm) are—within experimental error—in agreement with the FCS data but have larger margins of error.^{21,24} Furthermore, the FCS data (*cf.* Table 2) indicate that temperature variation between 9 and 43 °C does not affect the hydrodynamic

TABLE 1. Core (d_c) and Hydrodynamic (d_h) Diameters of NPs As Determined with TEM and DLS (at room temperature in PBS)

NP material	charge	d_c [nm]	d_h [nm]
FePt	Negative	3.5 ± 0.6	10 ± 5
FeO _x	Negative	15 ± 5	33 ± 8
FeO _x	Neutral	22 ± 7	33 ± 10
FeO _x	Positive	17 ± 5	79 ± 7

TABLE 2. Temperature-Dependent Protein Adsorption onto FePt NPs As Derived from FCS Measurements in PBS^a

T [°C]	HSA				
	$r_h(0)$ [nm]	$r_h(N_{max})$ [nm]	K'_D [μ M]	n	N_{max}
13	5.5 ± 0.3	9.2 ± 0.4	10 ± 4	0.6 ± 0.1	31 ± 5
23	6.0 ± 0.1	9.3 ± 0.2	6.3 ± 2.2	0.9 ± 0.2	30 ± 3
43	6.0 ± 0.1	8.8 ± 0.2	0.8 ± 0.4	0.7 ± 0.2	23 ± 2
T [°C]	Apo-Tf				
	$r_h(0)$ [nm]	$r_h(N_{max})$ [nm]	K'_D [μ M]	n	N_{max}
9	5.1 ± 0.2	15.1 ± 0.8	13 ± 4	0.6 ± 0.1	47 ± 7
22	5.0 ± 0.2	14.3 ± 0.7	16 ± 6	0.7 ± 0.1	40 ± 6
43	5.3 ± 0.1	11 ± 0.4	5 ± 1	0.7 ± 0.1	17 ± 2

^a $r_h(0)$ and $r_h(N_{max})$ are the hydrodynamic radii of NPs without adsorbed proteins and upon saturation of the NP surface with proteins, respectively; n is the Hill coefficient, which controls the steepness of the binding curve, N_{max} is the maximum number of proteins adsorbing onto a single NP, and K'_D represents the concentration of protein molecules at half coverage. Data for two different proteins are shown, HSA and apo-Tf.

diameter of the bare FePt NPs. Thus, the polymer surface of these NPs can be considered to be stable in this temperature range. In a previous study, we also demonstrated that the polymer shell of the NPs dissolved in PBS remains stable over time.¹⁴

Protein adsorption was quantified in terms of changes in hydrodynamic radius, $r_h = d_h/2$, of the NPs by using FCS. We studied the adsorption of HSA and apo-Tf, two important serum proteins, onto polymer-coated FePt NPs. Please note that, due to the small size of the NPs and due to the thin protein shell (which provides only little contrast), TEM turned out not to be the method of choice for the analysis of the protein corona (*cf.* Supporting Information). FCS analysis was performed directly on NP solutions with varying protein concentrations. Because the fluorescent labels reside in the polymer shell of the FePt NPs and not on the proteins, there was no need for purification steps to remove unbound proteins, which may introduce errors in the quantitative assessment of protein–NP interactions. Thus, FCS measurements allow for the direct analysis of the proteins forming the protein corona *in situ*. Because the surface of our polymer-coated FePt NPs is homogeneous, a spherical shape will be maintained under saturating conditions, *i.e.*, when the whole NP surface is covered with protein. In the other limit, *i.e.*, upon binding of only one or two

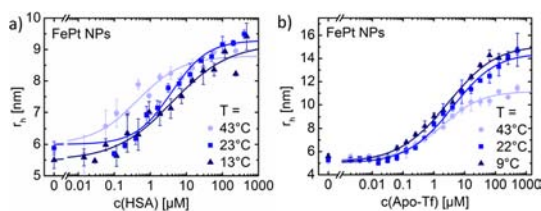


Figure 1. Change of the hydrodynamic radius, r_h , of negatively charged FePt NPs as a function of (a) HSA and (b) apo-Tf concentration in the solution due to protein adsorption at different temperatures T .

protein molecules per NP, the resulting shape is aspherical. However, FCS is not sensitive to small deviations from a spherical shape. In fact, in the analysis, we have made the approximation that the shape of the NPs remains spherical upon protein binding.

In accordance with our previous study²¹ at room temperature HSA adsorption increases with protein concentration in the solution up to the formation of a protein monolayer, as we have observed *in situ* by using FCS. In Figure 1a, we show HSA monolayer formation for a set of three temperatures (13, 23, 43 °C), as inferred from (i) the observed saturation behavior, *i.e.*, the NP size does not continue to increase beyond a certain HSA concentration, and (ii) the increase in NP size due to HSA binding, which corresponds to the physical size of the HSA molecules. The structure of HSA can be modeled as a 3 nm thick equilateral triangle with sides that are 8 nm long. At 13 and 23 °C the thickness of the protein corona is in agreement with our previous results taken at room temperature, $r_h \approx 3.3$ nm.^{21,24} The measured protein corona thickness of 3.3 nm indicates that the HSA molecules adsorb with their triangular surface facing the NPs, supposedly *via* the big, positively charged patch on the surface of one of the two triangular faces, which binds to the negatively charged NPs *via* Coulomb interactions.²⁴ At 43 °C, the radius increase upon HSA binding is slightly smaller, which may result from an enhanced flexibility of the polymer shell wrapping the FePt core of the NPs at higher temperature, so that the adsorbed HSA proteins may partially penetrate the shell, leading to an overall radius increase just slightly below 3.3 nm. Most remarkable, however, is the finding that the binding affinity displays a marked temperature dependence, as seen from the values of K'_D , the concentration at half coverage (Table 2). Surprisingly, K'_D decreases with temperature, so the highest protein binding affinity is found at the highest temperature. Usually, one would expect that a system tends to dissociate into its individual components at higher temperature so as to increase the overall translational entropy. The observed stronger binding of HSA to the NPs at 43 °C, however, may arise from structural fluctuations of the proteins and/or the polymer shell

around the NPs, which will be enhanced at higher temperature. These could induce structural changes that lead to a free energy-optimized binding interface.

We also note that the maximum number, N_{max} , of HSA molecules per NP appears to decrease at 43 °C (Table 2). The N_{max} values, however, should be taken with a grain of salt. They are based on a geometrical model that assumes (1) that the NPs have a smooth spherical surface and (2) that the added volume due to protein adsorption, which we infer from the change in r_h , is homogeneously filled with protein. At 43 °C, N_{max} will be underestimated if HSA molecules partially enter the polymer shell, as we expect from the smaller thickness of the protein corona. At 23 or 13 °C, N_{max} may be overestimated if the monolayer formed is not completely densely packed.

The binding of apo-Tf onto the FePt NPs was studied at 9, 22, and 43 °C (*cf.* Figure 1b). The data indicate formation of a monolayer of apo-Tf around each NP under saturating conditions.²² As for HSA, the affinity of apo-Tf toward the FePt NPs is greater at 43 °C than at room temperature, as indicated by the smaller ligand concentration producing half occupation K'_D at 43 °C (*cf.* Table 2). The affinities of Apo-Tf toward the NPs are identical within experimental error at 22 °C and at 9 °C. The measured protein corona thickness is also very similar at 22 and 9 °C, *i.e.*, 9.3 and 10 nm. The overall size of apo-Tf protein is around $4.2 \times 10 \times 7$ nm³. It consists of two identical subunits each having dimensions of $4.2 \times 5 \times 7$ nm³.²⁵ Because the thickness of the protein corona correlates with one dimension of the protein, Apo-Tf presumably binds to the NPs with the 4.2×7 nm² face. We note that, in earlier experiments,²² we had observed an apo-Tf corona of 7 nm, which suggests that apo-Tf binds to the NP surface with the 4.2×10 nm² face. Considering the surface charge and the structure of apo-Tf (*cf.* the Supporting Information) and assuming that apo-Tf binds to the negatively charged NPs *via* positive patches on its surface, apo-Tf may be able to adsorb to the NPs with the 4.2×7 nm² as well as with the 4.2×10 nm² face. In fact, we have observed different corona thicknesses on apo-Tf with different protein batches purchased from the same supplier. For the same batch of apo-Tf, however, the results were always reproducible. At 43 °C, the experiments revealed a 3 to 4 nm reduced thickness of the protein corona as compared with 22 or 9 °C. Therefore, the added volume due to apo-Tf adsorption is significantly smaller, which results in only 17 apo-Tf molecules attached per NP under saturation conditions in our analysis (*cf.* Table 2). As for HSA, this may be due to conformational changes of the proteins upon binding, which could involve changes in how the positive patches on the surface of the proteins are exposed to the solvent. Consequently, the overall orientation of the proteins on the surface may also change. Another possible scenario is that the proteins

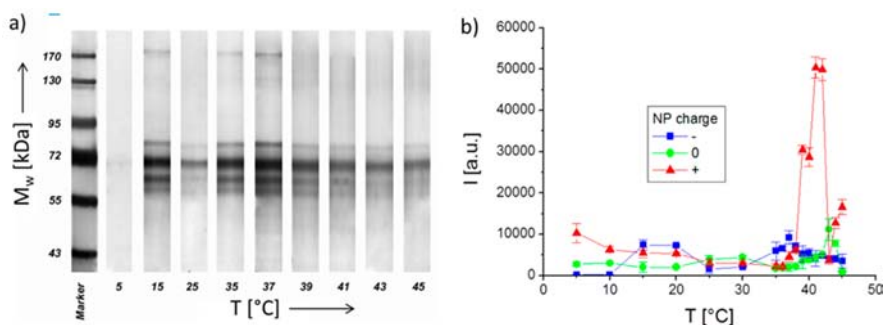


Figure 2. (a) SDS-PAGE gel of proteins adsorbed onto the surfaces of negatively charged FeO_x NPs after 1 h incubation in FBS at different temperatures. The molecular weights M_w of the proteins in the marker lane on the left are reported for reference. (b) Quantification of the amount of adsorbed proteins on negatively charged (–), neutral (0), and positively charged (+) NPs as derived from the total band intensities of proteins on the SDS-PAGE gels.

partially penetrate the polymer shell, which may be more flexible at this temperature.

Compound-Specific Adsorption of FBS onto FeO_x NPs. Because magnetic separation of the small, colloidal stable, and highly defined FePt NPs was not feasible due to their small size, data involving removal of unbound protein were carried out with the bigger FeO_x NPs. Structural and colloidal properties of dextran-coated FeO_x NPs were investigated with TEM and DLS. The diameter d_c of the inorganic FeO_x core and the hydrodynamic diameter d_h (as determined in PBS), respectively, are included in Table 1. Due to their larger size, these NPs allow for convenient magnetic separation and, thus, removal of unbound proteins. However, the NP cores have a relatively large size distribution and were partly agglomerated (especially the positively charged NPs), as indicated by hydrodynamic diameters much bigger than the diameters of the inorganic cores (*cf.* the Supporting Information). After incubation of the NPs in protein solution (10% FBS + 90% PBS) for 1 h at different temperatures, unbound or loosely bound proteins were removed by two washing steps in succession, during which the magnetic NPs were trapped in a strong magnetic field, while the eluted washing solutions were discarded. All washing steps were performed using prewarmed/–cooled washing solutions of the same temperature as during incubation. Only strongly attached proteins are retained on the NP surface after washing.

The proteins were afterward extracted from the NPs and then run on SDS-PAGE. The amount of protein was inferred from the integrated intensities along each line in the gel. An example of a gel with proteins that had adsorbed onto negatively charged NPs (incubated at different temperatures) is shown in Figure 2a (further data and details are included in the Supporting Information). The temperature dependence of the total amount of adsorbed proteins is reported in Figure 2b for the three types of FeO_x NPs. Our data indicate that even a slight temperature increase can already cause remarkable changes in the band intensities and, consequently, the composition of the protein adsorption

layer. In order to challenge these findings, control experiments were performed to study the influence of possible sources of error. (i) As FeO_x NPs were found to be partly agglomerated, batch-to-batch variations were probed. (ii) During the washing steps, some NPs might get lost and the amount of the detached proteins might also vary. Thus, variations among different purification runs were probed. (iii) SDS-PAGE and the subsequent quantification of protein may introduce errors: therefore, also these variations were also examined. The observed peak variations were below 10%, which in addition to the smooth connection between the data points indicates that the peaks in the amount of detected corona proteins (Figure 2b) are real. The amount of adsorbed proteins was highest around 40 °C. Also, for neutral and negatively charged NPs, less pronounced maxima exist around 43 and 37 °C, respectively.

The contribution of individual proteins to the corona under conditions of varying NP functionalization and incubation temperature was investigated with liquid chromatography/mass spectrometry (LC-MS/MS) (Figure 3). Significant differences were found between the protein profiles at various temperatures. In particular, we focused on the adsorption of three important serum proteins, for which association to FePt NPs has been previously investigated by using FCS: serum albumin ($M_w = 66$ kDa),^{21,24} serotransferrin ($M_w = 76$ kDa),²² and apolipoprotein A-I ($M_w = 28$ kDa).²⁴ In addition, we also studied alpha-2-HS-glycoprotein ($M_w = 49$ kDa). The contributions of serum albumin, serotransferrin, apolipoprotein A-I, and alpha-2-HS-glycoprotein demonstrate a temperature-dependent corona. Noticeably, increased protein adsorption can be seen around 40 °C, in particular for positively charged NPs and for alpha-2-HS-glycoprotein. The significance of this peak, which also appears in the SDS-PAGE data (Figure 2), is further strengthened by the fact that it extends consistently over several data points. However, due to the large error bars (*cf.* the Supporting Information) and also due to limited quality of the FeO_x NPs concerning size distribution

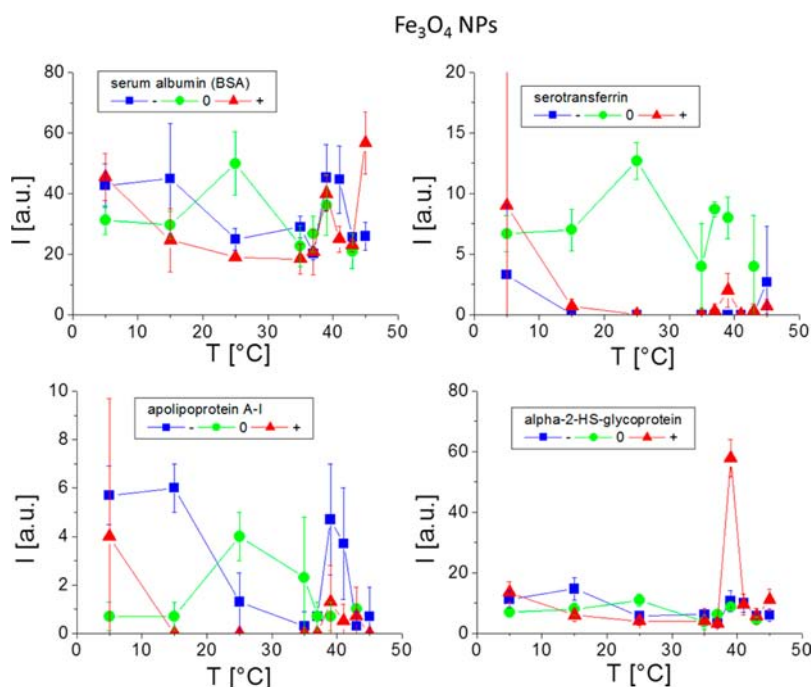


Figure 3. Temperature-dependent amounts of specific proteins in the protein corona of negatively charged (–), positively (+), charged, and neutral (0) Fe_3O_4 NPs, as obtained from LC-MS/MS data. Mean values over three independent measurements are shown with their corresponding standard deviations.

and colloidal dispersion, the data presented here rather have to be interpreted in a qualitative than in a quantitative way. Also, in the FCS data on FePt NPs, a noticeable difference in the protein corona was observed between room temperature and 43 °C. Thus, our data indicate that the composition of the corona strongly depends on the temperature at which the corona is formed (*i.e.*, the incubation temperature).

NP Interaction with Cells. Cellular endocytotic processes are intrinsically temperature-dependent.^{26–28} For example, below 4 °C, active internalization is suppressed. Also the protein layers formed on the NP surface affect their uptake and trafficking inside cells.^{29,30} We have demonstrated above that the formation of the protein corona is temperature-dependent. Thus one may ask how much of this temperature-dependent formation of the protein corona is reflected in temperature-dependent internalization of NPs by cells. In order to investigate this, uptake of fluorescence-labeled FePt NPs under serum-free and serum-containing conditions was analyzed with confocal microscopy at different incubation temperatures. Active cellular uptake of NPs involves the transfer of NPs into endosomes and subsequently lysosomes.¹ Thus we quantified uptake in terms of the amount of NPs found inside cells and of the amount of NPs found inside lysosomes.

In accordance with previous studies,^{14,22,30,31} we noticed that NP uptake was reduced by protein corona formation compared to bare NPs, as inferred from measurements with incubation in serum-containing versus serum-free medium (*cf.* Figure 4c,f). We also

observed a clear enhancement of NP uptake (in terms of mean NP intensity inside cells) with increasing temperatures, as well as with serum-free (Figure 4a) and serum-containing media (*cf.* Figure 4b). This trend was not as clear in the case where only NPs inside lysosomes were considered (*cf.* Figure 4c,d). In order to infer whether the protein corona plays a role in the temperature-dependent uptake of NPs, we analyzed the temperature dependence of the ratio of the uptake of NPs under serum-free and serum-containing conditions. Within our experimental errors we at best can speculate that the amount of NPs internalized by cells may rise faster with temperature under serum-free than under serum-containing conditions (*cf.* Figure 4c). In the case where NP uptake is quantified only by NPs localized inside lysosomes a different tendency was observed (*cf.* Figure 4f). Thus, even without considering that the impact of identical NPs on various cells can be significantly different^{4,32,33} our data do not allow for deriving a sharp conclusion about the correlation between the temperature-dependence of protein corona formation and NP uptake. Taking into account the different methods of quantification we applied, neither can we prove that the temperature-dependent formation of the protein corona around NPs may have some influence on the temperature-dependence of NPs uptake by cells, nor can we claim the opposite. Other temperature-dependent effects, such as active NP transport, are likely to play important roles in the temperature dependence in NP uptake, and thus the importance of the temperature dependence of protein

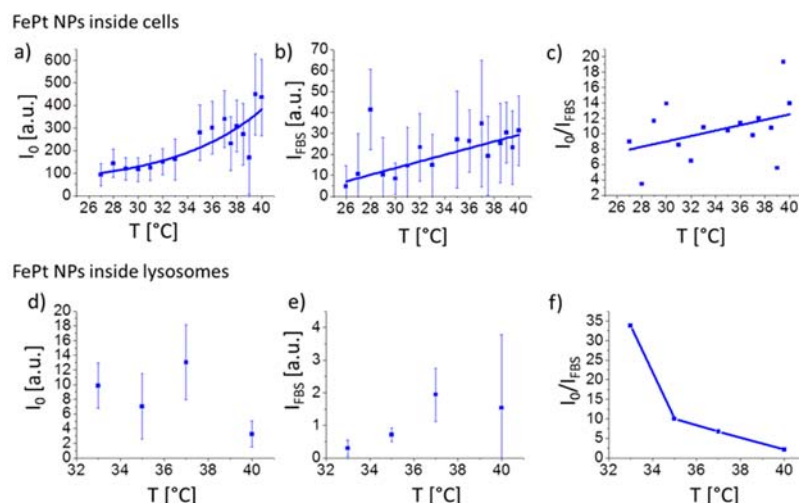


Figure 4. Uptake of fluorescently labeled FePt(–) NPs by HeLa cells after 3 h of incubation. Mean fluorescence intensities I of NPs upon using serum-free (I_0) and serum-containing (I_{FBS}) culture media are plotted. (a, b, c) Mean fluorescence intensities I of NPs that are localized inside cells. Each data point corresponds to the mean value of at least 2000 analyzed cells and the corresponding standard deviation. Exponential curves are added in order to serve as guide to the eyes. Also the ratio I_0/I_{FBS} is plotted for the different incubation temperatures T . (d, e, f) Mean fluorescence intensities I of NPs that are localized inside lysosomes. Each data point corresponds to the mean value of at least 30 analyzed cells and the corresponding standard deviation.

corona formation on the temperature dependence in NP uptake can be fully elucidated with more sophisticated assays. Also entanglement of size and protein corona formation needed to be considered, as NP uptake is also size-dependent.³⁴ In Figure 1 we demonstrated that at the same protein concentration the effective NP radius can be significantly different due to different corona formation, and a detailed analysis also would need to take size effects into account.

CONCLUSIONS

In this study, we have investigated the influence of the exposure temperature, ranging from 5 to 45 °C, on the formation and composition of the protein corona on magnetic NPs. The influence of temperature on

NP–cell interactions was also investigated. We have shown that changes in the incubation temperature can cause significant effects in protein corona formation and composition, although this is not necessarily always the case. Temperature effects for the NPs investigated by us were especially pronounced in the physiologically highly relevant temperature window of 37–41 °C. Thus, our findings suggest that studies on the formation of a protein corona on NPs should be carried out at well-controlled temperatures to enable comparison and reproduction of results from different laboratories. The results presented are expected to apply to other classes of NPs, such as fluorescent or plasmonic NPs, with similar surface functionalization, although we did not prove this yet experimentally.

MATERIALS AND METHODS

Synthesis of FePt NPs and Investigation of Adsorbed HSA with FCS. Synthesis of polymer-coated FePt NPs with a fluorophore (DY-636) in the polymer shell has been reported previously.²¹ Our two-focus fluorescence correlation spectroscopy setup has recently been described.²⁴ For incubation with proteins, FePt NPs and proteins were mixed and incubated at a controlled temperature, T , for 10 min. HSA and apo-Tf were purchased from Sigma Aldrich as lyophilized powders (A8763 and T4382, respectively). The proteins were suspended in PBS without Ca²⁺ and Mg²⁺ ions (PAA Laboratories) at room temperature at a concentration of 1 mM or less. Subsequently, FCS measurements were carried out for 4 min at the same temperature, T . A 40 μL amount of solution was filled into a sample chamber consisting of a small borosilicate glass cylinder glued to a coverslip with epoxy. The sample chamber was kept in a small water bath within an aluminum block heated or cooled to the desired temperature with a Peltier element. Thermal expansion effects due to temperature changes in the objective led to small variations in the focusing properties and, thus, to slight changes of the confocal volume, as was observed by measuring the point spread function (PSF) using laser light reflected off 100 nm gold NPs.

We compensated the temperature effect by changing the position of the correction collar normally used to correct for different coverslip thicknesses. The position of the correction collar was adjusted so as to achieve maximum fluorescence intensity, which also correlates with the smallest dimensions of the measured confocal volume. Furthermore, we measured deviations in the interfoci distance resulting from temperature changes with a reference sample, Atto655 in buffer solution. The measured size of the NPs was corrected according to the calibration obtained with the reference sample. Temperature was directly measured in the sample solution. Hydrodynamic radii, r_h , were determined by FCS and plotted versus the HSA concentration in solution, $c(\text{HSA})$, as shown in Figure 1. At saturation, the hydrodynamic radius of one NP was calculated according to²¹

$$r_h(N_{\text{max}}) = r_h(0) \sqrt[3]{1 + cN_{\text{max}}} \quad (1)$$

where $c = V_p/V_0$ is the volume ratio of protein molecules to NP. For the NPs, the volume was simply calculated by using $V_0 = (4\pi/3)(r_h(0))^3$. For apo-Tf, the volume was estimated from the physical dimensions, i.e., $V_p = 10 \times 7 \times 4.2 = 294 \text{ nm}^3$. Likewise,

for HSA, the volume of a triangular prism with 8 nm side length and 3 nm thickness was computed, *i.e.*, $V_p = 3 \times (8/2) \times (8^2 - 4^2)^{1/2} = 83 \text{ nm}^3$. Note that, for HSA, which is a compact globular protein, V_p can equally well be calculated by using $V_p = (M_w/N_A)/\rho_p$, with the molecular weight, M_w , of HSA, Avogadro's constant, N_A , and the protein density, $\rho_p = 1.35 \text{ g/cm}^3$. N_{max} is the maximum number of adsorbed molecules. Concentration-dependent adsorption was described by the Hill equation,

$$N = N_{\text{max}} \frac{1}{1 + (K'_D/[Pr])^n} \quad (2)$$

where N is the number of adsorbed protein molecules per NP, K'_D represents the concentration of protein molecules for half coverage, and n is the Hill coefficient, which determines the steepness of the binding curve.²¹

Synthesis of FeO_x NPs and Investigation of Adsorbed FBS with PAGE and MS. Syntheses of dextran-coated FeO_x NPs (SPIONs, inorganic core diameter) with negative, neutral, and positive surface charges were performed according to our previously published protocols (hydrodynamic radii together with their characterization are presented in the Supporting Information).³⁵ To study the interactions of the NPs with FBS, 100 μL of NP solution (with a concentration of 100 $\mu\text{g/mL}$) was mixed with 900 μL of FBS and incubated at $T = 5, 15, 25, 35, 37, 39, 41, 43,$ and $45 \text{ }^\circ\text{C}$. The protein/NP mixtures were run through a strong magnetic field using a magnetic-activated cell sorting system. NPs were trapped inside the magnetic column, and the flow-through fraction (two washing steps with 500 μL of PBS buffer) was removed. We ensured that all washing solutions were at the same temperature as the media used during incubation. Finally, the column was removed from the magnetic field, and the released NPs were collected. The protein/NP mixtures were immediately resuspended in protein loading buffer containing 10% dithiothreitol, followed by boiling for 5 min at $100 \text{ }^\circ\text{C}$ to remove the proteins from the NPs.³ To quantify the amount of proteins on the surface of the various NPs, equal sample volumes of the solution were loaded into sodium dodecyl sulfate polyacrylamide gel electrophoresis (1D SDS-PAGE). Gel electrophoresis was carried out at 120 V, 400 mA, for about 60 min each, until the proteins approached the end of the gel. While the NPs stick in the wells of the gels, the desorbed proteins migrate in the applied electric field. The gels were stained by silver nitrate in order to visualize the proteins and scanned using a Biorad GS-800 calibrated densitometer scanner, and gel densitometry was performed using Image J (1.410 version). Intensity profiles of the stained proteins along the migration direction of the proteins were recorded to quantify the total amount of protein in each lane and the contribution of the proteins of different molecular weight to the total amount. An example of a gel after SDS-PAGE is shown in Figure 2a. To determine the relative amounts of proteins adsorbed onto different NPs, the collected proteins were digested with trypsin and analyzed by LC-MS/MS. A semiquantitative evaluation of the data was done by using the peptide spectrum matches (*i.e.*, "spectral counts") assigned to a distinct protein by Proteome Discoverer software.

Uptake of FePt NPs by Cells. HeLa cells were incubated with polymer-coated FePt NPs with integrated fluorophore (DY-636) at different temperatures for 3 h with and without serum (FBS) in the culture medium. Nuclei, membranes, and lysosomes of the cells were stained, and fluorescence images of these cellular compartments together with images of the NP distribution were recorded with confocal microscopy (for details refer to the Supporting Information). Cellular compartments were identified with the open source software CellProfiler. NPs located in the specific compartments (here either inside cells or inside lysosomes) were identified by overlay of a mask corresponding to the locations of the compartments with the image of the NP distribution.³⁶ As well, the total amount of NPs incorporated per cell (as quantified by the mean fluorescence intensity I inside cells), as the amount of NPs that co-localized with the lysosome (as quantified by the mean fluorescence intensity I inside lysosomes),³⁷ was determined. Please note the limited depth resolution of confocal microscopy, which makes it complicated to distinguish between NPs only adherent to the outer cell

surface and internalized NPs. One could clearly distinguish between both cases using pH-sensitive fluorophores attached to the NPs.^{38,39} In our case we also stained the cell membrane. We did not observe a significant amount of NPs at positions close to the cell membrane, and thus the error in the quantification of internalized NPs by wrongfully counting also NPs attached to the outer membrane is very small.

Conflict of Interest: The authors declare no competing financial interest.

Acknowledgment. This work was supported by the Deutsche Forschungsgemeinschaft DFG (grants CFN, NI291/7, and NI291/8 to G.U.N. and grant PA794/4-2 to W.J.P.). The authors thank Faheem Amin for helping with the synthesis and polymer coating of FePt NPs, Dr. Andreas Schaper for discussions about TEM, Alexander Hepting for his efforts with the temperature-controlled measurement chamber, and Dominik Hühn for proofreading the manuscript.

Supporting Information Available: Full methodology and additional data are available free of charge via the Internet at <http://pubs.acs.org>.

REFERENCES AND NOTES

- Nel, A. E.; Madler, L.; Velegol, D.; Xia, T.; Hoek, E. M. V.; Somasundaran, P.; Klaessig, F.; Castranova, V.; Thompson, M. Understanding Biophysicochemical Interactions at the Nano-Bio Interface. *Nat. Mater.* **2009**, *8*, 543–557.
- Mahmoudi, M.; Lynch, I.; Ejtehadi, M. R.; Monopoli, M. P.; Bombelli, F. B.; Laurent, S. Protein-Nanoparticle Interactions: Opportunities and Challenges. *Chem. Rev.* **2011**, *111*, 5610–5637.
- Monopoli, M. P.; Walczyk, D.; Campbell, A.; Elia, G.; Lynch, I.; Bombelli, F. B.; Dawson, K. A. Physical-Chemical Aspects of Protein Corona: Relevance to *in Vitro* and *in Vivo* Biological Impacts of Nanoparticles. *J. Am. Chem. Soc.* **2011**, *133*, 2525–2534.
- Laurent, S.; Burtea, C.; Thirifays, C.; Hafeli, U. O.; Mahmoudi, M. Crucial Ignored Parameters on Nanotoxicology: The Importance of Toxicity Assay Modifications and "Cell Vision". *PLoS One* **2012**, *7*, e29997.
- Walczyk, D.; Bombelli, F. B.; Monopoli, M. P.; Lynch, I.; Dawson, K. A. What the Cell "Sees" in Bionanoscience. *J. Am. Chem. Soc.* **2010**, *132*, 5761–5768.
- Cedervall, T.; Lynch, I.; Foy, M.; Berggard, T.; Donnelly, S.; Cagney, G.; Linse, S.; Dawson, K. Detailed Identification of Plasma Proteins Adsorbed on Copolymer Nanoparticles. *Angew. Chem., Int. Ed.* **2007**, *46*, 5754–5756.
- Lundqvist, M.; Stigler, J.; Cedervall, T.; Berggard, T.; Flanagan, M. B.; Lynch, I.; Elia, G.; Dawson, K. The Evolution of the Protein Corona around Nanoparticles: A Test Study. *ACS Nano* **2011**, *5*, 7503–7509.
- Tenzen, S.; Docter, D.; Rosfa, S.; Wlodarski, A.; Kuharev, J.; Reikik, A.; Knauer, S. K.; Bantz, C.; Nawroth, T.; Bier, C.; *et al.* Nanoparticle Size Is a Critical Physicochemical Determinant of the Human Blood Plasma Corona: A Comprehensive Quantitative Proteomic Analysis. *ACS Nano* **2011**, *5*, 7155–7167.
- Maiorano, G.; Sabella, S.; Sorce, B.; Brunetti, V.; Malvindi, M. A.; Cingolani, R.; Pompa, P. P. Effects of Cell Culture Media on the Dynamic Formation of Protein-Nanoparticle Complexes and Influence on the Cellular Response. *ACS Nano* **2010**, *4*, 7481–7491.
- Gebauer, J. S.; Malissek, M.; Simon, S.; Knauer, S. K.; Maskos, M.; Stauber, R. H.; Peukert, W.; Treuel, L. Impact of the Nanoparticle-Protein Corona on Colloidal Stability and Protein Structure. *Langmuir* **2012**, *28*, 9673–9679.
- Casals, E.; Pfaller, T.; Duschl, A.; Oostingh, G. J.; Puentes, V. F. Time Evolution of the Nanoparticle Protein Corona. *ACS Nano* **2010**, *4*, 3623–3632.
- Milani, S.; Bombelli, F. B.; Pitek, A. S.; Dawson, K. A.; Radler, J. Reversible versus Irreversible Binding of Transferrin to Polystyrene Nanoparticles: Soft and Hard Corona. *ACS Nano* **2012**, *6*, 2532–2541.

13. Walkey, C. D.; Chan, W. C. Understanding and Controlling the Interaction of Nanomaterials with Proteins in a Physiological Environment. *Chem. Soc. Rev.* **2012**, *41*, 2780–2799.
14. Hühn, D.; Kantner, K.; Geidel, C.; Brandholt, S.; De Cock, I.; Soenen, S. J. H.; Rivera Gil, P.; Montenegro, J.-M.; Braeckmans, K.; Müllen, K.; *et al.* Polymer-Coated Nanoparticles Interacting with Proteins and Cells: Focusing on the Sign of the Net Charge. *ACS Nano* **2013**, *7*, 3253–3263.
15. Lesniak, A.; Campbell, A.; Monopoli, M. P.; Lynch, I.; Salvati, A.; Dawson, K. A. Serum Heat Inactivation Affects Protein Corona Composition and Nanoparticle Uptake. *Biomaterials* **2010**, *31*, 9511–9518.
16. Petersdorf, R. G. Chills and Fever. In *Harrison's Principles of Internal Medicine*; McGraw-Hill: New York, 1974.
17. Hasday, J. D.; Singh, I. S. Fever and the Heat Shock Response: Distinct, Partially Overlapping Processes. *Cell Stress Chaperones* **2000**, *5*, 471–480.
18. Rhoades, R. A.; Pflanzner, R. G. *Human Physiology*; Saunders College Publishing: Philadelphia, PA, 1989; pp 823–840.
19. Yang, J. M.; Yang, H.; Lin, L. W. Quantum Dot Nano Thermometers Reveal Heterogeneous Local Thermogenesis in Living Cells. *ACS Nano* **2011**, *5*, 5067–5071.
20. Donner, J. S.; Thompson, S. A.; Kreuzer, M. P.; Baffou, G.; Quidant, R. Mapping Intracellular Temperature Using Green Fluorescent Protein. *Nano Lett.* **2012**, *12*, 2107–2111.
21. Röcker, C.; Pötzl, M.; Zhang, F.; Parak, W. J.; Nienhaus, G. U. A Quantitative Fluorescence Study of Protein Monolayer Formation on Colloidal Nanoparticles. *Nat. Nanotechnol.* **2009**, *4*, 577–580.
22. Jiang, X.; Weise, S.; Hafner, M.; Röcker, C.; Zhang, F.; Parak, W. J.; Nienhaus, G. U. Quantitative Analysis of the Protein Corona on FePt Nanoparticles Formed by Transferrin Binding. *J. R. Soc., Interface* **2010**, *7*, S5–S13.
23. Lehmann, A. D.; Parak, W. J.; Zhang, F.; Ali, Z.; Röcker, C.; Nienhaus, G. U.; Gehr, P.; Rothen-Rutishauser, B. Fluorescent-Magnetic Hybrid Nanoparticles Induce a Dose-Dependent Increase in Proinflammatory Response in Lung Cells *in Vitro* Correlated with Intracellular Localization. *Small* **2010**, *6*, 753–762.
24. Maffre, P.; Nienhaus, K.; Amin, F.; Parak, W. J.; Nienhaus, G. U. Characterization of Protein Adsorption onto FePt Nanoparticles Using Dual-Focus Fluorescence Correlation Spectroscopy. *Beilstein J. Nanotechnol.* **2011**, *2*, 374–383.
25. Bailey, S.; Evans, R. W.; Garratt, R. C.; Gorinsky, B.; Hasnain, S.; Horsburgh, C.; Jhoti, H.; Lindley, P. F.; Mydin, A.; Sarra, R.; *et al.* Molecular-Structure of Serum Transferrin at 3.3-Å Resolution. *Biochemistry* **1988**, *27*, 5804–5812.
26. Mamdouh, Z.; Giocondi, M. C.; Laprade, R.; LeGrimellec, C. Temperature Dependence of Endocytosis in Renal Epithelial Cells in Culture. *Biochim. Biophys. Acta* **1996**, *1282*, 171–173.
27. Weigel, P. H.; Oka, J. A. Temperature-Dependence of Endocytosis Mediated by the Asialoglycoprotein Receptor in Isolated Rat Hepatocytes - Evidence for 2 Potentially Rate-Limiting Steps. *J. Biol. Chem.* **1981**, *256*, 2615–2617.
28. Hong, G. S.; Wu, J. Z.; Robinson, J. T.; Wang, H. L.; Zhang, B.; Dai, H. J. Three-Dimensional Imaging of Single Nanotube Molecule Endocytosis on Plasmonic Substrates. *Nat. Commun.* **2012**, *3*.
29. Jedlovszky-Hajdu, A.; Bombelli, F. B.; Monopoli, M. P.; Tombacz, E.; Dawson, K. A. Surface Coatings Shape the Protein Corona of Spions with Relevance to Their Application *in Vivo*. *Langmuir* **2012**, *28*, 14983–14991.
30. Lesniak, A.; Fenaroli, F.; Monopoli, M. R.; Aberg, C.; Dawson, K. A.; Salvati, A. Effects of the Presence or Absence of a Protein Corona on Silica Nanoparticle Uptake and Impact on Cells. *ACS Nano* **2012**, *6*, 5845–5857.
31. Mirshafiee, V.; Mahmoudi, M.; Lou, K.; Cheng, J.; Kraft, M. L. Protein Corona Significantly Reduces Active Targeting Yield. *Chem. Commun.* **2013**, *49*, 2557–2559.
32. Mahmoudi, M.; Laurent, S.; Shokrgozar, M. A.; Hosseinkhani, M. Toxicity Evaluations of Superparamagnetic Iron Oxide Nanoparticles: Cell "Vision" versus Physicochemical Properties of Nanoparticles. *ACS Nano* **2011**, *5*, 7263–7276.
33. Mahmoudi, M.; Saeedi-Eslami, S. N.; Shokrgozar, M. A.; Azadmanesh, K.; Hassanlou, M.; Kalhor, H. R.; Burtua, C.; Rothen-Rutishauser, B.; Laurent, S.; Sheibani, S.; *et al.* Cell "Vision": Complementary Factor of Protein Corona in Nanotoxicology. *Nanoscale* **2012**, *4*, 5461–5468.
34. Chithrani, B. D.; Chan, W. C. W. Elucidating the Mechanism of Cellular Uptake and Removal of Protein-Coated Gold Nanoparticles of Different Sizes and Shapes. *Nano Lett.* **2007**, *7*, 1542–1550.
35. Mahmoudi, M.; Simchi, A.; Milani, A.; Stroeve, P. Cell Toxicity of Superparamagnetic Iron Oxide Nanoparticles. *J. Colloid Interface Sci.* **2009**, *336*, 510–518.
36. Rivera Gil, P.; Yang, F.; Thomas, H.; Li, L.; Terfort, A.; Parak, W. J. Development of an Assay Based on Cell Counting with Quantum Dot Labels for Comparing Cell Adhesion within Cocultures. *Nano Today* **2011**, *6*, 20–27.
37. Schweiger, C.; Hartmann, R.; Zhang, F.; Parak, W. J.; Kissel, T.; Rivera Gil, P. Quantification of the Internalization Patterns of Superparamagnetic Iron Oxide Nanoparticles with Opposite Charge. *J. Nanobiotechnol.* **2012**, *10*, 28.
38. Semmling, M.; Kreft, O.; Muñoz Javier, A.; Sukhorukov, G. B.; Käs, J.; Parak, W. J. A Novel Flow-Cytometry-Based Assay for Cellular Uptake Studies of Polyelectrolyte Microcapsules. *Small* **2008**, *4*, 1763–1768.
39. Zhang, F.; Lees, E.; Amin, F.; Rivera Gil, P.; Yang, F.; Mulvaney, P.; Parak, W. J. Polymer-Coated Nanoparticles: A Universal Tool for Biolabelling Experiments. *Small* **2011**, *7*, 3113–3127.

The Cellular Interactions of PEGylated Gold Nanoparticles: Effect of PEGylation on Cellular Uptake and Cytotoxicity

Stefaan J. Soenen, Bella B. Manshian, Abuelmagd M. Abdelmonem, José-María Montenegro, Sisareuth Tan, Lieve Balcaen, Frank Vanhaecke, Alain R. Brisson, Wolfgang J. Parak,* Stefaan C. De Smedt,* and Kevin Braeckmans

Poly(ethylene glycol) (PEG) is frequently used to coat various medical nanoparticles (NPs). As PEG is known to minimize NP interactions with biological specimens, the question remains whether PEGylated NPs are intrinsically less toxic or whether this is caused by reduced NP uptake. In the present work, the effect of gold NP PEGylation on uptake by three cell types is compared and evaluated the effect on cell viability, oxidative stress, cell morphology, and functionality using a multiparametric methodology. The data reveal that PEGylation affects cellular NP uptake in a cell-type-dependent manner and influences toxicity by different mechanisms. At similar intracellular NP numbers, PEGylated NPs are found to yield higher levels of cell death, mostly by induction of oxidative stress. These findings reveal that PEGylation significantly reduces NP uptake, but that at similar functional (= cell-associated) NP levels, non-PEGylated NPs are better tolerated by the cells.

in vitro cell imaging, cancer therapy, cell transplantation, and as carriers for drug and/or gene delivery.^[1] There are no “naked” NPs in biological environments as their surface is always covered with organic matter.^[2] One frequently used intentional organic surface coating of NPs is based on poly(ethylene glycol) (PEG).^[3] This flexible molecule, available in various chain lengths and terminal functional groups, effectively shields the surface from the surrounding environment. Thereby, it provides colloidal stability by sterically hindering NP agglomeration.^[2] Furthermore, PEGylation of NPs under in vitro conditions has shown reduced cellular uptake and improved biocompatibility.^[4] Under in vivo conditions, PEGylation promotes

the in vivo blood circulation time of NPs by reducing their opsonization and thereby impeding clearance of the NPs by the reticuloendothelial system.^[4e,5] Recently, however, the use of PEG has been described to induce inflammation and cause hypersensitivity.^[5a] In vitro, the effect of PEG density and PEG chain length has been well studied with respect to their effect on cellular NP uptake,^[4d] where PEG has been shown to reduce

1. Introduction

The interest in the use of nanoparticles (NPs) for biomedical applications is vastly increasing owing to the wide plethora of enticing features that NPs possess.^[1] This makes them frequently studied as tools for improved noninvasive in vivo and

S. J. Soenen, S. C. De Smedt, K. Braeckmans
Lab of General Biochemistry and Physical Pharmacy
Faculty of Pharmaceutical Sciences
Ghent University
Harelbekestraat 72, B-9000, Gent, Belgium
Fax: + 32 9 264 81 89; + 49 6421 28 24131
E-mail: Stefaan.DeSmedt@UGent.be

S. J. Soenen, K. Braeckmans
Centre for Nano- and Biophotonics
Ghent University
Harelbekestraat 72, B-9000, Gent, Belgium

S. J. Soenen, B. B. Manshian
Biomedical MRI unit/MoSAIC
Department of Imaging and Pathology, KU Leuven,
Herestraat 49, B-3000, Leuven, Belgium

B. B. Manshian
DNA Damage Group, College of Medicine (Institute of Life Science)
Swansea University
Singleton Park, SA2 8PP, Swansea, UK

A. M. Abdelmonem, J.-M. Montenegro, W. J. Parak
Fachbereich Physik
Philipps University of Marburg
Renthof 7, D-35037, Marburg, Germany
E-mail: Wolfgang.Parak@physik.uni-marburg.de

S. Tan, A. R. Brisson
UMR-CBMN CNRS-Université Bordeaux-1,
F-33600, Pessac, France

L. Balcaen, F. Vanhaecke
Department of Analytical Chemistry
Ghent University
Krijgslaan 281-S12, B-9000, Ghent, Belgium

W. J. Parak
CIC biomaGUNE
Paseo Miramón 182, 20009, San Sebastián, Spain



DOI: 10.1002/ppsc.201300357

NP binding and associated uptake levels of NPs where the uptake kinetics of bound NPs were not affected.^[6] Indirectly, some studies have also pointed to a higher biocompatibility of PEGylated NPs, which is likely to be a direct result of the lower amount of cell-associated nanomaterials.^[4d] For cell labeling applications in which a minimal number of cell-internalized NPs is essential, it is as of yet unclear whether higher levels of PEGylated NPs would be a better choice than lower levels of non-PEGylated NPs (resulting in similar cellular NP levels) as little data are available on the effect of PEG on cell homeostasis at similar cellular NP levels.

Nanotoxicology is a complex field where minor changes in NP surface chemistry can drastically alter the interaction of NPs with cells.^[7] Therefore, it is of interest to investigate the effect of applying a PEG coating to Au NPs in terms of their cytotoxicity. PEG can be attached directly via thiol groups to the surface of Au NPs.^[4c,8] Alternatively, PEG can also be covalently attached to more complex NP surfaces, such as NPs stabilized with an amphiphilic polymer,^[9] for example, poly(isobutylene-*alt*-maleic anhydride)-dodecylamine (PMA). PMA-coated Au NPs were prepared, analogously as previously described.^[9b] Presence of PEG can be conveniently verified by retarded mobilities in gel electrophoresis experiments (see Supporting Information).^[2,9b]

The number of PEG molecules per NP can also be quantified by NMR.^[10]

2. Results and Discussion

2.1. Nanoparticle Characterization

It has to be noted that PEGylation does not only change the surface chemistry of NPs but also influences other physico-chemical parameters.^[2] Obviously, addition of PEG increases the hydrodynamic diameter of the NPs.^[9b] However, it also changes the surface charge of the NP by the complexation of cations.^[11] In addition, PEGylation, in general, improves the colloidal stability of NPs by introducing sterical repulsion between the NPs.^[2,12] In the present study, polymer (PMA)-coated Au NPs with a saturated methoxy-PEG (mPEG) shell were investigated and compared with the same Au NPs without PEG, which were analyzed in a previous study.^[13] Au NPs with a core diameter of 4.6 ± 1.1 nm were used (Figure 1). Whereas the polymer-coated Au NPs without saturated PEG shell had a hydrodynamic diameter of 12.6 ± 1.1 nm and a ζ -potential of

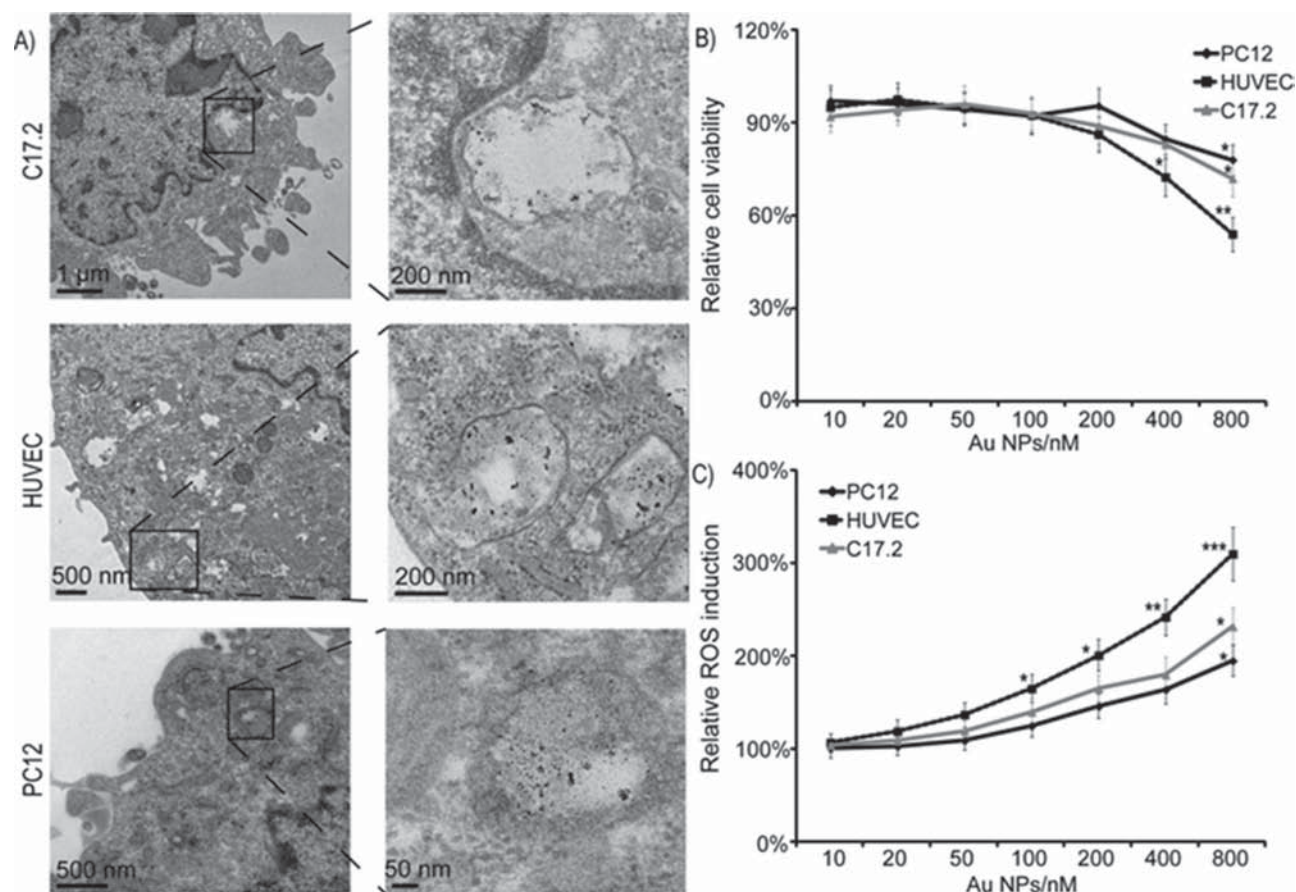


Figure 1. A) Transmission electron microscopy (TEM) images of C17.2, HUVEC, and PC12 cells exposed to 50×10^{-9} M of PEGylated Au NPs for 24 h revealing clear cellular uptake. B,C) Effects of PEGylated Au NPs on B) cell viability and C) reactive oxygen species (ROS) induction at different Au NP incubation concentrations. Data are expressed relative to untreated control cells as mean \pm SEM ($n = 5$). When appropriate, the degree of significance is indicated (*: $p < 0.05$, **: $p < 0.01$, ***: $p < 0.001$).

Table 1. Overview of the total NP numbers of non-PEGylated and PEGylated Au NPs at which significant levels of bio-effects were occurring.

Bio-effect	Non-PEGylated NPs		PEGylated NPs	
	Exposure conc. [$\times 10^{-9}$ M]	Intracellular NP amount [$\times 10^5$ NPs/cell]	Exposure conc. [$\times 10^{-9}$ M]	Intracellular NP amount [$\times 10^5$ NPs/cell]
<i>Cell death</i>	200	62	400	27.4
<i>ROS</i>	50	21	100	9.3
Cell morphology	50	21	400	27.4
<i>PC12 functionality</i>	20	9	100	4.5
<i>No toxicity observed</i>	10	6	50	3.5

*The total NP numbers of non-PEGylated and PEGylated Au NPs at which significant levels of bio-effects were occurring are given for both the concentration of NPs in the media upon incubation (expressed as m) as well as the intracellular number of NPs (expressed as 10^5 particles per cell). For all effects, the level of NPs in HUVEC cells was selected, apart from PC12 functionality, where the level is chosen in PC12 cells and the level where no toxicity is observed is the average value for all three cell types. Bio-effects, which occurred at lower intracellular NP numbers for PEGylated NPs, are indicated in italic, those which occurred at lower levels of non-PEGylated NPs are highlighted in bold.

-31.9 ± 5.2 mV.^[13] The addition of a saturated shell of methoxy-terminated PEG ($M_w = 2$ kDa) resulted in a hydrodynamic diameter of 21.7 ± 2.9 nm and a ζ -potential of -7.6 ± 0.8 mV, as measured by dynamic light scattering (DLS) using a zetasizer. The hydrodynamic diameter determined here for the PEGylated NPs is significantly higher than the ones determined with different methods in previous studies. Data indicate an increase in hydrodynamic diameter and a less negative ζ -potential due to the complexation of cations upon PEGylation.

To evaluate the effect of PEGylation on cellular uptake of NPs and its consequent cytotoxicity, a recently described multiparametric methodology was used.^[14] This methodology allows to define the noncytotoxic concentration of the NP tested for a variety of cell types and to identify the mechanisms underlying the NP's cytotoxic profile. Furthermore, this methodology enables to evaluate and compare the intrinsic toxicity levels and the mechanisms underlying these events. Although the Au NPs evaluated in this study are very interesting for biomedical research, their toxicological profile still has not been fully unraveled.^[15] Previously, the same Au NPs as used in this study, but without the PEG shell, were evaluated through this methodology, revealing NP-concentration-dependent cytotoxicity (see **Table 1**) and defining the nontoxic concentration of the NPs at 10×10^{-9} M.^[13] In the present work, identical Au NPs saturated with methoxy-terminated PEG ($M_w = 2$ kDa) are used to evaluate the effect of PEGylation on NP uptake and interactions with cultured cells.

2.2. Cellular Nanoparticle Uptake

In the present study, the PEGylated Au NPs were used to label three different cell types, being human umbilical vein endothelial cells (HUVECs), murine C17.2 neural progenitor cells, and rat PC12 pheochromocytoma cells. These cells have previously shown to be efficient model systems for cytotoxicity studies,^[16] where both HUVEC and C17.2 cells are extensively explored in cell transplantation studies and are thus often used for dosing with nanomaterials in order to facilitate in vivo cellular tracking.^[17] These cells additionally differ quite a bit, including human and rodent cells as well as endothelial and neural cell types, which are common target cell types. Therefore, these cells

can provide a nice overview of how cells, in general, interact with a certain type of NP. Additionally, these cells have been used in various previous studies, allowing a direct comparison of any toxicity data obtained for different types of materials.

In terms of uptake, PEGylated Au NPs were found to be taken up by all three cell types used. As evidenced by transmission electron microscopy (TEM) (Figure 1A), the Au NPs are typically located in endosomal structures, though it is known that they also can reach other intracellular compartments.^[4c] The images themselves reveal the presence of the NPs in structures consisting out of a unilamellar-enclosed cytoplasmic compartment, which is typical for endosomal compartments. Recently, the role of NPs in inducing autophagy as a key nanotoxicity mechanism has gained a lot of importance.^[18] The TEM structure revealed in these images, however, differs from those observed for autophagosomes,^[19] in that the latter compartments consist of a double lamellar membrane.^[18a] As such, no clear signs of autophagy have been observed, suggesting that autophagy likely does not play a major role in the cellular processing of these nanomaterials, but more research on this interesting phenomenon should be performed before any firm conclusions can be drawn.

An important finding in this regard is the localization of the NPs with endosomal compartments, which is similar to the localization observed for the non-PEGylated Au NPs.^[13] This finding reveals that PEGylation of the Au NPs did not affect the intracellular distribution of the NPs and suggests that a similar uptake mechanism is involved. Although, in neither study, any NPs were observed in the cell nuclei, the transfer of a limited number of NPs toward the nuclear region cannot be ruled out completely and may also follow a dose-dependent trend.^[20] The similar intracellular distribution of the NPs is of great importance for a direct comparison of any toxicological effects as the nature and degree of any effects observed depends on the exact intracellular location of the NPs.^[20]

The TEM images qualitatively show large differences in the levels of NP uptake between the different cell types, where HUVECs have the highest uptake levels, followed by C17.2 and PC12 cells. This qualitative measurement was further confirmed by quantitative determination of cellular NP levels by inductively coupled plasma-mass spectrometry (ICP-MS) after 24 h (Table S2, Supporting Information). A similar

trend was observed and the uptake efficacy of HUVECs was approximately twofold higher than that of the C17.2 and PC12 cells. These data are in sharp contrast with the data for non-PEGylated Au NPs, as shown in Table 1. For non-PEGylated NPs, C17.2 and HUVEC cells had similar uptake levels, where the addition of PEG has significantly reduced the uptake of the NPs in all cell types,^[13] in accordance with previous studies.^[4c] However, the extent of the effects of PEGylation on NP uptake is clearly cell type-dependent, where for HUVECs, maximally a fourfold reduction is observed, compared with an eightfold reduction for PC12 cells and a tenfold reduction in C17.2 cells. These data clearly indicate that the effect of PEGylation on NP uptake can vary significantly between different cell types and that specific targeting will be significantly mediated by PEGylation of the NPs.

2.3. Effect of PEGylated Nanoparticles on Cell Viability and Oxidative Stress

After 24 h of incubation, cell viability was found to be affected at high Au NPs doses (starting from 400×10^{-9} M of exposure concentrations) and was found to be cell type-dependent. These data were in correlation with the cell uptake levels (Figure 1B), resulting in highest toxicity levels for HUVEC cells compared with PC12 or C17.2 cells. Similarly, a concentration-dependent induction of reactive oxygen species (ROS) was observed (Figure 1C) in all three cell lines. Interestingly, the addition of 5×10^{-3} M *N*-acetylcysteine (NAC), an FDA-approved free-radical scavenger, completely inhibited ROS induction and restored cell viability (Figure S9, Supporting Information). Furthermore, high NP levels were found to affect mitochondrial membrane potential, cytoplasmic Ca^{2+} levels, and DNA damage (Figure 2) that are important pathways involved in ROS-dependent cell death.^[21] Compared with non-PEGylated Au NPs, the induction of ROS at identical incubation doses was approximately 1.7-fold lower,^[13] which is in line with other studies where PEGylation of NPs resulted in a lower induction of oxidative stress.^[22] However, more interestingly, when comparing similar intracellular NP levels (as determined by ICP-MS) the induction of ROS was approximately 1.6-fold higher for PEGylated NPs in all three cell types. These findings are in contrast with the general belief that PEGylation reduces ROS levels and can be explained by the fact that, here, ROS levels were compared at similar intracellular levels of PEGylated and non-PEGylated NPs whereas in nearly

all previous studies, NPs have been compared with respect to their exposure concentrations.^[4d,22] However, in plant cells, PEG chains have been found to induce ROS indirectly as a result of altering water stress levels.^[23] The precise mechanism for the enhanced ROS production here remains unclear but can probably be attributed to the altered physicochemical properties of the NPs upon PEGylation. One important contributor to the level of oxidative stress may be p53, a key transcription regulator for many intracellular pathways including inflammation and oxidative stress sensing.^[24] It would be interesting to see whether PEG chains in themselves are ROS inducing and whether this involved p53 activity. Taken together, these data point to the importance of ROS in the toxicological profile of the PEGylated Au NPs, with a cell type-dependent correlation between ROS levels, stemming from the intracellular localization of the NPs and a reduction of cell viability.^[25] Interestingly, ROS-associated secondary effects, such as DNA damage, are significantly higher for PEGylated NPs than for their corresponding non-PEGylated counterparts for similar intracellular NP levels (= the number of NPs per cell).

2.4. Effect of PEGylated Nanoparticles on Cell Morphology

Apart from ROS, which is an important mediator in the toxic potential of NPs,^[26] several other mechanisms have been suggested to play an important role, such as cellular deformations and effects on the cell cytoskeleton architecture.^[27] To further define the mechanisms underlying the toxicity of the PEGylated Au NPs, the effect of the NPs on HUVEC cell morphology and cytoskeleton architecture was analyzed as described previously (Figure 3).^[16] For this analysis, only the HUVEC cells were considered as the rounded PC12 and C17.2 cells are intrinsically far less spread and are therefore not well suited for this type of analysis. The functionality of these cell types is investigated using specific assays later on in this manuscript. No effect on cell morphology or cytoskeleton architecture could be observed at nontoxic concentrations of the PEGylated Au NPs, i.e., up to 400×10^{-9} M (added exposure concentration). These observations were different to the results obtained for various types of non-PEGylated Au NPs,^[28] including PMA-coated Au NPs, where cellular deformations were already observed at 50×10^{-9} M.^[13] Interestingly, at 400×10^{-9} M (added exposure concentration) of PEGylated Au NPs, higher intracellular NP levels (1.3-fold) and higher ROS levels (1.6-fold) were found

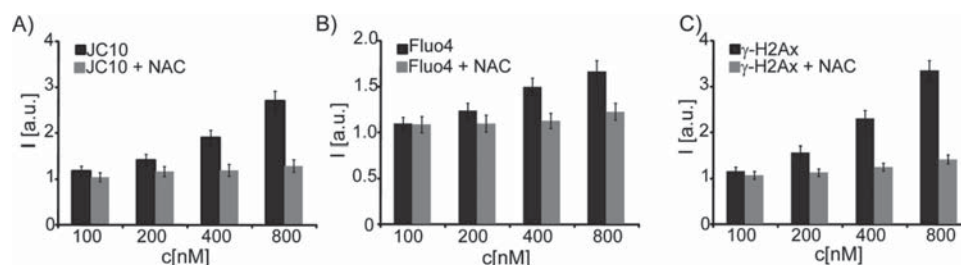


Figure 2. Effects of PEGylated Au NPs (incubation concentration $c \times 10^{-9}$ M) on HUVEC cell as given as relative signal intensities I [a.u.]. A) mitochondrial membrane potential, B) cytoplasmic calcium levels, and C) DNA double-strand breaks in the absence (dark gray) and presence of 5×10^{-3} M NAC (light gray), when cells were exposed to PEGylated Au NPs for 24 h at 100, 200, 400 or 800×10^{-9} M. Data are expressed relative to the values obtained for untreated control cells as mean \pm SEM ($n = 4$).

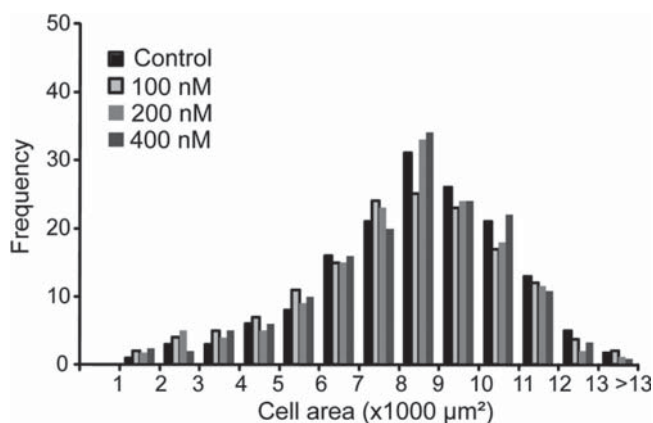


Figure 3. Histogram representing the distribution of cell areas of control HUVEC cells or cells exposed to PEGylated Au NPs at 100, 200, or 400×10^{-9} M incubation concentration for 24 h and analyzed at 24 h post-cell labeling, as described in the Supporting Information.

than for non-PEGylated Au NPs at 50×10^{-9} M (external concentration). However, even at higher intracellular NP levels, PEGylated NPs were not found to induce any morphological or cytoskeletal alterations (Table 1). These data suggest that the cellular morphological changes observed previously for the Au NPs are ROS independent and furthermore, the addition of PEG appears to be able to overcome these effects.

To test this more thoroughly, the effect of the PEGylated Au NPs on the expression and activation of two key signaling pathways [NF κ B and focal adhesion kinase (FAK)] was analyzed in the HUVEC cells. Whereas the NF κ B pathway is known to be an important mediator in ROS-induced signaling,^[29] the activation status of FAK is linked to the cytoskeletal architecture^[30]

and was previously shown not to be prone to direct ROS-induced signaling.^[16a,b] Figure 4A,B shows a clear concentration-dependent activation of the NF κ B pathway, which could be overcome by co-treatment with NAC, indicating a ROS dependence. No effect was seen on the expression or activation of FAK (Figure 4C,D), supporting our earlier findings that PEGylation of Au NPs protects the cells from cytoskeletal deformations, even at conditions where similar intracellular NP concentrations have been obtained (Table 1). In the latter experiment, PC12 cells were not included as these cells are only semi-attached and therefore only form minimal focal adhesions. The level of FAK activation is closely linked to the formation of fully mature focal adhesions, which results in minimal levels of active FAK in the PC12 cells.

2.5. Effect of PEGylated Nanoparticles on Cell Functionality

As a final test, the effect of the PEGylated Au NPs on PC12 functionality was assessed, where the ability of the cells to induce the outgrowth of neurites was evaluated as described elsewhere.^[31] Figure 5 shows a clear concentration-dependent inhibition of PC12 functionality, where effects were noticeable from 100×10^{-9} M, which is in line with the onset of ROS induction. These data show that the induced ROS effects can result in reduced cell functionality, which has important consequences for the use of such labeled cells for any biomedical purposes. Based on these results, we define the nontoxic concentration of PEG Au NPs as 50×10^{-9} M (exposure concentration), which is higher than the nontoxic concentration of 10×10^{-9} M (exposure concentration) for non-PEGylated Au NPs, which was obtained using exactly the same methodology.^[13] However, given the lower uptake efficiency of cells for

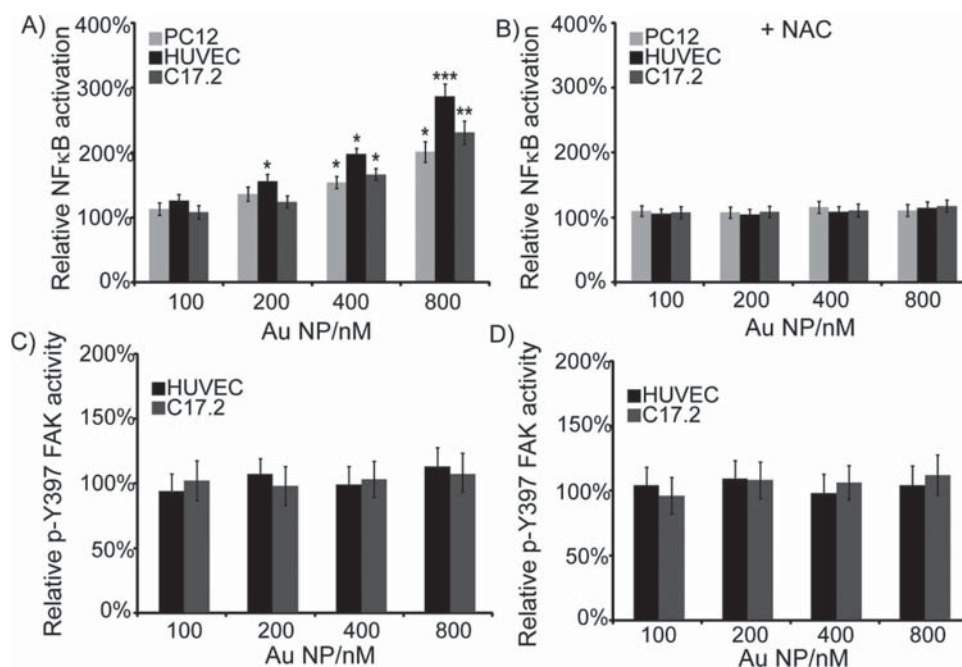


Figure 4. The effects of PEGylated Au NPs in dependence of incubation concentration on activation of A,B) NF κ B and C,D) FAK in the A,C) absence or B,D) presence of NAC, a ROS scavenger.

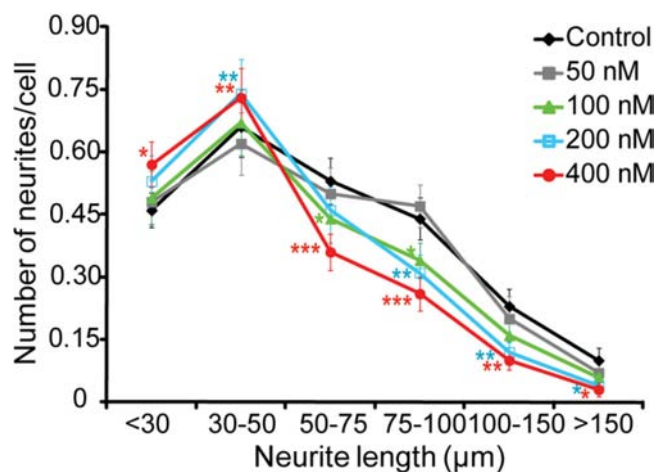


Figure 5. Effect of PEGylated Au NPs on neurite induction from PC12 cells exposed to incubation concentrations of Au NPs of 0, 50, 100, 200, and 400×10^{-9} M for 24 h followed by 48 h exposure to nerve growth factor. Data are expressed as the total number of neurites of a certain length per cell as mean \pm SEM ($n = 4$).

PEGylated Au NPs, the higher level of PEGylated Au NPs in the incubation medium does not correspond to a higher level of intracellular Au NPs, as is also shown in Tables S2 and S3 (Supporting Information).

Overall, the current study highlights the importance of a thorough investigation into the effect of altering the surface chemistry of the NP of interest with regard to its effect on cultured cells. PEGylation in itself will drastically alter the chemistry of the NP surface. As shown in Section 2.1., addition of the PEG chains increases the hydrodynamic diameter and alters the surface charge of the NPs. Additionally, the colloidal stability of NPs is generally improved by PEGylation due to steric repulsion between NPs. The effect of PEGylation therefore influences quite a large number of different parameters, all known to affect cellular interaction.^[11,12] However, the precise effect of any of these individual parameters is hard to predict as all of them are closely linked. For instance, with regard to cellular uptake, the enhanced colloidal stability likely results in higher uptake values for smaller NPs, where extensive agglomeration is known to impede NP uptake.^[32] Alternatively, the increase in hydrodynamic diameter, the decrease in surface charge, and the presence of a long, flexible hydrocarbon chain that hinders the actual NPs of coming into close contact with the cell membrane will all impede cellular uptake. One key aspect of the addition of PEG chains is their influence on the protein corona, which forms around any type of nanomaterial in serum-containing media.^[33] Given the loss in charges and the flexible nature of the PEG chains, PEGylation is known to impede protein binding onto the particle surface.^[34] Therefore, the protein corona formed around non-PEGylated and PEGylated particles will be quite different. This protein corona is however extremely important in determining “cell vision,” i.e., the way in which cells will see the foreign NPs and how they will interact with them.^[35] This effect of PEGylation is therefore quite important and cannot be ignored when trying to understand the precise mechanisms behind the observed effects in our study.

3. Conclusion

The data summarized in Table 1 indicate that on average, for the different cell types, higher intracellular levels of non-PEGylated Au NPs can be achieved without inducing any toxic effects than is the case for PEGylated NPs. In general, these data therefore show that the reduced toxic effects of NPs upon PEGylation is primarily driven by a significant drop in cellular NP uptake levels, as at least for PMA-coated Au NPs, the intrinsic toxicity for similar intracellular numbers of NPs appears to be higher upon PEGylation. Interestingly, PEGylation of the Au NPs had a clear cell type-dependent effect on NP uptake and toxicity. In addition, in terms of toxicity mechanisms, PEGylation of NPs was found to affect the underlying causes, resulting in higher ROS levels and higher secondary ROS mechanisms but no effect on cytoskeletal aberrations for similar intracellular levels of PEGylated NPs compared with non-PEGylated NPs (Table 1). The exact reason for this currently remains unclear, but the addition of a flexible shielding layer appears to drastically alter cell–NP interactions and requires further studies to shed more light on this complex issue. The question therefore remains whether PEGylation of NPs is actually beneficial or potentially hazardous for in vitro labeling of cultured cells.

4. Experimental Section

A full experimental methodology including NP synthesis and characterization, and setup of cell–NP interaction studies can be found in the Supporting Information that accompanies this manuscript.

Supporting Information

Supporting Information is available from the Wiley Online Library or from the author.

Acknowledgements

S.J.S. and L.B. are post-doctoral fellows from the FWO Vlaanderen. The authors thank the FWO (Krediet aan Navorsers Grant to S.J.S.), the Center for Nano- and Biophotonics, and HFSP (project RGP0052/2012 to W.J.P.) for financial support.

Received: November 11, 2013

Revised: December 16, 2013

Published online:

- [1] M. L. Etheridge, S. A. Campbell, A. G. Erdman, C. L. Haynes, S. M. Wolf, J. McCullough, *Nanomed. Nanotechnol.* **2013**, *9*, 1.
- [2] P. Rivera-Gil, D. J. De Aberasturi, V. Wulf, B. Pelaz, P. Del Pino, Y. Y. Zhao, J. M. De La Fuente, I. R. De Larramendi, T. Rojo, X. J. Liang, W. J. Parak, *Acc. Chem. Res.* **2013**, *46*, 743.
- [3] A. S. Karakoti, S. Das, S. Thevuthasan, S. Seal, *Angew. Chem Int. Ed.* **2011**, *50*, 1980.
- [4] a) Arnida, A. Malugin, H. Ghandehari, *J. Appl. Toxicol.* **2010**, *30*, 212; b) S. Harakeh, R. M. Abdel-Massih, P. Rivera Gil, R. A. Sperling, A. Meinhardt, A. Niedwiecki, M. Rath, W. J. Parak, E. Baydoun, *Nanotoxicology* **2010**, *4*, 177; c) C. Brandenberger, C. Muhlfeld, Z. Ali,

- A. G. Lenz, O. Schmid, W. J. Parak, P. Gehr, B. Rothen-Rutishauser, *Small* **2010**, *6*, 1669; d) K. Lee, H. Lee, K. W. Lee, T. G. Park, *Biomaterials* **2011**, *32*, 2556; e) Y. Sheng, Y. Yuan, C. S. Liu, X. Y. Tao, X. Q. Shan, F. Xu, *J. Mater. Sci., Mater. M* **2009**, *20*, 1881.
- [5] a) K. Knop, R. Hoogenboom, D. Fischer, U. S. Schubert, *Angew. Chem Int. Ed.* **2010**, *49*, 6288; b) B. Ballou, B. C. Lagerholm, L. A. Ernst, M. P. Bruchez, A. S. Waggoner, *Bioconjugate Chem.* **2004**, *15*, 79; c) T. J. Daou, L. Li, P. Reiss, V. Jossierand, I. Texier, *Langmuir* **2009**, *25*, 3040; d) J. Lipka, M. Semmler-Behnke, R. A. Sperling, A. Wenk, S. Takenaka, C. Schleh, T. Kissel, W. J. Parak, W. G. Kreyline, *Biomaterials* **2010**, *31*, 6574.
- [6] M. S. Martina, V. Nicolas, C. Wilhelm, C. Meenager, G. Barratt, S. Lesieur, *Biomaterials* **2007**, *28*, 4143.
- [7] H. F. Krug, P. Wick, *Angew. Chem Int. Ed.* **2011**, *50*, 1260.
- [8] A. G. Kanaras, F. S. Kamounah, K. Schaumburg, C. J. Kiely, M. Brust, *Chem. Commun.* **2002**, *20*, 2294.
- [9] a) C. A. J. Lin, R. A. Sperling, J. K. Li, T. Y. Yang, P. Y. Li, M. Zanella, W. H. Chang, W. G. J. Parak, *Small* **2008**, *4*, 334; b) R. A. Sperling, T. Liedl, S. Duhr, S. Kudera, M. Zanella, C. A. J. Lin, W. H. Chang, D. Braun, W. J. Parak, *J. Phys. Chem. C* **2007**, *111*, 11552; c) T. Pellegrino, R. A. Sperling, A. P. Alivisatos, W. J. Parak, *J. Biomed. Biotechnol.* **2007**, *2007*, 26796; d) K. Van Hoecke, K. A. C. De Schampelaere, Z. Ali, F. Zhang, A. Elsaesser, P. Rivera-Gil, W. J. Parak, G. Smagghe, C. V. Howard, C. R. Janssen, *Nanotoxicology* **2013**, *7*, 37.
- [10] A. Riedinger, F. Zhang, F. Dommershausen, C. Rucker, S. Brandholt, G. U. Nienhaus, U. Koert, W. J. Parak, *Small* **2010**, *6*, 2590.
- [11] R. A. Sperling, T. Pellegrino, J. K. Li, W. H. Chang, W. J. Parak, *Adv. Funct. Mater.* **2006**, *16*, 943.
- [12] T. Pellegrino, S. Kudera, T. Liedl, A. M. Javier, L. Manna, W. J. Parak, *Small* **2005**, *1*, 48.
- [13] S. J. Soenen, B. Manshian, J. M. Montenegro, F. Amin, B. Meermann, T. Thiron, M. Cornelissen, F. Vanhaecke, S. Doak, W. J. Parak, S. De Smedt, K. Braeckmans, *ACS Nano* **2012**, *6*, 5767.
- [14] S. J. Soenen, P. Rivera-Gil, J. M. Montenegro, W. J. Parak, S. C. De Smedt, K. Braeckmans, *Nano Today* **2011**, *6*, 446.
- [15] D. A. Giljohann, D. S. Seferos, W. L. Daniel, M. D. Massich, P. C. Patel, C. A. Mirkin, *Angew. Chem Int. Ed.* **2010**, *49*, 3280.
- [16] a) S. J. H. Soenen, U. Himmelreich, N. Nuytten, M. De Cuyper, *Biomaterials* **2011**, *32*, 195; b) S. J. Soenen, J. Demeester, S. C. De Smedt, K. Braeckmans, *Biomaterials* **2012**, *33*, 4882; c) S. J. Soenen, B. Manshian, S. H. Doak, S. C. De Smedt, K. Braeckmans, *Acta Biomater.* **2013**, *9*, 9183.
- [17] a) Y. Liang, P. Walczak, J. W. Bulte, *Biomaterials* **2013**, *34*, 5521; b) S. J. Soenen, S. F. De Meyer, T. Dresselaers, G. Vande Velde, I. M. Pareyn, K. Braeckmans, M. De Cuyper, U. Himmelreich, K. I. Vanhoorelbeke, *Biomaterials* **2011**, *32*, 4140.
- [18] a) F. T. Andon, B. Fadeel, *Acc. Chem. Res.* **2013**, *46*, 733; b) K. Peynshaert, B. B. Manshian, F. Joris, K. Braeckmans, S. De Smedt, J. Demeester, S. J. Soenen, *Chem. Rev.* **2014**.
- [19] Y. Zhao, J. L. Howe, Z. Yu, D. T. Leong, J. J. Chu, J. S. Loo, K. W. Ng, *Small* **2013**, *9*, 387.
- [20] C. Y. Tay, W. Fang, M. I. Setyawati, C. P. Sum, J. Xie, K. W. Ng, X. Chen, C. H. L. Hong, D. T. Leong, *Part. Part. Syst. Charact.* **2013**, *30*, 783.
- [21] G. Bin Park, Y. S. Kim, H. K. Lee, H. Song, S. Kim, D. H. Cho, D. Y. Hur, *Cancer Lett.* **2011**, *313*, 235.
- [22] M. Yu, S. H. Huang, K. J. Yu, A. M. Clyne, *Int. J. Mol. Sci.* **2012**, *13*, 5554.
- [23] M. Y. Jiang, J. H. Zhang, *J. Exp. Bot.* **2002**, *53*, 2401.
- [24] M. I. Setyawati, C. Y. Tay, D. T. Leong, *Biomaterials* **2013**, *34*, 10133.
- [25] a) S. J. Soenen, J. Demeester, S. C. De Smedt, K. Braeckmans, *Nano Today* **2013**, *8*, 121; b) F. Joris, B. Manshian, K. Peynshaert, S. C. De Smedt, K. Braeckmans, S. J. Soenen, *Chem. Soc. Rev.* **2013**, *42*, 8339.
- [26] A. Nel, T. Xia, L. Madler, N. Li, *Science* **2006**, *311*, 622.
- [27] M. Tarantola, A. Pietuch, D. Schneider, J. Rother, E. Sunnick, C. Rosman, S. Pierrat, C. Sonnichsen, J. Wegener, A. Janshoff, *Nanotoxicology* **2011**, *5*, 254.
- [28] a) N. Pernodet, X. Fang, Y. Sun, A. Bakhtina, A. Ramakrishnan, J. Sokolov, A. Ulman, M. Rafailovich, *Small* **2006**, *2*, 766; b) T. Mironava, M. Hadjiargyrou, M. Simon, V. Jurukovski, M. H. Rafailovich, *Nanotoxicology* **2010**, *4*, 120.
- [29] A. C. Chen, P. R. Arany, Y. Y. Huang, E. M. Tomkinson, S. K. Sharma, G. B. Kharkwal, T. Saleem, D. Mooney, F. E. Yull, T. S. Blackwell, M. R. Hamblin, *PLoS One* **2011**, *6*, e22453.
- [30] B. Fabry, A. H. Klemm, S. Kienle, T. E. Schaffer, W. H. Goldmann, *Biophys. J.* **2011**, *101*, 2131.
- [31] a) S. J. H. Soenen, M. De Cuyper, *Contrast Media Mol. I* **2011**, *6*, 153; b) T. R. Pisanic, J. D. Blackwell, V. I. Shubayev, R. R. Finones, S. Jin, *Biomaterials* **2007**, *28*, 2572.
- [32] C. Kirchner, T. Liedl, S. Kudera, T. Pellegrino, A. Muñoz Javier, H. E. Gaub, S. Stölzle, N. Fertig, W. J. Parak, *Nano Lett.* **2005**, *5*, 331.
- [33] S. Tenzer, D. Docter, J. Kuharev, A. Musyanovych, V. Fetz, R. Hecht, F. Schlenk, D. Fischer, K. Kiouptsi, C. Reinhardt, K. Landfester, H. Schild, M. Maskos, S. K. Knauer, R. H. Stauber, *Nat. Nanotechnol.* **2013**, *8*, 772.
- [34] J. L. Betker, J. Gomez, T. J. Anchordoquy, *J. Controlled Release* **2013**, *171*, 261.
- [35] S. Laurent, C. Burtea, C. Thirifays, U. O. Häfeli, M. Mahmoudi, *PLoS One* **2012**, *7*, e29997.



The effect of nanoparticle degradation on poly(methacrylic acid)-coated quantum dot toxicity: The importance of particle functionality assessment in toxicology



Stefaan J. Soenen^{a,b}, José-Maria Montenegro^c, Abuelmagd M. Abdelmonem^c, Bella B. Manshian^d, Shareen H. Doak^d, Wolfgang J. Parak^{c,e}, Stefaan C. De Smedt^{a,*}, Kevin Braeckmans^{a,b}

^a Faculty of Pharmaceutical Sciences, Ghent University, Ghent, Belgium

^b Center of Nano- and Biophotonics, Ghent University, Ghent, Belgium

^c Department of Physics, Philipps University of Marburg, Marburg, Germany

^d DNA Damage Group, Swansea University, Swansea, UK

^e CIC biomaGUNE, San Sebastián, Spain

ARTICLE INFO

Article history:

Received 16 May 2013

Received in revised form 24 September 2013

Accepted 30 September 2013

Available online 10 October 2013

Keywords:

Quantum dot

Cadmium

Toxicity

Degradation

Particle functionality

ABSTRACT

Colloidal semiconductor nanoparticles (quantum dots) have attracted a lot of interest in technological and biomedical research, given their potent fluorescent properties. However, the use of heavy-metal-containing nanoparticles remains an issue of debate. The possible toxic effects of quantum dots remain a hot research topic and several questions such as possible intracellular degradation of quantum dots and the effect thereof on both cell viability and particle functionality remain unresolved. In the present work, poly(methacrylic acid)-coated CdSe/ZnS quantum dots were synthesized and characterized, after which their effects on cultured cells were evaluated using a multiparametric setup. The data reveal that the quantum dots are taken up through endocytosis and when exposed to the low pH of the endosomal structures, they partially degrade and release cadmium ions, which lowers their fluorescence intensity and augments particle toxicity. Using the multiparametric method, the quantum dots were evaluated at non-toxic doses in terms of their ability to visualize labeled cells for longer time periods. The data revealed that comparing different particles in terms of their applied dose is challenging, likely due to difficulties in obtaining accurate nanoparticle concentrations, but evaluating particle toxicity in terms of their biological functionality enables an easy and straightforward comparison.

© 2013 Acta Materialia Inc. Published by Elsevier Ltd. All rights reserved.

1. Introduction

The use of colloidal nanoparticles (NPs) in technological and biomedical applications is vastly increasing [1,2]. There are currently over 800 consumer products containing NPs, including many foods, beverages and cosmetics. The nanotechnology industry is growing very rapidly, and is predicted to have a total value of US\$3.1 trillion by the year 2015 [3]. Currently, NPs are omnipresent in many different consumer products, but the number of biomedical applications is still limited due to several questions remaining on the possible induction of toxic side-effects by NPs [4–6]. Uncertainties regarding the safety of NPs are being fed by the continuous discovery of new pathways and mechanisms by which NPs may interfere with cellular wellbeing, which can either be beneficial for biomedical purposes or pose serious threats to human health [7]. One example is the recent finding that NPs can

induce DNA damage and chromosome mutations, as shown for carbon nanotubes that were found to selectively stabilize human telomeric i-motif DNA and inhibit telomerase activity [8]. To progress towards use of NPs without risks, more data are required on the (toxic) effects of NPs on cells, tissues and whole organisms [9]. In order to fulfill the current needs in nanotoxicity research, NPs should be screened rapidly on a variety of cells under standardized conditions, enabling a comparison of data obtained for different materials and between different research groups [10]. In this view, we recently established a multiparametric methodology that looks at the interactions between cultured cells and NPs in order to get a profound knowledge of the possible effects of these materials on cultured cells [11]. Using a variety of cell types that have shown great potential for nanotoxicity research [12–14], being primary human umbilical vein endothelial cells (HUVECs), murine C17.2 neural progenitor cells and rat PC12 pheochromocytoma cells, the obtained results are representative for a wide variety of cell types. This methodology therefore allows for determining the non-cytotoxic levels of NPs (i.e. the concentration of NPs

* Corresponding author. Tel.: +32 9264 8076; fax: +32 9264 8189.

E-mail address: Stefaan.Desmedt@ugent.be (S.C. De Smedt).

appropriate for cell labeling applications) and additionally helps in unraveling the mechanisms that are involved in the cytotoxic profile of the NPs under investigation. Furthermore, by comparing the data obtained against data for other NPs that have been tested under identical conditions, physicochemical features of the NPs that contribute to their cytotoxicity can be defined, paving the way for a more rational and safer NP design.

One important aspect with respect to rigorous NP toxicity testing is the design, purification and characterization of the NPs under investigation [15]. If any cytotoxic effects are to be ascribed to specific physicochemical features of the NPs, it is of utmost importance to test well-characterized NPs free of contaminants or impurities [16]. In this direction, poly(methacrylic acid) (PMA)-coated CdSe/ZnS core-shell quantum dots (QDots) are a useful system, as these NPs are well defined and have been extensively characterized. QDots are small semiconductor NPs that possess several exciting features such as high photostability, narrow and tunable emission spectra and high brightness [17]. Owing to these properties, QDots have shown great potential for many biomedical applications, including cell labeling applications [18–21], long-term tracking of (single) molecules [22], in vivo imaging [23,24] and photodynamic therapy [25,26]. However, despite their excellent photophysical properties, their toxicity, in particular due to the release of Cd²⁺ ions [27,28], remains an issue of debate [29,30].

2. Materials and methods

2.1. Nanoparticles

CdSe/ZnS colloidal nanoparticles were synthesized and made water-soluble as described in the [Supplementary information](#). The nanoparticles were carefully characterized as also described in full detail in the accompanying [Supplementary information](#).

2.2. Cell culture

C17.2 neural progenitor cells and PC12 cells are maintained in high glucose Dulbecco's modified Eagle's medium (DMEM), supplemented with 10% fetal bovine serum, 5% horse serum, 2 mM L-glutamine and 1% penicillin/streptomycin (Gibco, Invitrogen, Merelbeke, Belgium). Cells were maintained in a humidified atmosphere at 5% CO₂ and fresh medium was given every other day. C17.2 cells were passaged (1/10) when reaching 90% confluency. PC12 cells were grown in 25 cm² cell culture flasks (Corning, Amsterdam, The Netherlands) that were coated with collagen (rat tail collagen type I, Invitrogen, Belgium) and passaged (1/5) when growing in small clumps (~5 cells per clump and reaching 70–80% confluency). Fresh medium was given every other day.

For some long-term experiments, such as the effect of intracellular pH on Cd²⁺ in time, and the toxicity derived from this free Cd²⁺, non-proliferating cell cultures are required as dilution of the number of particles per cell due to cell division abolishes any attempt to analyze these parameters. Therefore, in the current study, non-proliferating cell populations were established to enable the investigation the time-dependent effects of the intracellular environment on QDot functionality and toxicity. Next to analyzing these effects without the problem of exponential QDot dilution, these conditions also better mimic the in vivo conditions where autologous cells or stem cells after transplantation show minimal proliferation. To establish non-proliferating cell populations, cells were exposed with 60 μM Apigenin (Sigma-Aldrich, Bornem, Belgium) together with the Sil NP exposure. After removal of the medium, fresh media containing 60 μM Apigenin were used, where media were replaced for 50% every other day with fresh

Apigenin-containing medium for the duration of the experiments. Under these conditions, cell death was found to be minimal and cell proliferation was reduced to ~9% of the normal value. Furthermore, removal of the medium with normal cell culture medium not containing any Apigenin resulted in a recovery of cell proliferation to near-control levels after ~3 days.

Primary human umbilical vein endothelial cells (HUVECs) were kindly provided by Dr. Aldo Ferrari (ETH Zurich, Switzerland). For cultivation, cells were kept in 75 cm² cell culture flasks (Corning, Amsterdam, The Netherlands) coated with collagen (rat tail collagen type I, Invitrogen, Belgium) prior to cell seeding. The cells were maintained in endothelial cell basal growth medium and growth supplement (Cell Applications, Tebu-Bio, Le Perray en Yvelines, France) and passaged (1/5) when reaching 80–90% confluency. Every other day, fresh medium was given. For HUVEC cells, the Apigenin treatment resulted in slight toxic effects and proliferation could be impeded better using serum-free conditions. To establish non-proliferating HUVEC cultures, cells were given endothelial cell serum-free defined medium (Cell Applications, Tebu-Bio, Le Perray en Yvelines, France) when reaching high levels of confluency. Confluent HUVEC monolayers could then be maintained for at least 1 week without any observable signs of cell death or reactive oxygen species (ROS) induction.

2.3. Cell-nanoparticle interaction studies

The following cell-NP interactions were studied; a full methodology can be found in the [Supplementary information](#) that accompanies this paper.

2.3.1. Intracellular QDot localization

To evaluate possible endosomal localization of the QDots, C17.2, HUVEC or PC12 cells were seeded in collagen-coated 35 mm diameter glass bottom MatTek dishes (MatTek Corporation, Ashland, MA, USA) at 4 × 10⁴ cells per dish in 1.5 ml of full culture medium. Cells were allowed to settle overnight prior to being incubated with the lipophilic membrane tracer dye 3,3'-dioctadecyloxycarbocyanine perchlorate (DiO; Molecular Probes, Invitrogen, Belgium) for 30 min at 2.5 μg ml⁻¹. Next, a mixture of the QDot at 15 nM and the lipophilic dye DiO (2.5 μg ml⁻¹) in full cell medium was prepared and added to the cells for 30 min at 37 °C at a humidified atmosphere. Subsequently, the media were removed, cells washed three times with phosphate buffered saline (PBS) and fixated with 4% paraformaldehyde (PFA) for 15 min at ambient temperature prior to visualization using a Nikon Cs1 confocal laser scanning microscope (Nikon Belux, Brussels, Belgium).

Cellular uptake of the PMA-coated QDots was also evaluated using transmission electron microscopy (TEM), following 24 h exposure of the various cell types to 10 nM of QDots, as described in the [Supplementary information](#).

2.3.2. Quantitative determination of cellular QDot levels

The number of QDots per cell was determined by measuring the cellular Cd²⁺ levels using the Measure-iT kit (Molecular Probes, Invitrogen, Merelbeke, Belgium) as described in the [Supplementary information](#).

2.3.3. Effect of pH on QDot stability

The effect of pH on QDot fluorescence intensity and release of Cd²⁺ ions was determined by preparing three buffer solutions of pH 7.4, 5.5 and 4.5, after which the QDots (5 nM) were exposed to these buffers for a period up to 5 days. Every 24 h, fluorescence intensity or Cd²⁺ release was measured, as described in the [Supplementary information](#).

2.3.4. Determination of intracellular QDot degradation

C17.2, PC12 or HUVEC cells were seeded in 75 cm² cell culture flasks at a density of 2.5×10^6 cells per flask and allowed to settle overnight. Then, the cells were given fresh medium containing 10 nM of QDots and allowed to incubate for 24 h. For C17.2 and PC12 cells, their medium was supplemented with 60 μ M Apigenin. For HUVEC cells, cells were allowed to form confluent monolayers after cell labeling and medium was transferred to serum-free defined medium for culture of non-proliferative HUVECs. Next, media were aspirated, cells washed twice with PBS and fresh media optimized for non-proliferating cultures was given as described above, after which the cells were kept in culture for the duration of the experiment. After 1, 2, 3, 4 and 5 days of further culture under proliferation-restricted conditions, cells from the various flasks were lifted and centrifuged at 0.4 rcf. The cells were redispersed in PBS and counted using a Bürker chamber. Then, 2×10^6 cells were taken, which were centrifuged again, after which 50 μ l of DMSO was added to every pellet to lyse all cells. A 10 μ l aliquot was collected from every sample and transferred to wells of a 96-well plate, after which 200 μ l per well of the Measure-iT kit was added and Cd²⁺ concentrations were measured according to the manufacturer's instructions (λ_{ex} : 490 nm; λ_{em} : 520 nm) using a Wallac Envision plate reader instrument. The Cd²⁺ concentrations were determined using the Cd²⁺ calibration curve which is part of the kit. Note that, as this is an end-point assay, the samples measured after 1, 2, 3, 4 and 5 days were all obtained from different flasks. Data are expressed as mean \pm SEM for three independent experiments.

Along with the determination of free cellular Cd²⁺ levels, the total Cd²⁺ levels were determined at the same time points as described above. These data revealed no significant differences in the total Cd²⁺ content (both free and QDot-associated) at the different time points. Previous experiments furthermore revealed no interference of the QDots themselves with the assay readout, see [Supplementary information Section V](#).

For CdCl₂-treated cells, a similar approach was followed, where cells were incubated with CdCl₂ at different concentrations (0, 1, 5, 20, 50, 100, 250 or 500 nM) for 24 h, after which the cells were washed twice with PBS, lifted and centrifuged at 0.4 rcf. The cells were redispersed in PBS and counted using a Bürker chamber. Then, 2×10^6 cells were taken, which were centrifuged again, after which 50 μ l of DMSO was added to every pellet to lyse all cells and Cd²⁺ concentrations were then determined as described above.

2.3.5. Determination of cell viability

Cell viability for all three cell types was assessed using an MTT assay, both in proliferative and in non-proliferative cell populations. This assay was performed both for cells exposed to QDots and cells exposed to CdCl₂. A full description of both methodologies can be found in the accompanying [Supplementary information](#).

2.3.6. Determination of reactive oxygen species

Induction of reactive oxygen species for all three cell types was assessed using 10 μ M 5-(and-6)-chloromethyl-2',7'-dichlorodihydrofluorescein diacetate, acetyl ester (CM-H₂DCFDA; Molecular Probes, Invitrogen, Merelbeke, Belgium), both in proliferative and in non-proliferative cell populations. This assay was performed for both cells exposed to QDots and cells exposed to CdCl₂. A full description of both methodologies can be found in the accompanying [Supplementary information](#).

2.3.7. Determination of mitochondrial membrane potential and DNA damage

For these studies, cells were incubated with the PMA-coated QDots for 24 h at various concentrations (from 0 to 30 nM), after

which mitochondrial membrane potential was evaluated spectrofluorometrically using 20 μ M JC-10 dye and DNA damage was assessed by staining for phosphorylated γ -H2Ax using fluorescent antibodies followed by fluorometric plate reading as described in full in the [Supplementary information](#).

2.3.8. Determination of HUVEC cell morphology

The morphology of HUVEC cells was evaluated by exposing the cells to the PMA-coated QDots for 24 h at concentrations at which no acute toxicity was noticed (up to 20 nM), after which cells were stained for Tubulin and F-Actin and visualized using a Nikon Cs1 confocal laser scanning microscope as described in the [Supplementary information](#).

2.3.9. Determination of PC12 functionality

The ability of PC12 cells to induce neurite sprouting was evaluated after exposing the cells for 24 h to the PMA-coated QDots at concentrations at which no acute toxicity or effects on cell morphology were noticed (up to 10 nM). After QDot-exposure, the cells were incubated with nerve growth factor for 48 h and stained for α -tubulin followed by confocal laser scanning analysis as described in the [Supplementary information](#).

2.3.10. Determination of QDot transfer in proliferating cells

QDot distribution in proliferation cells was evaluated as follows: C17.2, PC12 or HUVEC cells were seeded at 1.25×10^5 cells per flask (5 ml total medium) and allowed to settle overnight, after which the cells were incubated with the QDots at 0 or 2 nM for 24 h. Following incubation, media were aspirated, cells washed twice with PBS, lifted by trypsin and kept in culture in full medium, without any QDots, where for half of the dishes, cells were reseeded in MatTek dishes at 2.5×10^4 cells per dish and 1.25×10^5 cells per flask every other day, at either the odd or even days after QDot exposure. The cells reseeded in the flasks were kept in culture for 2 more days and then treated similarly for the duration of the experiment (a total of 9 days), where the MatTek seeded cells were allowed to settle for 2 h. Prior to analysis, media were removed, cells washed three times with PBS, fixed in 2% PFA for 20 min at ambient temperature and permeabilized in 0.1% Triton X-100 for 15 min at ambient temperature. Cell nuclei were then counterstained using DAPI (300 nM; 5 min) after which the dishes were stored at 4 °C until being viewed by epifluorescence microscopy (Nikon Cs1).

The number of QDot positive cells was determined by analyzing the microscopy images using ImageJ. From the collected images, more than 250 cells per condition out of three independent experiments were analyzed for the total number of cell nuclei and the number of QDot-positive cells. Data are expressed as mean \pm SEM and are gathered for more than 250 cells analyzed per condition. Data are given as the number of QDot positive cells over the total number of DAPI-stained cells.

2.4. Statistical analysis

All data are expressed as mean \pm SEM unless indicated otherwise and data were analyzed using one-way analysis of variance (ANOVA). When comparing different QDot concentrations to the same control group (the reference group), the Dunnett post hoc analysis method was used. In all cases, the degree of significance is indicated when appropriate (* $p < 0.05$; ** $p < 0.01$; *** $p < 0.001$).

3. Results and discussion

3.1. Nanoparticle characterization

The synthesis of the PMA-QDots used in the present work has been well-documented in multiple studies. The PMA-QDots have been thoroughly characterized and display a decent batch-to-batch reproducibility [18,28,31]. The QDots used in the present study consist of spherical CdSe/ZnS core-shell structures with a diameter of the inorganic core-shell structure of $\sim 4.7 \pm 0.9$ nm diameter, as assessed by TEM (Supporting Fig. S.2), with initially hydrophobic surfactant capping. These QDots are overcoated with PMA molecules, which are amphiphilic. The hydrophobic side-chains of PMA can interdigitate the hydrophobic surfactants on the original QDot surface, while the hydrophilic backbone renders the resulting QDots water-soluble [29]. Upon applying the PMA coating and transferring the QDots to an aqueous environment (10 mM PBS, pH 7.4), QDots with a hydrodynamic diameter of $d_h 11 \pm 3$ nm and a zeta potential of -18 ± 1 mV were obtained, as determined by dynamic light scattering and electrophoretic mobility measurements, which is in line with previous reports. In PBS, the QDots remained stable in suspension for at least 3 months without any detectable agglomeration. The particles have a maximal emission at 597 nm and a quantum yield of 6.7%.

3.2. Cellular uptake of PMA-coated QDots

In view of cell labeling and NP-toxicity studies, cell uptake levels and intracellular localization of the QDots must be carefully evaluated. Upon incubating the cells with 15 nM QDots, which is a typical QDot concentration used for cell labeling [18], confocal microscopy revealed endolysosomal localization of the QDots in all three cell types (Fig. 1A) as is commonly observed for NPs [32–34]. For endosomal visualization, the lipophilic dye 3,3'-diocadecyloxycarbocyanine perchlorate (DiO) was used. As this dye eventually will stain multiple intracellular compartments, the exposure time of the cells was kept low (30 min), in which case mostly endosomes will be stained positive. Additionally, the QDots themselves were only allowed to be taken up by the cells for 30 min, resulting in relatively low uptake values compared to data obtained after longer incubations (see, for instance, Fig. 4). Note that due to the resolution limit of optical microscopy no individual QDots inside the endosomes can be resolved, and that the fluorescence signals originate from clusters of QDots within the same endosomal vesicles [35]. In order to obtain more quantitative information, the level of cell-associated Cd^{2+} was determined using a previously validated spectrophotometric technique [36], as described in the Supporting information. In short, this fluorescent dye-based technique makes use of an increase in fluorescence that occurs when the dye binds free Cd^{2+} ions and has been used by multiple groups [32,36]. Upon acidic digestion of cell-associated QDots, the level of free Cd^{2+} is determined, from which the number of QDots is calculated using a dilution series of the QDot stock-treated under identical conditions. The accuracy of this quantitative assessment therefore depends on the intrinsic problems associated with determining QDot concentrations and determining QDot-associated Cd^{2+} levels [16]. Therefore, the obtained absolute values are prone to error. However, relative values can be used for comparative purposes in between different experiments using the same samples. Quantitative determination of cellular QDot levels upon 24 h exposure to various QDot concentrations revealed a concentration-dependent, sub-linear increase in the number of QDots per cell as well as the total number of cell-associated QDots (Fig. 1B and C), suggestive of a saturable endosomal uptake mechanism for the QDots. Interestingly, C17.2 and HUVEC cells had similar uptake

levels, whereas PC12 cells had ingested lower numbers of QDots, which has been observed for various types of NPs [14,37]. This is likely due to the smaller overall size of the PC12 cells and their smaller surface area, resulting in a reduced area of interaction of NPs with the cell membrane, hereby impeding NP uptake.

As the lipophilic dye DiO and the QDots could only be used for short exposure times, the intraendosomal localization of the QDots at later time points was further shown by TEM of the three different cell types, following a 24 h exposure to the QDots at 10 nM. This slightly lower concentration was selected to avoid conditions at which acute toxic effects occur, as this might lead to artifacts in terms of cell organelle structure and organization. Fig. 2 shows that for all three cell types, the QDots reside in vesicular structures, bearing the morphological features of endosomal or lysosomal compartments. Together, these data indicate that the particles are taken up through the endosomal pathway and finally reside in the endolysosomal compartment, where they will be subjected to lower pH values, different ionic strengths and different protein compositions than in the extracellular or cytoplasmic environment.

3.3. Effect of pH-mediated QDot degradation on Cd^{2+} release and fluorescence intensity

For cadmium-based QDots, one primary cause of toxicity has been suggested to be free Cd^{2+} ions [27,28], a well-known metal toxicant [29,38]. However, it also has been shown that a ZnS shell around the CdSe core slows down corrosion of the QDots and thus reduces cytotoxicity [28]. By using the fluorescent dye-based assay, the presence of free Cd^{2+} ions in the 2 μM QDot stock suspension was evaluated, showing levels of 3.9 μM of free Cd^{2+} . Comparison to the Cd^{2+} concentration after acidic digestion of the QDots, as determined with the same assay, demonstrates that in neutral aqueous solution $\sim 1.6\%$ of the total Cd^{2+} content of the QDots is present as free Cd^{2+} , the rest is bound to the QDots. Note that this percentage may depend on the QDot concentration. Under diluted conditions the equilibrium can shift towards a larger percentage of dissolved Cd^{2+} . In previous work we calculated the percentage of Cd^{2+} which is on the surface of the CdSe core to be $\sim 4\%$ (cf. the Supporting information). Thus $\sim 40\%$ of the surface Cd^{2+} atoms from the CdSe cores (under the ZnS shell) in the 2 μM QDot stock solution had dissolved under equilibrium conditions.

Free Cd^{2+} has been found to be able to affect cells starting from concentrations of 1 μM , but this value has been found to be dependent of cell type and conditions of incubation [28]. In context with the determined value of 3.9 μM of free Cd^{2+} in the stock solution and the further dilution of the QDots in cell medium prior to cell labeling (at least by 100-fold), this suggests that the free QDot-derived Cd^{2+} (in the cell medium) is likely not to be solely responsible for acute cytotoxic effects. Although the dilution of the QDots will shift the equilibrium between free and NP-associated Cd^{2+} , the high dilution levels used here will likely not shift the equilibrium to such extent that more than 1 μM of free Cd^{2+} could be obtained. This was further verified by exposing cells for 24 h to pre-conditioned medium that was previously exposed to the QDots at the concentrations used for cell labeling (up to 20 nM) for 24 h and was subsequently ultracentrifuged at 115,584g. This medium then only contained free ions derived from the diluted QDot stocks, which was found not to result in significant effects on cell viability (Supporting Fig. S.5).

Upon endosomal uptake, the QDots will however be exposed to varying environmental pH values, ranging from 7.4 for extracellular medium to 4.5 in the lysosomes. As acidic conditions are known to induce acid etching of the QDot surface and hereby release Cd^{2+} [37,39], the effect of pH on Cd^{2+} release was evaluated using previously optimized endosomal-pH buffer systems [36] (see Support-

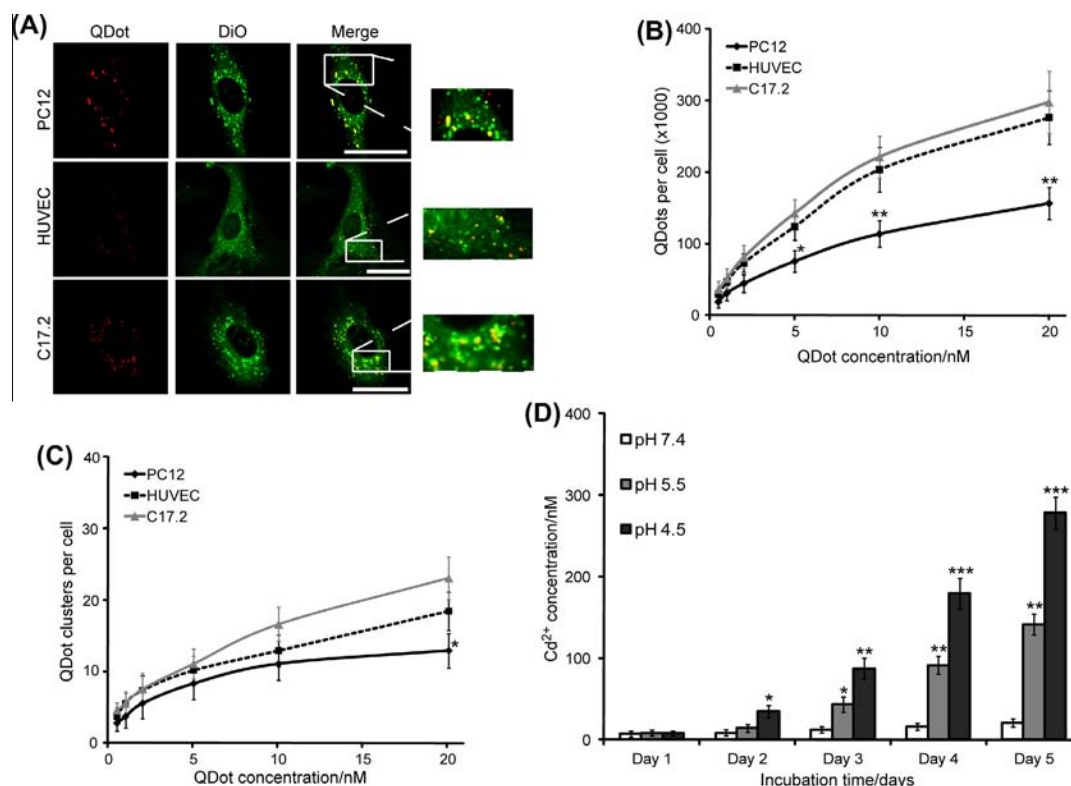


Fig. 1. (A) Representative confocal images of PC12 (top row), HUVEC (middle row) and C17.2 cells (bottom row) incubated with 15 nM PMA-coated QDots (left column: red) for 30 min in the presence of the lipophilic dye DiO (middle column: green). A merged image of both the QDots and the DiO positive endosomes is shown in the right column where the percentage of colocalization of both QDots and DiO positive endosomes is shown in the top right corner. Scale bars: 30 μm. (B) The total number of QDots per cell as a function of the QDot concentration after 24 h incubation. (C) The number of QDots containing endosomal vesicles per cell as quantified from the microscopy images after 24 h of cell exposure to the QDots. Data are shown as mean ± SEM (n = 4). For (B) and (C), any difference between the different cell types in terms of total QDots per cell or total QDot clusters per cell is indicated when statistically significant (*p < 0.05; **p < 0.01; ***p < 0.001). (D) Levels of free Cd²⁺ in suspensions of PMA-coated QDots at various pH values (7.4, 5.5, 4.5) as a function of time as determined by acid digestion of the QDots followed by quantitation of the level of Cd²⁺ by means of Cd²⁺-responsive fluorescence dye as described in the Supporting information. Data are expressed as mean ± SEM (n = 3). When appropriate, the degree of significance for any condition compared to the control value at pH 7.4 is indicated (*p < 0.05; **p < 0.01; ***p < 0.001).

ing information for full experimental details). Fig. 1D shows a clear pH-dependent release of Cd²⁺ under these cell-free conditions as a function of time, resulting in a ~15-fold increase in Cd²⁺ levels after 5 days at pH 4.5 compared to 5 days at pH 7.4.

The degradation of the QDots is also reflected in their fluorescence intensities, which rapidly drop upon exposure to lower pH values, but further decrease in time as a result of QDot surface etching (Fig. 3A). Transferring the QDots to PBS at pH 7.4 restores the initial loss of fluorescence intensity back to near control levels, whereas for QDots that were exposed to acidic environments for several days, the fluorescence intensities could not be fully recovered (Fig. S.4). Additionally, the effect of the low pH has also been investigated using TEM, where micrographs were taken of QDots in organic phase (Fig. 3B1) and of the same QDots after 2 days' exposure to pH 3 (Fig. 3B2). The data clearly indicate changes in the shape of the QDots after exposure to low pH values, which is consistent with surface etching of the QDots and associated release of Cd²⁺ ions. To evaluate the extent and kinetics of intracellular QDot degradation, the level of intracellular Cd²⁺ was evaluated in non-proliferating cells, established as previously described (see Supporting information for a full experimental methodology) [36]. Non-proliferating cells were used to enable an accurate follow-up of Cd²⁺ release in cells as a function of time, while minimizing the effect of QDot dilution due to cell division. The data show a clear time-dependent increase in cellular Cd²⁺ (only free Cd²⁺, not QDot-associated Cd²⁺) the level of which also correlated with intracellular QDot levels (Fig. 4).

3.4. Effects of QDot degradation on cell viability

Next, the cytotoxic effects of the QDots were evaluated, revealing a concentration-dependent toxicity in all three cell types, starting from 20 nM or higher for C17.2 and HUVEC cells and 30 nM for PC12 cells (Fig. 5A). The latter is likely explained by the lower levels of cell-associated QDots for the PC12 cells (Fig. 1B). Interestingly, when non-proliferating cells were loaded with QDots, the cytotoxic effects of the QDots significantly augmented in time, in close correlation with the elevated Cd²⁺ levels (Supporting Fig. S.6). When using CdCl₂ as a source of free Cd²⁺, only minimal cytotoxic effects were observed. Fig. 6 shows the intracellular level of Cd²⁺ measured in C17.2 cells after 24 h exposure to CdCl₂ at various concentrations. The data reveal that at the highest dose (500 nM CdCl₂), the intracellular level of Cd²⁺ was substantially higher than the level obtained when cells were exposed to QDots (Fig. 4C). Therefore, the data collectively show that the toxicity induced by Cd²⁺ ions by CdCl₂ addition is less substantial than the toxicity induced by Cd²⁺ derived from intracellular QDot degradation. Caution must be considered when trying to explain the lack of effect of CdCl₂ at the “same intracellular concentrations” as only free Cd²⁺ was considered and the Cd²⁺ still in the QDots, or the ions present on the QDot surface were not taken into account, which may all play a significant role in QDot-mediated toxicity. However, the low effects of free Cd²⁺ at high intracellular levels given by CdCl₂ suggest that other than immediate toxicity of free Cd²⁺, different mechanisms appear to be contributing to the QDot-induced

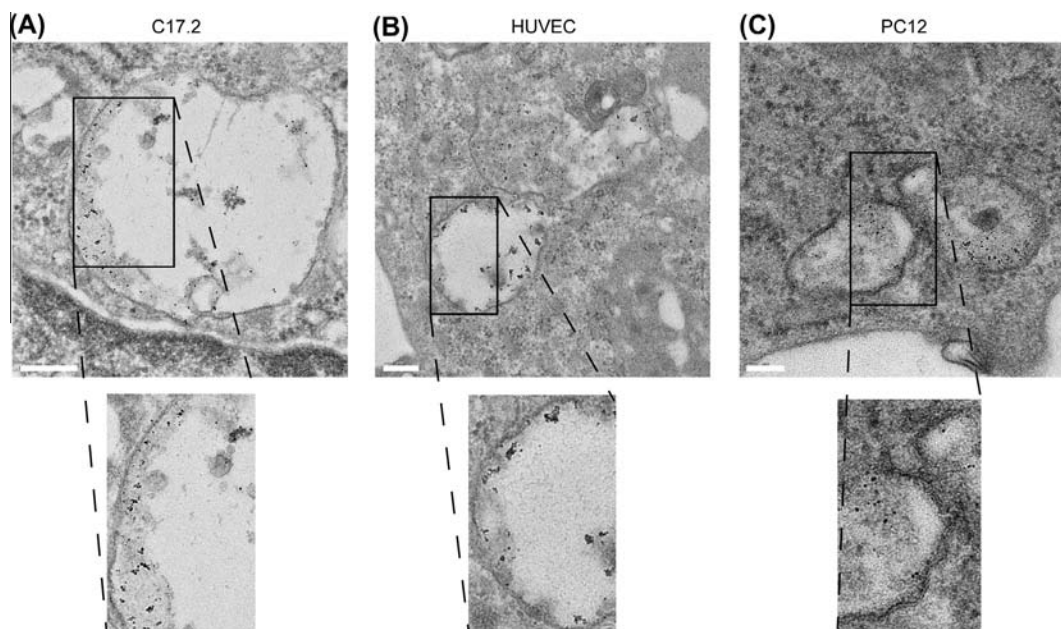


Fig. 2. Transmission electron micrographs of (A) C17.2, (B) HUVEC and (C) PC12 cells exposed to QDots for 24 h at 10 nM. The bottom figures are enlarged views of the respective areas indicated in the top figures. Scale bars: (A,B) 200 nm, (C) 100 nm.

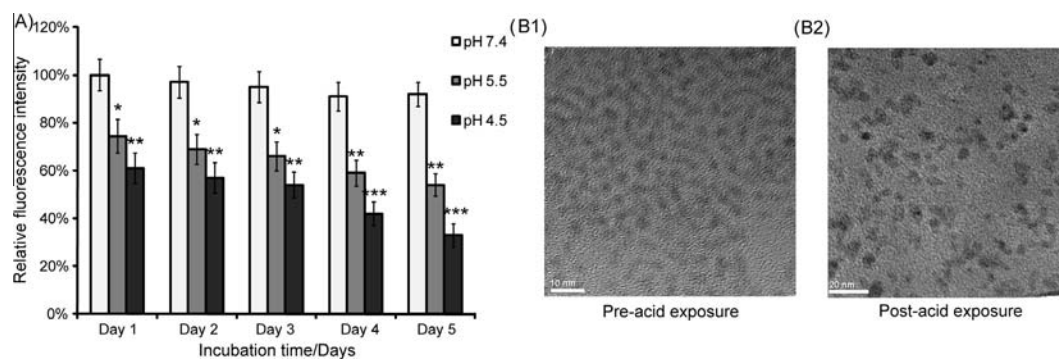


Fig. 3. (A) Effect of pH on QDot fluorescence intensity. Relative fluorescence intensity levels of 5 nM suspensions of PMA-coated QDots at various pH values (7.4, 5.5, 4.5) as a function of time. Data are expressed as mean \pm SEM ($n = 3$) and the degree of statistical significance of treated samples vs. control samples is indicated when appropriate (* $p < 0.05$; ** $p < 0.01$; *** $p < 0.001$). (B) Transmission electron micrographs of the QDots upon synthesis (B1) and after 2 days' exposure to pH 3 (B2). Scale bars: (B1) 10 nm, (B2) 20 nm.

toxicity (Supporting Figs. S.7 and S.8). One possible explanation for the clear correlation between QDot-induced toxicity and intracellular QDot-derived Cd^{2+} levels, lies in the endosomal enclosure of the QDots [36]. Where Cd^{2+} derived from CdCl_2 can more freely distribute throughout the cell cytoplasm and will be taken up by the cell in a short time span, this is not the same for Cd^{2+} derived from cadmium-based QDots. The intraendosomal degradation of the QDots likely results in a more heterogeneous distribution of Cd^{2+} , with very high local Cd^{2+} concentrations in a confined space (endosome) that easily exceed the toxic threshold, thereby affecting cell homeostasis. Additionally, the Cd^{2+} derived from QDots is gradually released over time and will immediately be subjected to a degradative environment of low pH, unlike the Cd^{2+} ions that are derived from CdCl_2 . The presence of the ions in the low pH environment of the endosomes at high local concentrations may result in higher toxic effects than more homogeneously distributed Cd^{2+} . Furthermore, NPs such as QDots are known to affect cellular well-being, for instance by the induction of ROS. When cells are already subject to stress induced by the intracellular presence of NPs, the additional presence of Cd^{2+} will likely result in toxic effects more quickly than the same levels of Cd^{2+} would in cells that have no

other stress inducers. This hypothesis also supports the earlier work of other groups [40,41] who found that intracellular Cd^{2+} release was more toxic than extracellular Cd^{2+} .

These data collectively show that minor toxic effects occur at concentrations of 500 nM of free Cd^{2+} . Compared to the QDots, similar minor toxic effects were noticeable at concentrations of 10 nM. Whereas the amount of free intracellular Cd^{2+} derived from the QDots was much lower than Cd^{2+} levels derived from CdCl_2 , the total amount of Cd^{2+} added was much higher in the case of the QDots (for 10 nM QDots; an experimental value of 1.32 μM Cd^{2+} was obtained). Based on these values, it can be concluded that the majority of QDot-associated Cd^{2+} is not released and remains confined within the QDot core. These ions do not appear to play any major role in the toxicological effects of Cd^{2+} as when comparing the toxicity of CdCl_2 and QDots based on the total amount of Cd^{2+} added, the QDots display less toxicity.

3.5. Effects of QDots on oxidative stress

To further test this hypothesis, the effect of CdCl_2 and QDots on oxidative stress were evaluated in non-proliferating cells, indicating a

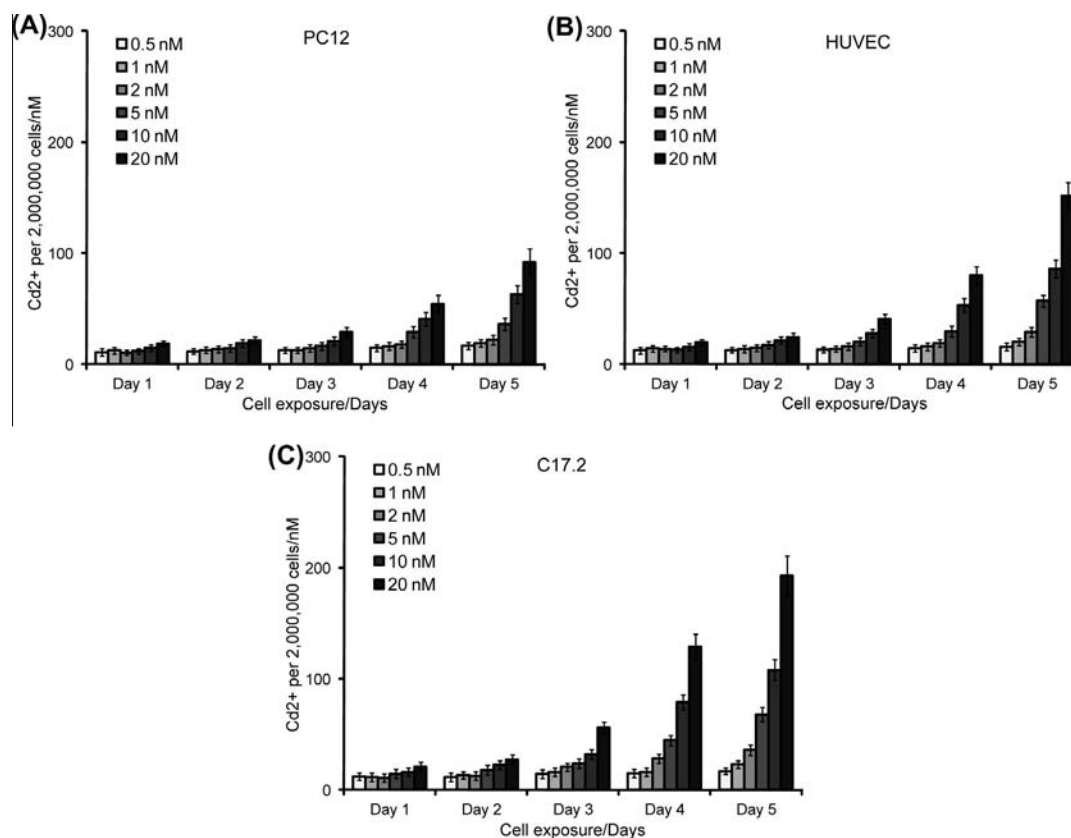


Fig. 4. (A–C) Levels of free Cd²⁺ in (A) PC12, (B) HUVEC and (C) C17.2 cells exposed to various concentrations of PMA-coated QDots for 24 h and subsequently kept in non-proliferating state, after which the cellular Cd²⁺ levels are measured after 1, 2, 3, 4 and 5 days. Data are expressed as mean \pm SEM ($n = 3$). Note that only free Cd²⁺ was measured, no acid digestion was employed and any remaining QDots were found not to significantly interfere with the assay readout.

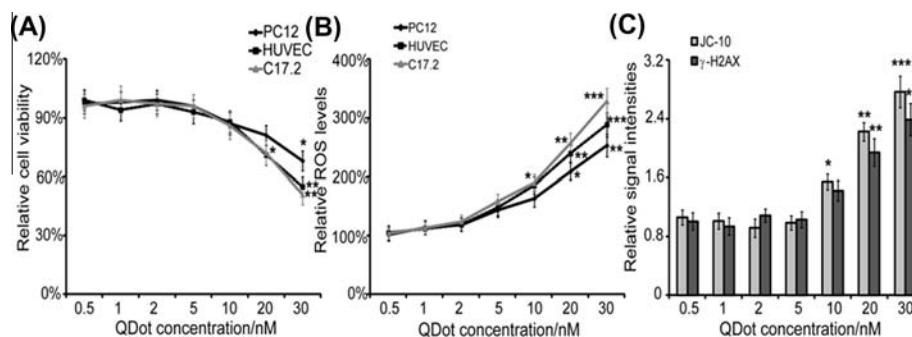


Fig. 5. (A) Viability and (B) ROS induction of PC12, HUVEC and C17.2 cells as a function of QDot concentration after 24 h incubation. Data are represented as mean \pm SEM ($n = 6$) and expressed as relative to untreated control cells. (C) Quantitative levels of JC-10 (light grey) and γ -H₂Ax (dark grey) for HUVEC cells exposed for 24 h to different concentrations of QDots. Data are expressed as mean \pm SEM ($n = 3$) and are presented as relative to that of untreated control cells (=100%). When appropriate, the degree of significance is indicated (* $p < 0.05$; ** $p < 0.01$; *** $p < 0.001$).

clear concentration-dependent induction of ROS for either CdCl₂ or QDots (Fig. 5B, Supporting Figs. S.8 and S.9). However, for the QDots, the level of ROS also increased in time, which is in line with the increasing Cd²⁺ concentrations. As the level of ROS is higher for the QDots than for CdCl₂, this supports our hypothesis on local high Cd²⁺ concentrations obtained upon intraendosomal QDot degradation. When cells were co-incubated with 5 mM *N*-acetylcysteine (NAC), an FDA-approved free radical scavenger, ROS levels were reduced to near control levels (Supporting Fig. S.8). The addition of NAC was also able to partially restore cell viability (Supporting Fig. S.6), indicating that ROS are an important mediator in QDot-induced toxicity, but other mechanisms must also contribute to the overall cytotoxicity.

To evaluate whether the elevated ROS levels have any secondary effects on cell physiology, mitochondrial membrane potential

($\Delta\Psi_m$) and DNA damage were evaluated. The $\Delta\Psi_m$ was evaluated using the JC-10 dye, which remains in the cytoplasm as green monomers until it is taken up by healthy mitochondria with a normal $\Delta\Psi_m$, which will make the dye aggregate and its fluorescence emission will shift (red color). The ratio of green over red (as shown in Fig. 5C) therefore indicates the ratio of damaged over healthy mitochondria. The data show that, in line with the onset of ROS, at QDot concentrations from 10 nM and above, a clear and significant increase in damaged mitochondria can be seen, at levels below those at which acute toxicity occurs (30 nM). The significant effects at concentrations below toxic levels clearly indicate that these results are not artifacts caused by cell death, but rather that the QDot-mediated onset of ROS precedes cell death. Together with the observation that NAC treatment can partially overcome QDot-induced toxicity, these

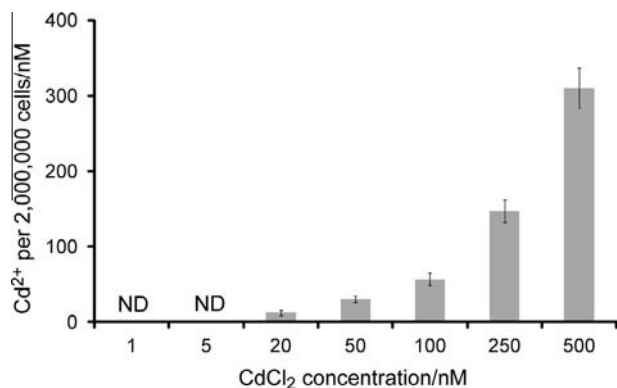


Fig. 6. Levels of free Cd²⁺ in C17.2 cells exposed to various concentrations (1, 5, 20, 50, 100, 250 and 500 nM) of CdCl₂ for 24 h. Data are expressed as mean ± SEM (*n* = 3). ND: non-detectable (values are within noise-level of the assay and cannot be distinguished from the background level).

results show that ROS induction is one of the prime mechanisms by which these NPs elicit toxic effects.

As elevated ROS levels are known to possibly result in DNA damage, which may have far-reaching consequences in the safety of these materials as this a hallmark of carcinogenicity, the occurrence of DNA double strand breaks was evaluated (Fig. 5C). This was done by staining for phosphorylated γ -H2Ax foci, which are formed by the rapid phosphorylation of histone H2Ax at sites of DNA double strand breaks. Similar as for the loss of $\Delta\Psi_m$, significant DNA damage was found to occur at doses at which acute toxicity was minimal (20 nM).

Taken together, these data indicate that the QDot-induced ROS levels result in secondary effects which, at higher levels, will result in cell death, but are still significant even at lower levels, where they induce cell stress or carcinogenicity.

3.6. Effects of QDots on cell morphology and functionality

To further refine the non-toxic concentration of PMA-coated QDots and to analyze the contribution of time-dependent Cd²⁺ release, the morphology of QDot-exposed HUVECs was evaluated. As a primary human cell type with a typical well-spread morphology, these cells are perfectly suited to assess QDot-mediated disturbance of actin or tubulin cytoskeleton [14]. Furthermore, previous data on iron oxide NPs has shown that cell deformations usually occur after 2–3 days after initial cell exposure [14], making this an interesting parameter to study with respect to time-dependent Cd²⁺ release. Fig. 7A and B reveals a concentration-dependent reduction in cell-spreading, which is in line with previous reports on various types of nanoparticles [36,42,43]. Note that for these assays, only low QDot concentrations (up to 20 nM) were selected that do not induce significant levels of acute cell death as the occurrence of apoptotic bodies or condensed cells would substantially influence the results obtained. The reduction in cell spreading correlates well with the onset of ROS, suggesting a possible influence of ROS in the cytoskeletal deformations. However, previous data have suggested that the conjoined effects of multiple mechanisms play a role in cell deformations, including (1) the endosomal localization of QDots resulting in enlarged lysosomal compartments [30] and (2) a loss of lysosomal functionality, resulting in large compartments containing high numbers of rigid NPs and hereby occupying a substantial part of the cellular cytoplasmic compartment, sterically hindering normal cytoplasmic functionality [36].

Next, the effect of the QDots on cell functionality was investigated. To evaluate the effect of Cd²⁺ release, the PC12 model system was used, which was previously found to be an excellent model for a fast, sensitive and quantifiable assessment of cell functionality upon nanoparticle exposure. In this assay, cell functionality is evaluated by induction of neurite outgrowth upon

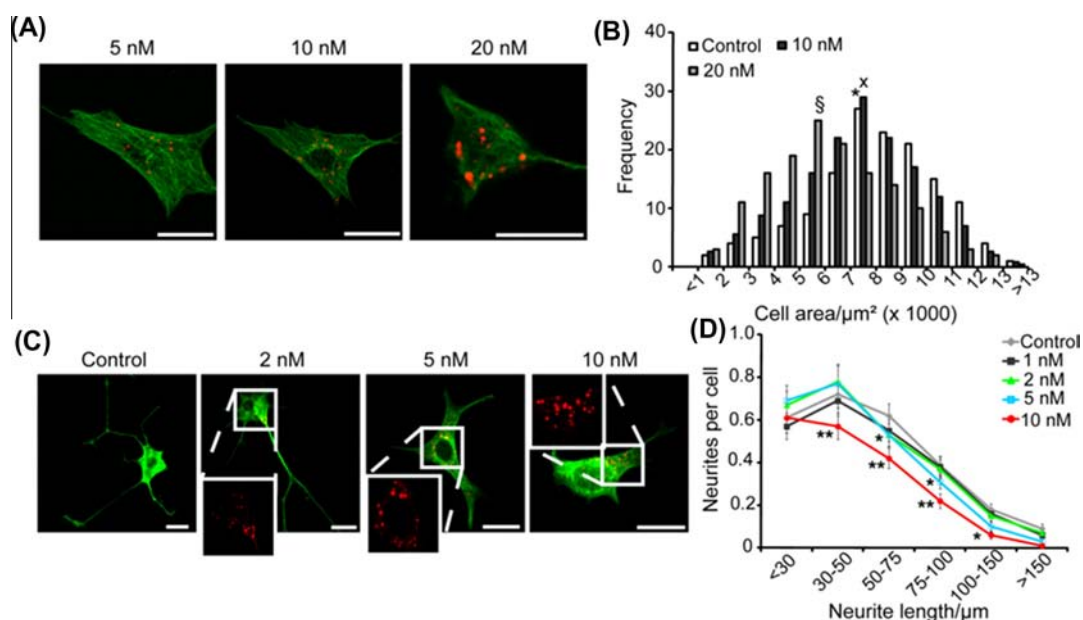


Fig. 7. (A) Representative confocal images of HUVEC cells exposed for 24 h to PMA-coated QDots at 5 nM (left column), 10 nM (middle row) and 20 nM (right column). The images shown are merged images of QDots (red) and α -tubulin cytoskeleton (green). Scale bars: 50 μm . (B) Histograms representing the cell area distribution of HUVECs exposed to PMA-coated QDots for 24 h and stained after 2 additional days of culture. The average cell areas are indicated with * for control cells, X for 10 nM-treated cells and § for 20 nM-treated cells. (C) Effect of QDots on PC12 cell functionality. Representative confocal images of PC12 cells exposed to PMA-coated QDots for 24 h at 0 (left column), 2 (2nd column), 5 (3rd column) or 10 nM (4th column) and subsequently exposed to nerve growth factor (NGF; 100 ng ml⁻¹) for 2 days. Images shown are merged images of QDots (red) and α -tubulin (green). The area indicated by the white rectangle is magnified at the bottom of the image, showing only the QDot fluorescence. Scale bars: 30 μm . (D) The number of neurites of a certain length per cell after 3 days of NGF exposure for cells exposed to 0, 1, 2, 5 or 10 nM of PMA-coated QDots. When appropriate, the degree of significance is given when compared with untreated control cells (**p* < 0.05; ***p* < 0.01; ****p* < 0.001).

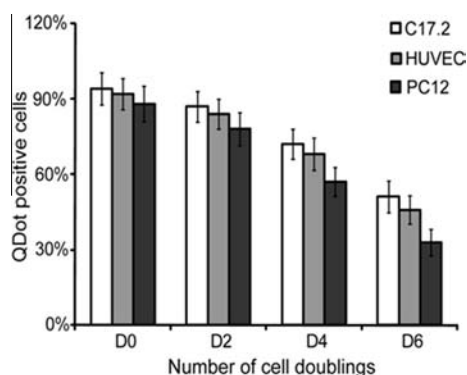


Fig. 8. The percentage of QDot positive cells for cells incubated with 2 nM QDots for 24 h after 0, 2, 4 and 6 average cell doubling times as evaluated by microscopy analysis. The data are expressed as mean \pm SEM ($n = 3$).

stimulation with nerve growth factor (NGF) [13]. When cells were exposed to QDots at nominally non-toxic concentrations, the outgrowth of neurites after 2 days of stimulus with NGF (4 days after initial cell exposure) was found to be significantly impeded at higher QDot concentrations (Fig. 7C and D).

3.7. Assessment of QDot functionality for comparative data analysis

Based on all the data obtained, the non-cytotoxic concentration of PMA-coated core/shell QDots of 4.7 nm CdSe/ZnS diameter is ~ 2 nM. Previously, the multiparametric methodology applied in the current study has been used to evaluate PMA-coated Au NPs of the same size and identical (PMA) surface coating [43] as well as commercially available polymer-coated core-shell QDots [36]. For the Au particles, the non-toxic level was found to be 10 nM, indicating a fivefold higher toxicity of the QDots, owing to differences in the metal core of the NPs and the forthcoming photophysical properties of these materials as QDots, for instance, are well-known to produce ROS under light irradiation which less outspoken for Au NPs. Interestingly this value fits remarkably to very early studies, in which PMA-coated CdSe/ZnS QDots were found to be more than three times toxic than PMA-coated Au NPs [28]. Given the difficulties in accurately assessing NP concentrations [16], differences in the uniformity by which the PMA polymer covers the NPs and polydispersity differences between the two different NP types, these absolute values should, however, be treated with care and making comparisons should be done cautiously.

Given the difficulties in comparing different NPs due to the problems associated with accurately determining NP concentrations [16], the applicability of the QDots for fluorescence cell tracking was evaluated at their non-toxic concentration (2 nM). In previous work, it was found that carboxyl-functionalized commercially available QDots of similar size tested under identical conditions were found to be non-toxic at 1 nM [36]. Note that also the PMA-coated QDots as used in this study are terminated by carboxyl-groups. Differences in the methods used for determining QDot concentrations are most likely the reason for the slight difference in the values of these studies [16]. At non-toxic concentrations, labeled cells were able to be monitored by fluorescence microscopy for approximately four cell doublings (Fig. 8). In the end, the duration by which QDot labeled cells could be efficiently visualized at non-toxic conditions (approximately four cell doublings) was the same for both types of carboxylated Qdots (commercial and synthesized ones), indicating that both types of QDots resulted in similar efficiencies in terms of cell labeling strategies. The ability to track the cells by fluorescence microscopy is influenced by the number of QDots internalized by the cell, as well as other factors such as their coating and quantum yield. These

data demonstrate that when assessing NP toxicity, the number of cell-associated NPs determines cytotoxic effects rather than the total number of NPs added to the cells, which is in line with earlier findings [44]. Here, we demonstrated the importance of intracellular NP concentrations in the cytotoxicity of nanomaterials as well as the necessity to assess the functionality of the nanomaterials at non-toxic conditions. In the end, it is important to evaluate whether the NPs at their non-toxic concentration are still functional for the desired application, such as cell tracking. Especially given the difficulties in accurately determining NP concentrations, assessing their biomedical functionality appears like an informative and fruitful tool, which allows the comparison of particles with respect to both toxicological and technical features of the NPs, thereby providing a good overview of the respective NP strength for a selected purpose.

4. Conclusions

In conclusion, the present work demonstrates the importance of NP degradation in the cellular microenvironment in the cytotoxic effects of nanomaterials. Therefore, the data collectively show that the toxicity induced by Cd^{2+} ions by CdCl_2 addition is less substantial than the toxicity induced by Cd^{2+} derived from intracellular QDot degradation (when compared at the same intracellular free Cd^{2+} concentration). Note that under the conditions used in this study, the majority of QDot-associated Cd^{2+} is not released and remains confined within the QDot core. These ions do not appear to play any major role in the toxicological effects of Cd^{2+} as when comparing the toxicity of CdCl_2 and QDots based on the total amount of Cd^{2+} added, the QDots display less toxicity. Together, these data reveal that while current cadmium-containing QDots are well-suited for monitoring cell behavior by fluorescence microscopy for a low number of cell divisions, Cd^{2+} -based QDot formulations do not appear to be optimally suited for long-term cell tracking after endosomal uptake. Optimization of QDot formulations can occur at both the level of the QDot core as at the level of the coating applied for QDot biofunctionalization. The current study demonstrates the need for specialized model systems, such as non-proliferating cells, in order to be able to study this effect in more detail at later time points under conditions close to relevant physiological conditions. Additionally, there is a need for techniques that enable one to determine the chemical state of all NP-associated ions in real-time in live cells. Considering the technical difficulties in terms of accurately assessing NP concentrations, it is also vital to accurately assess functional (= cell-associated) NP levels. In order to enable a comparison of different NPs, it is therefore more suited to use NP functionality (e.g. the ability to fluorescently visualize labeled cells) at non-toxic concentrations as the final parameter which determines NP safety, rather than comparing various NP concentrations, which may not be very insightful.

Acknowledgements

S.J.S. is a postdoctoral fellow from the FWO-Vlaanderen. Financial support from the FWO-Vlaanderen (Krediet aan Navorsers to S.J.S.), the UGent consortium NB Photonics, and from the European Commission (grant Nandiatream to W.J.P.) are gratefully acknowledged. The authors wish to thank Prof. Alain R. Brisson, Université Bordeaux, for his expertise in cellular TEM.

Appendix A. Supplementary data

Supplementary data associated with this article can be found, in the online version, at <http://dx.doi.org/10.1016/j.actbio.2013.09.041>.

Appendix B. Figures with essential colour discrimination

Certain figures in this article, particularly Figures 1 and 7, are difficult to interpret in black and white. The full colour images can be found in the on-line version, at doi:<http://dx.doi.org/10.1016/j.actbio.2013.09.041>.

References

- [1] Magnuson BA, Jonaitis TS, Card JW. A brief review of the occurrence, use, and safety of food-related nanomaterials. *J Food Sci* 2011;76:R126–33.
- [2] Nasir A, Friedman A. Nanotechnology and the nanodermatology society. *J Drugs Dermatol* 2010;9:879–82.
- [3] Report L. Nanomaterials state of the market: stealth success, broad impact; 2008. Available from: <http://portalluxresearchinecom/research/document3735:2008>.
- [4] Fairbrother A, Fairbrother JR. Are environmental regulations keeping up with innovation? A case study of the nanotechnology industry. *Ecotoxicol Environ Saf* 2009;72:1327–30.
- [5] Faunce T, Watal A. Nanosilver and global public health: international regulatory issues. *Nanomedicine (Lond)* 2010;5:617–32.
- [6] Hamburg MA. Science and regulation. FDA's approach to regulation of products of nanotechnology. *Science* 2012;336:299–300.
- [7] Soenen SJ, Demeester J, De Smedt SC, Braeckmans K. Turning a frown upside down: exploiting nanoparticle toxicity for anticancer therapy. *Nano Today* 2013;8:121–5.
- [8] Chen Y, Qu K, Zhao C, Wu L, Ren J, Wang J, et al. Insights into the biomedical effects of carboxylated single-wall carbon nanotubes on telomerase and telomeres. *Nat Commun* 2012;3:1074.
- [9] Joris F, Manshian BB, Peynshaert K, De Smedt SC, Braeckmans K, Soenen SJ. Assessing nanoparticle toxicity in cell-based assays: influence of cell culture parameters and optimized models for bridging the in vitro–in vivo gap. *Chem Soc Rev* 2013. <http://dx.doi.org/10.1039/C3CS60145E>.
- [10] Thomas CR, Xia T, Rallo R, Zhao Y, Ji Z, Lin S, et al. Nanomaterials in the environment: from materials to high-throughput screening to organisms. *ACS Nano* 2011;5:13–20.
- [11] Soenen SJ, Rivera-Gil P, Montenegro JM, Parak WJ, De Smedt SC, Braeckmans K. Cellular toxicity of inorganic nanoparticles: common aspects and guidelines for improved nanotoxicity evaluation. *Nano Today* 2011;6:446–65.
- [12] Elder A, Yang H, Gwiazda R, Teng X, Thurston S, He H, et al. Testing nanomaterials of unknown toxicity: an example based on platinum nanoparticles of different shapes. *Adv Mater* 2007;19:3124–8.
- [13] Pisanic 2nd TR, Blackwell JD, Shubayev VI, Finones RR, Jin S. Nanotoxicity of iron oxide nanoparticle internalization in growing neurons. *Biomaterials* 2007;28:2572–81.
- [14] Soenen SJ, Himmelreich U, Nuytten N, De Cuyper M. Cytotoxic effects of iron oxide nanoparticles and implications for safety in cell labelling. *Biomaterials* 2011;32:195–205.
- [15] Rivera Gil P, Oberdorster G, Elder A, Puentes V, Parak WJ. Correlating physicochemical with toxicological properties of nanoparticles: the present and the future. *ACS Nano* 2010;4:5527–31.
- [16] Rivera-Gil P, Jimenez De Aberasturi D, Wulf V, Pelaz B, Del Pino P, Zhao Y, et al. The challenge to relate the physicochemical properties of colloidal nanoparticles to their cytotoxicity. *Acc Chem Res* 2013;46:743–9.
- [17] Chan WCW, Maxwell DJ, Gao XH, Bailey RE, Han MY, Nie SM. Luminescent quantum dots for multiplexed biological detection and imaging. *Curr Opin Biotech* 2002;13:40–6.
- [18] Rivera-Gil P, Yang F, Thomas H, Li L, Terfort A, Parak WJ. Development of an assay based on cell counting with quantum dot labels for comparing cell adhesion within cocultures. *Nano Today* 2011;6:20–7.
- [19] Azzazy HM, Mansour MM, Kazmierczak SC. From diagnostics to therapy: prospects of quantum dots. *Clin Biochem* 2007;40:917–27.
- [20] Bhirde A, Xie J, Swierczewska M, Chen X. Nanoparticles for cell labeling. *Nanoscale* 2011;3:142–53.
- [21] Wu X, Liu H, Liu J, Haley KN, Treadway JA, Larson JP, et al. Immunofluorescent labeling of cancer marker Her2 and other cellular targets with semiconductor quantum dots. *Nat Biotechnol* 2003;21:41–6.
- [22] Pinaud F, Clarke S, Sittner A, Dahan M. Probing cellular events, one quantum dot at a time. *Nat Methods* 2010;7:275–85.
- [23] Kim S, Lim YT, Soltész EG, De Grand AM, Lee J, Nakayama A, et al. Near-infrared fluorescent type II quantum dots for sentinel lymph node mapping. *Nat Biotechnol* 2004;22:93–7.
- [24] Ballou B, Ernst LA, Andreko S, Harper T, Fitzpatrick JAJ, Waggoner AS, et al. Sentinel lymph node imaging using quantum dots in mouse tumor models. *Bioconjug Chem* 2007;18:389–96.
- [25] Tsay JM, Trzoss M, Shi LX, Kong XX, Selke M, Jung ME, et al. Singlet oxygen production by peptide-coated quantum dot-photosensitizer conjugates. *J Am Chem Soc* 2007;129:6865–71.
- [26] Zhu XC, Lu WT, Zhang YZ, Reed A, Newton B, Fan Z, et al. Imidazole-modified porphyrin as a pH-responsive sensitizer for cancer photodynamic therapy. *Chem Commun* 2011;47:10311–3.
- [27] Derfus AM, Chan WCW, Bhatia SN. Probing the cytotoxicity of semiconductor quantum dots. *Nano Lett* 2004;4:11–8.
- [28] Kirchner C, Liedl T, Kudara S, Pellegrino T, Javier AM, Gaub HE, et al. Cytotoxicity of colloidal CdSe and CdSe/ZnS nanoparticles. *Nano Lett* 2005;5:331–8.
- [29] Chen N, He Y, Su Y, Li X, Huang Q, Wang H, et al. The cytotoxicity of cadmium-based quantum dots. *Biomaterials* 2012;33:1238–44.
- [30] Ambrosone A, Mattera L, Marchesano V, Quarta A, Susa AS, Tino A, et al. Mechanisms underlying toxicity induced by CdTe quantum dots determined in an invertebrate model organism. *Biomaterials* 2012;33:1991–2000.
- [31] Zhang F, Lees E, Amin F, Gil PR, Yang F, Mulvaney P, et al. Polymer-coated nanoparticles: a universal tool for biolabelling experiments. *Small* 2011;7:3113–27.
- [32] Cho SJ, Maysinger D, Jain M, Roder B, Hackbarth S, Winnik FM. Long-term exposure to CdTe quantum dots causes functional impairments in live cells. *Langmuir* 2007;23:1974–80.
- [33] Soenen SJ, Brisson AR, Jonckheere E, Nuytten N, Tan S, Himmelreich U, et al. The labeling of cationic iron oxide nanoparticle-resistant hepatocellular carcinoma cells using targeted magnetoliposomes. *Biomaterials* 2011;32:1748–58.
- [34] Parak WJ, Boudreau R, Le Gros M, Gerion D, Zanchet D, Micheel CM, et al. Cell motility and metastatic potential studies based on quantum dot imaging of phagokinetic tracks. *Adv Mater* 2002;14:882–5.
- [35] Brandenberger C, Muhlfeld C, Ali Z, Lenz AG, Schmid O, Parak WJ, et al. Quantitative evaluation of cellular uptake and trafficking of plain and polyethylene glycol-coated gold nanoparticles. *Small* 2010;6:1669–78.
- [36] Soenen SJ, Demeester J, De Smedt SC, Braeckmans K. The cytotoxic effects of polymer-coated quantum dots and restrictions for live cell applications. *Biomaterials* 2012;33:4882–8.
- [37] Moulis JM. Cellular mechanisms of cadmium toxicity related to the homeostasis of essential metals. *Biomaterials* 2010;23:877–96.
- [38] Su Y, Hu M, Fan C, He Y, Li Q, Li W, et al. The cytotoxicity of CdTe quantum dots and the relative contributions from released cadmium ions and nanoparticle properties. *Biomaterials* 2010;31:4829–34.
- [39] Soenen SJ, Himmelreich U, Nuytten N, Pisanic 2nd TR, Ferrari A, De Cuyper M. Intracellular nanoparticle coating stability determines nanoparticle diagnostics efficacy and cell functionality. *Small* 2010;6:2136–45.
- [40] Chang E, Thekkekk N, Yu WW, Colvin VL, Drezek R. Evaluation of quantum dot cytotoxicity based on intracellular uptake. *Small* 2006;2:1412–7.
- [41] Schneider R, Wolpert C, Guilloteau H, Balan L, Lambert J, Merlin C. The exposure of bacteria to CdTe-core quantum dots: the importance of surface chemistry on cytotoxicity. *Nanotechnology* 2009;20:225101.
- [42] Mahto SK, Park C, Yoon TH, Rhee SW. Assessment of cytocompatibility of surface-modified CdSe/ZnSe quantum dots for BALB/3T3 fibroblast cells. *Toxicol In Vitro* 2010;24:1070–7.
- [43] Soenen SJ, Manshian B, Montenegro JM, Amin F, Meermann B, Thiron T, et al. The cytotoxic effects of gold nanoparticles: a multiparametric study. *ACS Nano* 2012;6:5767–83.
- [44] Soenen SJ, Manshian B, Doak SH, De Smedt SC, Braeckmans K. Fluorescent non-porous silica nanoparticles for long-term cell monitoring: Cytotoxicity and particle functionality. *Acta Biomater* 2013;9:9183–93.

Photoelectrochemical Sensor Based on Quantum Dots and Sarcosine Oxidase

Marc Riedel,^[a] Gero Göbel,^[a] Abuelmagd M. Abdelmonem,^[b] Wolfgang J. Parak,^[b] and Fred Lisdat^{*[a]}

In this study, a photobioelectrochemical sensor for the detection of sarcosine is reported. For this purpose, CdSe/ZnS quantum dot (QD) modified electrodes are prepared and the oxygen-dependent photocurrent is evaluated under illumination. By using sarcosine oxidase (SOD), the photocurrent can be suppressed because of biocatalytic oxygen reduction. For the construction of a sensor, SOD is immobilised on the QDs by means of the polyelectrolyte poly(allylamine hydrochloride)

(PAH). Multi-layer systems have been built up to six bilayers through electrostatic interactions. The assembly can be verified by surface plasmon resonance measurements. By varying the number of layers, the influence of the amount of enzyme on the sensitivity of the sensor can be shown. The [SOD/PAH]₆-layer system results in a signal change of 0.041% μM^{-1} in the linear range from 100 μM to 1 mM of sarcosine.

1. Introduction

The combination of nanostructures and biomolecules has been followed with growing interest in the last decade.^[1,2] Different nanostructures, such as quantum dots (QDs),^[3] nanowires,^[4] nanorods^[5] or nanotubes,^[6,7] have been established and characterised. Through their small size in at least one dimension, nanostructures often possess different chemical and physical properties than those of their bulk counterparts.

QDs, in particular, have been intensively investigated because of their unique optical properties.^[8,9] They can consist of different semiconductors, such as CdSe, CdS, ZnS or ZnSe, with sizes of only a few nanometres. Through illumination, QDs can be excited to generate electron–hole pairs. Relaxation of electrons in the initial state may result in light emission; the band gap defines the emission energy and increases with decreasing QD diameter. QDs also possess broad absorption spectra.^[3,10] Size-tuneable emission spectra allow the multiple read-out of differently sized QDs in a sample.^[11,12] These properties make them a more attractive biological label than alternative organic dyes.^[13] Thus, QD labels coupled to recognition molecules have been investigated *in vivo* and *in vitro*.^[14]

In addition to the use of QDs as an optical marker, several investigations have been performed for coupling QDs to electrochemistry.^[15–17] Hereby, the generation of light-induced electron–hole pairs in QDs is utilised to achieve electron transfer


from the electrode via the QDs to a redox-active molecule in solution or vice versa. This enables the construction of light-triggered sensors; a concept that has been discussed for many years.^[19–21] Direct protein electrochemistry can also be shown with QD electrodes, allowing the construction of sensor schemes for superoxide^[21] or enzyme substrates such as lactate or nitrate.^[22]

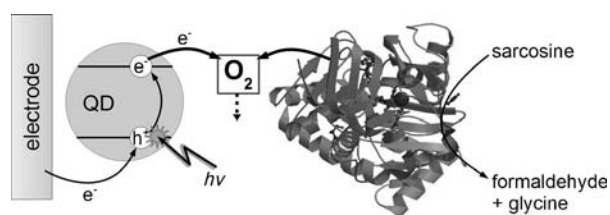
Various approaches exist to create a surface that makes QDs more suitable for applications in biological systems. When QD synthesis is performed in organic solvents, the resulting QDs are capped with ligands such as trioctylphosphine oxide (TOPO). For investigations in biological systems, QDs have to be transferred to aqueous solutions.^[23,24] Thus, various layers consisting of silicone oxide,^[25] polymers^[26] or proteins^[27] have been attached to the QD surface. Another method applies ligand exchange with thiol-containing substances, such as 4-mercaptophenol,^[28] 11-mercaptoundecanoic acid,^[29] 1,4-benzenedithiol (BDT)^[30] or dihydrolipoic acids.^[31] For the coupling of biomolecules to water-soluble QDs, different methods have been investigated, of which the covalent linkage of an amino group and a carboxylic group of the QD ligand is the most widely used one.^[3] Another possibility is coupling between differently charged QDs and proteins through electrostatic interactions.

Herein, a light-triggered CdSe/ZnS QD sensor for the enzymatic detection of sarcosine is demonstrated. The sensor is based on the influence of oxygen on QDs, as verified in previous studies.^[32–33] To build a sensor, the oxygen-consuming enzyme sarcosine oxidase (SOD) is immobilised on a QD-modified electrode, leading to suppression of the photocurrent in the presence of sarcosine. This is illustrated in Scheme 1.

[a] M. Riedel, G. Göbel, Prof. Dr. F. Lisdat
Biosystems Technology
Technical University of Applied Sciences Wildau
Bahnhofstraße 1, 15745 Wildau (Germany)
E-mail: flisdat@th-wildau.de

[b] A. M. Abdelmonem, Prof. Dr. W. J. Parak
Biophotonic, Philipps University Marburg
Renthof 7, 35037 Marburg (Germany)

 Supporting information for this article is available on the WWW under <http://dx.doi.org/10.1002/cphc.201201036>.



Scheme 1. Sensing principle of the QD electrode in combination with the enzyme SOD. During the enzymatic conversion of sarcosine, oxygen is reduced to hydrogen peroxide. This process competes with electron transfer from the excited QDs to oxygen, resulting in a photocurrent change that is detected at the electrode.

2. Results and Discussion

2.1. Oxygen Influence on the QD Electrode and the Sensing Principle

Herein, we use CdSe/ZnS QDs with an absorption maximum at 524 nm and a diameter of around 3.1 nm. A TEM image and fluorescence spectrum of the QDs are given in the Supporting Information.

For the preparation of a functional QD electrode, BDT-functionalised QDs are immobilised on a gold electrode by chemisorption. Under illumination, a photocurrent can be generated. Previous studies have shown that, by varying the wavelength of excitation, the photocurrent follows the absorption spectra of the QDs used.^[21] The photocurrent is potential dependent, resulting from electron-transfer reactions from or to the excited QDs. The clear potential dependence can be seen as evidence of the quality of the QDs prepared with a low number of surface states. This is mainly caused by the ZnS shell around the CdSe core. The change from cathodic to anodic photocurrent depends on several parameters, such as the modification of the QDs, and also on the solution composition (such as the presence or absence of donor/acceptor compounds). For further sensor applications, we first investigate the influence of oxygen on the photocurrent of the QD electrode. These measurements are performed in air-saturated and argon-purged buffer at pH 7.6 at a potential of -350 mV (vs Ag/AgCl). During illumination, a photocurrent is obtained that becomes stable after six to eight light pulses. The influence of oxygen on the photocurrent is shown in Figure 1. The results illustrate a decreased cathodic photocurrent in the absence of oxygen; this is about 50–60% smaller than the signal in air-saturated solution. Thus, under illumination, electron-hole pairs are generated in the QDs and electron transfer from the conduction band to molecular oxygen is feasible under these experimental conditions. Oxygen acts as an electron acceptor here, and thus, helps to separate light-generated charge carriers in the QDs, which limits recombination processes and results in a stable photocurrent response. A potential variation of the QD electrode verifies, on the one hand, that increasing potential results in smaller photocurrents. On the other hand, more negative potentials than -350 mV versus Ag/AgCl do not significantly enhance the current. Thus, this potential is used hereafter for further studies.

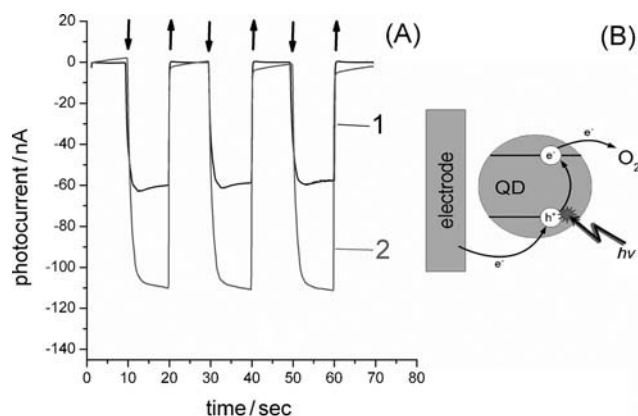


Figure 1. A) Photocurrent measurements of CdSe/ZnS QD-modified electrodes in argon-purged (1) and air-saturated (2) buffer [100 mM *N*-(2-hydroxyethyl)piperazine-*N*-(2-ethanesulfonic acid) (HEPES) pH 7.6; -350 mV vs Ag/AgCl; arrows indicate the switching on (\downarrow) and off (\uparrow) of the light source]. B) Illustration of the electron-transfer steps at the QD electrode.

The influence of oxygen found provides the basis for the combination of QDs with the enzyme SOD to detect sarcosine through the enzymatic consumption of the co-substrate. This leads to a competition situation between the enzyme and the QDs to reduce oxygen in the presence of the analyte, as illustrated in Scheme 1.

Sarcosine is an intermediate in the enzymatic analysis of creatinine, and thus, a sarcosine sensor could be beneficial for the diagnosis of kidney diseases. Different creatinine detection methods have been established by the use of SOD^[34–36] and sarcosine sensors have also been reported.^[37,38]

2.2. Optimisation of Biocatalyst Deposition

To attach the enzyme to the QD electrode surface at a high concentration, we chose a layer-by-layer assembly with the polyelectrolyte poly(allylamine hydrochloride) (PAH; as illustrated in Figure 2B). This is based on electrostatic interactions be-

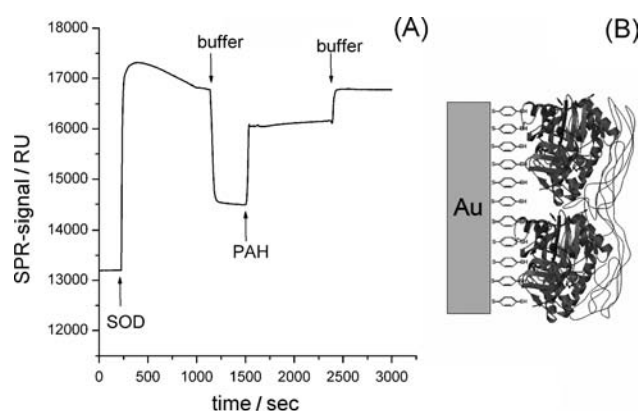


Figure 2. A) Surface plasmon resonance (SPR) measurements of the assembly of one SOD/PAH bilayer on a BDT-modified Au SPR chip [5 mM sodium phosphate buffer (NaPP) pH 7.6; flow rate $1 \mu\text{L min}^{-1}$]. B) Illustration of the SOD/PAH layer assembling on a BDT-modified SPR chip.

tween the negatively charged enzyme (pI 5.3) and the positively charged polyelectrolyte at pH 7.6.^[39] This immobilisation method is investigated by SPR to obtain information on the assembling conditions. To simulate the QD electrode surface, SPR Au chips are modified with BDT. When the assembly is performed with 2 mM NaPP at pH 7.6, only very weak deposition of the enzyme is found. However, with 5 mM NaPP at pH 7.6, SOD and PAH are successfully immobilised in a layer-like format. Figure 2B shows the formation of one bilayer on the surface. Thus, these conditions are used for further sensor constructions with SOD.

2.3. Study of the Behaviour of the SOD–QD Electrode

Firstly, a QD electrode was combined with a six-layer system [SOD/PAH]₆ to verify that the sensing principle is working. Therefore, the photocurrent measurement is started in pure buffer and then increasing concentrations of sarcosine are added. Figure 3 shows the current response to single light pulses at various sarcosine concentrations and illustrates the decrease of the photocurrent through enzymatic substrate oxidation accompanied by oxygen consumption. A constant photocurrent is formed three to four light pulses after a change of concentration in solution.

To investigate the influence of the number of layers on the sensing properties, different [SOD/PAH]_n-layer systems are built up on QD electrodes. Figure 4 shows the relative photocurrent change of multi-layer systems with different numbers of layers. All of the multi-layer systems prepared show significant photocurrent suppression in the presence of sarcosine. The magnitude of the photocurrent change depends on the number of bilayers deposited. While the two-layer system [SOD/PAH]₂ and the four-layer system [SOD/PAH]₄ give only slight differences, the sarcosine response of the [SOD/PAH]₆-layer system is clearly higher. The investigations show that sarcosine can diffuse into the whole layer system and enzyme molecules immobilised near the electrode are also involved in the generation of the enzymatic signal. Under substrate saturation, up to 60% of the whole photocurrent can be suppressed. This corresponds to the oxygen-dependent part of the photocurrent, as demonstrated by the measurements recorded before without enzyme. It can be concluded that, with a six-layer assembly, a sufficient SOD amount can be immobilised to make use of the full range of oxygen sensitivity of the QD electrode. The linear range is between 100 μM and 1 mM sarcosine for all multi-layer systems, whereby the [SOD/PAH]₆-layer system has the highest sensitivity (0.041 % μM⁻¹). The dynamic range proceeds up to 30 mM sarcosine. Higher concentrations do not lead to a further photocurrent suppression. The apparent *K*_m value of the immobilised SOD is determined to be 1 mM compared with a *K*_m value of 12 mM for SOD of *Bacillus* sp. in solution.^[40] The sensitivity of the system is slightly too low to allow the detection of sarcosine concentrations that would appear during creatinine analysis in

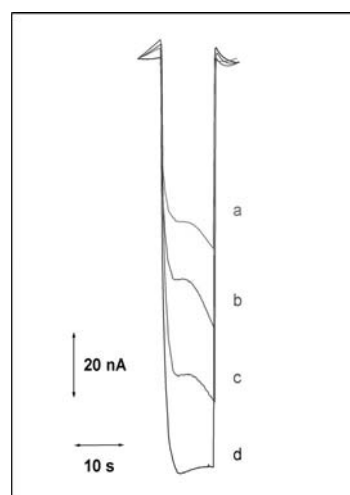


Figure 3. Photocurrent measurements of a [SOD/PAH]₆-layer modified QD electrode in solutions with different sarcosine concentrations (*a* = 30 mM, *b* = 1 mM, *c* = 500 μM, *d* = 0 μM; 6 light pulses after substrate addition; −350 mV vs Ag/AgCl, 100 mM HEPES pH 7.6).

serum samples. However, as already shown in a previous study,^[33] the adjustment of the enzyme immobilisation conditions (e.g. concentration or cross-linking) offers the possibility of tuning the sensitivity to a suitable dynamic range.

After substrate measurement, the photocurrent can be recovered very well in buffer solution and the sensor is ready for further analysis. The first stability tests of the [SOD/PAH]_n-layer systems do not show a significant decrease in the signal, but give a stable photocurrent response for up to three days. For this period, preserved enzyme activity and sustained inclusion of SOD in the layered system are achieved.

In sample solutions for analysis, a high number of different molecules can occur, which could disturb application of the

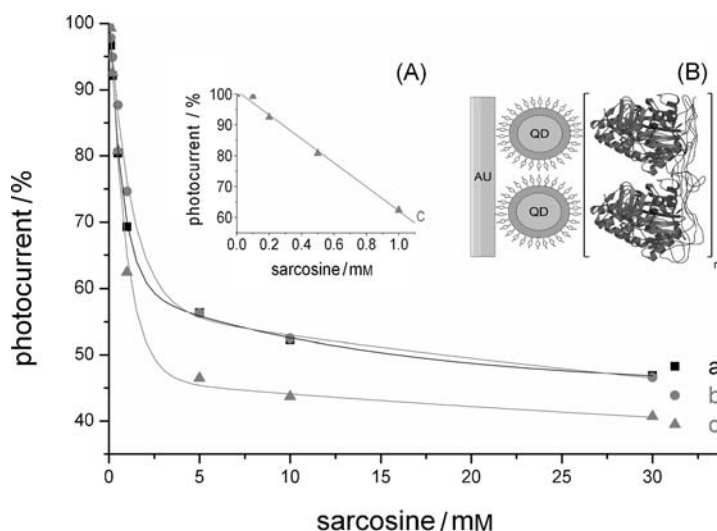


Figure 4. Relative change of the photocurrent of different QD-modified electrodes with immobilised SOD depending on the sarcosine concentration in the range of 0–30 and 0–1 mM (inset A) for a) [SOD/PAH]₂, b) [SOD/PAH]₄ and c) [SOD/PAH]₆ (100 mM HEPES pH 7.6; −350 mV vs Ag/AgCl). Inset B) Schematic illustration of the [SOD/PAH]_n-layer assembly on the QD-modified electrode.

sensor. Therefore, initial investigations with potentially interfering molecules, such as hydrogen peroxide, urea and glycine, are realised under working conditions with concentrations of 200 μM . It can be shown that these molecules do not influence the photocurrent behaviour of a QD electrode with immobilised SOD. Because the redox-active hydrogen peroxide, in particular, is co-produced during sarcosine conversion, these studies also demonstrate that no products of the enzyme reaction are responsible for the signal depression found. Furthermore, whether sarcosine could be directly converted at the excited QDs under negative polarisation is studied. Again no change in photocurrent behaviour is found when the sarcosine concentration in solution increases. Because direct analyte conversion can be excluded, in contrast to, for example, glucose detection with illuminated QDs,^[41] a defined signal generation process can be verified here for the proposed system. As for all biosensors based on oxygen consumption, sufficient air contact of the sample solution to be analysed has to be ensured.

The biosensor principle illustrated in this study is based on photocurrent measurements of a QD electrode. It possesses great potential for parallel analysis of different enzyme substrates when the corresponding enzymes can be separately fixed on the surface and spatially resolved illumination is used. The spatially resolved immobilisation of SOD in small and defined spots, however, needs further investigation.

3. Conclusions

A photobioelectrochemical sensor based on CdSe/ZnS QDs and SOD is developed to determine sarcosine concentrations. Firstly, the oxygen dependence of the cathodic photocurrent of the QD electrode during illumination is demonstrated as the basis for an analytical application. Secondly, the layer-by-layer assembling technique, utilising positively charged PAH as a polyelectrolyte, is performed as an efficient method to deposit SOD at a high concentration onto the QD electrode; this is verified by SPR. We show that SOD in combination with the QD electrode leads to a photocurrent change in the presence of sarcosine because of a competitive situation with respect to oxygen. The linear range is from 100 μM to 1 mM and the sensitivity depends on the number of immobilised enzyme layers. It is demonstrated that the [SOD/PAH]₆-layer system is well suited for sensitive sarcosine detection. The study opens the way for utilising other oxygen-consuming enzymes, and thus, a tool box is created for multi-analyte sensing on one sensor surface through illumination of the respective area and photocurrent detection.

Experimental Section

Procedures

Benzenedithiol (BDT) is purchased from Alfa Aesar (Karlsruhe, Germany). Argon is acquired from Air Liquide (Düsseldorf, Germany). Anhydrous sodium dihydrogen phosphate, 99.5% HEPES, sodium hydroxide ($\geq 97\%$), sarcosine, toluene, SOD (EC 1.5.3.1, SOD) from *Bacillus* sp. and PAH are purchased from Sigma-Aldrich (Steinheim, Germany). Sulfonic acid (96%) and methanol (99.9%, ≤ 50 ppm

H₂O) are obtained from Roth (Karlsruhe, Germany). All aqueous solutions are prepared with ultrapure water. Structural images of SOD are obtained from the RCSB Protein Data Bank.

CdSe/ZnS nanoparticles (QDs) are synthesised by following an established protocol.^[42] In the presence of TOPO, the diameter of the inorganic part of the QDs synthesised is 3.1 nm and they are stored in toluene.

Electrode Cleaning

Gold electrodes (3 mm diameter BASi, UK) are polished for 4 min with Al₂O₃ powder of various sizes (1 μm , 0.05 μm). Thereafter, the electrodes are sonicated for 10 min. Each electrode is electrochemically cleaned by cyclic voltammetry in 1 M NaOH (−800 to +200 mV vs Ag/AgCl, 1 M KCl, scan rate 300 mV s^{−1}) and 0.5 M H₂SO₄ (−200 mV to +1.75 V vs Ag/AgCl, 1 M KCl, scan rate 300 mV s^{−1}).

Electrode Modification

A 10 μM solution of CdSe/ZnS QDs is incubated with a 100 mM solution of BDT in toluene for 3 h in a thermoshaker at 40 °C to exchange the ligand TOPO. Afterwards methanol is added (1:1) and the solution is centrifuged at 14500 rpm for 40 min. The precipitated QDs in the pellet are re-suspended in toluene before the cleaned Au electrodes are immersed in BDT-coated QDs for 24 h on a shaker. After incubation, the electrodes are rinsed with toluene to remove insufficiently attached QDs.

SOD Immobilisation

For layer-by-layer deposition of the enzyme, the QD-modified Au electrodes are incubated first in 1 mM SOD solution (pH 7.6, 5 mM NaPP) for 15 min. After a washing step, the electrodes are immersed in PAH (1.8 mg mL^{−1}, pH 7.6, 5 mM NaPP) for another 15 min before a next washing step is performed. This layer-by-layer deposition procedure is repeated to establish two, four and six bilayer systems with alternating layers of SOD and PAH. Before measurements are recorded, the modified electrodes are stored for 15 min in sarcosine solution (30 mM, pH 7.6, 100 mM HEPES buffer) to condition the system.

Measurements

Photocurrent measurements are performed amperometrically with a three-electrode arrangement consisting of the QD working electrode, an Ag/AgCl reference electrode and a platinum wire as the counter electrode. A halogen reflector lamp from Schott (Mainz, Germany) with a light intensity of about 230 mW (before the optical window of the measuring cell) is used as the light source. The light is placed opposite the working electrode. For all photocurrent measurements, 100 mM HEPES buffer (pH 7.6) is used and a potential of −350 mV (vs Ag/AgCl) is applied. Every 10 s during the measurement, the light is switched on and off to generate a photocurrent.

To study the O₂ dependency on the photocurrent, QD-modified Au electrodes are investigated in air-saturated and in argon-purged buffer.

Furthermore, the effects of different SOD/PAH multi-layers on the photocurrent are analysed. Sarcosine solutions between 0.1 and 30 mM are prepared with 100 mM HEPES at pH 7.6. Before these investigations are carried out, buffer is added to the measurement cell to evaluate the system. Afterwards sarcosine solutions with in-

creasing concentrations are added by exchanging the whole solution.

To investigate enzyme immobilisation, a Biacore T100 device is used to perform SPR spectroscopy. Therefore, a SPR chip is incubated for 12 h in a 100 mM solution of BDT in toluene. Thereafter, the SPR chip is integrated into the SPR device. For measurements, a 2 or 5 mM sodium phosphate running buffer at pH 7.6 is used ($1 \mu\text{Lmin}^{-1}$). SOD (15 μL ; 2 or 5 mM sodium phosphate buffer, pH 7.6) and PAH (0.02 M monomer concentration; 2 or 5 mM sodium phosphate buffer, pH 7.6) are injected alternately. After each injection, a washing step is performed to remove weakly attached molecules.

Acknowledgements

This work was partially supported by the BioNapa project (BMBF Germany, Project PNT51513), the DFG (Li706/8-1) and the DFG graduate research school (GRK 1782).

Keywords: electrochemistry · enzymes · photochemistry · quantum dots · sensors

- [1] H. G. Craighead, *J. Vac. Sci. Technol. A* **2003**, *21*, S216.
[2] L. Wang, X. Chen, X. Wang, X. Han, S. Liu, C. Zhao, *Biosens. Bioelectron.* **2011**, *30*, 151–157.
[3] R. Gill, M. Zayats, I. Willner, *Angew. Chem.* **2008**, *120*, 7714–7736; *Angew. Chem. Int. Ed.* **2008**, *47*, 7602–7625.
[4] W. Lu, C. M. Lieber, *J. Phys. D* **2006**, *39*, R387.
[5] J. Pérez-Juste, I. Pastoriza-Santos, L. M. Liz-Marzán, P. Mulvaney, *Coord. Chem. Rev.* **2005**, *249*, 1870–1901.
[6] D. Sarauli, M. Riedel, C. Wettstein, R. Hahn, K. Stiba, U. Wollenberger, S. Leimkühler, P. Schmuki, F. Lisdat, *J. Mater. Chem.* **2012**, *22*, 4615–4618.
[7] Y. Xia, P. Yang, Y. Sun, Y. Wu, B. Mayers, B. Gates, Y. Yin, F. Kim, H. Yan, *Adv. Mater.* **2003**, *15*, 353–389.
[8] X. Gao, L. Yang, J. A. Petros, F. F. Marshall, J. W. Simons, S. Nie, *Curr. Opin. Biotechnol.* **2005**, *16*, 63–72.
[9] W. J. Parak, T. Pellegrino, C. Plank, *Nanotechnology* **2005**, *16*, R9–R25.
[10] M. P. Bruchez, Jr., M. Moronne, P. Gin, S. Weiss, A. P. Alivisatos, *Science* **1998**, *281*, 2013–2016.
[11] J. Deng, Y. Zhang, J. Yue, F. Tang, Q. Wie, *J. Phys. Chem. B* **2007**, *111*, 12024–12031.
[12] E. R. Goldman, A. R. Clapp, G. P. Anderson, H. T. Uyeda, J. M. Mauro, I. L. Mednitz, H. Mattoussi, *Anal. Chem.* **2004**, *76*, 684–688.
[13] W. C. W. Chan, S. Nie, *Science* **1998**, *281*, 2016–2018.
[14] S. K. Chakraborty, J. A. J. Fitzpatrick, J. A. Phillippi, S. Andreko, A. S. Waggoner, M. P. Bruchez, B. Ballou, *Nano Lett.* **2007**, *7*, 2618–2626.
[15] C. Stoll, S. Kuder, W. J. Parak, F. Lisdat, *Small* **2006**, *2*, 741–743.
[16] E. Katz, A. N. Shipway, *Bioelectronics* (Eds.: I. Willner, E. Katz), Wiley-VCH, Weinheim, **2005**, pp. 332–335.
[17] W. R. Algar, A. J. Tavares, U. J. Krull, *Anal. Chim. Acta* **2010**, *673*, 1–25.
[18] W. Moritz, I. Gerhardt, D. Roden, M. Xu, S. Krause, *Fresenius J. Anal. Chem.* **2000**, *367*, 329–333.
[19] J. C. Owicki, L. J. Bousse, D. G. Hafeman, G. L. Kirk, J. D. Olson, H. G. Wada, J. W. Parce, *Annu. Rev. Biophys. Biomol. Struct.* **1994**, *23*, 87–113.
[20] T. Yoshinobu, H. Iwasaki, Y. Ui, K. Furuichi, Y. Ermolenko, Y. Mourzina, T. Wagner, N. Näther, M. J. Schöning, *Methods* **2005**, *37*, 94–102.
[21] C. Stoll, C. Gehring, K. Schubert, M. Zanella, W. J. Parak, F. Lisdat, *Biosens. Bioelectron.* **2008**, *24*, 260–265.
[22] E. Katz, M. Zayats, I. Willner, F. Lisdat, *Chem. Commun.* **2006**, 1395–1397.
[23] F. Zhang, E. Lees, F. Amin, P. R. Gil, F. Yang, P. Mulvaney, W. J. Parak, *Small* **2011**, *7*, 3113–3127.
[24] X. Michalet, F. F. Pinaud, L. A. Bentolila, J. M. Tsay, S. Doose, J. J. Li, G. Sundaresan, A. M. Wu, S. S. Gambhir, S. Weiss, *Science* **2005**, *307*, 538–544.
[25] A. Barski, M. Derivaz, J. L. Rouvière, D. Buttard, *Appl. Phys. Lett.* **2000**, *77*, 3541–3543.
[26] D. E. Fogg, L. H. Radzilowski, B. O. Dabbousi, R. R. Schrock, E. L. Thomas, M. G. Bawendi, *Macromolecules* **1997**, *30*, 8433–8439.
[27] J. N. Mason, I. D. Tomlinson, S. J. Rosenthal, R. D. Blakely, *Methods Mol. Biol.* **2005**, *303*, 35–50.
[28] S. F. Wuister, C. de Mello Donegá, A. Meijerink, *J. Phys. Chem. B* **2004**, *108*, 17393–17397.
[29] S. Kim, M. G. Bawendi, *J. Am. Chem. Soc.* **2003**, *125*, 14652–14653.
[30] K. Schubert, W. Khalid, Z. Yue, W. J. Parak, F. Lisdat, *Langmuir* **2010**, *26*, 1395–1400.
[31] A. R. Clapp, E. R. Goldman, H. Mattoussi, *Nat. Protoc.* **2006**, *1*, 1258–1266.
[32] F. Koberling, A. Mews, T. Basché, *Adv. Mater.* **2001**, *13*, 672–676.
[33] J. Tanne, D. Schäfer, W. Khalid, W. J. Parak, F. Lisdat, *Anal. Chem.* **2011**, *83*, 7778–7785.
[34] G. F. Khan, W. Wernet, *Anal. Chim. Acta* **1997**, *351*, 151–158.
[35] J. Wang, M. P. Chatrathi, *Anal. Chem.* **2003**, *75*, 525–529.
[36] U. Lad, S. Khokhar, G. M. Kale, *Anal. Chem.* **2008**, *80*, 7910–7917.
[37] Y. Yang, S. Mu, *J. Electroanal. Chem.* **1996**, *415*, 71–77.
[38] C. S. Pundir, N. Chauhan, G. Kumari, Vandana, *Indian J. Biotechnol.* **2011**, *10*, 219–223.
[39] F. Lisdat, R. Dronov, H. Möhwald, F. W. Scheller, D. G. Kurth, *Chem. Commun.* **2009**, 274–283.
[40] Y. Matsuda, H. Hoshika, Y. Inouye, S. Ikuta, K. Matsuura, S. Nakamura, *Chem. Pharm. Bull.* **1987**, *35*, 711–717.
[41] M. Zheng, Y. Cui, X. Li, S. Liu, Z. Tang, *J. Electroanal. Chem.* **2011**, *656*, 167–173.
[42] B. O. Dabbousi, J. Rodriguez-Viejo, F. V. Mikulec, J. R. Heine, H. Mattoussi, R. Ober, K. F. Jensen, M. G. Bawendi, *J. Phys. Chem. B* **1997**, *101*, 9463–9475.

Received: December 11, 2012

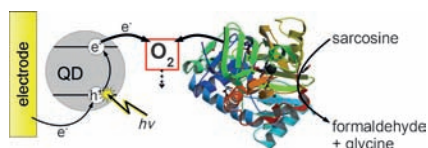
Published online on ■ ■ ■ ■, 2013

ARTICLES

M. Riedel, G. Göbel, A. M. Abdelmonem,
W. J. Parak, F. Lisdat*



Photoelectrochemical Sensor Based on Quantum Dots and Sarcosine Oxidase



Sarcosine sensor: A photobioelectrochemical sensor based on the combination of quantum dots (QDs) with an enzyme is developed to allow a light-directed sensor read-out (see picture). The generation of charge carriers in the QDs by illumination is coupled to charge transfer with the electrode and the co-substrate of the enzyme.



Bridge over troubled waters: understanding the synthetic and biological identities of engineered nanomaterials

Bengt Fadeel,^{1*} Neus Feliu,¹ Carmen Vogt,¹ Abuelmagd M. Abdelmonem² and Wolfgang J. Parak²

Engineered nanomaterials offer exciting opportunities for ‘smart’ drug delivery and *in vivo* imaging of disease processes, as well as in regenerative medicine. The ability to manipulate matter at the nanoscale enables many new properties that are both desirable and exploitable, but the same properties could also give rise to unexpected toxicities that may adversely affect human health. Understanding the physicochemical properties that drive toxicological outcomes is a formidable challenge as it is not trivial to separate and, hence, to pinpoint individual material characteristics of nanomaterials. In addition, nanomaterials that interact with biological systems are likely to acquire a surface corona of biomolecules that may dictate their biological behavior. Indeed, we propose that it is the combination of material-intrinsic properties (the ‘synthetic identity’) and context-dependent properties determined, in part, by the bio-corona of a given biological compartment (the ‘biological identity’) that will determine the interactions of engineered nanomaterials with cells and tissues and subsequent outcomes. The delineation of these entwined ‘identities’ of engineered nanomaterials constitutes the bridge between nanotoxicological research and nanomedicine. © 2013 Wiley Periodicals, Inc.

How to cite this article:

WIREs Nanomed Nanobiotechnol 2013, 5:111–129. doi: 10.1002/wnan.1206

INTRODUCTION

Nanomaterials are in the same size range as biomolecules and cellular structures; this fact lies at the very heart of nanomedicine, a field in which many applications rely on nanoscale interactions. However, this is also the reason for the current concern surrounding nanomaterials: the interference of man-made nanomaterials with biological systems could also lead to hazardous effects on human health.¹ While the interest in nanoscale materials has increased tremendously in recent years, important observations on their interactions with biological

systems were reported much earlier. For instance, the fact that nanoparticles are typically incorporated by cells via endocytosis was known for decades.² In addition, colloidal nanoparticles were shown to induce alterations in the blood–air barrier in the mouse lung more than half a century ago.³ Numerous studies have been published more recently in which exposure to engineered nanoparticles has been linked to toxicity.^{4–6} However, understanding which of the physicochemical properties of nanomaterials that are driving toxicity remains a challenge; if one could connect material properties (size, shape, surface charge, porosity, colloidal stability, purity/degree of contamination, etc.) with toxicity, then this would enable prediction of potential hazards and could also lead to the design of nanomaterials with minimal toxicity.⁷ In addition, a thorough understanding of the properties of nanomaterials that determine biological

*Correspondence to: bengt.fadeel@ki.se

¹Division of Molecular Toxicology, Institute of Environmental Medicine, Karolinska Institutet, Stockholm, Sweden

²Fachbereich Physik and Wissenschaftlichen Zentrum für Materialwissenschaften, Philipps Universität Marburg, Marburg, Germany

responses would also facilitate the design of better nanomedicines for the treatment of human disease.

In this review, we discuss the bridging of nanotoxicological research and nanomedicine. We suggest that a careful understanding of nanomaterial physicochemical properties, i.e., the 'synthetic identity', constitutes the bridge between these two disciplines. Moreover, we propose that the 'biological identity' of nanomaterials is determined, in part, by the adsorption of biomolecules onto the nanomaterial surface upon introduction into a living system. In fact, as pointed out by Walkey and Chan⁸ in their excellent review on the protein corona as it applies to nanomaterials, 'once fully mapped, the relationships between synthetic identity, biological identity, and physiological response will enable researchers to predict the physiological response of a nanomaterial by characterizing its synthetic identity'. This statement points toward a *predictive nanotoxicology*, the ultimate goal of which is to decode nanomaterial properties to enable redesign of materials that are both useful and safe.⁹

NANOMATERIALS IN MEDICINE

Engineered nanomaterials offer great potential in medical applications.¹⁰ The variety of possible applications is very broad. Here, we provide some highlights, and we attempt to emphasize the physicochemical properties that make nanomaterials so favorable, in particular for medical imaging and drug or gene delivery.

Medical Imaging

Medical imaging is typically based on the use of contrast agents, which facilitate visualization of tissues and organs. For imaging, two basic properties are required. First, the contrast agent should provide contrast compared to the local environment, and second, the contrast agent should be specifically localized at the region of interest. What may nanoparticles contribute in this direction? The first answer to this question is relatively obvious: nanoparticles can provide higher contrast because of their larger size compared to individual molecules. Furthermore, instead of having only one fluorophore for fluorescence imaging, or just one chelated ion such as Gd^{2+} to provide contrast for magnetic resonance imaging (MRI), several fluorophores or Gd^{2+} ions can be combined in one nanoparticle, and this multivalent display may provide higher contrast. In fact, the combination of different contrast agents in a single nanoparticle allows for multimodal imaging.¹¹ The

combination of diagnostic and therapeutic functions in a single 'theranostic' platform has also been attempted. Yang et al.¹² functionalized a reduced graphene oxide-iron oxide nanoparticle (RGO-IONP) complex with poly(ethylene glycol) (PEG), obtaining a RGO-IONP-PEG theranostic nanoprobe that was used for *in vivo* trimodal fluorescence, photoacoustic, and MR imaging, uncovering high passive tumor targeting, which was further exploited for thermal ablation of tumors in mice.

The second answer to the aforementioned question is less obvious. Nonetheless, because of their larger size compared to molecules, nanoparticles are passively trapped in tumors; this phenomenon is known as the enhanced permeability and retention (EPR) effect. Nanoparticles are small enough to leak out from the bloodstream into tumors, yet big enough to be trapped in the tumor vasculature. Hence, nanoparticles with many fluorophores can passively accumulate in tumors more efficiently than the same individual fluorophores.¹³ However, subsequent penetration into the tumor itself is not readily achieved. Wong et al.¹⁴ generated a multistage nanoparticle delivery system for deep penetration into tumors. Hence, the gelatin core of 100-nm nanoparticles was degraded by proteases present in the tumor microenvironment thereby releasing 10-nm quantum dots (QDs) after extravasation. Chauhan et al.¹⁵ investigated how vascular normalization affects nanoparticle delivery by studying whether a vascular endothelial growth factor receptor-2-blocking antibody modulates nanoparticle penetration rates in mammary tumors *in vivo*. The authors demonstrated that 12-nm particles penetrate tumors better than larger particles (125 nm) once abnormal vessels are repaired, suggesting that small nanoparticles less than 12 nm are superior because of higher tumor penetration.

Kim et al.¹⁶ provided a particularly relevant example of nanoparticle-based imaging involving QD-based fluorescence labeling, allowing for sentinel lymph node mapping in large animals under image guidance. This approach could have significant impact on such surgical procedures in cancer patients, provided that toxicity of QDs is controlled. This is a nontrivial question, as QDs are typically made from inherently toxic components such as cadmium, a heavy metal with known adverse effects on human health. A recent study in nonhuman primates suggested that phospholipid micelle-encapsulated CdSe/CdS/ZnS QDs do not induce major signs of toxicity up to 90 days postexposure; however, chemical analysis revealed that most of the initial

dose of cadmium remained in the liver, spleen, and kidneys.¹⁷

Finally, it is noteworthy that nanoparticles also afford label-free detection. Hence, carbon nanotubes have been shown to be useful for photoacoustic imaging, an approach that offers higher spatial resolution and allows deeper tissues to be imaged compared with most optical imaging techniques.¹⁸ In a more recent study, Tong et al.¹⁹ reported that transient absorption microscopy offers an alternative, label-free method to image both semiconducting and metallic single-walled carbon nanotubes (SWCNTs) *in vitro* and *in vivo*, in real time, with submicrometer resolution.

Drug Delivery

Nanoparticles clearly offer novel features for 'smart' drug delivery.²⁰ First of all, nanoparticles offer potential as passive carrier systems for delivery. This is due to the fact that drug-loaded nanoparticles interact differently with cells than the corresponding drug alone.¹³ Nanoparticles can also be loaded with drugs in a way that allows for their slow release. Fine tuning of the surface of nanoparticles allows for regulation of nanoparticle interactions with cells and thus the mode of delivery.^{21,22} Nanoparticles can be used to increase the local concentration of drugs in, for instance, cancer cells. Ashley et al.²³ designed porous nanoparticle-supported lipid bilayers termed protocells that synergistically combined properties of liposomes and nanoporous particles. The protocells can be loaded with combinations of therapeutic agents, e.g., drugs or small interfering RNAs. The very high capacity of the high-surface area nanoporous core combined with the enhanced targeting efficacy toward cancer cells enabled by the fluid-supported lipid bilayer enabled a single protocell loaded with a drug cocktail to kill a drug-resistant human hepatocellular carcinoma cell, representing a million-fold improvement over comparable liposomes. Further *in vivo* studies are certainly warranted. Davis et al.²⁴ administered nanoparticles functionalized with a targeting ligand (transferrin) systemically to a small number of cancer patients and were able to demonstrate successful RNA interference, i.e., specific inhibition of gene expression.

Notably, in a recent landmark study, the gap between preclinical development and clinical translation was bridged using targeted doxorubicin-loaded nanoparticles.²⁵ The nanoparticles were developed from a combinatorial library of more than 100 targeted nanoparticle formulations varying with respect to particle size, targeting ligand density, surface

hydrophilicity, drug loading, and drug release properties. In tumor-bearing mice, rats, and nonhuman primates, doxorubicin-loaded nanoparticles displayed pharmacokinetic characteristics consistent with prolonged circulation of nanoparticles in the vascular compartment and controlled release of the drug. In addition, clinical data in patients with advanced solid tumors indicated a pharmacokinetic profile consistent with the preclinical data as well as some cases of tumor shrinkage at doses below the solvent-based doxorubicin formulation dose typically used in the clinic.²⁵ This study shows that the 'valley of death' between preclinical research and clinical applications can be bridged through a rational design approach (Figure 1).

Moreover, inorganic nanoparticles can be used for introducing new functionalities. Here, two fascinating examples are given. First, magnetic nanoparticles can be used for locally trapping drugs (which are attached to the nanoparticles) by application of magnetic field gradients.²⁶ Magnetic targeting has been applied both *in vitro*²⁷ and *in vivo*.²⁸ Although clinical applications so far are limited to pets, this technology has the potential for being applied to humans in the future, in particular in cases of tumors close to the skin, as sufficiently high magnetic field gradients can be directed to the body surface.²⁸ Second, plasmonic nanoparticles, in particular those based on gold, can be used for light-controlled release of drugs.²⁹ Upon optical excitation at the plasmon resonance frequency, collective motion of electrons ultimately leads to dissipation and thus local heating of the environment of the nanoparticle surface.³⁰ Initially, gold nanoparticles directed to tumor tissue have been used for local tissue destruction by light-induced heating, also referred to as hyperthermal ablation.³¹ Hence, nanoparticles may not only deliver drugs but can also act as therapeutic agents *per se* (further examples of such nanomaterial-intrinsic effects are discussed below). The same phenomenon, however, can be employed for controlled delivery. Upon heat formation on the nanoparticle surface, molecular bonds can be broken and attached molecules can thus be released based on light triggers. Double-stranded DNA is a good linker, as it can be molten at temperatures well below the boiling point of water. Light-controlled heating can also be used for the regulated opening of the nanoscale containers.³² This may thus enable release of drugs by local illumination. Because of absorption of light by tissue [even in the near-infrared (NIR)], the most likely *in vivo* applications will be for tumors located close to the skin.

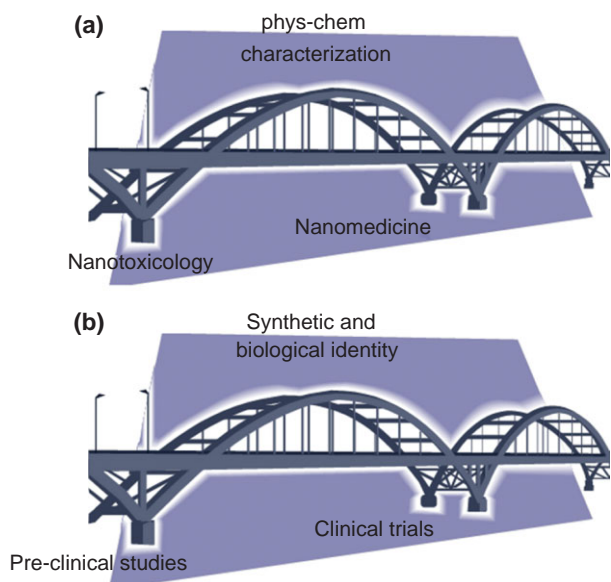


FIGURE 1 | Bridging nanotoxicology and nanomedicine. We posit that careful assessment of the physicochemical properties of engineered nanomaterials constitutes the 'bridge' between nanotoxicological research and nanomedicine insofar as a detailed understanding of material properties, i.e., the 'synthetic identity' is critical both for toxicological assessment of nanomaterials and for the development of novel nanomedicines (a). Furthermore, understanding the 'synthetic' and 'biological' identities of nanomaterials will facilitate the bridging of preclinical studies and the use of nanomaterials in medical imaging, drug delivery, and regenerative medicine (b). The 'biological' identity of a nanomaterial is largely determined by the 'corona' of biomolecules that forms in a biological environment; see text for details.

Regenerative Medicine

Nanomaterials may also have considerable impact on regenerative medicine, i.e., the replacement or regeneration of human cells, tissues, or organs.³³ For instance, magnetic nanoparticles can be used to image and guide stem cells to their target in stem cell-based therapies.^{34,35} Cells interact with the surrounding environment by making nanoscale interactions with extracellular signals and nanomaterials can be employed as biomimetic scaffolds to stimulate tissue growth. Intriguingly, supramolecular nanostructures that mimic, for instance, a growth factor can be used as a strategy for tissue regeneration and repair.^{36,37} Furthermore, in a recent clinical study, Jungebluth et al.³⁸ reported the first transplantation of an artificial trachea in a cancer patient. After complete tumor resection, the patient's airway was replaced with a tailored bioartificial nanocomposite previously seeded with autologous bone marrow mononuclear cells in a bioreactor. The cells differentiated into appropriate cell types. There are several advantages to this approach. For instance, by using the patient's own stem cells to populate the

scaffold, there are no concerns over rejection of the transplant.³⁹

SAFETY ASSESSMENT OF NANOMATERIALS

Rational design of 'nanomedicines' began almost half a century ago, and several products including liposomes (i.e., passive nanoscale carriers) have entered into routine clinical use (see Duncan and Gaspar⁴⁰ for an excellent historical perspective). However, countless other, more sophisticated nanomedicines are in the pipeline and the potential risks to human health of these novel entities need to be seriously considered. The latter is certainly true for all pharmaceutical products. Nanotoxicology attempts to investigate the interactions of nanomaterials with biological systems.⁴¹ However, there are several important and complicating aspects to address in nanotoxicological studies including not only the need for standardized assays and reference materials⁹ but also the issue of the most appropriate dose metric to use (surprisingly, this remains largely unresolved), and it may as yet be too early to draw general conclusions regarding toxicity of nanomaterials; the prevailing view today is that nanomaterials should be studied on a case-by-case basis.⁴² Nevertheless, some lessons can be garnered from studies conducted over the past several years. In the following sections, we will discuss why engineered nanoparticles are potentially hazardous, with the aim to elucidate physicochemical properties that have been linked to toxicity. We also provide an overview of emerging trends in nanotoxicology including high-throughput screening (HTS) and *in silico* modeling approaches.

High-Throughput Screening

As pointed out recently,⁴³ results of toxicological studies using extraordinarily high doses of nanomaterials have to be interpreted with caution. Indeed, while *in vitro* tests may prove useful for hazard identification, *in vivo* studies are needed to bridge the gap between cell culture model systems and the human exposure situation, in order to understand whether nanomaterials pose any risk to human health. At the same time, it is not ethically, economically, or practically feasible or reasonable to screen all nanomaterials using animal models. Moreover, a model is only a model (and 'essentially, all models are wrong, but some are useful', as the statistician George Box famously wrote) and we would be amiss to assume that results coming from animal studies are always relevant.⁴⁴ How, then, do we move forward? Lai⁴⁵ has proposed a

nanotoxicity testing strategy based on short-term *in vivo* animal studies (i.e., shorter than a conventional 90-day study) in conjunction with HTS and mechanistic *in vitro* studies, and comparing the data with those of reference nanomaterials for the specific subclass in question—an approach in concordance with the ‘Toxicity Testing in the 21st Century’ strategy for chemicals.⁴⁶

To this end, more advanced *in vitro* models are needed, in particular, assays that can be adapted for HTS. Huh et al.⁴⁷ reported on a biomimetic microsystem that reconstitutes the critical functional alveolar-capillary interface of the human lung. This ‘lung mimic’ revealed that cyclic mechanical strain accentuates toxic and inflammatory responses of the lung to silica nanoparticles. The authors concluded that mechanically active ‘lung-on-a-chip’ microdevices that reconstitute tissue–tissue interfaces critical to organ function may provide low-cost alternatives to animal studies for toxicity testing. The ‘lung mimic’ might also be amenable to HTS.⁴⁷

Naturally, it is important to validate *in vitro* assays. Han et al.⁴⁸ administered doses of titanium dioxide nanoparticles of different sizes (3–100 nm) to a rat alveolar epithelial cell line *in vitro* and the same nanoparticles by intratracheal instillation in rats *in vivo* to examine the correlation between *in vitro* and *in vivo* responses. The *in vivo* endpoint was the number of neutrophils in bronchoalveolar lavage fluid following exposure to nanoparticles. The correlations were based on toxicity rankings of nanoparticles after adopting surface area as dose metric and response per unit surface area as response metric. Slope analyses of the dose response curves showed that *in vitro* and *in vivo* responses were well correlated. This study underlines the importance of determining the appropriate dose metric in nanotoxicity studies. Shaw et al.⁴⁹ applied a high-content approach, i.e., a battery of test for multiple endpoints using multiple cell lines to test nanoparticles and derived detailed structure–activity relationships for the various nanomaterials tested. Importantly, nanoparticles with similar activity profiles *in vitro* exerted similar effects on monocyte numbers *in vivo*.

HTS is a method for scientific experimentation that comprises the screening of large chemical libraries for activity against biological targets via the use of automation, miniaturized assays, and large-scale data analysis.⁵⁰ HTS techniques have emerged as a potentially useful tool to predict the possible hazards of nanomaterials.^{51,52} However, the fact that nanomaterials may interfere with commonly used *in vitro* assays needs to be taken into account.⁴ Indeed,

novel nanotoxicity assays based on label-free detection of cellular responses are needed.⁵³

Mortimer et al.⁵⁴ demonstrated that the so-called kinetic *Vibrio fischeri* luminescence inhibition test is a potentially useful tool for screening of the toxicity of nanomaterials that can be adapted for HTS of ecotoxicological effects of nanomaterials. Jan et al.⁵⁵ reported on high-content screening for ‘fingerprinting’ of nanomaterials using cancer cell lines of neuronal and hepatic origin. George et al.⁵⁶ provided evidence that an *in vitro*-based HTS approach combined with *in silico* data handling and zebrafish testing may constitute a paradigm for rapid screening of nanomaterials.

***In Silico* (Modeling) Approaches**

Toxicology assessment of nanomaterials is expensive and time-consuming. Therefore, in addition to experimental approaches for hazard assessment, there is a need for *in silico* methods in order to develop structure–activity relationships that correlate toxicity endpoints. These structure–activity relationships can be quantitative or qualitative in nature and they can predict toxicological effects directly from the physicochemical properties of the entities, e.g., nanoparticles of interest.⁵⁷

There are currently only a handful of nano-QSAR modeling studies. In one recent study, the authors developed a model to describe the cytotoxicity of 17 different types of metal oxide nanoparticles to *Escherichia coli*. The model was found to reliably predict the toxicity of metal oxide nanoparticles.⁵⁸ Using a more extensive dataset of 109 nanoparticles possessing the same metal core but different organic molecules on their surface, Fourches et al.⁵⁹ found that the cellular uptake of nanoparticles can be predicted by taking into account the chemical structure of the coating molecules. The chemical or structural properties of nanomaterials are represented by mathematical objects called descriptors, many of which can be calculated rather than measured. Examples of descriptors suitable for nanomaterials include particle size, shape, and surface area, ionization potentials of metals, zeta potentials, and physicochemical properties of molecules covalently bound to nanoparticle surfaces.⁵⁷ In a physiological environment, nanoparticles selectively absorb proteins to form a nanoparticle ‘corona’, a process governed by molecular interactions between chemical groups on the nanoparticle surfaces and the amino acid residues of the proteins (see below). Recently, a biological surface adsorption index (BSAI) was developed based on the competitive adsorption onto nanoparticles of

a set of small-molecule probes that mimic amino acid residues.⁶⁰ By assuming that the adsorption was governed by five basic molecular forces, the measured adsorption coefficients were used to develop descriptors, which, in turn, could be used to predict the adsorption of small molecules to other nanomaterials. In a subsequent study of a panel of 16 different nanomaterials, the nanomaterials were classified into distinct clusters according to their surface adsorption properties.⁶¹ It will be of interest to see whether the BSAI could be used to predict the formation of a protein corona in a physiological setting.

Linking Toxicity to Material Properties

To systematically investigate toxic effects of the nanoparticles, it would be highly desirable to correlate their toxic effects with their physicochemical properties.^{5,62} However, unfortunately, this approach is not straightforward, as many physicochemical properties are strongly entangled and are difficult to control independently.⁷ Nevertheless, in the following section, we discuss selected studies showing how material properties may be linked to toxicity. Careful assessment of material properties serves as the bridge between nanotoxicology and nanomedicine (Figure 1).

Size matters, in particular, for cellular uptake of nanoparticles. Moreover, in general, the greater the intracellular dose of nanoparticles, the more the toxic effects they generate. Chan and coworkers demonstrated in a series of experiments that there can be an optimal size for nanoparticle uptake.^{63,64} Similar claims have been made by several other authors, but the latter work stands out, as size was controlled in an exclusive way. Indeed, the nanoparticles were colloidally stable and thus were not agglomerated, i.e., they did not have the effectively larger diameter of an agglomerate of nanoparticles, and surface chemistry was the same for all sizes. In this way, the size dependence of nanoparticle uptake and cytotoxicity could be investigated. However, cellular uptake is not mandatory for cytotoxicity to occur: cobalt–chromium nanoparticles can damage human fibroblasts across an intact cellular barrier without having to cross the barrier. The outcome, which includes DNA damage without significant cell death, is different from that observed in cells subjected to direct exposure to nanoparticles.⁶⁵

Also, shape can be important, though it is probably overrated. The classical example is carbon nanotubes, which are thought to exert toxicity by virtue of their ‘needle-like’ shape, i.e., an extremely high aspect ratio enabling these materials to pierce cell membranes. This may be relevant at least for

multiwalled carbon nanotubes (MWCNTs) with high width and, therefore, high rigidity.⁶⁶ Interestingly, in the latter study, thin and thick nanotubes similarly affected macrophages, while the deleterious effects of carbon nanotubes on human mesothelial cells were diameter-dependent. However, it is important to ask when a fiber is a fiber, and when is it, effectively, a particle? Murray et al.⁶⁷ have recently shown that it is important to factor in agglomeration when assessing the *in vivo* toxicity of SWCNTs. Shape can influence the mode of cellular uptake. Consider a rod-shaped nanoparticle and a spherical nanoparticle of the same volume: the leading edge of the rod-shaped nanoparticle has a much smaller cross-section and may therefore penetrate cell membranes more effectively. However, in many studies, in particular, in theoretical simulations, aspect ratios are calculated for the nanoparticle cores, neglecting the surface coating and the adsorbed protein corona (discussed below), which reduces the effective aspect ratio and thus nullifies potential shape effects. Furthermore, agglomeration in physiological media may rule out effects of the shape of individual nanoparticles.⁶⁸ Schaeublin et al.⁶⁹ investigated two gold nanoparticles with different aspect ratios using a keratinocyte cell line and found that gold nanospheres were nontoxic, whereas the gold nanorods induced apoptosis. Notably, both nanoparticles formed agglomerates in cell culture medium, but the spherical particles had a large fractal dimension (i.e., tightly bound and densely packed) while the nanorod agglomerates had a small fractal dimension (i.e., loosely bound).

Surface charge strongly influences uptake of nanoparticles. In general, positively charged nanoparticles are incorporated faster by cells than negatively charged ones, which is typically explained by the overall net negative charge of cellular surfaces. Although studies exist that demonstrate that in some cases positively charged nanoparticles interact with cells differently when compared to negatively charged ones, resulting in different mechanisms of cytotoxicity, the higher toxicity of positively charged nanoparticles is generally correlated to their enhanced cellular uptake.⁷⁰ To elucidate surface charge-dependent toxicity, nanoparticles with different surface charge, but with other physicochemical parameters constant are required, which often is experimentally complicated to achieve.^{71,72} However, as pointed out by Walkey and Chan,⁸ the protein corona tends to give nanomaterials a zeta potential of about -10 to -20 mV irrespective of the nanomaterial chemistry; this ‘normalization’ of zeta potentials is related to the fact that most plasma proteins carry a net negative charge at physiological

pH. In other words, the ‘biological’ identity may override the ‘synthetic’ identity.

Perhaps, the most important physicochemical parameter that interferes with most others is colloidal stability. Obviously, agglomerated nanoparticles do not have the size of the individual nanoparticles but the size of the agglomerate. This means, therefore, that unless nanoparticles are very well dispersed, any statement about size- or shape-dependent uptake or cytotoxicity is not sound, as the cell would interact with the agglomerates and not with the individual nanoparticles. Besides the fact that agglomeration masks effects of other physicochemical parameters, it can also directly affect interaction with cells. ‘Sticky’ agglomerates of nanoparticles tend to precipitate on top of cells and thus can cause cytotoxic effects.⁷³

Many metal and metal oxide nanoparticles can undergo dissolution within acidic compartments (lysosomes) in the cell which could drive toxicity. This phenomenon, sometimes referred to as a Trojan horse-type uptake mechanism because it circumvents the plasma membrane barrier and allows toxic ions to ‘sneak’ into cells, has been shown, for instance, for oxides of zinc, iron, manganese, and cobalt.⁷⁴ Cho et al.⁷⁵ evaluated the pulmonary inflammogenicity of 15 different metal/metal oxide nanoparticles and showed that toxicity of the nanomaterials displayed a significant correlation with one of two physicochemical parameters: zeta potential under acid conditions for low-solubility nanoparticles and solubility (degree of dissolution) for high-solubility nanoparticles. The authors suggested that in the case of high-solubility nanoparticles, inflammogenicity depends on the ions that are produced during dissolution of nanoparticles inside the acidic phagolysosomes of the cells.

Catalytic effects at the nanoparticle surface play an important role in the generation of reactive oxygen species (ROS).⁷⁶ Sayes et al.⁷⁷ studied the effects of titanium dioxide nanoparticles in cell culture and found that the extent to which nanoscale titania affected cellular behavior was not dependent on surface area; what did correlate strongly to cytotoxicity, however, was the phase composition of the nanoscale titania insofar as anatase TiO₂ was 100 times more toxic than rutile TiO₂. The most cytotoxic nanoparticle samples were also the most effective at generating ROS.

In synopsis, it may seem disappointing that one cannot pinpoint how a certain physicochemical parameter influences the toxicity of (all) nanomaterials. This is due, in part, to the fact that many studies published to date are based on poorly defined nanoparticles, in which many physicochemical

parameters are entangled. In fact, it is nontrivial to change only one physicochemical parameter, without affecting others. In addition, not all nanomaterials are created equal. Thus, a conclusive picture remains elusive. To be more conclusive, toxicity studies should be performed with well-defined model nanoparticles, in which specific particle properties can be independently varied. Advanced synthesis approaches are pointing in this direction, for instance by creating nanoparticles in which surface charge can be tuned (almost) independently from other particle properties.⁷² However, most studies are performed with nanoparticles of poor definition and/or agglomerated nanoparticle systems. To remedy this situation, enhanced communication between material scientists and toxicologists is needed.

THE NANO-BIO-CORONA CONCEPT

To go one step further in terms of understanding the interactions of engineered nanomaterials with living systems, we need to consider the fact that nanomaterials may adopt a ‘new’ identity through the adsorption of biomolecules, a phenomenon that, in turn, is linked to nanomaterial-intrinsic properties, e.g., size (surface curvature) and hydrophobicity. Indeed, as stated recently by Mahon et al.,⁷⁸ ‘pristine nanoparticles in biological fluids act as a scaffold for biomolecules, which adsorb rapidly to the nanoparticle surface, conferring a new biological identity’. Furthermore, the formation of a ‘bio-corona’ on nanoparticles is an inherently bilateral phenomenon, as proteins that adsorb to nanoparticle surfaces may also alter their behavior as a result of unfolding⁷⁹ or fibrillation.⁸⁰ The opsonization of particles with serum proteins is, however, not really a ‘new’ phenomenon⁸¹ even though recent research has provided new insights into the parameters that control this process.

It is generally believed that immediately after contact with biological media, an initial corona is formed on nanoparticles by loosely bound, low-affinity proteins. Prolonged incubation in plasma allows the formation of a denser, irreversibly attached ‘hard’ corona with high-affinity proteins^{82,83} and a satellite ‘soft’ corona that undergoes intensive exchange with the surrounding media.⁸⁴ The ‘hard’ corona is formed because of the direct interaction of proteins with the surface of the nanoparticles, whereas protein–protein interactions dominate the interactions of the ‘soft’ corona with the ‘hard’ corona.⁸⁵ The time scale of the process probably is very short. The ‘hard’ protein corona that is strongly attached to the surface of nanoparticles is likely

the most relevant one for the *in vivo* fate of long-circulating nanoparticles.⁸⁶ Furthermore, changes in the ‘hard’ corona may occur when nanoparticles are transferred to a new biological compartment, e.g., upon translocation of nanoparticles across the plasma membrane.⁸⁶ Recent studies have shown that the corona of biomolecules attached to nanoparticles is degraded by the protease cathepsin L within the endosomal compartment following endocytosis of nanoparticles.⁸⁷ This needs to be taken into account when designing nanomaterials for intracellular applications. Sund et al.⁸⁸ noted that the binding of cytoplasmic proteins depends on the surface chemistry of the nanoparticles. Hence, uncoated anatase and rutile phases of TiO₂ nanoparticles adsorbed proteins similarly, whereas alumina and silicone-coated rutile forms of TiO₂ bound only a few proteins.

Walkey and Chan⁸ recently provided a compilation of 26 published studies on the plasma-derived protein corona, and concluded that ‘the protein corona is complex, that there is no one ‘universal’ plasma protein corona for all nanomaterials, and that the relative densities of the adsorbed proteins do not, in general, correlate with their relative abundances in plasma’ (in other words, there is a degree of specificity). Instead, it is suggested that the protein corona depends on the ‘synthetic identity’ of each nanomaterial.⁸ Indeed, the adsorption of biomolecules is driven by surface charge, hydrophobicity/hydrophilicity, and particle size.^{83,89,90} Our recent studies show that superparamagnetic iron oxide nanoparticles (SPIONs) with different surface coating display distinct plasma protein corona compositions (Vogt et al., manuscript in preparation). Does the bio-corona cover the nanoparticle surfaces completely or will targeting ligands remain accessible? Simberg et al.⁹¹ reported that both the dextran coat and the iron oxide core of dextran-coated SPIONs remained accessible to specific probes after incubation in plasma, suggesting that the nanoparticle surface could be available for recognition by cells despite the bio-corona.

The majority of bio-corona studies have been performed with plasma proteins,⁹² which is certainly relevant in cases when nanoparticles are administered into the bloodstream. Nevertheless, it is important to also consider other portals of entry of nanomaterials into the body, e.g., via inhalation or through the skin or via the gastrointestinal tract as the corona composition is likely to change as a function of the anatomical site and the specific biofluids encountered at each of these sites. Kapralov et al.⁹³ reported on the *in vivo* formation of a lipid–protein corona on the surface of SWCNTs following administration

by pharyngeal aspiration in mice. The bio-corona was identical to lung surfactant and subsequent *in vitro* studies demonstrated a role for the surfactant corona of lipids + proteins in macrophage uptake of carbon nanotubes. Of note, plasma protein adsorption to MWCNTs is influenced by prior adsorption of pulmonary surfactant lipids.⁹⁴

There are, overall, few studies on long-term effects of nanomaterials and few, if any, of these studies have addressed the potential role of the ‘intrinsic’ versus the ‘biological’ identity of the nanomaterials in question. Nevertheless, it may be useful to consider whether the bio-corona plays a role under such conditions. In a recent study, Ruge et al.⁹⁵ studied the impact of lung surfactant components on macrophage clearance of nanoparticles and they concluded that because of the interplay of both surfactant lipids and proteins, the alveolar macrophage clearance of nanoparticles is essentially the same, regardless of different intrinsic surface properties. The latter study thus suggests that the ‘biological’ identity may override the ‘synthetic’ identity of nanoparticles (at least in the short term). However, we postulate that in the long term, material-intrinsic properties (i.e., the ‘synthetic’ identity) will come into play and the long-term fate of nanoparticles will depend largely on whether the nanoparticles undergo dissolution and/or are susceptible to biodegradation, or whether they escape clearance by the reticuloendothelial system and are subsequently cleared from the body. Indeed, in the chronic phase, at which point the nanoparticles have left the systemic circulation and have been uptaken by cells, the body’s own responses to the nanoparticles may predominate. For instance, inhalation of SWCNTs in mice will trigger a cascade of pathological events realized through early inflammatory responses and the induction of oxidative stress culminating in the development of multifocal granulomatous pneumonia and interstitial fibrosis.⁹⁶ Thus, while the carbon nanotubes represent the initial offending trigger, the long-term effects (including potential carcinogenic effects) are manifested through subsequent cellular responses to this trigger; moreover, such organ and tissue responses may follow a common pattern of host defense reactions (oxidative stress, inflammation, etc.) toward foreign intrusion. In another recent study, Mahler et al.⁹⁷ showed that chronic oral exposure to polystyrene nanoparticles can influence iron uptake and iron transport in an *in vivo* chicken intestinal loop model. Importantly, chronic exposure caused remodeling of the intestinal villi in exposed animals, which increased the surface area available for iron absorption. In other words, the physiological

responses triggered by the nanoparticles (in this case, tissue remodeling) may determine long-term outcomes, not the nanoparticles *per se* and not the bio-corona.

Controlling the Bio-Corona

From a nanomedicine point of view, it may be desirable to avoid 'nonspecific' protein adsorption, i.e., bio-corona formation. This is commonly achieved by grafting PEG onto nanoparticles; this may prevent nonspecific uptake of nanoparticles by cells of the immune system, thereby prolonging their half-life in circulation.¹⁰ Modifying the surface of nanoparticles with an antifouling polymer makes the protein adsorption thermodynamically unfavorable, while the high-molecular-weight polymeric chains induce protein 'repulsion' because of their conformational flexibility and induced steric hindrance. PEGylation does not, however, prevent protein adsorption altogether.⁷⁸ Increased PEG grafting density on the surface of gold nanoparticles positively correlates with a decrease in total protein adsorption and reduced uptake in J774A.1 murine macrophages.⁹⁸

On the other hand, one may consider to exploit the bio-corona phenomenon for targeting purposes. PEG-polyhexadecylcyanoacrylate (PEG-PHDCA) nanoparticles have been shown to translocate into the brain after intravenous injection in rats, whereas PHDCA nanoparticles do not. Kim et al.⁹⁹ found that, after incubation with rat serum, apolipoprotein E (ApoE) adsorbed more onto PEG-PHDCA than onto PHDCA nanoparticles. Moreover, ApoE or ApoB-100 preadsorption onto PEG-PHDCA nanoparticles was required for efficient penetration into rat brain endothelial cells. These data suggest the involvement of apolipoproteins in the transport of PEG-PHDCA nanoparticles across the blood-brain barrier, which could be deployed for delivery of drugs into the brain. Prapainop et al.¹⁰⁰ attempted cell-specific uptake of nanomaterials by 'reprogramming' of the behavior of the protein corona on nanomaterials. Specifically, the surface of CdSe/ZnS QDs possessing an amino-functionalized, PEGylated hydrophilic surface was decorated with the inflammatory metabolite, cholesterol 5,6-secosterol atheronal-B, and the resulting nanoparticles were shown to bind to and induce the misfolding of apolipoprotein B leading to uptake by RAW264.7 murine macrophages. As pointed out by the authors, the ability to program the bio-corona on nanoparticles with small molecules could be developed to direct nanoparticles into cell types that they may not have been able to reach before.¹⁰⁰

Impact of Bio-Corona on Cellular Functions

The protein corona has been shown to play an important role in modulating uptake and toxicity of SWCNTs.^{101,102} However, it remains to be firmly established whether the biological identity of nanoparticles is the result of a specific protein(s) in the nanoparticle corona or a nonspecific effect related to the fact that proteins may alter the agglomeration behavior of nanoparticles leading to a difference in cellular uptake, which, in turn, has an impact on cytotoxicity. Ehrenberg et al.¹⁰³ reported that the capacity of polystyrene nanoparticle surfaces to adsorb protein is indicative of their tendency to associate with cells. However, removal of the most abundant proteins from cell culture media did not affect the level of cell association, and the authors concluded that cellular association is not dependent on the identity of adsorbed proteins. Lartigue et al.¹⁰⁴ studied the adsorption of proteins on biomedically relevant iron oxide nanoparticles by magneto-optical birefringence; the effect of plasma at different concentrations ranging from 1 to 100% on nanoparticle behavior was assessed. It was noted that at low plasma concentrations (representative of most *in vitro* conditions), the nanoparticles tended to form clusters triggered by proteins such as fibrinogen, whereas at high plasma concentrations (closer to the physiological situation) other proteins such as apolipoproteins tended to coat and subsequently to stabilize individual nanoparticles. This, in turn, affected *in vitro* uptake by macrophages. Lesniak et al.¹⁰⁵ reported that silica nanoparticles incubated with A549 cells in the absence of serum have a stronger adhesion to the cell membrane and higher internalization efficiency when compared with nanoparticles with a preformed surface corona.

In a key study of the bio-corona phenomenon, Deng et al.⁷⁹ demonstrated that negatively charged poly(acrylic acid)-conjugated gold nanoparticles bind to and induce unfolding of fibrinogen, which promotes interaction with integrin receptors on macrophage-like THP.1 cells, resulting in the release of inflammatory cytokines (Figure 2). In a follow-up study, the authors showed that fibrinogen bound with high affinity to positively and negatively charged gold nanoparticles.¹⁰⁶ However, only the negatively charged nanoparticles triggered cytokine release in THP.1 cells, perhaps because of a different orientation of the protein on the different particles. Thus, while common proteins may bind to different nanoparticles, the physiological response may not be the same.

The complement system constitutes an important barrier to infection or other foreign intrusion. Nanoparticles may also activate complement;

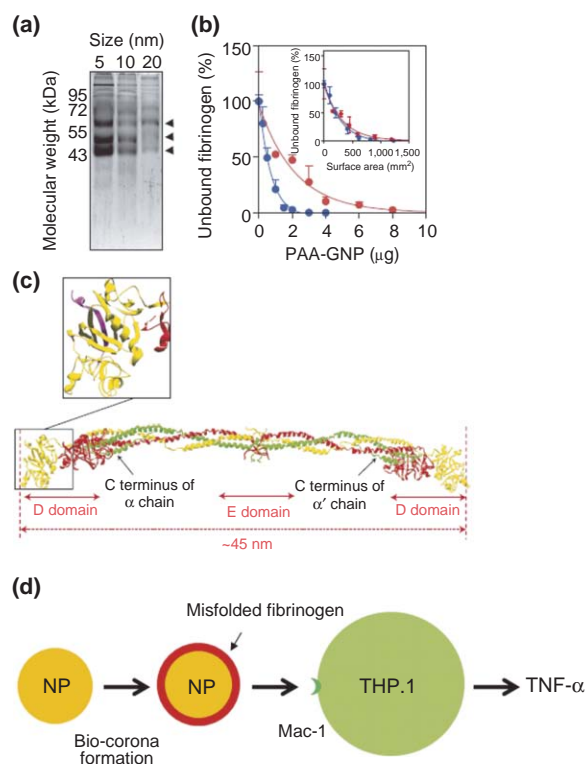


FIGURE 2 | Protein corona: role in proinflammatory responses. Fibrinogen is the major human plasma protein bound by poly(acrylic acid)-coated gold nanoparticles (PAA-GNP). (a) SDS-PAGE of human plasma proteins bound to PAA-GNP with diameters of 5, 10, and 20 nm. Three major protein bands were observed at 65, 55, and 45 kDa. (b) Unbound fibrinogen following pull-down with PAA-GNP with diameters of 5 nm (blue) or 20 nm (red). Purified fibrinogen (0.6 mg) was incubated with increasing amounts of PAA-GNP. Inset: unbound fibrinogen is plotted against total surface area for the two nanoparticles. (c) Crystal structure of fibrinogen. The protein was drawn using Swiss-PdbViewer and coordinates for PDB entry 3GHG. Common domains are shown. Inset: the C-terminus of the g chain (purple) that interacts with the Mac-1 receptor. (Reprinted with permission from Ref 79. Copyright 2011 Macmillan Publishers Ltd.) (d) The schematic diagram illustrates how unfolding of fibrinogen on the surface of PAA-GNP leads to interaction with the integrin receptor, Mac-1, on the surface of THP.1 monocytes, which in turn increases NF- κ B signaling leading to secretion of tumor necrosis factor- α . It is pertinent to note that fibrinogen, which has a length of 45 nm and a diameter of 5 nm, is much larger than the 5-nm PAA-GNP. Deng et al.⁷⁹ showed that the maximum protein binding was 2 μ g for the 5-nm PAA-GNP, which represents one to two nanoparticles per fibrinogen molecule.

this may be viewed as a special case of bio-corona formation and one that is of particular relevance in nanomedicine. Nanomaterial interaction with the complement system is complex and regulated by interrelated physicochemical factors such as size, morphology, and surface properties.¹⁰⁷ Hamad et al.¹⁰⁸ investigated polystyrene nanoparticles with surface-projected polyethylene oxide chains

in ‘mushroom-brush’ and ‘brush’ configurations and found that distinct polymer architectures mediate switching of complement activation pathways. As pointed out by the authors, these studies suggest a rational basis for the design of targetable nanosystems for nanomedicine applications.

THE *IN VIVO* FATE OF NANOPARTICLES

In addition to understanding the synthetic and biological identities of nanomaterials, it is important to take into consideration the *context-dependent* behavior of a nanomaterial. In other words, to consider how the biological identity of a nanomaterial may change depending on the specific biological compartment (in the body or within a cell). Indeed, as noted previously, ‘one of the key features of nanoscale materials, and the one that may suggest novel and unanticipated health risks, may very well be the propensity of such materials to cross biological barriers in a manner not predicted from studies of larger particles of the same chemical composition’.⁹ Here, we discuss some studies illustrating how nanoparticles may cross biological barriers, and how material-intrinsic properties may dictate such interactions. We will also touch on factors that regulate nanoparticle pharmacokinetics. Understanding the *in vivo* fate and behavior of nanomaterials is another area of common interest in nanotoxicology and nanomedicine.

Crossing Biological Barriers

Nanoparticles can cross biological barriers and enter and distribute within cells by different pathways and for this reason they are considered a primary vehicle for targeted therapies. In the body, we find cellular barriers that include the cell membrane, and endosomal-lysosomal and nuclear membranes, and physiological barriers that prevent extravasation of foreign substances from the blood such as the blood-brain barrier. The skin is the main barrier that protects our body from the external environment. Understanding the barriers imposed by a biological system is critical to the design of nanomaterials for biomedical applications (see Kievit and Zhang¹⁰⁹ for an excellent review). It is also important to consider whether one should attempt to breach biological barriers between bodily compartments with nanoparticles as this may trigger unexpected toxicities and disease processes.¹¹⁰

Yamashita et al.¹¹¹ showed that silica and titanium dioxide nanoparticles with diameters of 70 and 35 nm, respectively, can cross the placenta

and cause pregnancy complications when injected intravenously into pregnant mice. Larger (300 and 1000 nm) silica particles did not induce such complications. It remains unclear if the fetotoxicity was caused by direct exposure to the nanoparticles or by the damage to the placenta. Nonetheless, the detrimental effects were abolished when the surfaces of the silica nanoparticles were modified with carboxyl and amine groups. Hence, size and surface charge both may impact on the propensity of nanoparticles to cause damage to the unborn fetus. Similarly, Schleh et al.¹¹² demonstrated that size and surface charge of gold nanoparticles determine absorption across intestinal barriers and accumulation in secondary target organs after oral administration in a rat model. Choi et al.¹¹³ determined that nanoparticles with hydrodynamic diameter less than 34 nm with noncationic surface charge translocate rapidly from the lungs to regional lymph nodes in rats following intratracheal instillation. Furthermore, nanoparticles with a hydrodynamic diameter less than 6 nm were found to traffic rapidly from the lungs to lymph nodes and the bloodstream, ultimately being cleared from the body through the kidneys. Moreover, as discussed in further detail below, nanoparticle behavior was found to depend strongly on surface coating. These findings suggest strategies for the rational design of nanoparticles for drug delivery via lung inhalation. Kannan et al.¹¹⁴ recently devised a prodrug approach to treat cerebral palsy, a developmental disorder resulting from an insult to a growing fetal or infant brain. In this preclinical study, *N*-acetyl-cysteine (NAC) was linked to polyamidoamine dendrimers that enabled NAC to cross the blood–brain barrier and reach microglia and astrocytes. This nanoformulation (D-NAC) was administered within 6 h of birth with improvement in motor performance and amelioration of inflammation in newborn animals.

However, nanoparticles may disrupt or even remodel biological barriers. Mahler et al.⁹⁷ reported that chickens acutely exposed to carboxylated polystyrene nanoparticles had a lower iron absorption than unexposed or chronically exposed birds. As mentioned earlier, Chronic exposure caused remodeling of the intestinal villi, which increased the surface area available for iron absorption, and this increase in intestinal surface area compensated for the lowered iron transport caused by nanoparticle exposure.

Biodistribution and Tumor Targeting

Pharmacokinetics is concerned with quantifying the adsorption, distribution, metabolism, and elimination (ADME) of chemicals and drugs in the body; the

aim is to relate drug dose or chemical exposure to biological effects.¹¹⁵ Evaluation of ADME properties of nanomaterials is crucial for the medical implementation of these materials. To this end, *in vivo* model systems are certainly needed. Riviere¹¹⁵ has provided a concise overview of studies on the *in vivo* disposition of fullerenes, carbon nanotubes, and QDs after parenteral administration. Functionalized, water-soluble SWCNT and MWCNT may negotiate the glomerular filtration barrier and undergo renal excretion without extensive accumulation in the body, in a manner dependent upon the degree of individualization of the nanotubes.^{116,117} Notably, pristine SWCNTs may undergo enzymatic biodegradation *in vitro*¹¹⁸ and *in vivo*¹¹⁹; biodegradation by neutrophils is promoted when the carbon nanotubes are coated with a corona of immunoglobulins, which leads to enhanced cellular uptake via Fc receptors expressed on neutrophils.¹¹⁸

How about the disposition of biomedically relevant nanomaterials? Schädlich et al.¹²⁰ investigated the influence of the size of biodegradable PEG-PLA nanoparticles both *in vivo* and *ex vivo* and found that nanoparticles of 111 and 141 nm accumulated in human xenograft tumor tissue while slightly bigger nanoparticles (166 nm) were rapidly eliminated by the liver. These studies demonstrate how different biodistribution may occur because of small nanoparticle size differences. The importance of further miniaturizing nanocarrier size to optimize tumor accumulation and penetration was recently shown¹²¹ (and see above, section on Medical Imaging, for additional examples).

The EPR effect and/or targeting approaches may enable nanoscale carriers to reach a tumor, but this does not necessarily mean that the nanoparticles will also penetrate into the tumor and deliver their payload of anticancer drugs. Cabral et al.¹²² compared the accumulation and effectiveness of different sizes (30, 50, 70, and 100 nm) of long-circulating, drug-loaded polymeric micelles in highly versus poorly permeable tumors in a preclinical model, and found that only the 30-nm micelles could penetrate poorly permeable, hypovascular pancreatic tumors to achieve an antitumor effect. Interestingly, the penetration and efficacy of the larger nanoparticles could be enhanced by pharmacologically increasing the permeability of the tumors.

Choi et al.¹¹³ followed the fate of intratracheally instilled NIR fluorescent nanoparticles that were varied systematically in size, surface modification, and core composition and showed that nanoparticle behavior depends strongly on the surface coating, which affects protein adsorption in body

fluids; hence, for charged nanoparticles, nonspecific adsorption of endogenous proteins, mostly albumins, resulted in a large increase in hydrodynamic size of the nanoparticles, and this affected the biodistribution of the nanoparticles following their uptake in this rat model.

Finally, von Maltzahn et al.¹²³ have provided a fascinating example of ‘communicating’ nanoparticle systems based on nanotechnological mimicry of the recruitment of immune cells to an inflammatory lesion to improve *in vivo* tumor-targeting efficiency. Hence, the authors designed multifunctional systems whereby the coagulation cascade in tumors is activated by photothermal heating of gold nanorods in order to ‘broadcast’ tumor location to clot-targeted nanoparticles, i.e., doxorubicin-loaded liposomes coated with Factor XIII, a component of the coagulation cascade. This approach, which thus takes advantage of the endogenous coagulation cascade, yielded over 40 times higher doses of doxorubicin in tumors when the drug is loaded with Factor XIII-covered liposomes when compared to plain liposomes.¹²³

A CASE OF STOLEN IDENTITY

Nature may inspire the design of synthetic nanoparticles. Bertram et al.¹²⁴ developed ‘artificial platelets’ based on Arg-Gly-Asp (RGD)-functionalized nanoparticles, which halved the bleeding time after intravenous administration in a rat model of major trauma. The synthetic platelets consisting of poly(lactic-co-glycolic acid)–poly-L-lysine block copolymer cores conjugated with PEG chains terminated with RGD functionalities were cleared within 24 h, and no toxicity was seen up to 7 days postinjection. Hu et al.¹²⁵ presented a novel approach in particle functionalization by coating biodegradable polymeric nanoparticles with a corona of natural membranes derived from red blood cells, including both membrane lipids and associated membrane proteins, in order to achieve ‘stealthy’, long-circulating nanoparticles for drug delivery. The latter study represents an example of ‘borrowed identity’ of nanomaterials. Indeed, biomimetic design could be exploited for drug delivery.¹²⁶ Interestingly, the immune system utilizes its very own nanoparticles (exosomes) to transmit information between cells. Exosomes may contain both mRNA and microRNA, and the transferred exosomal mRNA has been shown to be translated in the recipient cell.¹²⁷ More recent studies confirmed that the transmitted microRNA is also functional.¹²⁸ Hence, exosomes serve as a template for the delivery of short RNAs for modulation of gene expression using

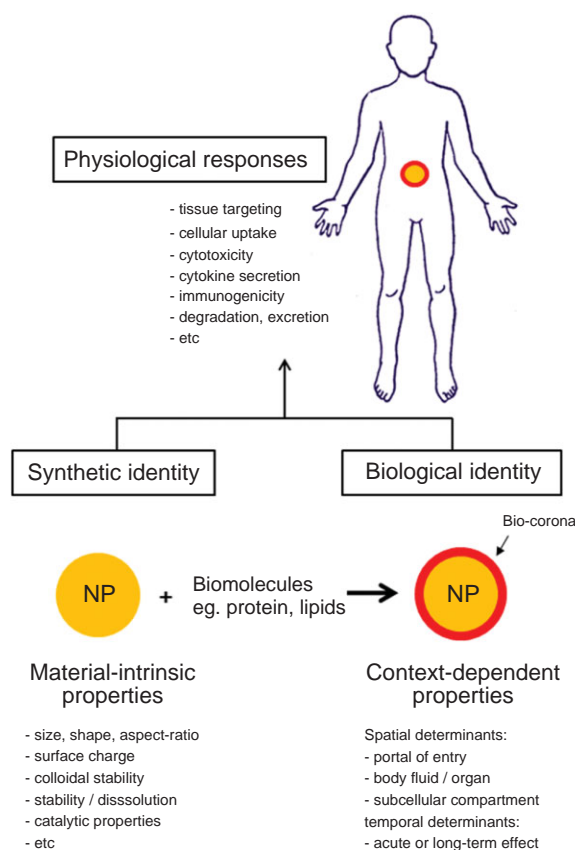


FIGURE 3 | Synthetic and biological identities of nanomaterials. Schematic view of the ‘synthetic’ identity of nanomaterials that is determined by material-intrinsic properties and the ‘biological’ identity that is manifested in a living system and can be viewed as the sum of the context-dependent properties of the nanomaterial. As discussed in this review, the biological identity is shaped, in part, by the adsorption of biomolecules (proteins and lipids) that form a ‘corona’ on the surface of nanoparticles; the composition of the bio-corona depends on the particular biofluid (e.g., blood, lung fluid, and gastrointestinal fluid) and may exhibit dynamic changes as the nanoparticle crosses from one biological compartment to another. The physiological responses to nanomaterials are dictated by the synthetic and biological identities; a partial list of possible biological/toxicological outcomes is shown in this figure.

nanoscale delivery vehicles that are, by definition, biocompatible.

Stark has pointed out that nanoparticles differ from molecules in several respects; nevertheless, he concludes that ‘from a functional point of view, chemically well-defined nanoparticles are an extension of the classical concept of the molecule’, as they combine the properties of solids with mobility (a property of molecules).⁷⁴ Indeed, certain nanoparticles appear to bridge the gap between molecules and particles. Dendrimers are polymeric nanoparticles with perfectly defined structure and molecular weight.¹²⁹ Hayder et al.¹³⁰ reported recently that azabisphosphonate

(ABP)-capped dendrimers selectively target monocytes and direct them toward anti-inflammatory activation. The dendrimers also exhibited antiosteoclastic activity, thus preventing bone erosion. Intravenous injections of ABP-capped dendrimers inhibited the development of inflammatory arthritis in two animal models. This exciting study suggests that dendrimers could function as novel therapeutics for rheumatoid arthritis. Moreover, dendrimers conjugated to glucosamine and glucosamine 6-sulfate were shown to possess immunomodulatory and antiangiogenic properties, respectively, and when administered together, the nanoparticles increased the long-term success of glaucoma surgery in an animal model by preventing scar tissue formation.¹³¹ Thus, in some cases, the synthetic and biological identities of a nanomaterial appear to blend into one: dendrimers may function as drugs *per se* by virtue of their unique physicochemical properties, i.e., size and multivalent surface functionalities, which allow these nanoparticles to directly engage biological receptors and modulate cell function.

CONCLUSIONS AND PERSPECTIVES

The Stone Age did not end because they ran out of stones. New technologies inevitably replace old ones. We are now at the dawn of a nanotechnological revolution with far-reaching implications for society and it is crucial that we ensure the safety of these novel materials while not impeding their implementation in important areas such as in medicine. In this review, we have attempted to highlight the role of physicochemical properties of engineered nanomaterials and their impact on nanomaterial behavior in biological systems. Importantly, a growing body of evidence indicates that the adsorption of biomolecules onto nanoparticle surfaces may bestow a new 'biological identity' onto these materials.^{8,78} This has considerable ramifications not only for nanotoxicological assessment of synthetic nanoscale materials but also for their implementation in medicine. Of note, the bio-corona of serum proteins should not necessarily be viewed as an undesirable biological phenomenon; the bio-corona can be controlled¹⁰⁰ and may even be exploited for drug delivery.¹³² In addition, we would be amiss to ignore fundamental physicochemical properties of nanomaterials: the cells may also 'see' what is beneath the corona.

Careful assessment of material-intrinsic properties and how these properties are linked to physiological responses is thus essential both in nanotoxicology and in nanomedicine. Notably, the very same property may be highly desirable for certain clinical applications (for instance, the delivery of small particles to exploit the EPR effect) but could also yield unwanted hazardous effects. Taking into consideration not only the synthetic identity but also the biological identity of nanomaterials, and how these identities may evolve over time and as a function of different biological compartments in the body or at the subcellular level may enable a better understanding of nanomaterial-induced physiological responses (Figure 3). More studies are needed on the long-term effects of nanomaterials and on the relative importance of surface-adsorbed biomolecules (the bio-corona) versus material-intrinsic properties of nanomaterials under such conditions; understanding how common physiological reactions (oxidative stress, inflammation, etc.) are triggered is also of importance in order to mitigate adverse effects following nanomaterial exposure. Furthermore, more refined techniques to study the corona of adsorbed proteins, lipids, and other biomolecules on nanomaterial surfaces are warranted along with a greater emphasis on the potential impact of individual components of the corona on physiological responses. Bioinformatics-based approaches may prove helpful when deciphering the bio-corona data. New approaches including HTS for the rapid screening and ranking of the hazard potential of vast numbers of engineered nanomaterials and mathematical modeling of structure–activity relationships of nanomaterials may also facilitate the development of safe and useful nanomaterials for *in vivo* imaging, drug delivery, and other clinical applications.

ACKNOWLEDGMENTS

The authors are supported, in part, through grants from the Swedish Research Council for Environment, Agricultural Sciences and Spatial Planning (FORMAS), the Swedish Cancer and Allergy Foundation, the Seventh Framework Programme of the European Commission (FP7-MARINA-263215 and FP7-NANOGNOSTICS-242264), and BMFM Germany (Umsicht). BF holds a Senior Investigator Award from the Swedish Research Council.

REFERENCES

1. Shvedova AA, Kagan VE, Fadeel B. Close encounters of the small kind: adverse effects of man-made materials interfacing with the nano-cosmos of biological systems. *Annu Rev Pharmacol Toxicol* 2010, 50:63–88.
2. Harford CG, Hamlin A, Parker E. Electron microscopy of HeLa cells after the ingestion of colloidal gold. *J Biophys Biochem Cytol* 1957, 3:749–756.
3. De Groot N, Lagasse A, Sebruyens M. Alterations in the ultrastructure of the blood-air barrier in the mouse lung after inhalation of colloidal gold particles. *Nature* 1958, 181:1418–1419.
4. Lewinski N, Colvin V, Drezek R. Cytotoxicity of nanoparticles. *Small* 2008, 4:26–49.
5. Fadeel B, Garcia-Bennett AE. Better safe than sorry: understanding the toxicological properties of inorganic nanoparticles manufactured for biomedical applications. *Adv Drug Deliv Rev* 2010, 62:362–374.
6. Shvedova AA, Pietroiusti A, Fadeel B, Kagan VE. Mechanisms of carbon nanotube-induced toxicity: focus on oxidative stress. *Toxicol Appl Pharmacol* 2012, 261:121–133.
7. Rivera-Gil P, De Aberasturi DJ, Wulf V, Pelaz B, Del Pino P, Zhao Y, De La Fuente J, De Larramendi IR, Rojo T, Liang XJ, et al. The challenge to relate physico-chemical properties of colloidal nanoparticles to their cytotoxicity. *Acc Chem Res* (Epub ahead of print; July 11, 2012).
8. Walkey CD, Chan WC. Understanding and controlling the interaction of nanomaterials with proteins in a physiological environment. *Chem Soc Rev* 2012, 41:2780–2799.
9. Nyström AM, Fadeel B. Safety assessment of nanomaterials: implications for nanomedicine. *J Control Release* 2012, 161:403–408.
10. Riehemann K, Schneider SW, Luger TA, Godin B, Ferrari M, Fuchs H. Nanomedicine-challenge and perspectives. *Angew Chem Int Ed Engl* 2009, 48:872–897.
11. Ali Z, Abbasi AZ, Zhang F, Arosio P, Lascialfari A, Casula MF, Wenk A, Kreyling W, Plapper R, Seidel M, et al. Multifunctional nanoparticles for dual imaging. *Anal Chem* 2011, 83:2877–2882.
12. Yang K, Hu L, Ma X, Ye S, Cheng L, Shi X, Li C, Li Y, Liu Z. Multimodal imaging guided photothermal therapy using functionalized graphene nanosheets anchored with magnetic nanoparticles. *Adv Mater* 2012, 24:1868–1872.
13. Altinoglu EI, Russin TJ, Kaiser JM, Barth BM, Eklund PC, Kester M, Adair JH. Near-infrared emitting fluorophore-doped calcium phosphate nanoparticles for in vivo imaging of human breast cancer. *ACS Nano* 2008, 2:2075–2084.
14. Wong C, Stylianopoulos T, Cui J, Martin J, Chauhan VP, Jiang W, Popovic Z, Jain RK, Bawendi MG, Fukumura D. Multistage nanoparticle delivery system for deep penetration into tumor tissue. *Proc Natl Acad Sci U S A* 2011, 108:2426–2431.
15. Chauhan VP, Stylianopoulos T, Martin JD, Popovic Z, Chen O, Kamoun WS, Bawendi MG, Fukumura D, Jain RK. Normalization of tumour blood vessels improves the delivery of nanomedicines in a size-dependent manner. *Nat Nanotechnol* 2012, 7:383–388.
16. Kim S, Lim YT, Soltesz EG, Grand AMD, Lee J, Nakayama A, Parker JA, Mihaljevic T, Laurence RG, Dor DM, et al. Near-infrared fluorescent type II quantum dots for sentinel lymph node mapping. *Nat Biotechnol* 2004, 22:93–97.
17. Ye L, Yong KT, Liu L, Roy I, Hu R, Zhu J, Cai H, Law WC, Liu J, Wang K, et al. A pilot study in non-human primates shows no adverse response to intravenous injection of quantum dots. *Nat Nanotechnol* 2012, 7:453–458.
18. de la Zerda A, Zavaleta C, Keren S, Vaithilingam S, Bodapati S, Liu Z, Levi J, Smith BR, Ma TJ, Oralkan O, et al. Carbon nanotubes as photoacoustic molecular imaging agents in living mice. *Nat Nanotechnol* 2008, 3:557–562.
19. Tong L, Liu Y, Dolash BD, Jung Y, Slipchenko MN, Bergstrom DE, Cheng JX. Label-free imaging of semiconducting and metallic carbon nanotubes in cells and mice using transient absorption microscopy. *Nat Nanotechnol* 2011, 7:56–61.
20. Lehner R, Wang X, Wolf M, Hunziker P. Designing switchable nanosystems for medical application. *J Control Release* 2012, 161:307–316.
21. Verma A, Uzun O, Hu YH, Hu Y, Han HS, Watson N, Chen SL, Irvine DJ, Stellacci F. Surface-structure-regulated cell-membrane penetration by monolayer-protected nanoparticles. *Nat Mater* 2008, 7:588–595.
22. Leduc C, Jung JM, Carney RR, Stellacci F, Lounis B. Direct investigation of intracellular presence of gold nanoparticles via photothermal heterodyne imaging. *ACS Nano* 2011, 5:2587–2592.
23. Ashley CE, Carnes EC, Phillips GK, Padilla D, Durfee PN, Brown PA, Hanna TN, Liu J, Phillips B, Carter MB, et al. The targeted delivery of multi-component cargos to cancer cells by nanoporous particle-supported lipid bilayers. *Nat Mater* 2011, 10:389–397.
24. Davis ME, Zuckerman JE, Choi CH, Seligson D, Tolcher A, Alabi CA, Yen Y, Heidel JD, Ribas A. Evidence of RNAi in humans from systemically administered siRNA via targeted nanoparticles. *Nature* 2010, 464:1067–1070.
25. Hrkach J, Von Hoff D, Ali MM, Andrianova E, Auer J, Campbell T, De Witt D, Figa M, Figueiredo M,

- Horhota A, et al. Preclinical development and clinical translation of a PSMA-targeted docetaxel nanoparticle with a differentiated pharmacological profile. *Sci Transl Med* 2012, 4:128ra39.
26. Colombo M, Carregal-Romero S, Casula MF, Gutiérrez L, Morales MP, Böhm IB, Heverhagen JT, Prospero D, Parak WJ. Biological applications of magnetic nanoparticles. *Chem Soc Rev* 2012, 41:4306–4334.
27. Child HW, Del Pino PA, De La Fuente JM, Hursthouse AS, Stirling D, Mullen M, McPhee GM, Nixon C, Jayawarna V, Berry CC. Working together: the combined application of a magnetic field and penetratin for the delivery of magnetic nanoparticles to cells in 3D. *ACS Nano* 2011, 5:7910–7919.
28. Alexiou C, Arnold W, Klein RJ, Parak FG, Hulin P, Bergemann C, Erhardt W, Wagenpfeil S, Lübke AS. Locoregional cancer treatment with magnetic drug targeting. *Cancer Res* 2000, 60:6641–6648.
29. Ray PC. Size and shape dependent second order non-linear optical properties of nanomaterials and their application in biological and chemical sensing. *Chem Rev* 2010, 110:5332–5365.
30. Sperling RA, Rivera Gil P, Zhang F, Zanella M, Parak WJ. Biological applications of gold nanoparticles. *Chem Soc Rev* 2008, 37:1896–1908.
31. Hirsch LR, Stafford RJ, Bankson JA, Sershen SR, Rivera B, Price RE, Hazle JD, Halas NJ, West JL. Nanoshell-mediated near-infrared thermal therapy of tumors under magnetic resonance guidance. *Proc Natl Acad Sci U S A* 2003, 100:13549–13554.
32. Carregal Romero S, Ochs M, Rivera-Gil P, Gana C, Pavlov AM, Sukhorukov GB, Parak WJ. NIR-light triggered delivery of macromolecules into the cytosol. *J Control Release* 2012, 159:120–127.
33. Fadeel B, Kasemo B, Malmsten M, Strømme M. Nanomedicine: reshaping clinical practice. *J Intern Med* 2010, 267:2–8.
34. Mahmoudi M, Hosseinkhani H, Hosseinkhani M, Boutry S, Simchi A, Journeay WS, Subramani K, Laurent S. Magnetic resonance imaging tracking of stem cells in vivo using iron oxide nanoparticles as a tool for the advancement of clinical regenerative medicine. *Chem Rev* 2011, 111:253–280.
35. Pickard MR, Barraud P, Chari DM. The transfection of multipotent neural precursor/stem cell transplant populations with magnetic nanoparticles. *Biomaterials* 2011, 32:2274–2284.
36. Shah RN, Shah NA, Del Rosario Lim MM, Hsieh C, Nuber G, Stupp SI. Supramolecular design of self-assembling nanofibers for cartilage regeneration. *Proc Natl Acad Sci U S A* 2010, 107:3293–3298.
37. Webber MJ, Tongers J, Newcomb CJ, Marquardt KT, Bauersachs J, Losordo DW, Stupp SI. Supramolecular nanostructures that mimic VEGF as a strategy for ischemic tissue repair. *Proc Natl Acad Sci U S A* 2011, 108:13438–13443.
38. Jungebluth P, Alici E, Baiguera S, Le Blanc K, Blomberg P, Bozoky B, Crowley C, Einarsson O, Grinnemo KH, Gudbjartsson T, et al. Tracheobronchial transplantation with a stem-cell-seeded bioartificial nanocomposite: a proof-of-concept study. *Lancet* 2011, 378:1997–2004.
39. Badylak SF, Weiss DJ, Caplan A, Macchiarini P. Engineered whole organs and complex tissues. *Lancet* 2012, 379:943–952.
40. Duncan R, Gaspar R. Nanomedicine(s) under the microscope. *Mol Pharm* 2011, 8:2101–2141.
41. Oberdörster G, Oberdörster E, Oberdörster J. Nanotoxicology: an emerging discipline evolving from studies of ultrafine particles. *Environ Health Perspect* 2005, 113:823–839.
42. Krug HF, Wick P. Nanotoxicology: an interdisciplinary challenge. *Angew Chem Int Ed Engl* 2011, 50:1260–1278.
43. Oberdörster G. Safety assessment for nanotechnology and nanomedicine: concepts of nanotoxicology. *J Intern Med* 2010, 267:89–105.
44. Hartung T, Sabbioni E. Alternative in vitro assays in nanomaterial toxicology. *Wiley Interdiscip Rev Nanomed Nanobiotechnol* 2011, 3:545–573.
45. Lai DY. Toward toxicity testing of nanomaterials in the 21st century: a paradigm for moving forward. *Wiley Interdiscip Rev Nanomed Nanobiotechnol* 2012, 4:1–15.
46. Collins FS, Gray GM, Bucher JR. Toxicology. Transforming environmental health protection. *Science* 2008, 319:906–907.
47. Huh D, Matthews BD, Mammoto A, Montoya-Zavala M, Hsin HY, Ingber DE. Reconstituting organ-level lung functions on a chip. *Science* 2010, 328:1662–1668.
48. Han X, Corson N, Wade-Mercer P, Gelein R, Jiang J, Sahu M, Biswas P, Finkelstein JN, Elder A, Oberdörster G. Assessing the relevance of in vitro studies in nanotoxicology by examining correlations between in vitro and in vivo data. *Toxicology* 2012, 297:1–9.
49. Shaw SY, Westly EC, Pittet MJ, Subramanian A, Schreiber SL, Weissleder R. Perturbational profiling of nanomaterial biologic activity. *Proc Natl Acad Sci U S A* 2008, 105:7387–7392.
50. Mayr LM, Bojanic D. Novel trends in high-throughput screening. *Curr Opin Pharmacol* 2009, 9:580–588.
51. Feliu N, Fadeel B. Nanotoxicology: no small matter. *Nanoscale* 2010, 2:2514–2520.
52. Damoiseaux R, George S, Li M, Pokhrel S, Ji Z, France B, Xia T, Suarez E, Rallo R, Madler L, et al. No time to lose—high throughput screening to assess nanomaterial safety. *Nanoscale* 2011, 3:1345–1360.

53. Seiffert JM, Baradez MO, Nischwitz V, Lekishvili T, Goenaga-Infante H, Marshall D. Dynamic monitoring of metal oxide nanoparticle toxicity by label free impedance sensing. *Chem Res Toxicol* 2012, 25:140–152.
54. Mortimer M, Kasemets K, Heinlaan M, Kurvet I, Kahru A. High throughput kinetic *Vibrio fischeri* bioluminescence inhibition assay for study of toxic effects of nanoparticles. *Toxicol In Vitro* 2008, 22:1412–1417.
55. Jan E, Byrne SJ, Cuddihy M, Davies AM, Volkov Y, Gun'ko YK, Kotov NA. High-content screening as a universal tool for fingerprinting of cytotoxicity of nanoparticles. *ACS Nano* 2008, 2:928–938.
56. George S, Xia T, Rallo R, Zhao Y, Ji Z, Lin S, Wang X, Zhang H, France B, Schoenfeld D, et al. Use of a high-throughput screening approach coupled with in vivo zebrafish embryo screening to develop hazard ranking for engineered nanomaterials. *ACS Nano* 2011, 5:1805–1817.
57. Winkler DA, Mombelli E, Pietriusti A, Tran L, Worth A, Fadeel B, McCall MJ. Applying quantitative structure-activity relationship approaches to nanotoxicology: current status and future potential. *Toxicology*. (Epub ahead of print; Nov 16, 2012).
58. Puzyn T, Rasulev B, Gajewicz A, Hu X, Dasari TP, Michalkova A, Hwang HM, Toropov A, Leszczynska D, Leszczynski J. Using nano-QSAR to predict the cytotoxicity of metal oxide nanoparticles. *Nat Nanotechnol* 2011, 6:175–178.
59. Fourches D, Pu D, Tassa C, Weissleder R, Shaw SY, Mumper RJ, Tropsha A. Quantitative nanostructure-activity relationship modeling. *ACS Nano* 2010, 4:5703–5712.
60. Xia XR, Monteiro-Riviere NA, Riviere JE. An index for characterization of nanomaterials in biological systems. *Nat Nanotechnol* 2010, 5:671–675.
61. Xia XR, Monteiro-Riviere NA, Mathur S, Song X, Xiao L, Oldenberg SJ, Fadeel B, Riviere JE. Mapping the surface adsorption forces of nanomaterials in biological systems. *ACS Nano* 2011, 5:9074–9081.
62. Rivera-Gil P, Oberdörster G, Elder A, Puentes V, Parak WJ. Correlating physico-chemical with toxicological properties of nanoparticles: the present and the future. *ACS Nano* 2010, 4:5527–5531.
63. Chithrani BD, Ghazan AA, Chan CW. Determining the size and the shape dependence of gold nanoparticle uptake into mammalian cells. *Nano Lett* 2006, 6:662–668.
64. Chithrani BD, Chan WCW. Elucidating the mechanism of cellular uptake and removal of protein-coated gold nanoparticles of different sizes and shapes. *Nano Lett* 2007, 7:1542–1550.
65. Bhabra G, Sood A, Fisher B, Cartwright L, Saunders M, Evans WH, Surprenant A, Lopez-Castejon G, Mann S, Davis SA, et al. Nanoparticles can cause DNA damage across a cellular barrier. *Nat Nanotechnol* 2009, 4:876–883.
66. Nagai H, Okazaki Y, Chew SH, Misawa N, Yamashita Y, Akatsuka S, Ishihara T, Yamashita K, Yoshikawa Y, Yasui H, et al. Diameter and rigidity of multiwalled carbon nanotubes are critical factors in mesothelial injury and carcinogenesis. *Proc Natl Acad Sci U S A* 2011, 108:E1330–E1338.
67. Murray AR, Kisin ER, Tkach AV, Yanamala N, Mercer RR, Young SH, Fadeel B, Kagan VE, Shvedova AA. Factoring-in agglomeration of carbon nanotubes and nanofibers for better prediction of their toxicity versus asbestos. *Part Fibre Toxicol* 2012, 9:10.
68. Liu S, Wei L, Hao L, Fang N, Chang MW, Xu R, Yang Y, Chen Y. Sharper and faster “nano darts” kill more bacteria: a study of antibacterial activity of individually dispersed pristine single-walled carbon nanotube. *ACS Nano* 2009, 3:3891–3902.
69. Schaeublin NM, Braydich-Stolle LK, Maurer EI, Park K, MacCuspie RI, Afrooz AR, Vaia RA, Saleh NB, Hussain SM. Does shape matter? Bioeffects of gold nanomaterials in a human skin cell model. *Langmuir* 2012, 28:3248–3258.
70. Oh WK, Kim S, Choi M, Kim C, Jeong YS, Cho BR, Hahn JS, Jang J. Cellular uptake, cytotoxicity, and innate immune response of silica-titania hollow nanoparticles based on size and surface functionality. *ACS Nano* 2010, 4:5301–5313.
71. Sayes CM, Fortner JD, Guo W, Lyon D, Boyd AM, Ausman KD, Tao YJ, Sitharaman B, Wilson LJ, Hughes JB, et al. The differential cytotoxicity of water-soluble fullerenes. *Nano Lett* 2004, 4:1881–1887.
72. Geidel C, Schmachtel S, Riedinger A, Pfeiffer C, Müllen K, Klapper M, Parak WJ. A general synthetic approach for obtaining cationic and anionic inorganic nanoparticles via encapsulation in amphiphilic copolymers. *Small* 2011, 7:2929–2934.
73. Kirchner C, Liedl T, Kudera S, Pellegrino T, Munoz Javier A, Gaub HE, Stölzle S, Fertig N, Parak WJ. Cytotoxicity of colloidal CdSe and CdSe/ZnS nanoparticles. *Nano Lett* 2005, 5:331–338.
74. Stark WJ. Nanoparticles in biological systems. *Angew Chem Int Ed Engl* 2011, 50:1242–1258.
75. Cho WS, Duffin R, Thielbeer F, Bradley M, Megson IL, Macnee W, Poland CA, Tran CL, Donaldson K. Zeta potential and solubility to toxic ions as mechanisms of lung inflammation caused by metal/metal oxide nanoparticles. *Toxicol Sci* 2012, 126:469–477.
76. Nel A, Xia T, Madler L, Li N. Toxic potential of materials at the nanolevel. *Science* 2006, 311:622–627.
77. Sayes CM, Wahi R, Kurian PA, Liu Y, West JL, Ausman KD, Warheit DB, Colvin VL. Correlating nanoscale titania structure with toxicity: a cytotoxicity and inflammatory response study with human dermal fibroblasts and human lung epithelial cells. *Toxicol Sci* 2006, 92:174–185.

78. Mahon E, Salvati A, Baldelli Bombelli F, Lynch I, Dawson KA. Designing the nanoparticle-biomolecule interface for “targeting and therapeutic delivery”. *J Control Release* 2012, 161:164–174.
79. Deng ZJ, Liang M, Monteiro M, Toth I, Minchin RF. Nanoparticle-induced unfolding of fibrinogen promotes Mac-1 receptor activation and inflammation. *Nat Nanotechnol* 2011, 6:39–44.
80. Linse S, Cabaleiro-Lago C, Xue W-F, Lynch I, Lindman S, Thulin E, Radford SE, Dawson KA. Nucleation of protein fibrillation by nanoparticles. *Proc Natl Acad Sci U S A* 2007, 104:8691–8696.
81. Saba TM, Di Luzio NR. Kupffer cell phagocytosis and metabolism of a variety of particles as a function of opsonization. *J Reticuloendothel Soc* 1965, 2:437–453.
82. Cedervall T, Lynch I, Lindman S, Berggård T, Thulin E, Nilsson H, Dawson KA, Linse S. Understanding the nanoparticle–protein corona using methods to quantify exchange rates and affinities of proteins for nanoparticles. *Proc Natl Acad Sci U S A* 2007, 104:2050–2055.
83. Casals E, Pfaller T, Duschl A, Oostingh GJ, Puentes VF. Hardening of the nanoparticle–protein corona in metal (Au, Ag) and oxide (Fe₃O₄, CoO, and CeO₂) nanoparticles. *Small* 2011, 7:3479–3486.
84. Milani S, Baldelli Bombelli F, Pitek AS, Dawson KA, Rädler J. Reversible versus irreversible binding of transferrin to polystyrene nanoparticles: soft and hard corona. *ACS Nano* 2012, 6:2532–2541.
85. Walczyk D, Bombelli FB, Monopoli MP, Lynch I, Dawson KA. What the cell “sees” in bionanoscience. *J Am Chem Soc* 2010, 132:5761–5768.
86. Lundqvist M, Stigler J, Cedervall T, Berggård T, Flanagan MB, Lynch I, Elia G, Dawson K. The evolution of the protein corona around nanoparticles: a test study. *ACS Nano* 2011, 5:7503–7509.
87. See V, Free P, Cesbron Y, Nativo P, Shaheen U, Rigden DJ, Spiller DG, Fernig DG, White MRH, Prior IA, et al. Cathepsin L digestion of nanobioconjugates upon endocytosis. *ACS Nano* 2009, 3:2461–2468.
88. Sund J, Alenius H, Vippola M, Savolainen K, Puustinen A. Proteomic characterization of engineered nanomaterial–protein interactions in relation to surface reactivity. *ACS Nano* 2011, 5:4300–4309.
89. Lundqvist M, Stigler J, Elia G, Lynch I, Cedervall T, Dawson KA. Nanoparticle size and surface properties determine the protein corona with possible implications for biological impacts. *Proc Natl Acad Sci U S A* 2008, 105:14265–14270.
90. Tenzer S, Docter D, Rosfa S, Wlodarski A, Kuharev J, Rekić A, Knauer SK, Bantz C, Nawroth T, Bier C, et al. Nanoparticle size is a critical physicochemical determinant of the human blood plasma corona: a comprehensive quantitative proteomic analysis. *ACS Nano* 2011, 5:7155–7167.
91. Simberg D, Park JH, Karmali PP, Zhang WM, Merkulov S, McCrae K, Bhatia SN, Sailor M, Ruoslahti E. Differential proteomics analysis of the surface heterogeneity of dextran iron oxide nanoparticles and the implications for their in vivo clearance. *Biomaterials* 2009, 30:3926–3933.
92. Dufort S, Sancey L, Coll JL. Physico-chemical parameters that govern nanoparticles fate also dictate rules for their molecular evolution. *Adv Drug Deliv Rev* 2012, 64:179–189.
93. Kapralov AA, Feng WH, Amoscato AA, Yanamala N, Balasubramanian K, Winnica DE, Kisin ER, Kotchey GP, Gou P, Sparvero LJ, et al. Adsorption of surfactant lipids by single-walled carbon nanotubes in mouse lung upon pharyngeal aspiration. *ACS Nano* 2012, 6:4147–4156.
94. Gasser M, Rothen-Rutishauser B, Krug HF, Gehr P, Nelle M, Yan B, Wick P. The adsorption of biomolecules to multi-walled carbon nanotubes is influenced by both pulmonary surfactant lipids and surface chemistry. *J Nanobiotechnol* 2010, 8:31.
95. Ruge CA, Schaefer UF, Herrmann J, Kirch J, Cañadas O, Echaide M, Pérez-Gil J, Casals C, Müller R, Lehr CM. The interplay of lung surfactant proteins and lipids assimilates the macrophage clearance of nanoparticles. *PLoS One* 2012, 7:e40775.
96. Shvedova AA, Kisin E, Murray AR, Johnson VJ, Gorelik O, Arepalli S, Hubbs AF, Mercer RR, Keohavong P, Sussman N, et al. Inhalation vs. aspiration of single-walled carbon nanotubes in C57BL/6 mice: inflammation, fibrosis, oxidative stress, and mutagenesis. *Am J Physiol Lung Cell Mol Physiol* 2008, 295:L552–L565.
97. Mahler GJ, Esch MB, Tako E, Southard TL, Archer SD, Glahn RP, Shuler ML. Oral exposure to polystyrene nanoparticles affects iron absorption. *Nat Nanotechnol* 2012, 7:264–271.
98. Walkey CD, Olsen JB, Guo H, Emili A, Chan WCW. Nanoparticle size and surface chemistry determine serum protein adsorption and macrophage uptake. *J Am Chem Soc* 2012, 134:2139–2147.
99. Kim HR, Andrieux K, Gil S, Taverna M, Chacun H, Desmaële D, Taran F, Georgin D, Couvreur P. Translocation of poly(ethylene glycol-co-hexadecyl)cyanoacrylate nanoparticles into rat brain endothelial cells: role of apolipoproteins in receptor-mediated endocytosis. *Biomacromolecules* 2007, 8:793–799.
100. Prapainop K, Witter DP, Wentworth P. A chemical approach for cell-specific targeting of nanomaterials: small-molecule-initiated misfolding of nanoparticle corona proteins. *J Am Chem Soc* 2012, 134:4100–4103.
101. Dutta D, Sundaram SK, Teeguarden JG, Riley BJ, Fifield LS, Jacobs JM, Addleman SR, Kaysen GA,

- Moudgil BM, Weber TJ. Adsorbed proteins influence the biological activity and molecular targeting of nanomaterials. *Toxicol Sci* 2007, 100:303–315.
102. Ge C, Du J, Zhao L, Wang L, Liu Y, Li D, Yang Y, Zhou R, Zhao Y, Chai Z, et al. Binding of blood proteins to carbon nanotubes reduces cytotoxicity. *Proc Natl Acad Sci U S A* 2011, 108:16968–16973.
103. Ehrenberg MS, Friedman AE, Finkelstein JN, Oberdorster G, McGrath JL. The influence of protein adsorption on nanoparticle association with cultured endothelial cells. *Biomaterials* 2009, 30:603–610.
104. Lartigue L, Wilhelm C, Servais J, Factor C, Dencausse A, Bacri JC, Luciani N, Gazeau F. Nanomagnetic sensing of blood plasma protein interactions with iron oxide nanoparticles: impact on macrophage uptake. *ACS Nano* 2012, 6:2665–2678.
105. Lesniak A, Fenaroli F, Monopoli MP, Åberg C, Dawson KA, Salvati A. Effects of the presence or absence of a protein corona on silica nanoparticle uptake and impact on cells. *ACS Nano* 2012, 6:5845–5857.
106. Deng ZJ, Liang M, Toth I, Monteiro M, Minchin RF. Plasma protein binding of positively and negatively charged polymer-coated gold nanoparticles elicits different biological responses. *Nanotoxicology* (Epub ahead of print; March 6, 2012).
107. Moghimi SM, Andersen AJ, Ahmadvand D, Wibroe PP, Andresen TL, Hunter AC. Material properties in complement activation. *Adv Drug Deliv Rev* 2011, 63:1000–1007.
108. Hamad I, Al-Hanbali O, Hunter AC, Rutt KJ, Andresen TL, Moghimi SM. Distinct polymer architecture mediates switching of complement activation pathways at the nanosphere-serum interface: implications for stealth nanoparticle engineering. *ACS Nano* 2010, 4:6629–6638.
109. Kievit FM, Zhang M. Cancer nanotheranostics: improving imaging and therapy by targeted delivery across biological barriers. *Adv Mater* 2011, 23:H217–H247.
110. Moghimi SM, Hunter AC, Andresen TL. Factors controlling nanoparticle pharmacokinetics: an integrated analysis and perspective. *Annu Rev Pharmacol Toxicol* 2012, 52:481–503.
111. Yamashita K, Yoshioka Y, Higashisaka K, Mimura K, Morishita Y, Nozaki M, Yoshida T, Ogura T, Nabeshi H, Nagano K, et al. Silica and titanium dioxide nanoparticles cause pregnancy complications in mice. *Nat Nanotechnol* 2011, 6:321–328.
112. Schleh C, Semmler-Behnke M, Lipka J, Wenk A, Hirn S, Schaffler M, Schmid G, Simon U, Kreyling WG. Size and surface charge of gold nanoparticles determine absorption across intestinal barriers and accumulation in secondary target organs after oral administration. *Nanotoxicology* 2012, 6:36–46.
113. Choi HS, Ashitate Y, Lee JH, Kim SH, Matsui A, Insin N, Bawendi MG, Semmler-Behnke M, Frangioni JV, Tsuda A. Rapid translocation of nanoparticles from the lung airspaces to the body. *Nat Biotechnol* 2010, 28:1300–1303.
114. Kannan S, Dai H, Navath RS, Balakrishnan B, Jyoti A, Janisse J, Romero R, Kannan RM. Dendrimer-based postnatal therapy for neuroinflammation and cerebral palsy in a rabbit model. *Sci Transl Med* 2012, 4:130ra146.
115. Riviere JE. Pharmacokinetics of nanomaterials: an overview of carbon nanotubes, fullerenes and quantum dots. *Wiley Interdiscip Rev Nanomed Nanobiotechnol* 2009, 1:26–34.
116. Singh R, Pantarotto D, Lacerda L, Pastorin G, Klumpp C, Prato M, Bianco A, Kostarelos K. Tissue biodistribution and blood clearance rates of intravenously administered carbon nanotube radiotracers. *Proc Natl Acad Sci U S A* 2006, 103:3357–3362.
117. Lacerda L, Herrero MA, Venner K, Bianco A, Prato M, Kostarelos K. Carbon-nanotube shape and individualization critical for renal excretion. *Small* 2008, 4:1130–1132.
118. Kagan VE, Konduru NV, Feng W, Allen BL, Conroy J, Volkov Y, Vlasova II, Belikova NA, Yanamala N, Kapralov A, et al. Carbon nanotubes degraded by neutrophil myeloperoxidase induce less pulmonary inflammation. *Nat Nanotechnol* 2010, 5:354–359.
119. Shvedova AA, Kapralov AA, Feng WH, Kisin ER, Murray AR, Mercer RR, St Croix CM, Lang MA, Watkins SC, Konduru NV, et al. Impaired clearance and enhanced pulmonary inflammatory/fibrotic response to carbon nanotubes in myeloperoxidase-deficient mice. *PLoS One* 2012, 7:e30923.
120. Schädlich A, Caysa H, Mueller T, Tenambergen F, Rose C, Göpferich A, Kuntsche J, Mäder K. Tumor accumulation of NIR fluorescent PEG–PLA nanoparticles: impact of particle size and human xenograft tumor model. *ACS Nano* 2011, 5:8710–8720.
121. Tang L, Fan TM, Borst LB, Cheng J. Synthesis and biological response of size-specific, monodisperse drug-silica nanoconjugates. *ACS Nano* 2012, 6:3954–3966.
122. Cabral H, Matsumoto Y, Mizuno K, Chen Q, Murakami M, Kimura M, Terada Y, Kano MR, Miyazono K, Uesaka M, et al. Accumulation of sub-100 nm polymeric micelles in poorly permeable tumours depends on size. *Nat Nanotechnol* 2011, 6:815–823.
123. von Maltzahn G, Park J-H, Lin KY, Singh N, Schwöppe C, Mesters R, Berdel WE, Ruoslahti E, Sailor MJ, Bhatia SN. Nanoparticles that communicate in vivo to amplify tumour targeting. *Nat Mater* 2011, 10:545–552.
124. Bertram JP, Williams CA, Robinson R, Segal SS, Flynn NT, Lavik EB. Intravenous hemostat: nanotechnology to halt bleeding. *Sci Transl Med* 2009, 1:11ra22.

125. Hu CM, Zhang L, Aryal S, Cheung C, Fang RH, Zhang L. Erythrocyte membrane-camouflaged polymeric nanoparticles as a biomimetic delivery platform. *Proc Natl Acad Sci U S A* 2011, 108:10980–10985.
126. Yoo JW, Irvine DJ, Discher DE, Mitragotri S. Bio-inspired, bioengineered and biomimetic drug delivery carriers. *Nat Rev Drug Discov* 2011, 10:521–535.
127. Valadi H, Ekström K, Bossios A, Sjöstrand M, Lee JJ, Lötvall JO. Exosome-mediated transfer of mRNAs and microRNAs is a novel mechanism of genetic exchange between cells. *Nat Cell Biol* 2007, 9:654–659.
128. Montecalvo A, Larregina AT, Shufesky WJ, Stolz DB, Sullivan ML, Karlsson JM, Baty CJ, Gibson GA, Erdos G, Wang Z, et al. Mechanism of transfer of functional microRNAs between mouse dendritic cells via exosomes. *Blood* 2012, 119:756–766.
129. Feliu N, Walter MV, Montanez MI, Kunzmann A, Hult A, Nyström A, Malkoch M, Fadeel B. Stability and biocompatibility of a library of polyester dendrimers in comparison to polyamidoamine dendrimers. *Biomaterials* 2012, 33:1970–1981.
130. Hayder M, Poupot M, Baron M, Nigon D, Turrin CO, Caminade AM, Majoral JP, Eisenberg RA, Fournie JJ, Cantagrel A, et al. A phosphorus-based dendrimer targets inflammation and osteoclastogenesis in experimental arthritis. *Sci Transl Med* 2011, 3:81ra35.
131. Shaunak S, Thomas S, Gianasi E, Godwin A, Jones E, Teo I, Mireskandari K, Luthert P, Duncan R, Patterson S, et al. Polyvalent dendrimer glucosamine conjugates prevent scar tissue formation. *Nat Biotechnol* 2004, 22:977–984.
132. Kah JC, Chen J, Zubieta A, Hamad-Schifferli K. Exploiting the protein corona around gold nanorods for loading and triggered release. *ACS Nano* 2012, 6:6730–6740.



Multiplexed Sensing and Imaging with Colloidal Nano- and Microparticles

Susana Carregal-Romero,^{1,2}
Encarnación Caballero-Díaz,^{1,3} Lule Beqa,¹
Abuelmagd M. Abdelmonem,¹ Markus Ochs,¹
Dominik Hühn,¹ Bartolome Simonet Suau,³
Miguel Valcarcel,³ and Wolfgang J. Parak¹

¹Fachbereich Physik and WZMW, Philipps Universität Marburg, Marburg 35043, Germany; email: susana.carregal@physik.uni-marburg.de, wolfgang.parak@physik.uni-marburg.de

²BIONAND, Centro Andaluz de Nanomedicina y Biotecnología, Málaga 29590, Spain

³Department of Analytical Chemistry, Campus de Rabanales, University of Córdoba, Córdoba 14071, Spain

Annu. Rev. Anal. Chem. 2013. 6:53–81

The *Annual Review of Analytical Chemistry* is online at anchem.annualreviews.org

This article's doi:
10.1146/annurev-anchem-062012-092621

Copyright © 2013 by Annual Reviews.
All rights reserved

Keywords

multifunctional colloidal nanoparticles, analyte recognition, bar-coding, multiplexing

Abstract

Sensing and imaging with fluorescent, plasmonic, and magnetic colloidal nano- and microparticles have improved during the past decade. In this review, we describe the concepts and applications of how these techniques can be used in the multiplexed mode, that is, sensing of several analytes in parallel or imaging of several labels in parallel.

1. INTRODUCTION

During the past decade, the use of colloidal nano- and microparticles in biological sciences has attracted a great deal of attention. They have long been used as contrast agents for imaging (1–3) and transducers for molecular sensing (4). Materials developed for these purposes range from single nanoparticles (NPs) and microparticles to complex hybrid nano- and microstructures. Nanoengineering allows for the integration of different functionalities into a single carrier system. Examples of multifunctional composites include the recently described nanocomposites based on silica, silver, and gold NPs (AuNPs), which have applications in photodynamic therapy, photothermolysis, and IR detection (5). Our review focuses on the use of inorganic NPs as building blocks of multifunctional composites on the nano- and micrometer scales, and on their applications in biosensing and diagnostics. After briefly introducing the main detection modes, we discuss why and how the assembly of individual NPs into multifunctional composites allows for multiplexing. Multiplexed sensing and imaging mean that several analytes can be detected in parallel and that different types of particles can be imaged simultaneously. Finally, we discuss some issues and new challenges concerning sensing and imaging involving hybrid materials based on inorganic NPs.

2. DETECTION MODES

In sensing and imaging applications, NPs are used to provide readout. In sensing applications, the transduction principle, which provides readout in the presence of a specific analyte, can depend on either direct interaction between the NP and the analyte or interaction between the analyte and another entity supported on the NP, which then interacts with the NP. The NP ultimately changes the signal for readout in the presence of the analyte. In the case of imaging, NPs are typically used as markers that provide contrast (and thus readout) for different imaging techniques. Readout is usually based on optical, electrical, or magnetic detection, as we discuss in detail below. However, naturally there are also other detection schemes, such as detection with X-rays (6), radioactivity (7), or mass changes (8); we do not focus on those techniques in this review.

2.1. Optical Detection

The principle of optical detection is based on the interaction between continuous or pulsed light and the sample to be analyzed. This interaction causes changes in the initial incident light wave in terms of frequency, amplitude, phase, polarization state, or time dependence. **Figure 1** summarizes some of the phenomena that are useful for analysis; these phenomena may occur when incident light interacts with a sample of dispersed colloidal particles (9). In general, transmission, elastic and inelastic scattering, and absorption processes can occur. In the case of transmission, light passes through the object and is normally affected in terms of amplitude or intensity. In the case of scattering phenomena, the interaction between light and the particles changes the direction of the incident light wave. However, following elastic scattering, the energy of the incident light, and thus the wavelength, remains unchanged. The Rayleigh and Mie theories describe typical particle-based scattering for small (<5-nm) and large (>5-nm) particles, respectively. In contrast, following inelastic scattering, the energy of the incident light, and thus the wavelength, changes. The inelastic scattering process (Raman scattering) is especially important for colloidal particles. The interaction between the incident light and the sample modifies the energy of the internal (typically rotational or vibronic) states of the particle, and the scattered light has either higher or lower energy, termed anti-Stokes or Stokes scattering, respectively. For luminescent particles, other interesting processes, such as the emission of light, may occur. This phenomenon is based

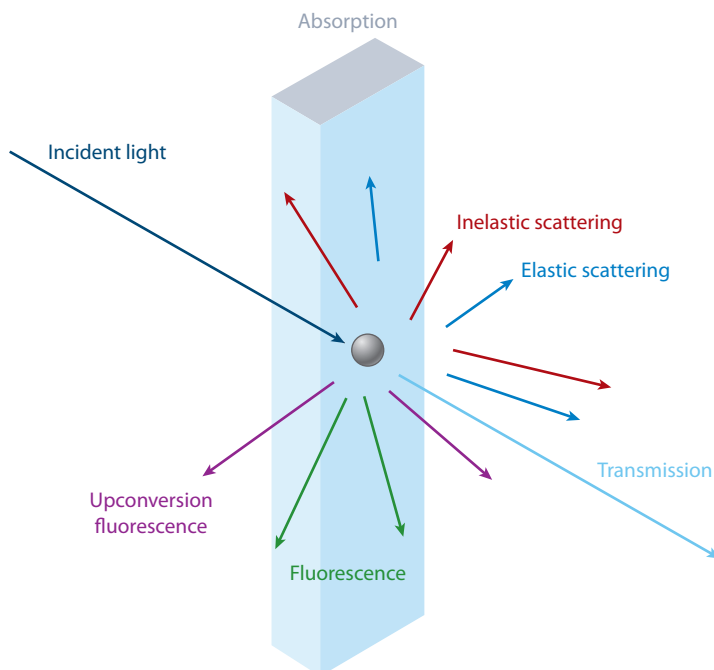


Figure 1

Possible interactions between a particle and light.

on the excitation of energetic states by the charge carrier's absorption of the incident wave energy, which in general is possible only if the incident wave is in resonance with the excited electronic state. The light that is reemitted following relaxation of the excited states to the ground states is termed fluorescence if the emitted light is less energetic than the incident light (more conventional process) and upconversion fluorescence if the emitted light is more energetic (less conventional process). Other parts of the energy can be converted into heat. This nonradiative energetic contribution is referred to as absorption, which does not lead to the emission of light, and whereby the energy remains in the sample.

Various techniques exist for the optical detection of particles on the basis of the above-mentioned mechanisms. Hereafter, we distinguish between plasmonic (10) and fluorescent (11) particles (12).

NPs of several metals, such as platinum, copper, gold, and silver, or alloys such as Cu_{2-x}Se , demonstrate surface plasmon resonance (SPR) due to the collective oscillation of the free electrons stimulated by incident light of an appropriate wavelength (13); they are therefore referred to as plasmonic NPs. This property has been exploited in many analytical techniques for sensing and imaging.

1. Localized surface plasmon resonance (LSPR) spectroscopy benefits from the high sensitivity of the plasmon resonance to changes in the local refractive index, and it can be applied to both individual NPs and periodic arrays of NPs. The light scattered by individual plasmonic NPs, for example, can be detected with dark-field microscopy (14). Plasmon resonance wavelength and intensity can be modified by the temporal or irreversible presence of an analyte (bound or adsorbed) on the NP surface. LSPR is a very sensitive tool for quantitative analyte analysis (15), allowing for even single-molecule detection (16, 17).

2. Colorimetric sensors are also based on LSPR techniques, but they were developed on the basis of the visible color changes that plasmonic NPs undergo in the presence of a target analyte that triggers the agglomeration (or redispersion) of an assembly of NPs (18). Although similar concepts have previously been used (19), the breakthrough in this technique was achieved by target DNA-mediated agglomeration of oligonucleotide-modified AuNPs, as introduced by the Mirkin group (4). In that study, the presence of target DNA was observed by the naked eye following a color change of a AuNP solution from red to blue. This concept has been further extended and has led to, for example, the development of scanometric sensors for DNA strands according to the specific binding of oligonucleotide-functionalized AuNPs in a DNA array. The change of color due to analyte recognition was further amplified through the addition of a silver layer onto the AuNPs. This process causes visible darkening of the array surface only in the presence of a complementary target (20). Colorimetric detection of analytes via analyte-induced agglomeration of plasmonic NPs is currently used for many different analytes (21, 22).
3. Surface-enhanced Raman spectroscopy (SERS) benefits from the intense electromagnetic field generated on some plasmonic nanostructures due to their LSPRs. Applications of this technique are expanding because of the possibility of ultrasensitive molecule detection without the need for special preparation of the sample. Imaging and sensing can be achieved with SERS labels in close contact with plasmonic NPs (23–26).
4. The nonradiative decay of plasmons can produce a localized increase of temperature on the plasmonic NP surface that can be exploited for imaging. Relevant techniques include photothermal microscopy (27, 28) and photoacoustic tomography (29, 30).

Fluorescence microscopy, spectroscopy, and flow cytometry are among the most powerful tools for imaging and analytical detection of molecules and ions. Several types of fluorescent particles can be used for sensing and imaging applications.

1. Quantum dots (QDs), namely semiconductor NPs, with tunable light emission. QDs composed by atoms in groups II–VI (CdSe, CdS, etc.) have been studied largely because of their higher stability against oxidation or agglomeration in biological fluids, compared with those of other semiconductor materials (31, 32). However, QDs based on silicon or carbon are more interesting for biological applications due to their reduced toxicity. Efforts to synthesize, stabilize, and use silicon and carbon QDs as contrast agents and sensors are under way in clinical applications (33–36).
2. Noble-metal clusters. Silver NPs or AuNPs with diameters less than 2 nm do not exhibit SPR, but they can present fluorescence owing to their molecule-like properties (37, 38). Such small NPs can be used as fluorescent labels within multifunctional nanostructures or individually if they are properly stabilized.
3. Upconversion NPs and complexes. Based mostly on lanthanide-doped materials, these materials are promising for *in vivo* imaging. Their range of excitation/emission wavelengths can be tuned to the near-IR region, in which tissue produces minimal absorption and scattering of light. Moreover, they have low cytotoxicity, a long lifetime, and a narrow emission bandwidth (39, 40).
4. Inorganic NPs acting as passive carriers. These NPs can accumulate organic dyes and bioluminescent or chemiluminescent molecules either on the surface of or within a particle (41).
5. Polymeric nanomatrices acting as passive carriers. Photonic explorers for bioanalysis with biologically localized embedding (PEBBLE) sensors are a prominent example. They can be loaded with several dyes, permitting ratiometric sensor preparation and multiplexing (42).

6. Microbeads and microcapsules. Due to their size, they can be simultaneously loaded with both organic dyes and fluorescent NPs. Multitasking can be readily achieved with such materials (43, 44).

Detection based on fluorescent particles depends on the physicochemical process involved in the modification of the emitted light upon analyte–particle interaction. The main applied concepts for fluorescence detection include the following.

1. Readout based on analyte-sensitive fluorophores. The presence of the analyte can directly modify the emission of the fluorophore (45).
2. Readout based on the quenching of QD fluorescence through the proximity of another NP, such as a AuNP (46).
3. Readout based on photoinduced electron-transfer (PET) sensors. They consist of one fluorescent species attached to a recognition group that acts as a quencher in the unbound dark state. The binding of the recognition component with the analyte (normally metal cations and protons) cancels the electron transfer and dequenches the fluorophore (47).
4. Readout based on Förster resonance energy transfer (FRET) between two fluorophores. Often, QDs act as donors and transfer energy to an analyte-sensitive fluorophore that acts as an acceptor, but FRET in which the QDs are acting as the acceptors can occur (48). The lifetime of and the response to analytes of the acceptor fluorophore are modified due to the presence [within a short (<10-nm) distance] of the donor fluorophore.
5. Readout based on chemiluminescence resonance energy transfer (CRET). In CRET, a chemiluminescent probe is the donor; it excites the acceptor fluorophore, which can be a dye or a particle. The chemiluminescent probe should be analyte sensitive and should be formed by two species that react to produce emission of light only in the presence of the analyte (49).
6. Readout based on bioluminescence resonance energy transfer (BRET). Bioluminescent proteins are efficient energy donors for QDs (50). Because CRET and BRET processes do not need light excitation, their sensitivity is high.

2.2. Electrical Detection

Electrical detection modes deal mainly with NPs that conduct electricity, such as noble metals or semiconductors, which are typically supported by a flat electrode (51, 52). However, oxide NPs and hybrid multifunctional NPs have also been used as electrochemical sensors and biosensors. The function of the NPs in such sensors varies not only according to the nature of the NP but also on the basis of how the analyte is detected. Luo et al. (53) provide some important examples of the functions of NPs in electrical sensors: (a) The NPs are reactants themselves (54), (b) they are catalysts of electrochemical reactions (55), (c) they provide an appropriate surface for immobilization of biomolecules (e.g., analyte receptors) (56), (d) they improve or vary the conductivity between the analyte receptor and the electrode (57, 58), (e) they enhance electron-transfer processes (59), and (f) they perform labeling (60). The four main electroanalytical categories of detection involving NPs are (a) classic potentiometry (which involves potential measurements) (61), (b) coulometry (by measuring current, the amount of matter transformed during the electrolysis reaction is calculated) (62), (c) amperometry (wherein ions are detected on the basis of current measurements) (54), and (d) voltammetry (in which current measurements are performed while the potential is changed) (55). Electrochemical biosensing is often applied to the detection of biomolecules such as enzymes, antigens, and DNA, which are responsible for specifically recognizing the analyte and, in the case of enzymes, for converting the analyte in the signal that is actually detected (such

as electrons, H^+ , and H_2O_2). Many comprehensive reviews summarizing the most significant improvements in nanomaterial-based electrical biosensing have been published, and we recommend reading them for further information (63, 64).

Hybrid systems that mix optical and electrical measurements for analyses involving NPs have been performed. Electrochemical-LSPR biosensors have been developed for label-free detection of peptide toxins through the use of core-shell NP arrays (65). The substrate comprised silica NPs used as the core and a thin gold film used as the shell, which simultaneously acted as a working electrode and an LSPR sensor. The binding of the peptide toxin melittin to the hybrid electrode was optically detected by LSPR, and the membrane-disturbing properties were assessed electrochemically (65). In the case of fluorescent NPs, optical excitation can be used to modulate the electrochemical signal. The illumination of QDs, immobilized on an electrode, generates charge carriers (electrons and holes) and gives rise to a photocurrent. This detection scheme has been employed in, for instance, the light-triggered electrochemical detection of aminophenyl phosphate (66).

2.3. Magnetic Detection

Functionalized magnetic nanoparticles (MNPs) are widely used for sensing and imaging in the context of magnetic resonance (MR) (67–69). When used as targeted contrast agents, molecules or functional groups on the MNP surface bind the targeted molecules, first producing local inhomogeneities in the applied magnetic field that affect the proton spin precession (decreasing the relaxation time) within the target molecules and then increasing the contrast. These changes in relaxation times have been extensively utilized for high-sensitivity detection. For example, a recently published study used polymerase chain reaction detection, which normally requires fluorescence readout methods (70).

Magnetic relaxation switches are MR-based assays that are associated with different spin-spin relaxation times between the dispersed and agglomerated states of MNPs (71). SQUIDS (superconducting quantum interference devices) have been used for sensing on the basis of the change of the relaxation magnetic moment in the presence or absence of the corresponding analyte (72). Moreover, magnetoresistance can be also applied to magnetic sensing (73). In this case, the change of the sensor's electrical resistance is measured following analyte binding in the presence of a magnetic field. Superparamagnetic NPs are normally used as magnetic field concentrators, but they need to be functionalized with a molecule that specifically binds the corresponding analyte. Proteins, DNA, and enzyme reactions have been detected with this technique, given that it is one of the most sensitive magnetic sensing methods (71, 74).

3. MULTIPLEXED SENSING

Analyte detection involving colloidal NPs often requires the use of multifunctional NPs. In this context, the simplest sensing system would be formed by NPs that produce or enhance a signal (which can be detected optically, electrically, magnetically, etc.), coated with a recognition element such as an antibody or an analyte-sensitive fluorophore. Multianalyte sensing could be achieved simply by producing similarly functionalized NPs with different recognition elements according to the respective analytes and with individually resolved readout (for example, by different wavelengths in the case of optical readout). However, practical problems, such as cross-reactivity between analytes to different recognition elements involving limited selectivity, signal overlap of the different readouts, and limitations related to the NP functionalization, have to be considered. Not only does multiplexed detection reduce costs, sample volume, and assay time,

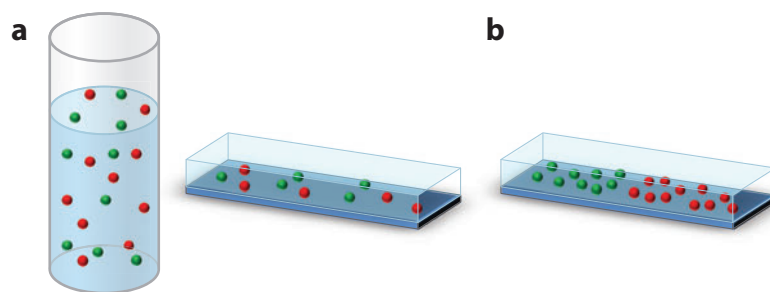


Figure 2

Classification of sensors on the basis of multifunctional particles. (a) Particles are dispersed in solution, and following analyte binding, readout can be performed in solution or on a planar surface, where sensor particles are randomly distributed. (b) Readout is based on structured surfaces on which the particles are bound to specific locations.

but it is convenient for the analysis of real samples, such as blood or river water, in which many different analytes can interfere with the signal of a specific sensor. Therefore, there is increasing interest in developing multiplexed sensors that can substitute individual analyte-detection assays, such as enzyme-linked immunosorbent assays (ELISAs) for tumor markers (75).

In this section, we discuss some recent nanotechnology strategies applied to multiplexed sensing. There are two different approaches: assays based on particles in suspension and assays based on planar arrays. Advantages of the use of particle sensors in suspension include (a) the higher surface-to-volume ratio for receptor conjugation and target analyte binding; (b) the better accessibility of the analyte to the sensing surface, given that sensor particles move in solution similarly to the analyte; and (c) the possibility of incorporation *in vivo* by targeted delivery. This approach also has some drawbacks: (a) Particles in suspension are normally less sensitive (i.e., have higher detection limits) than planar array sensors; (b) their stability and reusability are often lower; (c) multiplexing due to spatial separation is more easily achieved for planar arrays of NPs; and (d) in the case of *in vivo* sensing, one must take into account the fact that NPs may stay in the body for a long time and thus have cytotoxic effects. We describe two scenarios: sensing based on dispersed particles in solution and sensing based on particles associated with planar arrays. In the first case, readout is typically carried out without the particles having to be ordered on specific positions; in other words, the particles are randomly dispersed in solution (after the binding of the analyte) or are randomly associated with a surface (without order). In the second case, readout is based on structured surfaces on which the particles are bound to specific locations (**Figure 2**).

3.1. Multiplexed Sensors Based on Dispersed Particles in Solution

For multiplexed detection in solution, particles must be designed to carry receptors for specific analytes. Also required are the corresponding transducer and an encoding scheme for use in determining which receptor is emitting the signal (76). In this section, we focus on optical readout because it is the most frequently used technique for multiplexed sensing with dispersed particles.

Multiplexing can be achieved by spectral, spatial, and temporal separation of the readout originated from different particles (which are sensitive to different analytes) (77). Before we describe the different principles for multiplexed sensing, we note that in all sensing applications involving particle-based sensors, one must be aware that the analyte concentration close to the (sensitive) particle surface in general differs from that in bulk (76). This problem can be easily understood

with the following examples. First, in the case of ion detection, electrostatic interaction between the corresponding ion and the particle surface occurs when the particles are charged. Debye-Hückel-based screening on the particle charge with counterions thus involves ion concentrations close to the particle surface (where the actual detection takes place) that are different from those in bulk (78–80). Second, in the case of protein detection, one has to be aware that proteins often (nonspecifically) adsorb to the surface of particles, forming the so-called protein corona (81, 82). Thus, the protein concentration at particle surfaces is generally higher than in bulk. Third, the sensing element (for example, an analyte-sensitive fluorophore bound to the particle) can be influenced by the particle. If the sensing element, the actual probe, is bound inside a (porous) particle or to the particle surface, then the particle impregnates a different environment to the probe. The environment near the particle can be, for example, more apolar than the surrounding aqueous solution, which can affect the response of the probe (83). One must therefore be aware that what particle-based sensors actually detect are local analyte concentrations, not bulk concentrations.

In case the spectrally resolved readout is based on fluorescent particles, multiplexing can be performed by using a set of particles emitting at different wavelengths, whereby the fluorescence readout of each particle-based sensor is sensitive to one analyte species. Spectrally resolved fluorescence measurements allow several analytes to be detected in parallel. The most significant problem with this approach is spectral overlap of the fluorescence from different particles. QDs are better suited to this purpose than particles that are decorated or filled with organic fluorophores, given that the emission spectra of QDs are generally narrower and do not have a red tail (1). For example, investigators have simultaneously detected enzymatic activity from two different enzymes by using a simple assay procedure based on QDs with distinct emission spectra (46). The enzymatic biomarkers uPA protease and Her2 kinase were detected at concentrations that were clinically relevant for the determination of breast cancer prognosis by use of two differently functionalized QDs with different emission spectra. The first QD dequenched following enzymatic degradation (**Figure 3a,b**). FRET occurred between the second QD (donor) and an organic dye (acceptor) when the residue of the enzymatic reaction was bound to a specific antibody functionalized with organic dyes on the surface of the QD (**Figure 3c,d**). Another example, also based on various QD emissions, involves a direct multiplexed sensor for Ag^+ and Hg^{2+} . The QDs were functionalized with different nucleic acids that specifically bound Ag^+ or Hg^{2+} (84). Thereafter, the presence of these ions in solution caused the formation of Ag^+ -cytosine or Hg^{2+} -thymine complexes and resulted in QD electron-transfer quenching.

Multiplexed, spectrally resolved optical readout can also take place with plasmonic NPs because the LSPR depends on the size and shape of the plasmonic NPs (85). Thus, plasmons of different types of NPs can be recorded at different wavelengths. This property has been used to create a multiplexed LSPR sensor involving gold nanorods (AuNRs) with different aspect ratios (86). In this study, the ratio between the length and the thickness of the rods determined the respective readouts. NRs with different aspect ratios were modified with recognition molecules for various analytes. The binding of the analytes to the different AuNRs can shift the plasmon band position and modify its extent. In this context, investigators have carried out parallel detection of three different cell-surface markers and detection of two different types of bacteria (87, 88). Although these sensors can detect only a few different analytes in parallel (given that the plasmonic peaks are relatively broad and thus suffer from spectral overlap), they are interesting because of their simple design and ease of use.

The principles discussed above are based on ensemble measurements that allow for simultaneous readout. Each particle is responsible for the detection of one analyte, giving rise to the corresponding signals at different wavelengths. Thus, readout can be spectrally resolved. However, there is an alternative way to read out particles one by one; in other words, readout can

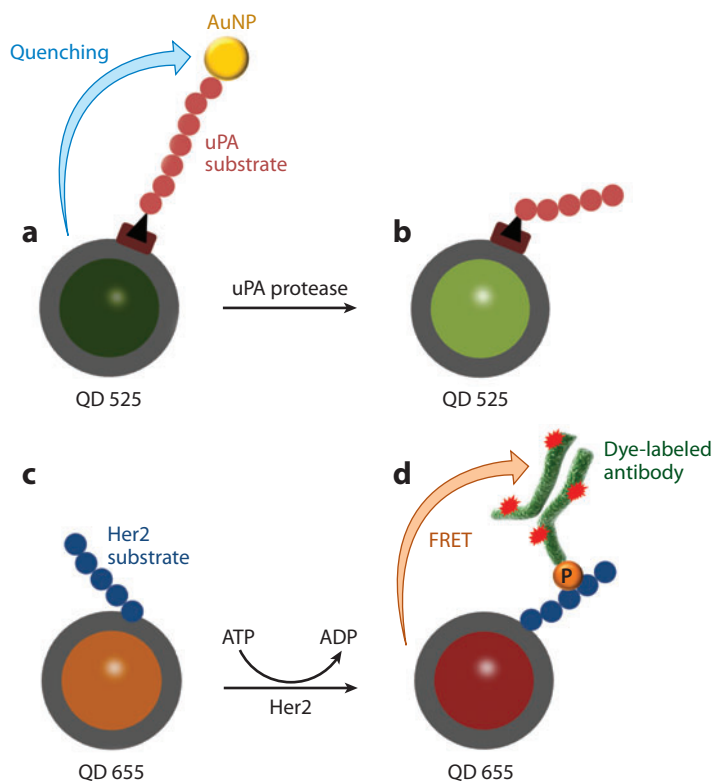


Figure 3

A multiplexed sensor for uPA protease and Her2 kinase. (*a,b*) The protease sensor is based on the quenching of quantum dots (QDs) emitting at 525 nm (*a*) and further dequenching in the presence of uPA that cleaves the substrate and releases the gold nanoparticles (AuNPs) responsible for the quenching. AuNPs absorb light very efficiently due to their surface plasmon resonance (*b*). (*c,d*) The kinase sensor is based on Förster resonance energy transfer (FRET) from QDs emitting at 655 nm to organic dyes that label the antibody bound to the analyte on the surface of the QDs following an enzymatic reaction. Modified from Reference 46 with permission.

be spatially resolved. In this case, spectral overlap does not pose a problem because the particles are spatially separated and readout can be correlated with individual particles (77). To read out particles one by one in solution, one can use either flow cytometry or microscopy.

In this context, there are two readout strategies both based on bar-coding. In the first strategy, analyte-sensitive readout can be combined with a bar code. The bar code identifies the analyte for each optical readout. Consider, for example, a class of fluorophores that are sensitive to Na^+ and another class sensitive to K^+ and that the emission spectra of both types of fluorophores overlap. If two types of particles that make up either the Na^+ - or K^+ -sensitive fluorophores, along with a corresponding bar code, are produced, then one can classify each particle by first reading the bar code, which reveals whether the fluorescence from the analyte-sensitive fluorophore corresponds to Na^+ or K^+ (77). QDs are very useful for the production of fluorescent bar codes due to their narrow emission band. Compared with that of organic dyes, the emission of different QD species can be better spectrally resolved, so more codes can be generated. For instance, the inner cavities of porous microparticles (polyelectrolyte capsules) were loaded with analyte-sensitive fluorophores, and the surfaces of the fluorophores were tagged with a QD-based fluorescence bar code. This

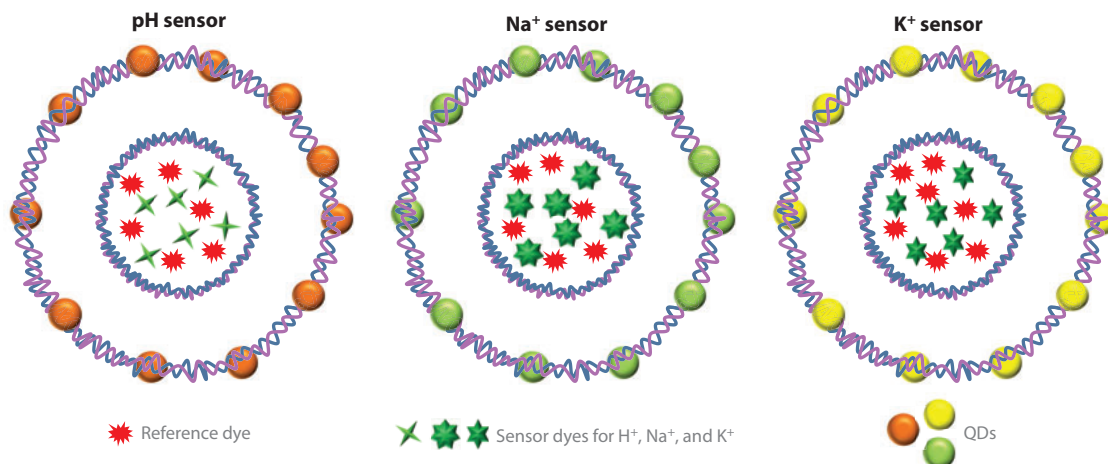


Figure 4

Simplified scheme of multiplexed sensors for H^+ , Na^+ , and K^+ based on quantum dot (QD) bar codes. Ion-sensitive dyes are encapsulated, together with a reference dye, in a permeable multiple-shell structure within the capsule to enable ratiometric measurements. The emission of the specific ion sensors may overlap, but the bar codes made with the different QDs allow for discrimination between signals.

system allowed three ions (H^+ , Na^+ , and K^+) to be detected in parallel, despite the spectral overlap of the analyte-sensitive fluorophores (**Figure 4**) (44).

The second bar code–based strategy is based not on active sensing (i.e., there is no molecule or particle of which the readout is altered following binding of the analyte), but on passive detection. On the basis of molecular recognition, analyte molecules in solution are tagged with a bar code; that is, bar codes need to be modified with analyte receptors. Consider a scenario in which different viruses are to be detected in solution. Antibodies for the different viruses would be modified with different bar codes. By observing one by one the conjugates that form (as mentioned above in the context of flow cytometry or with microscopy), one can identify the different viruses. An important example is a multiplexed sensor for five different genetic biomarkers (human immunodeficiency virus, malaria, hepatitis B, hepatitis C, and syphilis) developed by Giri et al. (43). These authors encoded microbeads with QDs of different emission wavelengths and intensities to produce a library of bar codes for multiplexed detection; this library exceeded the limit of 100 useful bar codes of similar systems involving organic dyes instead of QDs. The bar-coded particle bound the biomarker without causing any change in its fluorescent emission. A universal fluorescent probe that binds all biomarkers was used to discriminate between the unbound bar codes and the analyte–bar-coded particles. Only when there was colocalization between the emission of the bar code and the universal probe was the analyte bound to the bar code. Readout was performed with flow cytometry (**Figure 5**).

SERS-encoded NPs are a promising alternative to bar-coding (89). Particles should contain organic molecules (SERS reporters) in close contact with or bound to the plasmonic surfaces, providing the signature of the particle (90). The particle should be separately functionalized with an analyte receptor (91). Due to the uncountable number of molecules, each of which has specific vibrational spectra, a multiplexed sensor based on SERS-encoded NPs can be considered limitless. However, the number of codes that can be experimentally produced is restricted by several factors involved in the synthesis of multifunctional particles, such as the binding of the SERS reporter

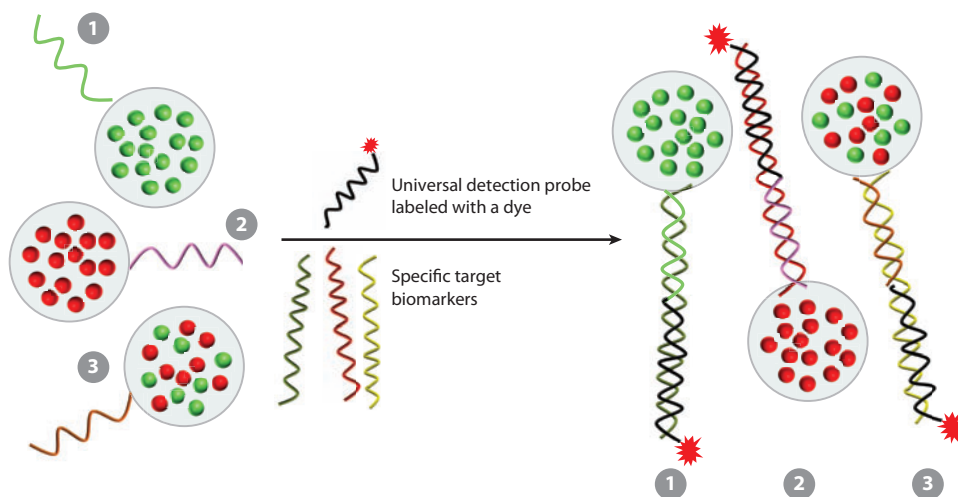


Figure 5

Microbeads labeled with different mixtures of quantum dots for multiplexed biomarker detection. Each sensor is functionalized with a capture DNA strand (steps 1 through 3). In solution, hybridization occurs between the specific target biomarkers and the universal detection probe. The universal labeled probe is used to differentiate between bar codes bound to the biomarkers and free ones. Finally, the sample is analyzed by flow cytometry, in which each particle is analyzed individually.

on the metallic surface, the insufficient field enhancement necessary to raise the SERS signal up to detectable levels, and the stability of the particles. Many examples of the synthesis of encoded NPs for SERS sensing in solution exist (92, 93) but the multiplexed sensing of a large number of analytes is still in its infancy, so more universal strategies for the SERS-encoding and detection should be performed. *In vivo* multiplexed sensing has been demonstrated only recently (94).

Another example involves plasmonic NPs assembled on a surface for the design of SERS-based multiplexed sensing platforms (95). So-called sandwich-type DNA coated silver NPs arrays have been used to specifically hybridize various DNA strands labeled with different SERS probes (96). Multiplexing can take place because different SERS labels can conveniently be spectrally resolved (Figure 6); thus, no structuring of the surface is required. The number of DNA strands that can be detected in parallel is limited by the number of SERS labels that can bind DNA and by the length of the DNA strand (with sufficient enhancement of the Raman signal, which depends on the number of labels and the distance between the labels and the surface). The creation of hot spots following DNA hybridization has also been exploited in multiplexed SERS-based sensors involving sandwich-type DNA arrays to reach a DNA detection limit of 10 pM (97).

Encoded hybrid materials can help improve the number of analytes detected in parallel, as discussed in the previous section. However, if a second encoding scheme is added to multifunctional NPs, then the number of parallel detected analytes can be multiplied. This idea was introduced by Wang et al. (98), who recently produced a hybrid system based on AuNRs coated with SiO₂ and encoded with different QDs with different emission and SERS labels. The resulting immunoassay has great potential for multiplexing.

In addition to spectral and spatial discrimination, temporal resolution of different optical sensors can also be performed. In the case of fluorescent particles, analyses of luminescence lifetime and the intensity-to-lifetime ratio allow for discrimination between signals that may be spectrally overlapped (99, 100). Sensors based on lifetime measurements of QDs exist (101),

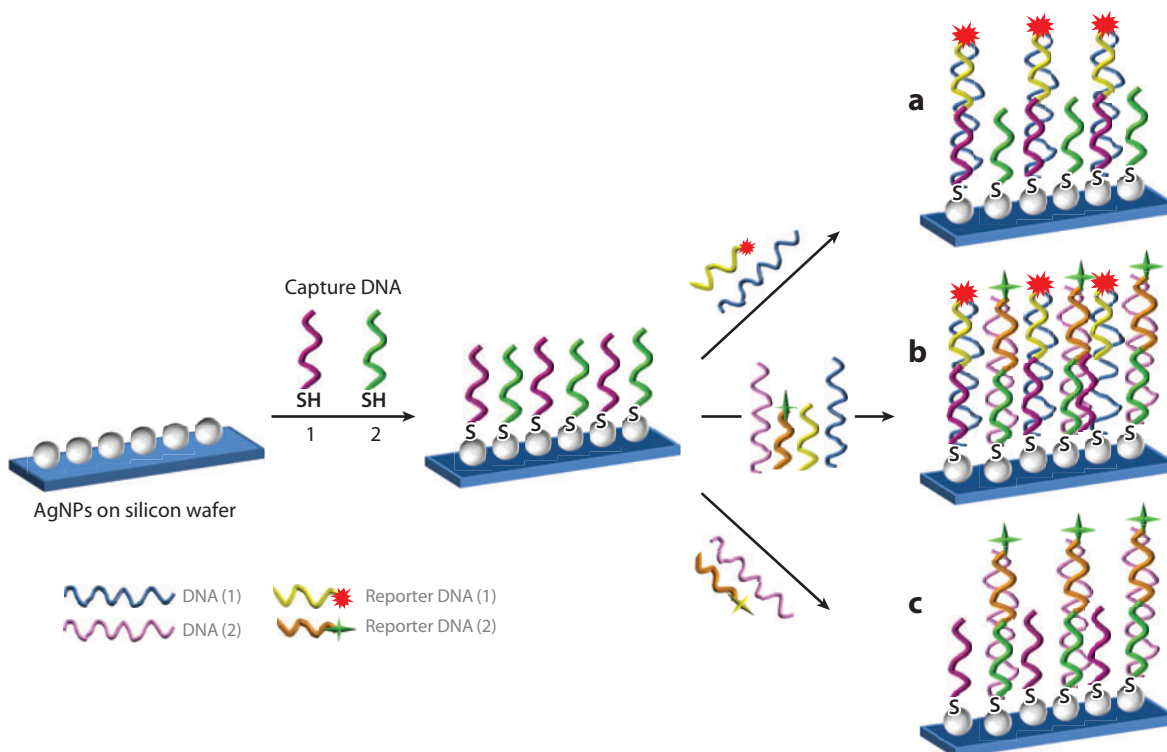


Figure 6

A multiplexed DNA sensor based on silver nanoparticles (AgNPs) deposited on silicon wafers and functionalized with thiolated DNA (1 and 2) strands for the specific hybridization of DNA (1) and DNA (2) and the corresponding surface-enhanced Raman spectroscopy-labeled DNA reporters. (a) Only DNA (1) in solution. (b) A mixture of DNA (1) and DNA (2) in solution. (c) Only DNA (2) in solution. Abbreviation: SH, thiol group termination. Modified from Reference 96 with permission.

but to the best of our knowledge, multiplexed sensors based on lifetime measurements are still uncommon. Techniques such as fluorescence lifetime imaging microscopy (FLIM) will probably extend the use of temporal discrimination in optical biosensing. Recently, cellular viscosity was studied with fluorescent ratiometry and FLIM (102), and multiplexed sensing is likely to evolve in this direction by simultaneously taking advantage of several measurements, either spectral and temporal or spatial and temporal (103). An example of a promising technique in multiplexing wherein lifetime and spectral measurements of fluorophores can reveal information about analyte binding involves multiplexed FRET assays. If FRET occurs, not only the emission intensity and wavelength of the donor and acceptor fluorophore but also the lifetime can be changed (Section 2). Multiplexed FRET assays for biosensing have been developed on the basis of (a) FRET from luminescent lanthanide complexes to several different QDs (acceptors) following molecular recognition (104) or (b) FRET from several QDs (donors) to organic dyes for the detection of DNA (105).

Although most of the examples of multifunctional NPs used for multiplexed sensing in solution involve optical detection, there are remarkable examples that mix several detection modes. These include magnetofluorescent nanoparticles, which can be used for flow cytometry and diagnostic MR detection (106, 107).

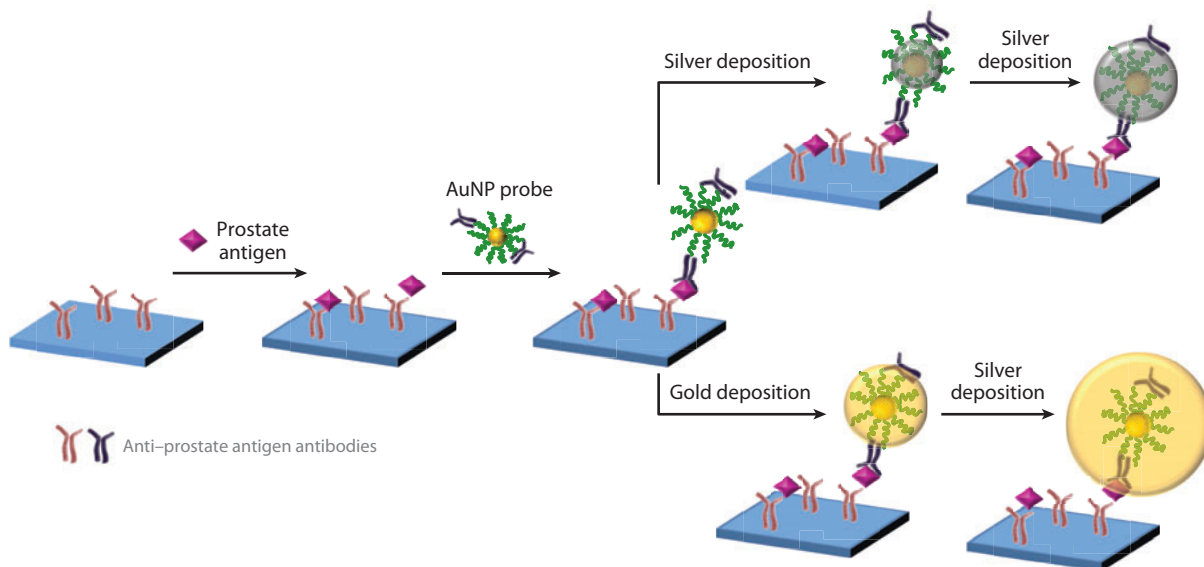


Figure 7

A scanometric immunoassay. Abbreviation: AuNP, gold nanoparticle. Modified in part from Reference 116.

3.2. Multiplexed Sensors Based on Particles Associated with Planar Arrays

Planar arrays, composed mainly of metallic and semiconductor NPs and arrays of biomolecules such as DNA and antibodies that bind NPs, have been extensively studied for use in NP-based optical or electrical biosensors (108–110). Multiplexed sensing with NPs associated with (typically planar) arrays can easily be performed because of the possibility of positional encoding (111). The general idea is to detect various analytes at different positions of the (generally structured) array. In this section, we discuss recent examples of multiplexed sensors based on NP planar arrays.

3.2.1. Localized surface plasmon resonance spectroscopy. LSPR-based multiplexed sensors detect, for example, changes in interparticle distance; modification of the refractive index; and changes in color in the LSPR of NPs due to the presence of analytes, whose individual signal can be differentiated by specific receptors, normally DNA or antibodies (112–114). Colorimetric assays can be produced through functionalization of a microstructure chip with different antibodies in different regions. The addition of a solution with antigen produces specific antibody–antigen binding, and depending on the amount of antigen, the response in color (and absorbance) may differ. This method is sensitive and specific. Endo et al. (115) applied this method to eight different proteins. In a similar approach, investigators modified the above-mentioned scanometric assay by using antibodies instead of DNA microarrays and electroless deposition of gold instead of silver. The light was thereby scattered by antibody–oligonucleotide hybrid AuNPs, and the amplification of the signal was greater than that of precedent scanometric assays due to gold deposition (**Figure 7**). The assay detected very low concentrations of different proteins, in this case in serum, without the need to trap of the analyte in solution with two differently labeled NPs. This process eliminated several steps from the production of the multiplexed sensors (116). Note that scanometric assays are US Food and Drug Administration–approved detection methods for biological samples. Therefore, they are among the most-studied and most widely used methods for multiplexed analyses involving NPs.

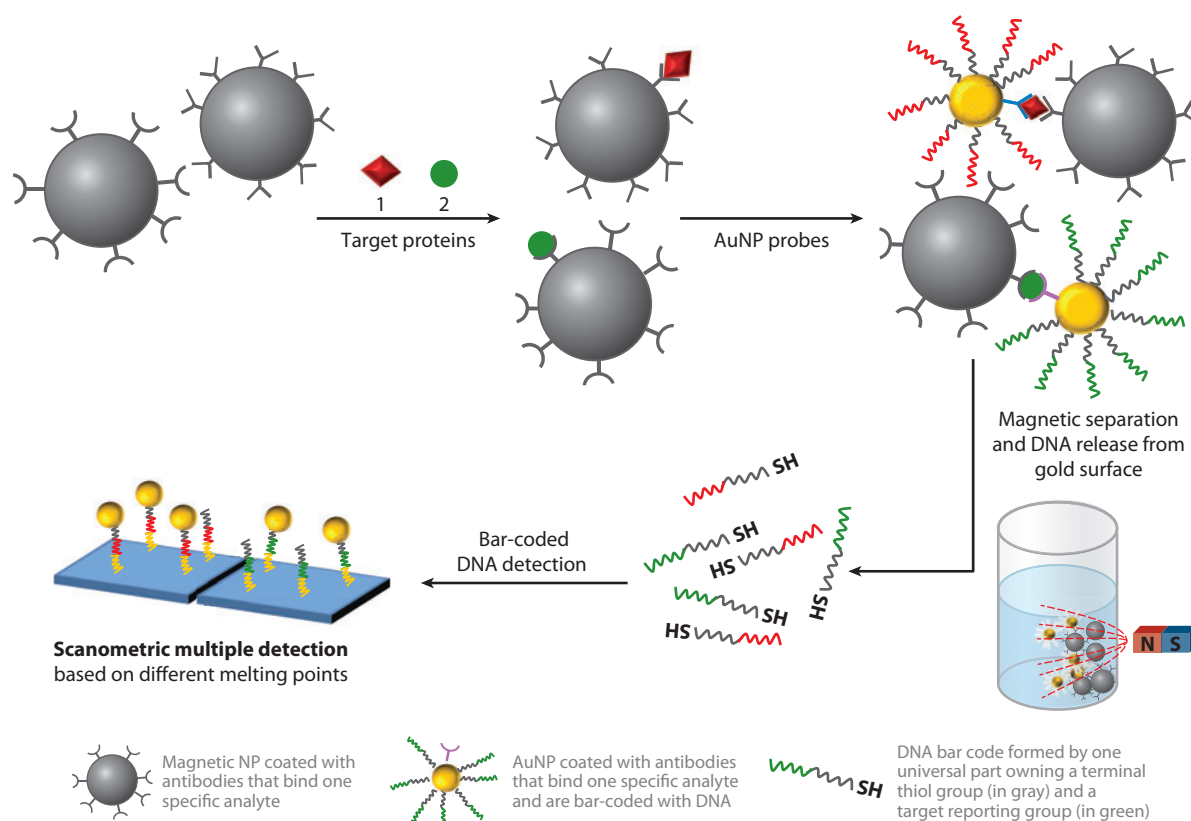


Figure 8

A bio-bar-coded gold nanoparticle (AuNP) assay for multiplexed protein detection. Scanometric detection also involves a silver coating to improve sensitivity (not shown for simplicity). Abbreviation: SH, thiol group termination. Modified from Reference 117 with permission.

In addition to direct arrangement of the NPs via recognition of the analyte on the array surface, NPs that have captured an analyte can also be arranged via bar codes. Bar codes can be made, for example, with biological molecules. An interesting example is a multiplexed sensor based on bio-bar-coded AuNPs and scanometric detection (involving colorimetric detection) (117). The analytes—in this case, protein cancer markers—are trapped by two different types of NPs, DNA bar-coded AuNPs and MNPs, which have different antibodies that bind the same protein in different epitopes. Magnetic separation is applied after the analytes are trapped in solution by the antibodies bound to the surface of the MNPs. The DNA used as a bar code is then released from the gold surface and quantified in a scanometric detector (LSPR-based detection). Again, the detector involves (smaller) AuNPs and a silver-layer coating that significantly amplified the signal and reduced the detection limits. **Figure 8** depicts this multiplexed sensor, which is very sensitive and specific. However, it requires many functionalization steps for numerous different NPs.

Recently, copper-capped silica particles have been used to develop a cost-effective optical setup on disposable chips capable of multiplexed sensing of biomolecules; the chips have a detection limit of 10 fM. The assay is based on measurable changes in the refractive index in the presence of analytes (in this case, different DNA strands), which arise from the LSPR of the copper layer deposited on the silica NPs (118). The combination of LSPR refractive-index sensing and the

well-known ELISA assay has led to the development of another colorimetric multiplexed sensor with single-molecule sensitivity. This new technique takes advantage of the amplification of the shift of the LSPR scattering maximum following an enzymatic reaction that allows for the detection of one or a few enzymes (119). The authors have not yet applied this new approach to multianalyte analyses, but due to the sensor configuration and the results from single-particle analyses, multiplexing is highly anticipated, along with the development of nonfluorescence single-molecule ELISA assays.

3.2.2. Electrochemical immunosensors and immunoassays. Electrochemical immunosensors and immunoassays (EIIs) are electrochemical sensors in which antibody–antigen interactions occur on an electrochemical transducer (in immunosensors) or the immunological material is immobilized on a solid support, such as a nanomaterial. Following sandwich or competitive immunoreactions, the solid support containing the immunological material is attached to the transducer surface (in immunoassays) (120). EIIs are excellent candidates for multianalyte analysis in terms of clinical diagnosis, in which the biological agents to be detected are present in very low concentrations (121). Multiplexed analysis can be performed in EIIs when the sensing electrodes are sufficient separated to prevent signal interference (cross talk) between neighboring electrodes. Very low analyte concentrations can be detected through amplification of the antibody–antigen interaction transduction signal with labels such as enzymes or NPs (122). NPs can have different functions within the sensor (Section 2.2), such as trapping analytes and improving the transducer surface for better antibody adhesion.

Interesting examples of EIIs involving multifunctional NPs have recently been provided (60, 123). Mani et al. (124) produced a multiplexed sensor for four different oral cancer biomarkers that can be used with clinical samples. These authors achieved ultralow detection ($5\text{--}50\text{ fg ml}^{-1}$) on the basis of amperometric measurements. In another study, magnetic nanobeads were functionalized with both an antibody to capture a specific analyte and horseradish peroxidase to amplify the signal during the detection on the planar electrode. In the first step of the detection, the magnetic beads functionalized with specific antibodies captured the corresponding analyte due to antibody–antigen interactions; then, these magnetic nanobeads were magnetically separated from the solution. The second step of the detection involved the binding of a second antibody with the corresponding antigen on a planar electrode. This time, the second antibody bound to another epitope of the same antigen, and the unbound magnetic nanobeads were washed out. Multiplexing was achieved through the use of several electrodes in parallel (125). **Figure 9** depicts this multiplexed sensor.

AuNP arrays are useful in immunoassays for several reasons. First, they increase the electrode surface area. Second, they facilitate the attachment of numerous antibodies due to the easy functionalization of gold surfaces. The production of high-AuNP-coverage electrodes depends on both the stabilizing molecule on the gold surface and the electrode surface. Often, it is necessary to coat the electrode with a layer of molecules that increase the adhesion of the AuNP. For example, positively charged polyelectrolytes such as PDDA [poly(diallyldimethylammonium chloride)] can be used to increase the AuNP's adhesion. Similar electrodes have been produced for multiplexed protein detection by use of carbon nanotube arrays, but their detection limits, reproducibility, and stability were lower than those of the AuNPs arrays (124, 126, –127).

Multiplexing, as discussed above, is based on the use of an array of differently functionalized electrodes. Geometrically, the number of electrodes that can be used in parallel is limited (128). However, as an alternative to electrode arrays, spatial resolution and, thus, multiplexing capability can be achieved by use of a light pointer in connection with a semiconducting electrode surface to select defined points on an electrode surface (129–131). The light pointer creates a local

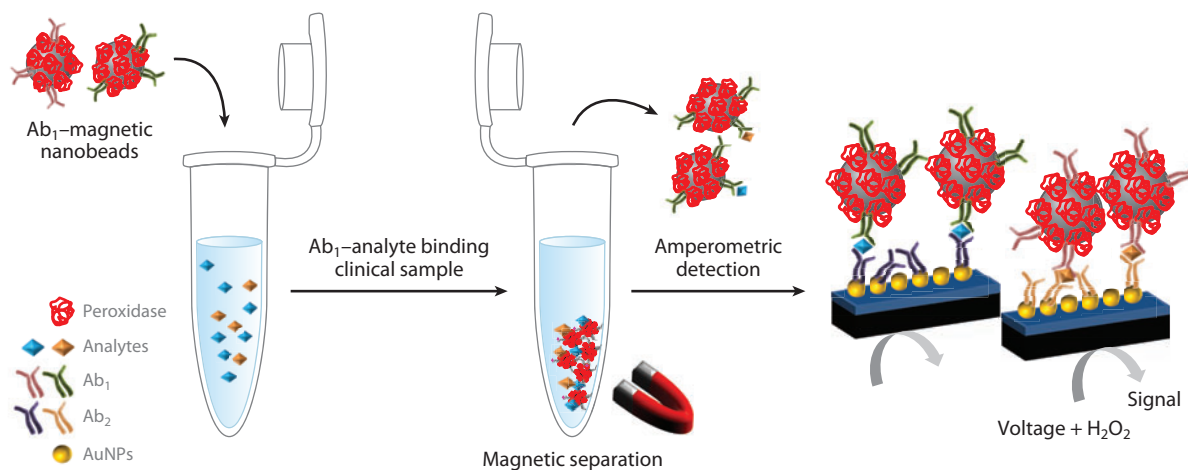


Figure 9

A gold nanoparticle (AuNP) array functionalized with antibodies (Ab_2) for the ultrasensitive detection of cancer biomarkers. The sensor also contains magnetic beads labeled with antibodies (Ab_1) and horseradish peroxidase for amplification and biomarker capture. Multiplexing is achieved through parallel detection in different electrodes.

photocurrent whose amplitude is influenced by local redox reactions on the electrode surface. The semiconductor layer can be constructed from QDs (57, 58). The first observations of enzymatic reactions have already been reported (55, 66, 132, 133). Although multiplexed analysis has not yet been practically demonstrated, its spatial resolution capability clearly demonstrates its potential.

3.2.3. Giant magnetoresistive sensors. Giant magnetoresistive (GMR) sensors are a promising and low-cost alternative for the detection of proteins and nucleic acids. In the former case, antibodies arrays must be prepared beforehand to specifically capture the corresponding analyte. Functionalized MNPs in solution that bind the same antigen are used to detect the presence of an analyte by measuring the small changes in resistance due to the binding event in the presence of a magnetic field. Multiplexed sensors have been developed using this technique, but their reproducibility and sensitivity remain compromised in extended sensing applications with real and untreated samples (134–138).

There are many other examples of the use of NP arrays or NPs as labels in immunoassays, such as chemiluminescence imaging immunoassays involving horseradish peroxidase and AuNPs (139). New strategies for multiplexing with planar arrays are continually being introduced due to their significant possibilities in multifunctional NP synthesis and the application of new materials, such as fluorescent nano-graphene oxide and ensemble aptamers instead of more specific DNAs for analyte recognition (140).

4. MULTIMODAL IMAGING

In recent years, many applications of NPs to bioimaging and diagnosis have been developed (141–143). The most important example is undoubtedly the use of MNPs in magnetic resonance imaging (MRI) (144–147). However, many other NP applications are expected to find clinical use in the near future. Advances in colloidal chemistry have enabled “à la carte” design of multifunctional particles. By combining elements such as radioactive isotopes, QDs (31, 148), and organic dyes in the same nanostructure or microparticle, one can easily obtain

multimodal nano- or microcomposites. The use of multimodal labels is necessary to overcome the limits of any single technique, such as spatial resolution or bleaching. Cheon & Lee (149) explored these ideas on the basis of multimodal imaging probes consisting of MNPs with further functionalities, namely radionuclides enabling positron emission tomography and fluorescent moieties for optical tracking. These probes can be modified with anchor molecules such as antibodies, peptides, DNA, and RNA, permitting the investigators to address specific targets.

Liong et al. (150) provided an example of advantageous MNP-based multimodal systems. These authors applied multifunctional iron oxide–mesoporous silica NPs that were detectable both optically and by MRI. They rendered the particles suitable for live-cell imaging and therapeutic purposes by targeting them specifically to human cancer cells. Moreover, those particles were simultaneously used to deliver hydrophobic anticancer drugs (or other molecules) into cells.

Nahrendorf et al. (151) investigated a comparable trimodal imaging system comprising MRI (iron oxide core), PET sensors (chelator ligand complexing the radiotracer Cu^{64}), and fluorescence (VivoTag-680TM) that enabled *in vivo* studies of the detection of macrophage markers, specifically, the detection of inflammatory atherosclerosis. Given the lower required concentration of NPs and their higher target-to-background ratio, the authors found this technique especially relevant for clinical use. The production of nano- or microprobes for multimodal imaging *in vivo* can be difficult, mainly because of targeting issues (152, 153), the colloidal stability and purity of the probes, the retention time *in vivo* (154), the long-term stability of the signal, degradability, possible toxicity, and the clearance mechanisms of the probes in humans. Degradation over the long term and dissolution of the nanoprobe within the body are very difficult to avoid, in particular in the case of corrosive NP materials such as CdSe or silver. Regarding *in vivo* applications, the use of toxic materials (e.g., radiotracers) or materials that deliver toxic ions during dissolution (e.g., CdSe QDs) should be minimized. Nevertheless, in specific instances, the lack of a diagnosis would be worse for the patient than the risk posed by the probe itself (e.g., a PET sensor).

Several types of multimodal particle platforms exist. On the NP level, for example, polymer-coated NPs purified with gel electrophoresis and size-exclusion chromatography fulfill most of the above-mentioned requirements (80, 155). They are very stable and pure (156–158); their size is reasonably small; and in the size range longest blood circulation time (10–100 nm) (159), the surface charge can be varied (160), the polymer shell itself does not impose enhanced cytotoxicity (161), and the polymer protecting the core can be loaded with functional entities (162). For these NPs, the inorganic core can be used as the first label (for example, it can be made magnetic, fluorescent, or radioactive), and the second label can be incorporated within the amphiphilic polymer that stabilizes the NP surface (155, 157, 158). Both labels are thereby protected from the biological environment, which helps improve signal stability and leaves the NP surface free for further functionalization by, for instance, cell-penetrating peptides, molecular receptors, or molecules that improve cell circulation such as poly(ethylene glycol) (154). **Figure 10** presents examples of such probes.

Fluorescent microscopy can be conveniently combined with SERS imaging through the incorporation of dyes, SERS probes, and even surface-enhanced resonance Raman scattering (SERRS)-active labels in the same multifunctional particle. Core-shell particles made from a gold core and an organosilica shell are good platforms for the simultaneous entrapment of fluorophores and SERS probes. Cui et al. (163) produced ~100-nm-diameter core-shell particles loaded with fluorescein isothiocyanate and malachite green isothiocyanate (green dye and SERS label). In a further demonstration of multiplexing, the authors synthesized similar particles with fluorescein isothiocyanate and X-rhodamine-5-(6)-isothiocyanate (green dye and SERRS label) (**Figure 11a**). Multimodal imaging in living cells was thereby demonstrated with these two differently labeled types of particles.

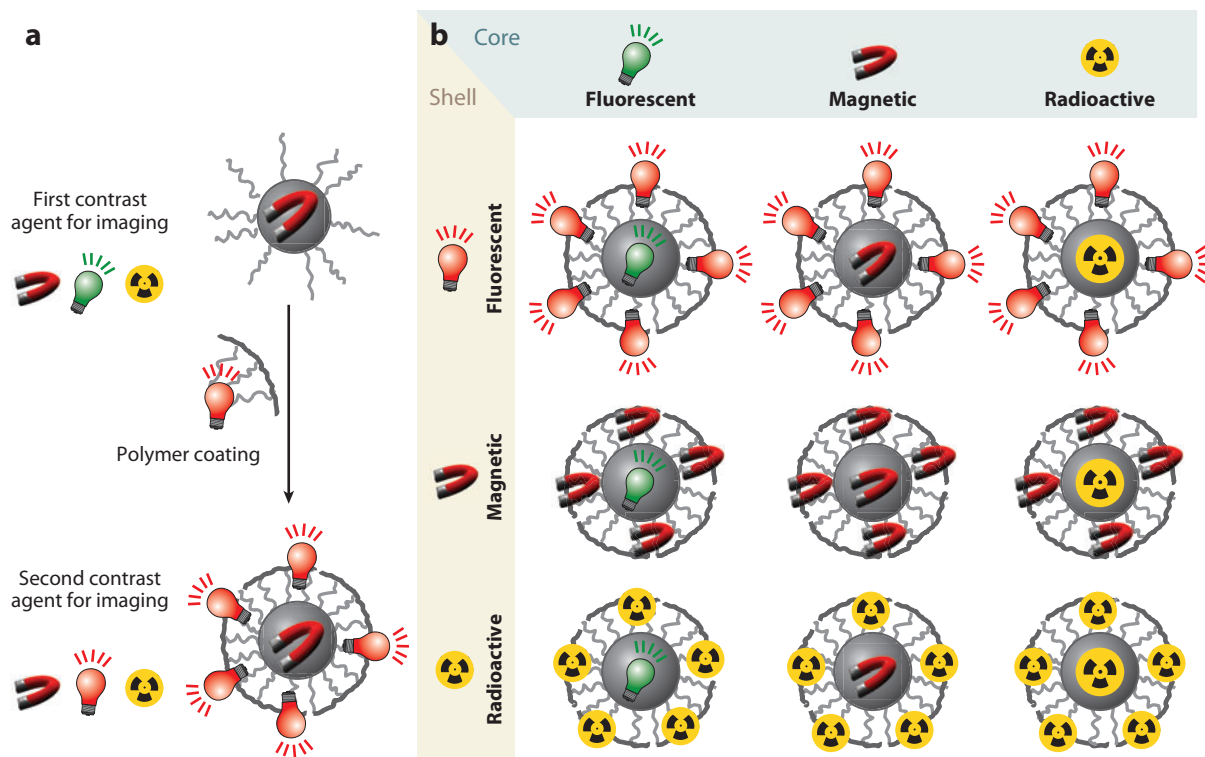


Figure 10

Strategy to produce multifunctional nanoparticles (NPs) for dual imaging. (a) Inorganic cores (gray) can be synthesized with different materials that are magnetic, fluorescent, or radioactive. Organic molecules are stabilized the NP surface following core synthesis. The cores are coated with an amphiphilic polymer that makes them water soluble. The amphiphilic polymer is loaded prior to coating with the second label (fluorophore, radioactive atom, etc.), and the final NP is double labeled. (b) Table including the possibilities of NPs for dual imaging based on polymer-coated NPs.

Currently, SERS imaging is limited by light penetration. NPs can be detected at a maximum depth of 1 cm (164). The combination of SERS with techniques such as spatially offset Raman spectroscopy could pave the way for clinical detection because the depth can be increased to up to 5 cm (165). In SERS applications and, more importantly, in bioimaging, the metallic surface of the NPs should be protected with an appropriate shell that hinders the adsorption of molecular species that could interfere with the vibrational code of the SERS probe. Silica shells have been used primarily for SERS applications and for multimodal imaging based on colloidal NPs because of their (a) reduced agglomeration, (b) biocompatibility, (c) optical transparency, (d) tunable porosity, (e) chemical inertness, and (f) ease of further functionalization (166). **Figure 11** shows several examples of multimodal NP imaging probes built up with silica shells and different inorganic cores. Not only do silica shells act as protective shells, but also they can be loaded with fluorophores, SERS and SERRS labels, or other NPs (**Figure 11a**). For example, the surface of $\text{Fe}_3\text{O}_4@\text{SiO}_2$ core-shell particles was further functionalized with AuNRs for in vivo MRI and IR imaging (167). Also, more than two imaging modalities can be used within one NP (**Figure 11c**). Hwang et al. (41) have produced quadruple-labeled particles by first coating cobalt ferrite NPs with a silica shell entrapping rhodamine B isothiocyanate and then functionalizing the silica surface with an organic dye. The bioluminescent protein luciferase was added as a third label and radioactive $^{68}\text{GaCl}_3$ as

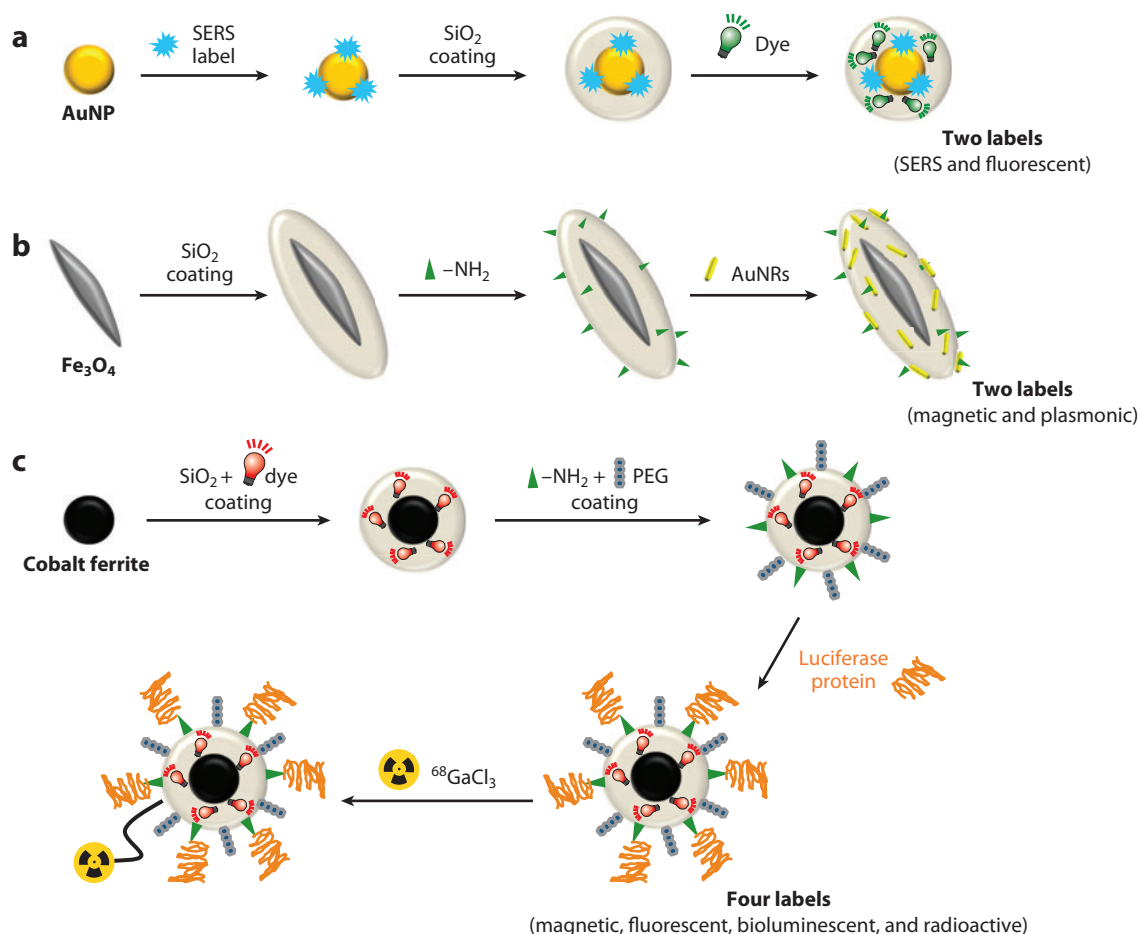


Figure 11

Different multimodal nanoparticle (NP) probes made with core-shell particles involving silica coating. (a) Particles for surface-enhanced Raman spectroscopy (SERS) and fluorescence imaging. Gold nanoparticles (AuNPs) are coated with a silica layer that entraps both the SERS probe and the fluorophore. Image adapted from Cui et al. (163). (b) Particles for in vivo magnetic resonance imaging and IR thermal imaging. Fe₃O₄ ellipsoids are coated with silica and gold nanorods (AuNRs). Image adapted from Ma et al. (167). (c) Quadruple imaging based on a magnetic core coated with a silica shell embedding a fluorophore, and further silica surface functionalization with a bioluminescent protein and a radioactive isotope. Abbreviation: PEG, poly(ethylene glycol). Data adapted from Hwang et al. (41).

the fourth. These particles were successfully used in five in vivo imaging techniques: fluorescence, bioluminescence, BRET, positron emission tomography, and MRI. The same authors monitored in vivo and in vitro uptake in target cells of similar particles that were functionalized with specific aptamers with fluorescent microscopy, radioactive detection, and MRI (168).

Silica shells have also helped produce lanthanide-based multifunctional NPs. Upconverting NPs are interesting for multimodal imaging due to their special 4f electron structure, their rich optical and magnetic properties, their biocompatibility, and the tunability of their emission wavelength (169). More importantly, the upconversion of light due to anti-Stokes emission significantly minimized the background and simplified the discrimination of the signal from the target tissues or cells, compared with other optical techniques. Core-shell trimodal particles involving silica shells

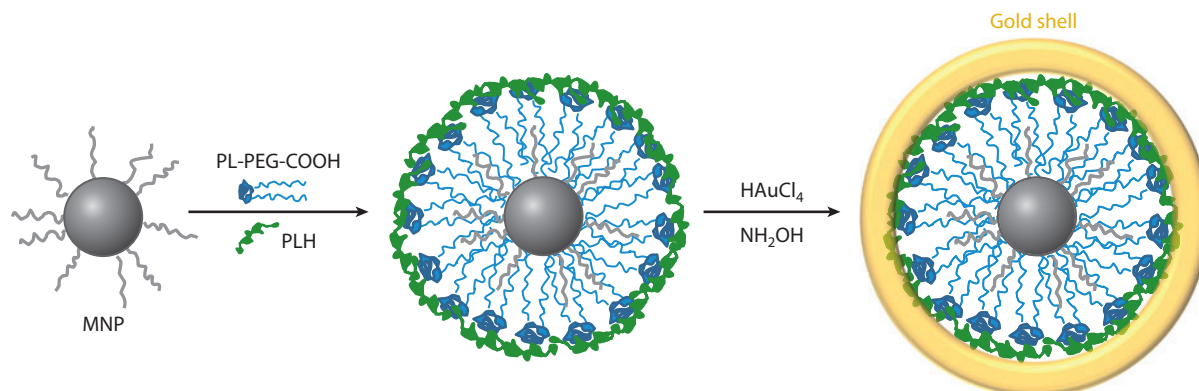


Figure 12

Core-shell iron oxide-gold nanoparticles. Magnetic nanoparticles (MNPs) were initially stabilized with oleic acid (*gray*), then coated with phospholipid-poly(ethylene glycol) (PL-PEG)-COOH and polyhistidine (PLH) to form a gold layer through the reduction of the salt HAuCl_4 by NH_2OH on the particle surface.

have recently been produced for X-ray computed tomography, MRI, and fluorescence imaging, demonstrating their suitability for further *in vitro* and *in vivo* applications (170, 171).

Multifunctional particles can also extend the application of certain imaging techniques, such as for magnetophotoacoustic (MPA) imaging. MPA imaging is based on the synergy of magnetomotive ultrasound, photoacoustic, and ultrasound imaging. It is a noninvasive technique that can be applied in diagnosis. To this end, Jin et al. (172) recently introduced a new class of core-shell NPs made from an iron oxide core and a gold shell separated by phospholipid-poly(ethylene glycol) and a layer of polyhistidine (**Figure 12**). Due to the hybrid nature of these NPs, their contrast, resolution, and sensitivity obtained in ultrasound imaging were acceptable. Otherwise, the technique is not yet good enough in terms of contrast, although it remains interesting due to its resolution at reasonable depths, nonionizing nature, cost-effectiveness, and portability. Moreover, the particles can be imaged with electron microscopy, MRI, and scattering-based techniques.

Multilayer polyelectrolyte capsules are promising candidates for multimodal imaging because they can simultaneously incorporate several labels that are spatially separated. In Section 3.1, we describe bar-coded capsules for multiplexed analysis (44). Multimodal imaging can be easily achieved in the same manner by combining organic labels with inorganic NPs that act as contrast agents. In addition to optical detection with fluorescence microscopy, the magnetic properties of capsules loaded with superparamagnetic NPs are suitable for MRI (173). Moreover, Johnston et al. (174) have demonstrated that it is possible to control the binding and uptake of such capsules on target cells by antibody labeling.

5. IMAGING AND SENSING

Many multifunctional NPs can be used for either imaging or sensing. The classical example is iron oxide-based NPs, which are useful in MRI as negative-contrast agents (image darkening) and in magnetoresistive immunoassays as nanotags (134, 144). However, there are fewer examples of particles that can be applied simultaneously to *in vivo* or *in vitro* imaging and sensing. The application of multifunctional particles for such purposes could lead to great advances in diagnosis. The size of NPs is similar to that of ribosomes and some proteins; therefore, NPs may be able to simultaneously detect and localize changes in biomolecule or ion concentrations that are related

to many diseases. In this context, nanoprobe based on organic polymers have been used to simultaneously image and estimate local concentrations of O_2 in vitro (175, 176). Moreover, polymer matrices such as PEBBLE nanosensors have incorporated several fluorophores for imaging and ratiometric determination of in vitro ion concentrations (177). Rare earth-doped NPs have been used as in vitro and in vivo luminescent tags and temperature sensors (178, 179). Recently, SERS nanotags were simultaneously employed to image and detect cancer biomarkers in vivo (94).

Another alternative, similar to PEBBLE sensors, is the nanostructured production of polymer microcapsules that simultaneously incorporate NPs and fluorophores that are sensitive to different analytes (44, 180). In vitro experiments to estimate pH changes in cells have been performed, but given the feasibility for multifunctionalization involving bar-coding, antibody functionalization, and ratiometric measurements, many future applications involving simultaneous imaging and sensing are likely (44, 174, 181).

6. OUTLOOK

This review describes many strategies for multiplexed sensing and multimodal imaging involving multifunctional nano- and microparticles. Although interesting examples have been published, most of these techniques have not yet been used for detection with real samples, such as blood serum, or for in vivo imaging. Some of these sensing techniques still lack reproducibility. With regard to in vitro detection, DNA arrays, for example, have been successfully used for multiplexed sensing of various analytes. However, the values obtained for the analyte concentrations are often only informative and not quantitative. Antibody arrays are promising substitutes for DNA arrays because they can detect, in the case of gene expression, proteins directly from protein-antigen interactions, so quantification should be easier to perform. However, the use of antibodies for analyte trapping or recognition poses certain problems. The epitope where antibody-antigen binding takes part is only a small part of the analyte, and antibodies often aberrantly bind epitopes of nontargeted analytes. Some of the examples discussed above regarding antibody arrays involve several antibody-antigen binding events to reduce cross-reactivity. New amplification methods are currently being developed to improve sensitivity by improving analyte-receptor interaction specificity, as is the case in applications of orthogonal chemistries to diagnosis and imaging (107, 182). Particle stability (76) still poses a problem for in vivo applications such as particle-based sensors and contrast agents for imaging. Circulation within the bloodstream and further uptake in target tissues remain the most critical challenges for nanomedicine (183).

DISCLOSURE STATEMENT

The authors are not aware of any affiliations, memberships, funding, or financial holdings that might be perceived as affecting the objectivity of this review.

ACKNOWLEDGMENTS

Parts of our work were supported by DFG (Germany; grant PA794/11-1 to W.J.P.) and the European Commission (a nanogistics grant to W.J.P.). We acknowledge technical discussions with Dr. Gaëlle Charron.

LITERATURE CITED

1. Bruchez MJ, Moronne M, Gin P, Weiss S, Alivisatos AP. 1998. Semiconductor nanocrystals as fluorescent biological labels. *Science* 281:2013-16

2. Chan WCW, Nie S. 1998. Quantum dot bioconjugates for ultrasensitive nonisotopic detection. *Science* 281:2016–18
3. Alivisatos AP. 2004. The use of nanocrystals in biological detection. *Nat. Biotechnol.* 22:47–51
4. Elghanian R, Storhoff JJ, Mucic RC, Letsinger RL, Mirkin CA. 1997. Selective colorimetric detection of polynucleotides based on the distance-dependent optical properties of gold nanoparticles. *Science* 277:1078–81
5. Khlebtsov B, Panfilova E, Khanadeev V, Bibikova O, Terentyuk G, et al. 2012. Nanocomposites containing silica-coated gold–silver Nanocages and Yb-2,4-dimethoxyhematoporphyrin: multifunctional capability of IR-luminescence detection, photosensitization, and photothermolysis. *Am. Chem. Soc. Nano* 5:7077–89
6. Jakhmola A, Anton N, Vandamme TF. 2012. Inorganic nanoparticles based contrast agents for X-ray computed tomography. *Adv. Healthc. Mater.* 1:413–31
7. Judenhofer MS, Wehrl HF, Newport DF, Catana C, Siegel SB, et al. 2008. Simultaneous PET-MRI: a new approach for functional and morphological imaging. *Nat. Med.* 14:459–65
8. Ross P, Hall L, Smirnov I, Haff L. 1998. High level multiplex genotyping by MALDI-TOF mass spectrometry. *Nat. Biotechnol.* 16:1347–51
9. Kotov N. 2011. Bioimaging: The only way is up. *Nat. Mater.* 10:903–4
10. Jans H, Huo Q. 2012. Gold nanoparticle-enabled biological and chemical detection and analysis. *Chem. Soc. Rev.* 41:2849–66
11. Freeman R, Willner I. 2012. Optical molecular sensing with semiconductor quantum dots (QDs). *Chem. Soc. Rev.* 41:4067–85
12. Jimenez de Aberasturi D, Montenegro JM, Ruiz de Larramendi I, Rojo T, Klar TA, et al. 2012. Optical sensing of small ions with colloidal nanoparticles. *Chem. Mater.* 24:738–45
13. Scotognella F, Della Valle G, Kandada ARS, Dorfs D, Zavelani-Rossi M, et al. 2011. Plasmon dynamics in colloidal Cu_{2-x}Se nanocrystals. *Nano Lett.* 11:4711–17
14. McFarland AD, Van Duyne RP. 2003. Single silver nanoparticles as real-time optical sensors with zeptomole sensitivity. *Nano Lett.* 3:1057–62
15. Rodríguez-Lorenzo L, de la Rica R, Álvarez-Puebla RA, Liz-Marzán LM, Stevens MM. 2012. Plasmonic nanosensors with inverse sensitivity by means of enzyme-guided crystal growth. *Nat. Mater.* 11:604–7
16. Claridge SA, Schwartz JJ, Weiss PS. 2011. Electrons, photons, and force: quantitative single-molecule measurements from physics to biology. *Am. Chem. Soc. Nano* 5:693–729
17. Ament I, Prasad J, Henkel A, Schmachtel S, Soennichsen C. 2012. Single unlabeled protein detection on individual plasmonic nanoparticles. *Nano Lett.* 12:1092–95
18. Saha K, Agasti SS, Kim C, Li X, Rotello VM. 2012. Gold nanoparticles in chemical and biological sensing. *Chem. Rev.* 112:2739–79
19. Leuvinger JHW, Thal P, Vanderwaart M, Schuurs A. 1981. A sol particle agglutination assay for human chorionic gonadotropin. *J. Immunol. Methods* 45:183–94
20. Taton TA, Mirkin CA, Letsinger RL. 2000. Scanometric DNA array detection with nanoparticle probes. *Science* 289:1757–60
21. Zhao W, Chiuman W, Lam JCF, McManus SA, Chen W, et al. 2008. DNA aptamer folding on gold nanoparticles: from colloid chemistry to biosensors. *J. Am. Chem. Soc.* 130:3610–18
22. Beqa L, Singh AK, Khan SA, Senapati D, Arumugam SR, Ray PC. 2011. Gold nanoparticle-based simple colorimetric and ultrasensitive dynamic light scattering assay for the selective detection of Pb(II) from paints, plastics, and water samples. *Am. Chem. Soc. Appl. Mater. Interfaces* 3:668–73
23. Aldeanueva-Potel P, Correa-Duarte MA, Álvarez-Puebla RA, Liz-Marzán LM. 2010. Free-standing carbon nanotube films as optical accumulators for multiplex SERRS attomolar detection. *Am. Chem. Soc. Appl. Mater. Interfaces* 2:19–22
24. Álvarez-Puebla RA, Agarwal A, Manna P, Khanal BP, Aldeanueva-Potel P, et al. 2011. Gold nanorods 3D supercrystals as surface enhanced Raman scattering spectroscopy substrates for the rapid detection of scrambled prions. *Proc. Natl. Acad. Sci. USA* 108:8157–61
25. Song J, Zhou J, Duan H. 2012. Self-assembled plasmonic vesicles of SERS-encoded amphiphilic gold nanoparticles for cancer cell targeting and traceable intracellular drug delivery. *J. Am. Chem. Soc.* 134:13458–69

26. Tsoutsis D, Montenegro JM, Dommershausen F, Koert U, Liz-Marzán LM, et al. 2011. Quantitative surface-enhanced Raman ultradetection of atomic inorganic ions: the case of chloride. *Am. Chem. Soc. Nano* 5:7539–46
27. Boyer D, Tamarat P, Maali A, Lounis B, Orrit M. 2002. Photothermal imaging of nanometer-sized metal particles among scatterers. *Science* 297:1160–63
28. Lasne D, Blab GA, Berciaud S, Heine M, Groc L, et al. 2006. Single nanoparticle photothermal tracking (SNaPT) of 5-nm gold beads in live cells. *Biophys. J.* 91:4598–604
29. Dreaden EC, Alkilany AM, Huang X, Murphy CJ, El-Sayed MA. 2012. The golden age: gold nanoparticles for biomedicine. *Chem. Soc. Rev.* 41:2740–79
30. Ku G, Zhou M, Song S, Huang Q, Hazle J, Li C. 2012. Copper sulfide nanoparticles as a new class of photoacoustic contrast agent for deep tissue imaging at 1,064 nm. *Am. Chem. Soc. Nano* 6:7489–96
31. Michalet X, Pinaud FF, Bentolila LA, Tsay JM, Doose S, et al. 2005. Quantum dots for live cells, in vivo imaging, and diagnostics. *Science* 307:538–44
32. Jamieson T, Bakhshi R, Petrova D, Pocock R, Imani M, Seifalian AM. 2007. Biological applications of quantum dots. *Biomaterials* 28:4717–32
33. Erogbogbo F, Yong K-T, Roy I, Xu G, Prasad PN, Swihart MT. 2008. Biocompatible luminescent silicon quantum dots for imaging of cancer cells. *Am. Chem. Soc. Nano* 2:873–78
34. Erogbogbo F, Chang C-W, May JL, Liu L, Kumar R, et al. 2012. Bioconjugation of luminescent silicon quantum dots to gadolinium ions for bioimaging applications. *Nanoscale* 4:5483–89
35. Fowley C, McCaughan B, Devlin A, Yildiz I, Raymo FM, Callan JF. 2012. Highly luminescent biocompatible carbon quantum dots by encapsulation with an amphiphilic polymer. *Chem. Commun.* 48:9361–63
36. Dong Y, Wang R, Li G, Chen C, Chi Y, Chen G. 2012. Polyamine-functionalized carbon quantum dots as fluorescent probes for selective and sensitive detection of copper ions. *Anal. Chem.* 84:6220–24
37. Lin CAJ, Yang TY, Lee CH, Huang SH, Sperling RA, et al. 2009. Synthesis, characterization, and bioconjugation of fluorescent gold nanoclusters toward biological labeling applications. *Am. Chem. Soc. Nano* 3:395–401
38. Huang S, Pfeiffer C, Hollmann J, Friede S, Chen JJ-C, et al. 2012. Synthesis and characterization of colloidal fluorescent silver nanoclusters. *Langmuir* 28:8915–19
39. Hilderbrand SA, Shao F, Salthouse C, Mahmood U, Weissleder R. 2009. Upconverting luminescent nanomaterials: application to in vivo bioimaging. *Chem. Commun.* 2009:4188–90
40. Wang F, Banerjee D, Liu Y, Chen X, Liu X. 2010. Upconversion nanoparticles in biological labeling, imaging, and therapy. *Analyst* 135:1839–54
41. Hwang DW, Ko HY, Kim S-K, Kim D, Lee DS, Kim S. 2009. Development of a quadruple imaging modality by using nanoparticles. *Chem. Eur. J.* 15:9387–93
42. Park EJ, Brasuel M, Behrend C, Philbert MA, Kopelman R. 2003. Ratiometric optical PEBBLE nanosensors for real-time magnesium ion concentrations inside viable cells. *Anal. Chem.* 75:3784–91
43. Giri S, Sykes EA, Jennings TL, Chan WCW. 2011. Rapid screening of genetic biomarkers of infectious agents using quantum dot barcodes. *Am. Chem. Soc. Nano* 5:1580–87
44. del Mercato LL, Abbasi AZ, Ochs M, Parak WJ. 2011. Multiplexed sensing of ions with barcoded polyelectrolyte capsules. *Am. Chem. Soc. Nano* 5:9668–74
45. del Mercato LL, Abbasi AZ, Parak WJ. 2011. Synthesis and characterization of ratiometric ion-sensitive polyelectrolyte capsules. *Small* 7:351–63
46. Lowe SB, Dick JAG, Cohen BE, Stevens MM. 2012. Multiplex sensing of protease and kinase enzyme activity via orthogonal coupling of quantum dot-peptide conjugates. *Am. Chem. Soc. Nano* 6:851–57
47. Marin MJ, Galindo F, Thomas P, Russell DA. 2012. Localized intracellular pH measurement using a ratiometric photoinduced electron-transfer-based nanosensor. *Angew. Chem. Int. Ed.* 51:9657–61
48. Algar WR, Wegner D, Huston AL, Blanco-Canosa JB, Stewart MH, et al. 2012. Quantum dots as simultaneous acceptors and donors in time-gated Förster resonance energy transfer relays: characterization and biosensing. *J. Am. Chem. Soc.* 134:1876–91
49. Freeman R, Liu X, Willner I. 2011. Chemiluminescent and chemiluminescence resonance energy transfer (CRET) detection of DNA, metal ions, and aptamer-substrate complexes using Hemin/G-quadruplexes and CdSe/ZnS quantum dots. *J. Am. Chem. Soc.* 133:11597–604

50. Xia Z, Xing Y, So MK, Koh AL, Sinclair R, Rao J. 2008. Multiplex detection of protease activity with quantum dot nanosensors prepared by intein-mediated specific bioconjugation. *Anal Chem* 80:8649–55
51. Maltez-da Costa M, de la Escosura-Muñiz A, Nogués C, Barrios L, Ibáñez E, Merkoçi A. 2012. Simple monitoring of cancer cells using nanoparticles. *Nano Lett.* 12:4164–71
52. Yáñez-Sedeño P, Pingarrón JM, Riu J, Rius FX. 2010. Electrochemical sensing based on carbon nanotubes. *Trends Anal. Chem.* 29:939–53
53. Luo X, Morrín A, Killard AJ, Smyth MR. 2006. Application of nanoparticles in electrochemical sensors and biosensors. *Electroanalysis* 18:319–26
54. Xu J-J, Luo X-L, Du Y, Chen H-Y. 2004. Application of MnO₂ nanoparticles as an eliminator of ascorbate interference to amperometric glucose biosensors. *Electrochem. Commun.* 6:1169–73
55. Khalid W, Helou ME, Murböck T, Yue Z, Montenegro J-M, et al. 2011. Immobilization of quantum dots via conjugated self-assembled monolayers and their application as a light-controlled sensor for the detection of hydrogen peroxide. *Am. Chem. Soc. Nano* 5:9870–76
56. Ko JW, Woo J-M, Jinhong A, Cheon JH, Lim JH, et al. 2011. Multi-order dynamic DNA sensor using a gold decorated SWCNT random network. *Am. Chem. Soc. Nano* 5:4365–72
57. Stoll C, Kudera S, Parak WJ, Lisdat F. 2006. Quantum dots on gold:electrodes for photoswitchable cytochrome *c* electrochemistry. *Small* 2:741–43
58. Katz E, Zayats M, Willner I, Lisdat F. 2006. Controlling the direction of photocurrents by means of CdS nanoparticles and cytochrome *c*-mediated biocatalytic cascades. *Chem. Commun.* 2006:1395–97
59. Hočevar SB, Wang J, Deo RP, Musameh M, Ogorevc B. 2005. Carbon nanotube modified microelectrode for enhanced voltammetric detection of dopamine in the presence of ascorbate. *Electroanalysis* 17:417–22
60. Liu B, Zhang B, Cui Y, Chen H, Gao Z, Tang D. 2011. Multifunctional gold-silica nanostructures for ultrasensitive electrochemical immunoassay of streptomycin residues. *Am. Chem. Soc. Appl. Mater. Interfaces* 3:4668–76
61. Zelada-Guillén GA, Sebastián-Avila JL, Blondeau P, Riu J, Rius FX. 2012. Label-free detection of *Staphylococcus aureus* in skin using real-time potentiometric biosensors based on carbon nanotubes and aptamers. *Biosens. Bioelectron.* 31:226–32
62. Zhang J, Song S, Zhang L, Wang L, Wu H, et al. 2006. Sequence-specific detection of femtomolar DNA via a chronocoulometric DNA sensor (CDS): effects of nanoparticle-mediated amplification and nanoscale control of DNA assembly at electrodes. *J. Am. Chem. Soc.* 128:8575–80
63. Wang J. 2005. Nanomaterial-based electrochemical biosensors. *Analyst* 130:421–26
64. Willner I, Willner B, Tel-Vered R. 2011. Electroanalytical applications of metallic nanoparticles and supramolecular nanostructures. *Electroanalysis* 23:13–28
65. Hiep HM, Endo T, Saito M, Chikae M, Kim DK, et al. 2008. Label-free detection of melittin binding to a membrane using electrochemical-localized surface plasmon resonance. *Anal. Chem.* 80:1859–64
66. Khalid W, Göbel G, Hühn D, Montenegro JM, Rivera Gil P, et al. 2011. Light triggered detection of aminophenyl phosphate with a quantum dot based enzyme electrode. *J. Nanobiotechnol.* 9:46
67. Pankhurst QA, Connolly J, Jones SK, Dobson J. 2003. Applications of magnetic nanoparticles in biomedicine. *J. Phys. D* 36:R167–81
68. Colombo M, Carregal-Romero S, Casula MF, Gutiérrez L, Morales MP, et al. 2012. Biological applications of magnetic nanoparticles. *Chem. Soc. Rev.* 41:4306–34
69. Moros M, Pelaz B, López-Larrubia P, García-Martin ML, Grazú V, de la Fuente JM. 2010. Engineering biofunctional magnetic nanoparticles for biotechnological applications. *Nanoscale* 2:1746–55
70. Alcantara D, Guo Y, Yuan H, Goergen CJ, Chen HH, et al. 2012. Fluorochrome-functionalized magnetic nanoparticles for high-sensitivity monitoring of the polymerase chain reaction by magnetic resonance. *Angew. Chem. Int. Ed.* 51:6904–7
71. Koh I, Josephson L. 2009. Magnetic nanoparticle sensors. *Sensors* 9:8130–45
72. Hathaway HJ, Butler KS, Adolphi NL, Lovato DM, Belfon R, et al. 2011. Detection of breast cancer cells using targeted magnetic nanoparticles and ultra-sensitive magnetic field sensors. *Breast Cancer Res.* 13:R108
73. Gaster RS, Xu L, Han S-J, Wilson RJ, Hall DA, et al. 2011. Quantification of protein interactions and solution transport using high-density GMR sensor arrays. *Nat. Nanotechnol.* 6:314–20

74. Perez JM, Josephson L, O'Loughlin T, Högemann D, Weissleder R. 2002. Magnetic relaxation switches capable of sensing molecular interactions. *Nat. Biotechnol.* 20:816–20
75. Wang Y, Fang F, Shi C, Zhang X, Liu L, et al. 2012. Evaluation of a method for the simultaneous detection of multiple tumor markers using a multiplex suspension bead array. *Clin. Biochem.* 45:1394–98
76. Rivera-Gil P, Jimenez de Aberasturi D, Wulf V, Pelaz B, del Pino P, et al. 2012. The challenge to relate the physicochemical properties of colloidal nanoparticles to their cytotoxicity. *Acc. Chem. Res.* In press. doi:10.1021/ar300039j
77. Abbasi AZ, Amin F, Niebling T, Friede S, Ochs M, et al. 2011. How colloidal nanoparticles could facilitate multiplexed measurements of different analytes with analyte-sensitive organic fluorophores. *Am. Chem. Soc. Nano* 5:21–25
78. Zhang F, Ali Z, Amin F, Feltz A, Oheim M, Parak WJ. 2010. Ion and pH sensing with colloidal nanoparticles: influence of surface charge on sensing and colloidal properties. *ChemPhysChem* 11:730–35
79. Riedinger A, Zhang F, Dommershausen F, Röcker C, Brandholt S, et al. 2010. Ratiometric optical sensing of chloride ions with organic fluorophore–gold nanoparticle hybrids: a systematic study of distance dependency and the influence of surface charge. *Small* 6:2590–97
80. Zhang F, Lees E, Amin F, Rivera-Gil P, Yang F, et al. 2011. Polymer-coated nanoparticles: a universal tool for biolabelling experiments. *Small* 7:3113–27
81. Cedervall T, Lynch I, Lindman S, Berggård T, Thulin E, et al. 2007. Understanding the nanoparticle–protein corona using methods to quantify exchange rates and affinities of proteins for nanoparticles. *Proc. Natl. Acad. Sci. USA* 104:2050–55
82. Jiang X, Weise S, Hafner M, Röcker C, Zhang F, et al. 2010. Quantitative analysis of the protein corona on FePt nanoparticles formed by transferrin binding. *J. R. Soc. Interface* 7:S5–13
83. Amin F, Yushchenko DA, Montenegro JM, Parak WJ. 2012. Integration of organic fluorophores in the surface of polymer-coated colloidal nanoparticles for sensing the local polarity of the environment. *ChemPhysChem* 13:1030–35
84. Freeman R, FINDER T, Willner I. 2009. Multiplexed analysis of Hg²⁺ and Ag⁺ ions by nucleic acid functionalized CdSe/ZnS quantum dots and their use for logic gate operations. *Angew. Chem. Int. Ed.* 48:7818–21
85. Jin R, Cao Y, Mirkin CA, Kelly KL, Schatz GC, Zheng JG. 2001. Photoinduced conversion of silver nanospheres to nanoprisms. *Science* 294:1901–3
86. Yu C, Irudayaraj J. 2007. Multiplex biosensor using gold nanorods. *Anal. Chem.* 79:572–79
87. Yu C, Nakshatri H, Irudayaraj J. 2007. Identity profiling of cell surface markers by multiplex gold nanorod probes. *Nano Lett.* 7:2300–6
88. Wang C, Irudayaraj J. 2008. Gold nanorod probes for the detection of multiple pathogens. *Small* 4:2204–8
89. Fernández-López C, Mateo-Mateo C, Álvarez-Puebla RA, Pérez-Juste J, Pastoriza-Santos I, Liz-Marzán LM. 2009. Highly controlled silica coating of PEG-capped metal nanoparticles and preparation of SERS-encoded particles. *Langmuir* 25:13894–99
90. Abalde-Cela S, Aldeanueva-Potel P, Mateo-Mateo C, Rodríguez-Lorenzo L, Álvarez-Puebla RA, Liz-Marzán LM. 2010. Surface-enhanced Raman scattering biomedical applications of plasmonic colloidal particles. *J. R. Soc. Interface* 7:S435–50
91. Raez J, Blais DR, Zhang Y, Álvarez-Puebla RA, Bravo-Vasquez JP, et al. 2007. Spectroscopically encoded microspheres for antigen biosensing. *Langmuir* 23:6482–85
92. Sanles-Sobrido M, Exner W, Rodríguez-Lorenzo L, Rodríguez-Gonzalez B, Correa-Duarte MA, et al. 2009. Design of SERS-encoded, submicron, hollow particles through confined growth of encapsulated metal nanoparticles. *J. Am. Chem. Soc.* 131:2699–705
93. Kim K, Lee YM, Lee HB, Shin KS. 2009. Silver-coated silica beads applicable as core materials of dual-tagging sensors operating via SERS and MEF. *Am. Chem. Soc. Appl. Mater. Interfaces* 1:2174–80
94. Maiti KK, Dinish US, Samanta A, Vendrell M, Soh K-S, et al. 2012. Multiplex targeted in vivo cancer detection using sensitive near-infrared SERS nanotags. *Nano Today* 7:85–93
95. Sanchez-Iglesias A, Aldeanueva-Potel P, Ni WH, Pérez-Juste J, Pastoriza-Santos I, et al. 2010. Chemical seeded growth of Ag nanoparticle arrays and their application as reproducible SERS substrates. *Nano Today* 5:21–27

96. Jiang ZY, Jiang XX, Su S, Wei XP, Lee ST, He Y. 2012. Silicon-based reproducible and active surface-enhanced Raman scattering substrates for sensitive, specific, and multiplex DNA detection. *Appl. Phys. Lett.* 100:203104
97. Kang T, Yoo SM, Yoon I, Lee SY, Kim B. 2010. Patterned multiplex pathogen DNA detection by Au particle-on-wire SERS sensor. *Nano Lett.* 10:1189–93
98. Wang Z, Zong S, Li W, Wang C, Xu S, et al. 2012. SERS-fluorescence joint spectral encoding using organic-metal-QD hybrid nanoparticles with a huge encoding capacity for high-throughput biodetection: putting theory into practice. *J. Am. Chem. Soc.* 134:2993–3000
99. Nagl S, Wolfbeis OS. 2007. Optical multiple chemical sensing: status and current challenges. *Analyst* 132:507–11
100. Grabolle M, Kapusta P, Nann T, Shu X, Ziegler J, Resch-Genger U. 2009. Fluorescence lifetime multiplexing with nanocrystals and organic labels. *Anal. Chem.* 81:7807–13
101. Ruedas-Rama MJ, Orte A, Hall EAH, Alvarez-Pez JM, Talavera EM. 2011. Quantum dot photoluminescence lifetime-based pH nanosensor. *Chem. Commun.* 47:2898–900
102. Peng X, Yang Z, Wang J, Fan J, He Y, et al. 2011. Fluorescence ratiometry and fluorescence lifetime imaging: using a single molecular sensor for dual mode imaging of cellular viscosity. *J. Am. Chem. Soc.* 133:6626–35
103. Kim J-H, Patra CR, Arkalgud JR, Boghossian AA, Zhang J, et al. 2011. Single-molecule detection of H₂O₂ mediating angiogenic redox signaling on fluorescent single-walled carbon nanotube array. *Am. Chem. Soc. Nano* 5:7848–57
104. Geissler D, Charbonnière L, Ziessel R, Butlin N, Löhmansröben HG, Hildebrandt N. 2010. Quantum dot biosensors for ultrasensitive multiplexed diagnostics. *Angew. Chem. Int. Ed.* 49:1396–401
105. Freeman R, Liu X, Willner I. 2011. Amplified multiplexed analysis of DNA by the exonuclease III-catalyzed regeneration of the target DNA in the presence of functionalized semiconductor quantum dots. *Nano Lett.* 11:4456–61
106. Haun JB, Devaraj NK, Marinelli BS, Lee H, Weissleder R. 2012. Probing intracellular biomarkers and mediators of cell activation using nanosensors and bioorthogonal chemistry. *Am. Chem. Soc. Nano* 5:3204–13
107. Peterson VM, Castro CM, Lee H, Weissleder R. 2012. Orthogonal amplification of nanoparticles for improved diagnostic sensing. *Am. Chem. Soc. Nano* 6:3506–13
108. Shipway AN, Katz E, Willner I. 2000. Nanoparticle arrays on surfaces for electronic, optical, and sensor applications. *ChemPhysChem* 1:18–52
109. Katz E, Willner I. 2004. Integrated nanoparticle-biomolecule hybrid systems: synthesis, properties, and applications. *Angew. Chem. Int. Ed.* 43:6042–108
110. Ferguson JA, Steemers FJ, Walt DR. 2000. High-density fiber-optic DNA random microsphere array. *Anal. Chem.* 72:5618–24
111. Pregibon DC, Toner M, Doyle PS. 2007. Multifunctional encoded particles for high-throughput biomolecule analysis. *Science* 315:1393–96
112. Zamborini FP, Bao L, Dasari R. 2012. Nanoparticles in measurement science. *Anal. Chem.* 84:541–76
113. Mayer KM, Hafner JH. 2011. Localized surface plasmon resonance sensors. *Chem. Rev.* 111:3828–57
114. He S, Liu K-K, Su S, Yan J, Mao X, et al. 2012. Graphene-based high-efficiency surface-enhanced Raman scattering-active platform for sensitive and multiplex DNA detection. *Anal. Chem.* 84:4622–27
115. Endo T, Kerman K, Nagatani N, Hiepa HM, Kim D-K, et al. 2006. Multiple label-free detection of antigen-antibody reaction using localized surface plasmon resonance-based core-shell structured nanoparticle layer nanochip. *Anal. Chem.* 78:6465–75
116. Kim D, Daniel WL, Mirkin CA. 2009. Microarray-based multiplexed scanometric immunoassay for protein cancer markers using gold nanoparticle probes. *Anal. Chem.* 81:9183–87
117. Stoeva SI, Lee J-S, Smith JE, Rosen ST, Mirkin CA. 2006. Multiplexed detection of protein cancer markers with biobarcode nanoparticle probes. *J. Am. Chem. Soc.* 128:8378–79
118. Kim D-K, Yoo S-M, Park T-J, Yoshikawa H, Tamiya E-I, et al. 2011. Plasmonic properties of the multispot copper-capped nanoparticle array chip and its application to optical biosensors for pathogen detection of multiplex DNAs. *Anal. Chem.* 83:6215–22

119. Chen S, Svedendahl M, Van Duyne RP, Kaell M. 2011. Plasmon-enhanced colorimetric ELISA with single molecule sensitivity. *Nano Lett.* 11:1826–30
120. Skladal P. 1997. Advances in electrochemical immunosensors. *Electroanalysis* 9:737–45
121. Wilson MS, Nie W. 2006. Electrochemical multianalyte immunoassays using an array-based sensor. *Anal. Chem.* 78:2507–13
122. Akter R, Rahman MA, Rhee CK. 2012. Amplified electrochemical detection of a cancer biomarker by enhanced precipitation using horseradish peroxidase attached on carbon nanotubes. *Anal. Chem.* 84:6407–15
123. Lai G, Yan F, Wu J, Leng C, Ju H. 2011. Ultrasensitive multiplexed immunoassay with electrochemical stripping analysis of silver nanoparticles catalytically deposited by gold nanoparticles and enzymatic reaction. *Anal. Chem.* 83:2726–32
124. Mani V, Chikkaveeraiah BV, Patel V, Gutkind JS, Rusling JF. 2009. Ultrasensitive immunosensor for cancer biomarker proteins using gold nanoparticle film electrodes and multienzyme–particle amplification. *Am. Chem. Soc. Nano* 3:585–94
125. Malhotra R, Patel V, Chikkaveeraiah BV, Munge BS, Cheong SC, et al. 2012. Ultrasensitive detection of cancer biomarkers in the clinic by use of a nanostructured microfluidic array. *Anal. Chem.* 84:6249–55
126. Chikkaveeraiah BV, Bhirde A, Malhotra R, Patel V, Gutkind JS, Rusling James F. 2009. Single-wall carbon nanotube forest arrays for immunoelectrochemical measurement of four protein biomarkers for prostate cancer. *Anal. Chem.* 81:9129–34
127. Zarei H, Ghourchian H, Eskandari K, Zeinali M. 2012. Magnetic nanocomposite of anti-human IgG/COOH-multiwalled carbon nanotubes/Fe₃O₄ as a platform for electrochemical immunoassay. *Anal. Biochem.* 421:446–53
128. George M, Parak WJ, Gaub HE. 2000. Highly integrated surface potential sensors. *Sens. Actuators B* 69:266–75
129. Hafeman DG, Parce JW, McConnell HM. 1988. Light-addressable potentiometric sensor for biochemical systems. *Science* 240:1182–85
130. Lundström I, Erlandsson R, Frykman U, Hedborg E, Spetz A, et al. 1991. Artificial “olfactory” images from a chemical sensor using a light-pulse technique. *Nature* 352:47–50
131. Parak WJ, Hofmann UG, Gaub HE, Owicki JC. 1997. Lateral resolution of light addressable potentiometric sensors: an experimental and theoretical investigation. *Sens. Actuators A* 63:47–57
132. Tanne J, Schafer D, Khalid W, Parak WJ, Lisdat F. 2011. Light-controlled bioelectrochemical sensor based on CdSe/ZnS quantum dots. *Anal. Chem.* 83:7778–85
133. Schubert K, Khalid W, Yue Z, Parak WJ, Lisdat F. 2010. Quantum dot–modified electrode for the detection of NAD-dependent dehydrogenase reactions. *Langmuir* 26:1395–400
134. Li Y, Srinivasan B, Jing Y, Yao X, Hugger MA, et al. 2010. Nanomagnetic competition assay for low-abundance protein biomarker quantification in unprocessed human sera. *J. Am. Chem. Soc.* 132:4388–92
135. Mak AC, Osterfeld SJ, Yu H, Wang SX, Davis RW, et al. 2010. Sensitive giant magnetoresistive–based immunoassay for multiplex mycotoxin detection. *Biosens. Bioelectron.* 25:1635–39
136. Osterfeld SJ, Yu H, Gaster RS, Caramuta S, Xu L, et al. 2008. Multiplex protein assay based on real-time magnetic nanotag sensing. *Proc. Natl. Acad. Sci. USA* 105:20637–40
137. Hall DA, Gaster RS, Osterfeld SJ, Murmann B, Wang SX. 2010. GMR biosensor arrays: Correction techniques for reproducibility and enhanced sensitivity. *Biosens. Bioelectron.* 25:2177–81
138. Hall DA, Gaster RS, Osterfeld SJ, Murmann B, Wang SX. 2011. GMR biosensor arrays: correction techniques for reproducibility and enhanced sensitivity. *Biosens. Bioelectron.* 25:2177–81
139. Zong C, Wu J, Wang C, Ju H, Yan F. 2012. Chemiluminescence imaging immunoassay of multiple tumor markers for cancer screening. *Anal. Chem.* 84:2410–15
140. Pei H, Li J, Lv M, Wang J, Gao J, et al. 2012. A graphene-based sensor array for high-precision and adaptive target identification with ensemble aptamers. *J. Am. Chem. Soc.* 134:13843–49
141. He X, Wang K, Cheng Z. 2010. In vivo near-infrared fluorescence imaging of cancer with nanoparticle-based probes. *Wiley Interdiscip. Rev. Nanomed. Nanobiotechnol.* 2:349–66
142. Rivera-Gil P, Parak WJ. 2008. Composite nanoparticles take aim at cancer. *Am. Chem. Soc. Nano* 2:2200–5

143. Peteiro-Cartelle J, Rodríguez-Pedreira M, Zhang F, Rivera-Gil P, del Mercato LL, Parak WJ. 2009. One example on how colloidal nano- and microparticles could contribute to medicine. *Nanomedicine* 4:967–79
144. Weissleder R, Moore A, Mahmood U, Bhorade R, Benveniste H, et al. 2000. In vivo magnetic resonance imaging of transgene expression. *Nat. Med.* 6:351–55
145. Alexiou C, Arnold W, Hulin P, Klein RJ, Renz H, et al. 2001. Magnetic mitoxantrone nanoparticle detection by histology, X-ray and MRI after magnetic tumor targeting. *J. Magn. Magn. Mater.* 225:187–93
146. Morales MP, Bomati-Miguel O, de Alejo RP, Ruiz-Cabello J, Veintemillas-Verdaguer S, O’Grady K. 2003. Contrast agents for MRI based on iron oxide nanoparticles prepared by laser pyrolysis. *J. Magn. Magn. Mater.* 266:102–9
147. Harisinghani MG, Barentsz J, Hahn PF, Deserno WM, Tabatabaei S, et al. 2003. Noninvasive detection of clinically occult lymph-node metastases in prostate cancer. *N. Engl. J. Med.* 348:2491–99
148. Wang C, Gao X, Su XG. 2010. In vitro and in vivo imaging with quantum dots. *Anal. Bioanal. Chem.* 397:1397–415
149. Cheon J, Lee J-H. 2008. Synergistically integrated nanoparticles as multimodal probes for nanobiotechnology. *Acc. Chem. Res.* 41:1630–40
150. Liong M, Lu J, Kovichich M, Xia T, Ruehm SG, et al. 2008. Multifunctional inorganic nanoparticles for imaging, targeting, and drug delivery. *Am. Chem. Soc. Nano* 2:889–96
151. Nahrendorf M, Zhang HW, Hembrador S, Panizzi P, Sosnovik DE, et al. 2008. Nanoparticle PET-CT imaging of macrophages in inflammatory atherosclerosis. *Circulation* 117:379–87
152. Altinoğlu EI, Russin TJ, Kaiser JM, Barth BM, Eklund BC, et al. 2008. Near-infrared emitting fluorophore-doped calcium phosphate nanoparticles for in vivo imaging of human breast cancer. *Am. Chem. Soc. Nano* 2:2075–84
153. Kumar R, Roy I, Ohulchansky TY, Vathy LA, Bergey EJ, et al. 2010. In vivo biodistribution and clearance studies using multimodal organically modified silica nanoparticles. *Am. Chem. Soc. Nano* 4:699–708
154. Lipka M, Semmler-Behnke M, Sperling RA, Wenk A, Takenaka S, et al. 2010. Biodistribution of PEG-modified gold nanoparticles following intratracheal instillation and intravenous injection. *Biomaterials* 31:6574–81
155. Ali Z, Abbasi AZ, Zhang F, Arosio P, Lascialfari A, et al. 2011. Multifunctional nanoparticles for dual imaging. *Anal. Chem.* 83:2877–82
156. Sperling RA, Pellegrino T, Li JK, Chang WH, Parak WJ. 2006. Electrophoretic separation of nanoparticles with a discrete number of functional groups. *Adv. Funct. Mater.* 16:943–48
157. Fernández-Argüelles MT, Yakovlev A, Sperling RA, Luccardini C, Gaillard S, et al. 2007. Synthesis and characterization of polymer-coated quantum dots with integrated acceptor dyes as FRET-based nanoprobe. *Nano Lett.* 7:2613–17
158. Corato RD, Quarta A, Piacenza P, Ragusa A, Figuerola A, et al. 2008. Water solubilization of hydrophobic nanocrystals by means of poly(maleic anhydride-*alt*-1-octadecene). *J. Mater. Chem.* 18:1991–96
159. Sperling RA, Liedl T, Duhr S, Kudera S, Zanella M, et al. 2007. Size determination of (bio-)conjugated water-soluble colloidal nanoparticles—a comparison of different techniques. *J. Phys. Chem. C* 111:11552–59
160. Geidel C, Schmachtel S, Riedinger A, Pfeiffer C, Müllen K, et al. 2011. A general synthetic approach for obtaining cationic and anionic inorganic nanoparticles via encapsulation in amphiphilic copolymers. *Small* 7:2929–34
161. Lehmann AD, Parak WJ, Zhang F, Ali Z, Röcker C, et al. 2010. Fluorescent-magnetic hybrid nanoparticles induce a dose-dependent increase in proinflammatory response in lung cells in vitro correlated with intracellular localization. *Small* 6:753–62
162. Lin C-AJ, Sperling RA, Li JK, Yang T-Y, Li P-Y, et al. 2008. Design of an amphiphilic polymer for nanoparticle coating and functionalization. *Small* 4:334–41
163. Cui Y, Zheng XS, Ren B, Wang R, Zhang J, et al. 2011. Au@organosilica multifunctional nanoparticles for the multimodal imaging. *Chem. Sci.* 2:1463–69

164. McQueenie R, Stevenson R, Benson R, MacRitchie N, McInnes I, et al. 2012. Detection of inflammation in vivo by surface-enhanced Raman scattering provides higher sensitivity than conventional fluorescence imaging. *Anal. Chem.* 84:5968–75
165. Stone N, Kerssens M, Lloyd GR, Faulds K, Graham D, Matousek P. 2011. Surface enhanced spatially offset Raman spectroscopic (SESORS) imaging—the next dimension. *Chem. Sci.* 2:776–80
166. Guerrero-Martinez A, Pérez-Juste J, Liz-Marzán LM. 2012. Recent progress on silica coating of nanoparticles and related nanomaterials. *Adv. Mater.* 22:1182–95
167. Ma M, Chen H, Chen Y, Wang X, Chen F, et al. 2012. Au capped magnetic core/mesoporous silica shell nanoparticles for combined photothermo-/chemo-therapy and multimodal imaging. *Biomaterials* 33:989–98
168. Hwang DW, Ko HY, Lee JH, Kang H, Ryu SH, et al. 2012. A nucleolin-targeted multimodal nanoparticle imaging probe for tracking cancer cells using an aptamer. *J. Nucl. Med.* 51:98–105
169. Wang F, Deng R, Wang J, Wang Q, Han Y, et al. 2011. Tuning upconversion through energy migration in core-shell nanoparticles. *Nat. Mater.* 10:968–73
170. Xia A, Chen M, Gao Y, Wu D, Feng W, Li F. 2012. Gd³⁺ complex-modified NaLuF₄-based up-conversion nanophosphors for trimodality imaging of NIR-to-NIR upconversion luminescence, X-ray computed tomography and magnetic resonance. *Biomaterials* 33:5394–405
171. Xing H, Bu W, Zhang S, Zheng X, Li M, et al. 2012. Multifunctional nanoprobe for upconversion fluorescence, MR and CT trimodal imaging. *Biomaterials* 33:1079–89
172. Jin Y, Jia C, Huang S-W, O'Donnell M, Gao X. 2010. Multifunctional nanoparticles as coupled contrast agents. *Nat. Commun.* 1:41
173. Abbasi AZ, Gutierrez L, del Mercato LL, Herranz F, Chubykalo-Fesenko O, et al. 2011. Magnetic capsules for NMR imaging: effect of magnetic nanoparticles spatial distribution and aggregation. *J. Phys. Chem. C* 115:6257–64
174. Johnston APR, Kamphuis MMJ, Such GK, Scott AM, Nice EC, et al. 2012. Targeting cancer cells: controlling the binding and internalization of antibody-functionalized capsules. *Am. Chem. Soc. Nano* 6:6667–74
175. Kondrashina AV, Dmitriev RI, Borisov SM, Klimant I, O'Brien I, et al. 2012. A phosphorescent nanoparticle-based probe for sensing and imaging of (intra)cellular oxygen in multiple detection modalities. *Adv. Func. Mater.* In press
176. Fercher A, Borisov SM, Zhdanov AV, Klimant I, Papkovsky DB. 2011. Intracellular O₂ sensing probe based on cell-penetrating phosphorescent nanoparticles. *Am. Chem. Soc. Nano* 5:5499–508
177. Si D, Epstein T, Lee Y-EK, Kopelman R. 2012. Nanoparticle PEBBLE sensors for quantitative nanomolar imaging of intracellular free calcium ions. *Anal. Chem.* 84:978–86
178. Vetrone F, Naccache R, Zamarrón A, Juarranz de la Fuente A, Sanz-Rodríguez F, et al. 2010. Temperature sensing using fluorescent nanothermometers. *Am. Chem. Soc. Nano* 4:3254–58
179. Dong B, Cao B, He Y, Liu Z, Li Z, Feng Z. 2012. Temperature sensing and in vivo imaging by molybdenum sensitized visible upconversion luminescence of rare-earth oxides. *Adv. Mater.* 24:1987–93
180. Carregal-Romero S, Ochs M, Parak WJ. 2012. Nanoparticle-functionalized microcapsules for in vitro delivery and sensing. *Nanophotonics* 1:171–80
181. Rivera-Gil P, Nazareus M, Ashraf S, Parak WJ. 2012. pH Sensitive capsules as intracellular optical reporters for monitoring lysosomal pH changes upon stimulation. *Small* 8:943–48
182. Yang KS, Budin G, Reiner T, Vinegoni C, Weissleder R. 2012. Bioorthogonal imaging of aurora kinase A in live cells. *Angew. Chem. Int. Ed.* 51:6598–603
183. Pelaz B, Jaber S, Jimenez de Aberasturi D, Wulf V, de la Fuente JM, et al. 2012. The state of nanoparticle-based nanoscience and biotechnology: progress, promises, and challenges. *Am. Chem. Soc. Nano* 6:8468–83